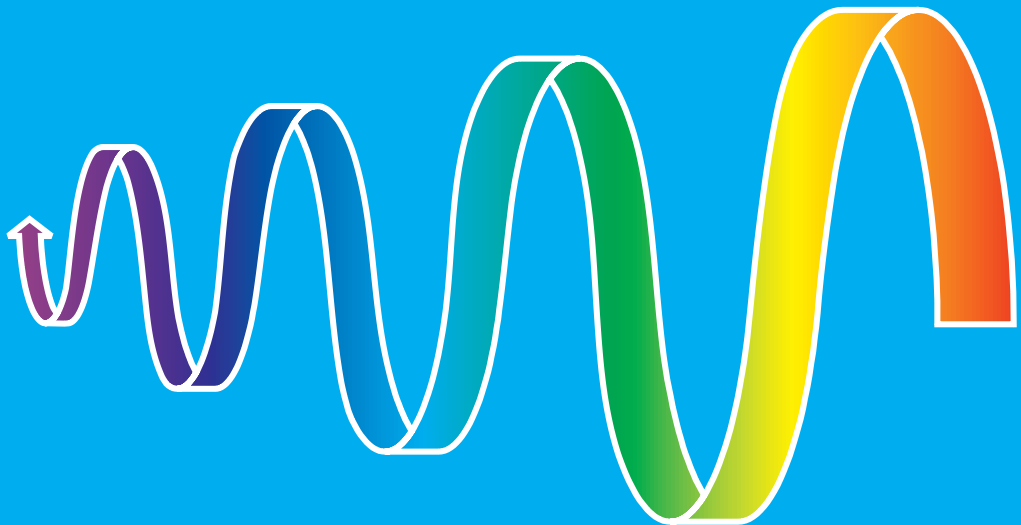


Turbid Flows and Their Deposits on Slopes with Minibasins

A Modelling Approach

Xiaoxi Wang



Turbid Flows and Their Deposits on Slopes with Minibasins

A Modelling Approach

Xiaoxi WANG

Turbid Flows and Their Deposits on Slopes with Minibasins

A Modelling Approach

Proefschrift

ter verkrijging van de graad van doctor
aan de Technische Universiteit Delft,
op gezag van de Rector Magnificus prof. dr. ir. K.C.A.M. Luyben,
voorzitter van het College voor Promoties,
in het openbaar te verdedigen op Maandag, 19 januari 2015 om 15.00 uur

door

Xiaoxi WANG

Master of Science
in Mineralogy, Petrology, Mineral Deposit Geology
Yangtze University, China
geboren te Puyang, Henan Province, China

Dit proefschrift is goedgekeurd door de promotor:

Prof. dr. S.M. Luthi

Samenstelling promotiecommissie:

| | |
|----------------------------|---|
| Rector Magnificus | voorzitter |
| Prof. dr. S.M. Luthi | Technische Universiteit Delft, promotor |
| Prof. dr. G. Bertotti | Technische Universiteit Delft |
| Prof. dr. S.B. Kroonenberg | Technische Universiteit Delft |
| Prof. dr. G.J. Weltje | Katholieke Universiteit Leuven, België |
| Dr. D. Sokoutis | Universiteit Utrecht |
| Dr. D.M. Hodgson | University of Leeds, UK |
| Dr. R.S. Jacinto | Ifremer, Brest, France |

This research was funded by the China Scholarship Council (CSC) and the Netherlands Research Centre For Integrated Solid Earth Science (ISES).

ISBN: 978-94-6295-067-2

Copyright © 2014 by Xiaoxi Wang. All rights reserved. No part of the material protected by this copyright notice may be reproduced or utilized in any form or by any means, electronic or mechanical, including photocopying, recording or by any information storage and retrieval system, without the prior permission of the copyright owner.

Published by: Uitgeverij BOX Press, 's-Hertogenbosch, The Netherlands

Printed by: Proefschriftmaken.nl

Dedicated to my dearest family

Content

| | |
|--|-----------|
| 1 Introduction | 1 |
| 1.1 Background | 1 |
| 1.2 Objective and methodology..... | 3 |
| 1.3 Thesis outline | 4 |
| 2 Salt Tectonics on Passive Margins and the Formation of Minibasins | 7 |
| 2.1 Introduction | 7 |
| 2.2 Salt tectonics and structures..... | 8 |
| 2.2.1 Salt properties | 8 |
| 2.2.2 Driving mechanisms of salt flow | 8 |
| 2.2.3 Diapirism and salt structures | 8 |
| 2.2.4 Salt-related minibasins..... | 12 |
| 2.3 Passive margins | 15 |
| 2.3.1 What is a passive margin?..... | 15 |
| 2.3.2 Evolution of passive margins..... | 15 |
| 2.4 Salt tectonics on passive margins..... | 17 |
| 2.4.1 Salt basins on passive margins | 17 |
| 2.4.2 Gravity-driven salt tectonics on passive margins..... | 19 |
| 2.4.3 Gravity gliding and spreading | 19 |
| 2.4.4 The northern Gulf of Mexico vs. offshore Angola..... | 22 |
| 2.5 Study methods of salt passive margins..... | 27 |
| 2.5.1 Outcrop..... | 27 |
| 2.5.2 Subsurface data..... | 27 |
| 2.5.3 Laboratory experiments | 27 |
| 2.5.4 Numerical experiments..... | 28 |
| 3 Experimental Modelling of Passive Margin Bathymetries under the Influence of Salt Tectonics | 31 |
| 3.1 Introduction | 31 |
| 3.2 Laboratory modelling of passive margin bathymetries | 32 |
| 3.2.1 The natural prototype..... | 32 |
| 3.2.2 Model material and scaling considerations..... | 33 |
| 3.2.3 Model setup | 35 |
| 3.2.4 Results of the experiments | 37 |
| 3.3 Comparison and discussion of experimental results..... | 48 |
| 3.3.1 Extensional structures..... | 48 |

| | | |
|----------|---|-----------|
| 3.3.2 | Compressional structures | 51 |
| 3.3.3 | Minibasins | 52 |
| 3.4 | Digital elevation model | 53 |
| 4 | A Review of Subaqueous Turbidity Currents, Turbidites and Their Confined Systems | 55 |
| 4.1 | Introduction | 55 |
| 4.2 | Density flows and sediment gravity flows..... | 56 |
| 4.2.1 | Density flows..... | 56 |
| 4.2.2 | Sediment gravity flows..... | 56 |
| 4.3 | Subaqueous turbidity currents and turbidites | 58 |
| 4.3.1 | Natural initiation and associated subaqueous turbidity currents .. | 58 |
| 4.3.2 | Experimental modelling and dynamics of subaqueous turbidity currents..... | 62 |
| 4.3.3 | Anatomy..... | 64 |
| 4.3.4 | Stratification..... | 67 |
| 4.3.5 | Flow abilities and turbidite deposits..... | 68 |
| 4.3.6 | Classic models of turbidite systems..... | 74 |
| 4.4 | Confined turbidity currents and turbidites..... | 78 |
| 4.4.1 | Turbidity currents encountering obstacles..... | 78 |
| 4.4.2 | Turbidites under topographic controls..... | 81 |
| 4.4.3 | Confinement of intraslope minibasins on passive margins | 83 |
| 4.4.4 | Confinement of depositional topographies | 91 |
| 5 | Numerical Modelling of Turbidity Currents and Depositional Stratigraphy in Slope Minibasins..... | 93 |
| 5.1 | Introduction | 93 |
| 5.2 | Methodology | 94 |
| 5.2.1 | FanBuilder | 94 |
| 5.2.2 | Input topography: seabed bathymetry | 95 |
| 5.2.3 | Flow parameters | 97 |
| 5.3 | Non-equilibrium inflows | 99 |
| 5.3.1 | Flow evolution..... | 99 |
| 5.3.2 | Flow-deposit interaction | 106 |
| 5.3.3 | Depositional architecture | 110 |
| 5.4 | Supercritical equilibrium inflows..... | 118 |
| 5.4.1 | Flow evolution..... | 118 |
| 5.4.2 | Flow-deposit interaction | 124 |
| 5.4.3 | Depositional architecture | 128 |
| 5.5 | Subcritical equilibrium inflows | 133 |
| 5.5.1 | Flow evolution..... | 133 |
| 5.5.2 | Deposit..... | 133 |
| 5.6 | Discussion | 140 |
| 5.6.1 | Comparison of experimental results | 140 |
| 5.6.2 | Comparison with other studies | 143 |

| | |
|--|------------|
| 6 Conclusions and Recommendations | 149 |
| 6.1 Main conclusions..... | 149 |
| 6.2 Recommendations for future work | 151 |
| References | 153 |
| Summary | 181 |
| Samenvatting | 183 |
| Acknowledgements | 187 |
| Curriculum Vitae | 189 |

CHAPTER 1

Introduction

1.1 Background

Deep-water siliciclastic systems are dominantly fed by turbidity currents, and a focus of geological research as they form some of the largest depositional systems on the planet, representing significant archives of environmental change and forming major hydrocarbon reservoirs. Early models of submarine fans emphasized a simple submarine slope profile that was dominated by bypass processes that fed sediment via turbidity currents on an unconfined bathymetric setting to form a composite body with a radial form that comprises lobe deposits fed by a distributary channel network (Normark, 1970, 1978; Walker, 1978; Stow et al., 1985; Reading and Richards, 1994). However, recent studies revealed that complicated pre-existing or dynamic seabed bathymetries are normal, even on passive margins, and that the changes in gradient and orientation of the seabed has a fundamental influence on turbidity current behavior, sediment dispersal patterns, and the geometries and architectures of depositional bodies (e.g., Van Andel and Komar, 1969; Pickering and Hiscott, 1985; Kneller et al., 1991; Alexander and Morris, 1994; Kneller, 1995; Simpson, 1997; Hodgson and Haughton, 2004; Gervais et al., 2006; Amy et al., 2007; Covault and Romans, 2009; Moody et al., 2012; Albertão et al., 2011, 2014).

Passive continental margins display a great diversity of seabed bathymetry on the submarine slope, between the shelf-edge-break, and the continental rise. These bathymetric perturbations can arise from a wide range of processes including underlying rigid structures, gravity-driven extensional faulting and concomitant compressional folding, and diapiric movements of salt or mud (Fig. 1.1). In many diapirically controlled settings, complicated slope bathymetries are characterized by numerous ridges and/or mini-basins such as offshore the Gulf of Mexico (e.g., Diegel et al. 1995; Rowan and Weimer, 1998; Prather, 2000; Lamb et al., 2006; Hudec et al., 2013a), West Africa (e.g., Duval et al., 1992; Liro and Coen, 1995; Marton et al., 2000; Hudec and Jackson, 2004; Brun and Fort, 2011), offshore Brazil (e.g., Demercian et al., 1993; Cobbold et al., 1995; Roberts et al., 2004; Mohriak et al., 2012; Guerra and Underhill, 2012) and the North Sea (Coward and Stewart 1995; Kockel, 1998; Mannie et al., 2014).

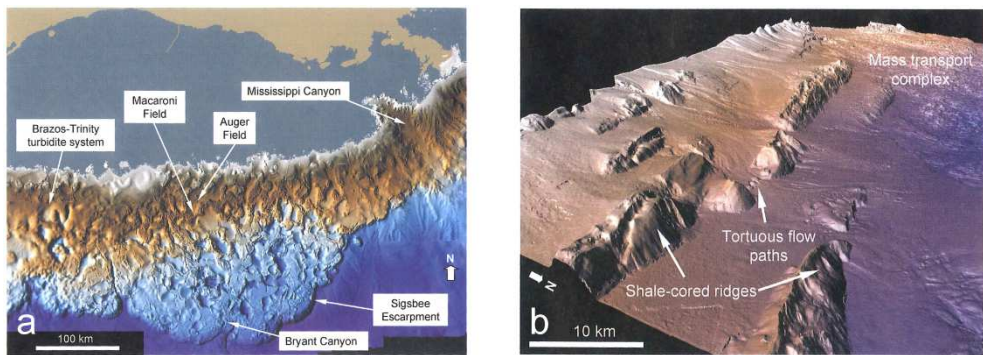


Figure 1.1: (a) A rendered seafloor image of the Gulf of Mexico salt-based slope. (b) Stepped topography on the northwest Borneo slope. From Smith (2004).

These bathymetries play a significant role in controlling turbidity current behavior, flow pathways and sediment distribution (Kneller and McCaffrey, 1999; McCaffrey and Kneller, 2001; Hodgson and Haughton, 2004; Gee and Gawthorpe, 2006; Lamb et al., 2006; Oluboyo et al., 2014; Albertão et al., 2011, 2014). Several conceptual models have been proposed to predict the filling history of linked minibasins, such as the fill-and-spill models (e.g., Winker, 1996; Prather et al., 1998; Weimer et al., 1998; Prather, 2000; Beauboeuf and Friedman, 2000; Sinclair and Tomasso, 2002). Smith (2004) distinguished two end members based on the degree and planform style of confinement: i) cascades of silled sub-basins and ii) connected tortuous corridors. More detailed conceptual models for successive mini-basins were described and modified by numerous researchers based on the specific confinement settings (e.g., Sinclair, 2000; Sinclair and Tomasso, 2002; Brunt et al., 2004; Lamb et al., 2004; Prather et al., 2012).

The depositional architectures on submarine slopes are used to unravel the interplay between sediment gravity flow processes and pre-existing and/or dynamic bathymetries. For this, well-exposed outcrops with 3D control or high-resolution 3D

reflection seismic data would be required. Only few case studies document such high quality data (e.g., Gervais et al., 2006; Moody et al., 2012; Van der Merwe, 2014). Most outcrops are exposed essentially in two dimensions and thus offer only partial information on the sedimentary architecture (Shanmugam and Muiola, 1991; Shanmugam, 2000; Satur et al., 2000). Due to inherent limitations of geophysical techniques, most seismic data is not adequate when trying to resolve the desired sedimentary details and small-scale stacking patterns. Commonly, surface and subsurface layers experience post-depositional processes such as compaction, diapirism, and tectonic deformation that can change their original geometry and architecture. For these reasons, the sediment dispersal and stacking patterns in bathymetrically complicated settings, including diapiric settings with ridges and minibasins, are still not well understood. Yet these confined turbidity systems have been increasingly attracting the attention of academic and industrial researchers, for conceptual and commercial reasons.

1.2 Objective and methodology

In order to better understand the interactions between the pre-existing bathymetries, turbidity currents and turbidite deposits, and to investigate the internal architecture and compensational patterns of confined turbidite systems in linked intraslope minibasins, a novel method that integrates laboratory tectonic analogue experiments (successive-minibasin topography) and numerical flow modelling (multiple turbidity-current events) is adopted in this study (Fig. 1.2).

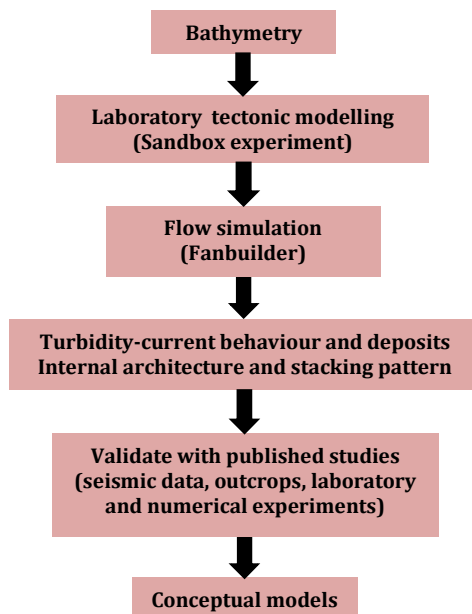


Figure 1.2: Flow diagram of the method adopted in this study.

The first step was to conduct analogue tectonic experiments using sandbox models in the ISES tectonic laboratory at the Vrije Universiteit Amsterdam, in order to obtain the bathymetry of minibasins on passive margins bearing salt. Sandbox analogue experiments are widely used to model the evolution of a large variety of deformation types in structural geology and tectonics (e.g., Colletta, et al., 1991; Sokoutis and Willingshofer, 2011; Willingshofer et al., 2013; Luth et al., 2013; Philippon et al., 2014). Analogue models driven by gravitational forces have proven to be an effective method in the investigation of deformation mechanisms of salt tectonics on passive margins (e.g., the Gulf of Mexico and the South Atlantic margins) (e.g., Vendeville and Cobbold, 1988; Cobbold and Szatmari, 1991; Vendeville and Jackson, 1992a, b; Demercian et al., 1993; Guerra and Szatmari, 2009; Brun and Fort, 2004, 2011). Layers with different properties are stacked on top of each other in order to simulate a clastic sedimentary succession that accumulated above a salt layer on a continental slope. The resulting topography is then scanned by a laser beam from which a digital elevation model is obtained. This is then upscaled to dimensions that are comparable to those that occur in nature. A channel is added on the shelf and the shelf-edge break to serve as point source for the flows. The detailed methodology of this approach is expanded upon in Chapter 3.

Numerical models of sediment gravity flows, especially process-based modelling, have been validated with physical models (Kubo, 2004), natural events (Pirmez and Imran, 2003; Dan et al., 2007; Salles et al., 2008; Abd El-Gawa et al., 2012) and the reconstruction of the internal architecture of turbidite systems based on studies of outcrop or seismic data (Aas et al., 2010, 2014; Albertao et al., 2011, 2014). In this study, the process-based numerical flow model FanBuilder (previously validated, Groenenberg et al., 2009, 2010; Athmer et al., 2010) is employed, in order to develop predictable conceptual models to account for changes in sediment dispersal and stacking patterns of turbiditic successions deposited in diapiric minibasins on passive margins. FanBuilder numerically simulates low-density turbidity currents. Flows were introduced from the incised channel down into the minibasins on the synthetic continental margin. A series of parameters within ranges expected to occur in nature were compiled from literature study and used in the flow simulation experiments. Multiple flow events (non-equilibrium and equilibrium flows) from the same point source were run whereby the deposits were stacked on top of their predecessors. The resulting synthetic sedimentary deposits were then analyzed in 3-D, in a series of strike and dip sections. The experimental results of a series of numerical simulations were compared and discussed in terms of the flow evolution, the flow-deposit interaction, and the internal architecture and stacking patterns. The results from the modeling are compared with the published natural and experimental examples that have been found to support our main conclusions.

1.3 Thesis outline

In Chapter 2 the background knowledge of salt tectonics on passive margins and associated minibasins is reviewed. It is a synthesis of published studies on the

evolution of passive margins bearing salt including studies that have used laboratory experiments, field outcrops and subsurface data.

The specific methods and processes of modelling the minibasins induced by the salt tectonics on passive margins are presented in Chapter 3. Four sandbox experiments with different configurations were conducted and the scanned 3D surface data were selected and modified as the topographic input parameter for the next-step numerical simulation.

Chapter 4 systematically reviews our understanding of subaqueous turbidity currents, their deposits (turbidites), and their characteristics in confined settings. The trigger mechanisms, the hydrodynamics, the depositional character and the sedimentary models of turbidite systems are also reviewed.

Chapter 5 presents the methodology and the results of a series of numerical simulation experiments of turbidity currents flowing over a bathymetry of channel-minibasins using the bathymetric template derived from work in Chapter 3. Two sets of flows are modeled, non-equilibrium and equilibrium flows. The results are compared with each other and discussed with related published literature.

Conclusions obtained from the simulation results and recommendations for future work are synthesized in Chapter 6.

CHAPTER 2

Salt Tectonics on Passive Margins and the Formation of Minibasins

2.1 Introduction

In this thesis, the objective is to use bathymetric data as input for the numerical modelling of turbidity currents and, as a prerequisite, to understand the interactions between salt tectonics, passive-margin topographies and turbidity-current sedimentation. Therefore, it is important to understand salt tectonics processes and their resultant structures on passive margins, which is also crucial for proper physical analogue experiments of modeling such tectonics. This chapter provides relevant background information on salt tectonics on passive margins in terms of salt properties, driving mechanisms of salt movement, typical salt structures (e.g., diapirs), salt-induced minibasins, and some actual field examples. Subsequently, methods of investigating salt tectonic evolution in passive margin settings are reviewed, including the use of subsurface data, numerical and physical analogue experiments.

2.2 Salt tectonics and structures

2.2.1 Salt properties

Salt tectonics in nature develop in the context of a series of geological activities and processes associated with subsurface salt layers and their ambient stratigraphic sequences. Such settings involve three fundamental strata: the underlying subsalt basement, the source salt layer, and the overlying sedimentary overburden. Salt possesses special physical properties of low viscosity and low density relative to its surrounding sedimentary strata, which can make it prone to move plastically much like a viscous fluid and deform easily (Hudec and Jackson, 2007).

2.2.2 Driving mechanisms of salt flow

The early explanation for salt movement stressed the buoyancy effect of salt owing to the density difference between salt and its denser overburden. This hypothesis simply and erroneously took the overlaying layer of subsurface salt for a viscous liquid with negligible yield strength (e.g., Nettleton, 1955; Talbot, 1992; Podladchikov et al., 1993). The overburden, however, is basically composed of brittle and stiff sedimentary rocks. Its strength, along with boundary frictions of the salt layer, restrict the flow of salt (Hudec and Jackson, 2007; Fossen, 2010). Salt flow and deformation is not driven by the salt itself. It is by virtue of external forces overcoming those resisting factors that salt is capable of flowing laterally and vertically into areas of lower pressure, intruding and even penetrating through the overlaying strata. At present, widely-accepted driving forces to trigger salt movement principally include differential loading (e.g., uneven weight distribution of the overburden caused by sedimentation or erosion) (Fig. 2.1a, b) (e.g., Harrison, 1927; Trusheim, 1960; Dailly, 1976; Jackson and Talbot, 1986; Last, 1988; Vendeville and Jackson, 1992a; Poliakov et al., 1993; Ge et al., 1997; Gemmer et al., 2004), external strain loading (regional contraction or extension) (Fig. 2.1c, d) (e.g., Jackson and Vendeville, 1994; Hudec and Jackson, 2007; Fossen, 2010) and thermal loading (Fig. 2.1e) (e.g., Talbot et al., 1982; Jackson et al., 1990). As a consequence, a variety of salt-related structures such as salt walls, domes, diapirs, nappes and canopies are built by the joint action of the above driving and restricting forces during the whole period of salt movement (Fig. 2.2).

2.2.3 Diapirism and salt structures

Salt diapirs are regarded as one of the typical salt tectonic products. They present varying forms of salt bodies controlled by different driving forces during different tectonic-sedimentary processes. Jackson (1995) defined salt diapirs as “any structurally discordant body of salt, regardless of its emplacement mechanism”.

Extensional Diapirism

A majority of salt-diapir provinces reveals that salt initiation and growth typically take place in extensional settings such as active rift basins and on the outer and upper

slope of passive margins (e.g., Tankard and Balkwill, 1989; Jackson and Vendeville, 1994; Rouby et al., 2002; Hudec and Jackson, 2007). Classical physical experiments carried out by Vendeville and Jackson (1992a) show that upwelling and growing of salt diapirs in extension primarily experiences four phases (Fig. 2.3a-d). Beginning with a reactive diapirism phase, the brittle overburden is weakened by normal faults and thinned by grabens and half grabens (Fig. 2.3a). This allows the system to induce differential loading and make space for the growth of the diapir. Salt closely responds to extension, which means that if regional extension stops, diapirism stops. This phenomena even can occur in settings where the overburden is equally or less dense than that the salt layer. If reactive diapirism is faster than the ongoing sedimentation and the salt's overlying layer is thinning to a critical thickness, the diapir is able to actively rise up against the overburden by buoyancy rather than extension. This stage is called active diapirism (Fig. 2.3b). Once active diapirism is sufficient to make the diapir break through its roof, a passive diapir may continue on its way up. Salt domes can be attributed to passive diapirism (Fig. 2.4c). If sedimentation is slower than the rate of passive diapirism, extrusive allochthonous salt sheets can form when the upwelling diapir reaches or even emplaces on its younger overburden surface (Fig. 2.3d). However, if the salt layer is too thin to maintain the diapirism, only extensional normal fault systems and associated salt rollers (Fig. 2.2) will dominate in extensional settings. Besides, salt movements in extensional settings also include the fall of preexisting salt diapirs (Fig. 2.1d) such as the subsidence of minibasins (Vendeville and Jackson, 1992b).

Compressional diapirism

In regional contractional settings, such as orogenic zones (e.g., the Zagros mountain belt, Koyi, 1988; the Northern Pyrenees collisional orogeny, Hayward and Graham, 1989) and the downdip toes of passive margins (e.g., the lower slope of the Lower Congo Basin passive margins, Cramez and Jackson, 2000), salt diapirs can be explained by the modification of many preexisting diapirs initiated in the earlier extensional stage (Jackson and Vendeville, 1994). In such settings, the salt roof is likely to uplift into an anticline or can be faulted by thrusts owing to lateral shortening. Therefore, preexisting deformed salt (e.g. salt domes) can be pressured up into anticlines (e.g. tear-drop shape; Fig. 2.4), squeezed up along thrust faults to a new location within sediment layers or even emplaced on newly-formed sediment layers (e.g. thrust allochthonous; Fig. 2.4). Later, these new salt structures are gradually detached from their sources. During this process, the system also can undergo active and passive diapirism and involve the related fault structures. In compressional settings, density inversion is not necessary for the formation of passive diapirs, because the major driving force is the salt pressure acting on the compactional forces (Hudec and Jackson, 2007). In the absence of preexisting diapirs, the salt layer only acts as a décollement surface. Associated thrusts, narrow box-fold anticlines and cored folds can develop depending on the availability of salt (Fig. 2.4).

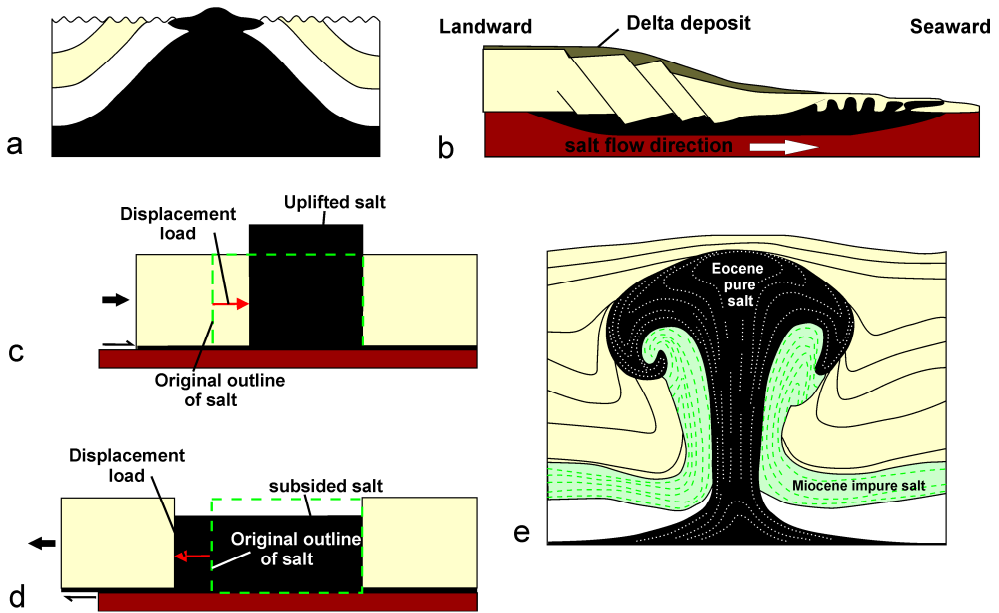


Figure 2.1: Schematic diagrams showing the mechanisms of salt movement. In all cases the salt is shown in black. (a) Upwelling of salt due to erosionally differential loading (modified from Hudec and Jackson, 2007). (b) Salt flow and structures driven by differential loading of the delta sediment wedge on the shelf. Landward extensional faulting is accommodated by the seaward contractive salt diapir and canopy (modified form Fossen, 2010). (c) Regional shortening strain forces the preexisting salt body to expel upwards (modified form Hudec and Jackson, 2007). (d) In regional extensional setting, the preexisting salt structure subsides and forms a local depression above salt (modified from Hudec and Jacson, 2007). (e) A salt diapir formed by salt flow resulted from increasing temperature in the Dasht-e Kavir desert, Iran (modified from Jackson et al., 1990).

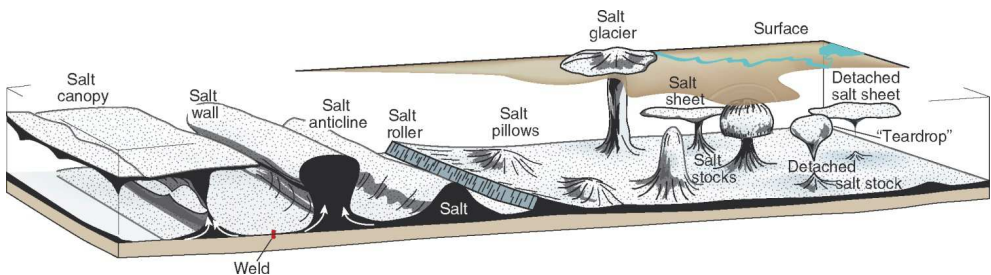


Figure 2.2: A variety of salt structural styles from linear structures on the left side to circular ones on the right. Increasing degree of maturity in salt movement away from the center towards the left and right (from Fossen, 2010).

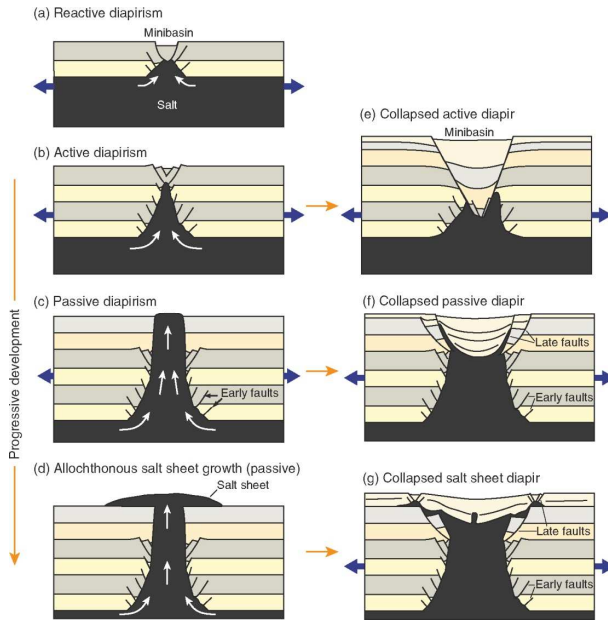


Figure 2.3: Schematic diagrams of an ideal evolution of diapir rise and fall in regional extension. Salt upwelling and growth can experience the stages of (a) reactive, (b) active, (c) and (d) passive diapirism, while (e) to (g) display the situations of a minibasin formation caused by the diapiric collapse corresponding to (d) to (e). From Fossen (2010). Diapirs do not necessarily experience all of these stages and the maturity of a given structure is determined by the availability of salt, the total amount of extension, and the relative rates of extension and sedimentation (Hudec and Jackson, 2007).

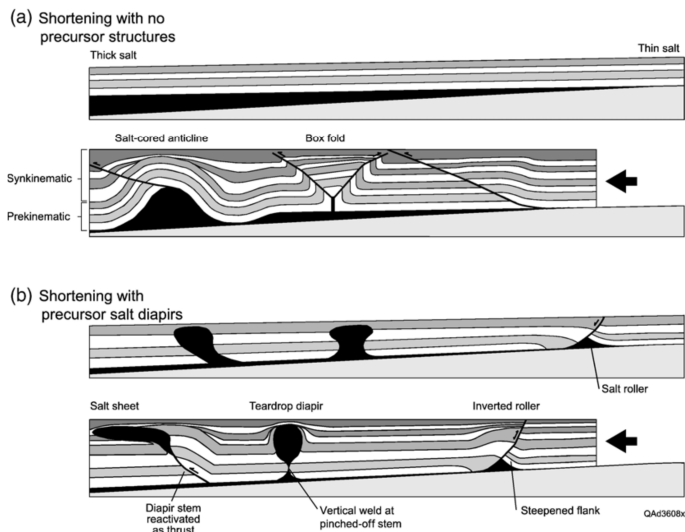


Figure 2.4: Schematic models of salt structures in settings with regional shortening (from Hudec and Jackson, 2007).

2.2.4 Salt-related minibasins

Salt-related minibasins are local depressions adjacent to diverse positive structures developed in salt tectonic settings. They form areas of accommodation on the slope that can be filled by turbidity currents. Such minibasins can be bounded by different structural elements such as normal faults, anticlines, folds, thrusts, and autochthonous and allochthonous salt bodies, depending on the regional strain, salt availability, subsequent sedimentation rates and so forth.

Minibasins with non-direct salt contact

These types of minibasins can be expressed as topographic lows surrounded by the deformed sedimentary overburden. Their boundaries are often faults, anticlines, folds and thrusts formed in the overburden of the salt, which are the direct cause for the occurrence of these minibasins. Small-scale depocenters formed in extensional domains can be graben-bounded by two normal faults in the overburden of a rising salt diapir (Fig. 2.3a); this graben may develop later into an antithetic rollover system with its seaward-concave flank boundary of pre-kinematic sediments and bottom boundary of salt roller or weld (Fig. 20 in Brun and Fort, 2011). A synthetic rollover system developed from a landward-dipping listric normal fault can also form in salt tectonics (Fig. 2.11 in this chapter; Fig. 9 in Brun and Mauduit, 2008). Local depressions may also be located between adjacent anticlines/folds of sedimentary layers cored by squeezed salt diapir ridges (Fig. 2.11).

Minibasins with direct salt contact

A salt-withdrawal minibasin is a subsiding depression that resulted from the underlying salt flowing away from the location of its depocenter (Jackson and Talbot, 1991; Hudec et al., 2009; Fossen, 2010). As a unique structural style of salt tectonics, it may be totally or partly bounded by allochthonous (Fig. 2.5F) or autochthonous salt (Fig. 2.3e, f) (Diegel et al., 1995; Loncke et al., 2006). Hudec et al. (2009) clarified that “the term *salt withdrawal* is not strictly accurate because the salt is expelled (pushed) from beneath the minibasin, rather than drawn (pulled) into an adjacent diapir. However, *salt withdrawal* is so entrenched and familiar that we use it here, with this caveat, in a nonmechanical sense”.

Similar to the history of salt tectonic research flowing, *salt withdrawal* was first explained as the result of buoyancy effect induced by density inversion. If the sediment accumulated on the salt is sufficiently thick to reach a weight that is larger than that of underlying salt bodies, the salt is pushed aside and makes space for the formation and subsidence of minibasins (Fig. 2.5A). This mechanism needs to be triggered by a considerable amount of sediment thickness. Taking minibasins in the Gulf of Mexico as examples, at least 2.3 km of sediment thickness can cause minibasins to form. Later, other mechanisms were proposed to explain the subsidence of salt-withdrawal minibasins in settings without thick sediments. For example, if the salt source gets exhausted or the extensional rate accelerates, the previous diapir may

collapse to form a local depression (Vendeville and Jackson, 1992b). Hudec et al. (2009) summarized six models of subsidence mechanism of salt withdrawal minibasins which can be formed by i) density-driven subsidence, ii) diapir shortening, diapir collapse, iii) decay of salt topography, iv) sedimentary topographic loading and v) subsalt deformation (Fig. 2.5).

Salt-withdrawal minibasins develop along many continental margins, for example, in the Gulf of Mexico (Lehner, 1969; Seglund, 1974; Spindler, 1977; Bouma et al., 1978; Humphris, 1978, 1979; Bouma, 1982; Diegel et al., 1995; Prather et al., 1998; Rowan and Weimer, 1998; Beaubouef and Friedmann, 2000; Prather, 2000; Winker and Booth, 2000; Lamb et al., 2006), in the Aptian salt basins of Brazil (e.g., Demercian et al., 1993; Cobbold et al., 1995; Roberts et al., 2004) and West Africa (e.g., Duval et al., 1992; Marton et al., 2000; Hudec and Jackson, 2004), in the Pricaspian Basin (e.g., Barde et al., 2002; Volozh et al., 2003; Ismail-Zadeh et al., 2004), in the Sverdrup Basin (Jackson and Harrison, 2006; Harrison and Jackson, 2014), in the Canadian Maritime basins (e.g., Balkwill and Legall, 1989; Shimeld, 2004), in the Zechstein salt basin (e.g., Stewart and Clark, 1999; Mohr et al., 2005), in the Flinders Ranges (e.g., Dyson, 1999; Rowan and Vendeville, 2006), in the Paradox Basin (Prochnow et al., 2005, 2006; Matthews et al., 2007; Hudec et al., 2009; Venus et al., 2014), in the Red Sea (Heaton et al., 1995), in several Mesozoic salt basins of northwest Africa (e.g., Tari et al., 2003) (summarized by Hudec et al. (2009)), and in the eastern Willouran Ranges, South Australia (Hearon IV et al., 2014).

Typical salt-withdrawal minibasins are a few tens of kilometers in diameter (Hudec et al., 2009; Fort et al., 2004) and have a diversity of shapes in map view due to the different degrees of salt withdrawal (Diegel et al., 1995). For example, the shelf minibasins in the Gulf of Mexico are circular to elliptical with a diameter range of 5-20 miles (Sumner et al., 1991). Midslope minibasins on the Nile deep-sea fan's margin are subcircular or polygonal in shape and bounded by salt ridges (Loncke et al., 2006).

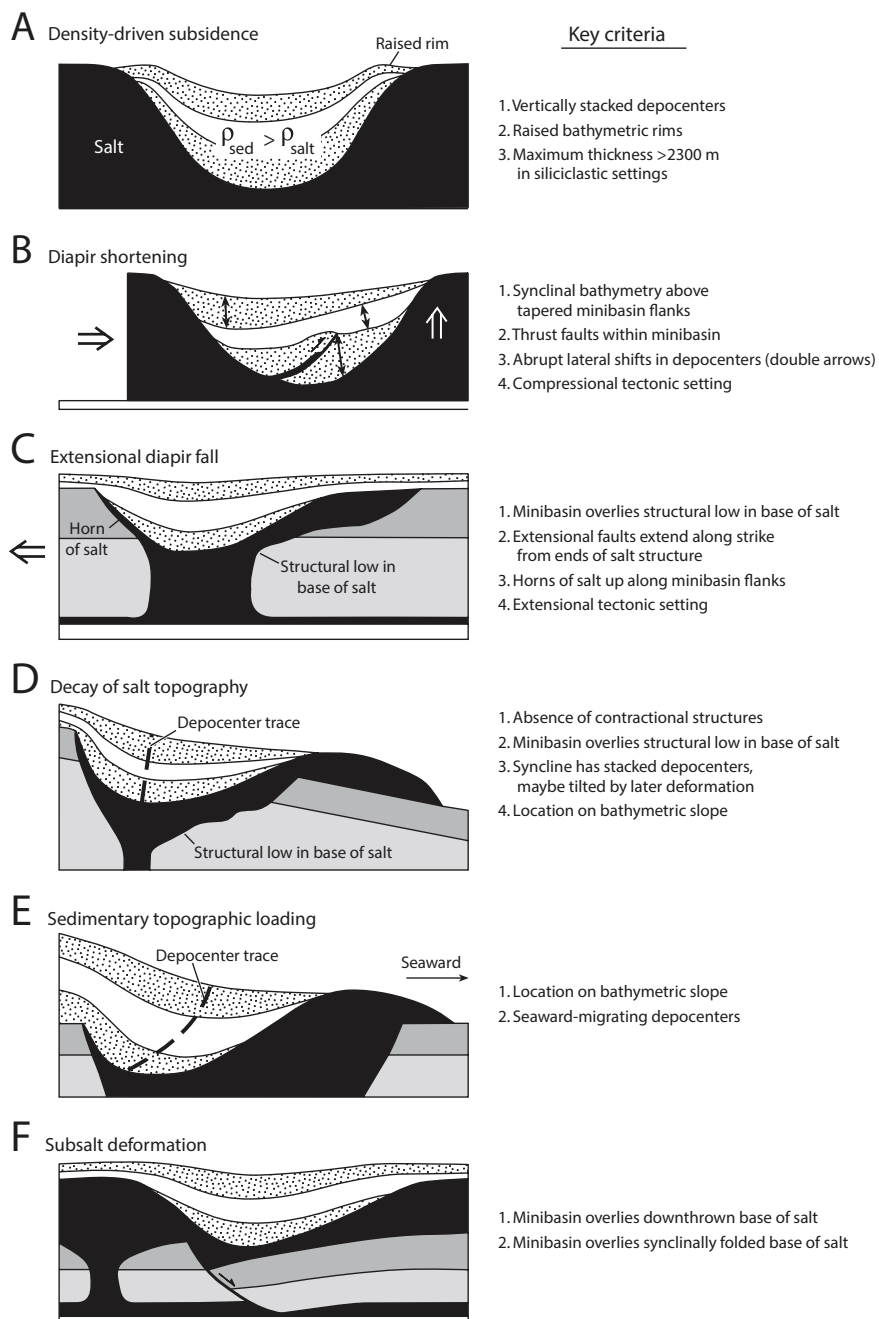


Figure 2.5: Five schematic models and criteria of salt-withdrawal minibasins (from Hudec et al., 2009).

2.3 Passive margins

2.3.1 What is a passive margin?

A passive continental margin is the ocean-continent crustal transition that was once created by crustal rifting but has experienced relatively long-term stability, unlike active continental margins formed by tectonics such as collision, uplift and subduction (Heezen, 1974). “Atlantic”-type continental margins are typical passive continental margins, which develop widely along the boundary between the Atlantic Ocean and its adjacent continents. Passive margins also bound the Arctic Ocean, the Norwegian Sea and the western Indian Ocean, and can be found on the western Europe, the east coast of North and South America, most of Antarctica, parts of Mediterranean margin and parts of the Pacific Ocean such as the South Asian margin in the South China Sea (Heezen, 1974; Steckler, 1978; Watts and Steckler, 1981).

2.3.2 Evolution of passive margins

In the classical model of Allen and Allen (2005), a passive margin undergoes three main stages in its evolutionary process (Fig. 2.6):

1. Pre-rift stage:

Before the onset of continental rifting, there is no significant deformation caused by crustal stretching and thinning. Pre-rift sedimentary sequence normally does not have great changes in deposit thickness, which can be unconformably overlain by the syn-rift packages and faulted in the syn-rift stage (Withjack et al., 2002; Jackson et al., 2006).

2. Syn-rift stage:

At the onset of rifting, large-scale doming and deep-going fracturing of the crust and lithosphere can happen due to early extension induced by the divergent movement of tectonic plates (Fossen, 2010). Continued stretching results in extensional normal faults formed in the crust (Withjack et al., 2002; Ziegler and Cloetingh, 2004; Cloetingh and Ziegler, 2007; Cloetingh et al., 2013). Significant extensional faulting and the subsidence of the crust result in the formation of syn-rift basins with complex topographies such as tilted fault blocks, half-grabens and relay ramps (Leeder and Gawthorpe, 1987; Ziegler and Cloetingh, 2004; Cloetingh and Ziegler, 2007; Cloetingh et al., 2013). Multi-environment sedimentary systems including alluvial, fluvial, deltaic, and gravity flows can participate in the development of synrift basins (Gawthorpe and Hurst, 1993). Evaporites can deposit in arid basins with restricted sea water circulation (Jackson and Vendeville, 1994). Ongoing crustal stretching and extension decrease and eventually end when the oceanic crust forms.

3. Post-rift stage:

The final breakup of lithosphere initiates the spreading of newly formed oceanic crust. Thick accumulations of prograding marine sediments build out over the shelf margin and slope. The subsidence of transitional crust and lithosphere results from cooling and thickening of the lithosphere, which can lead to salt deformation (Jackson and Vendeville, 1994).

Typical passive margins are characterized by thick accumulations of sediments that construct a relatively smooth relief. Topographically they consist of a wide continental shelf (from 30 to over 300 km) with deposits of terrigenous clasts and in situ carbonate, a dissected continental slope with submarine canyons, a gentle continental rise with turbidite systems and a vast abyssal plain. Although passive margins have relatively simple topographies in general, some passive margins involved in more complex tectonics such as salt tectonics can significantly be modified regionally or locally and through interaction with the associated sedimentary processes (Schlee, 1980; Morelock, 2004).

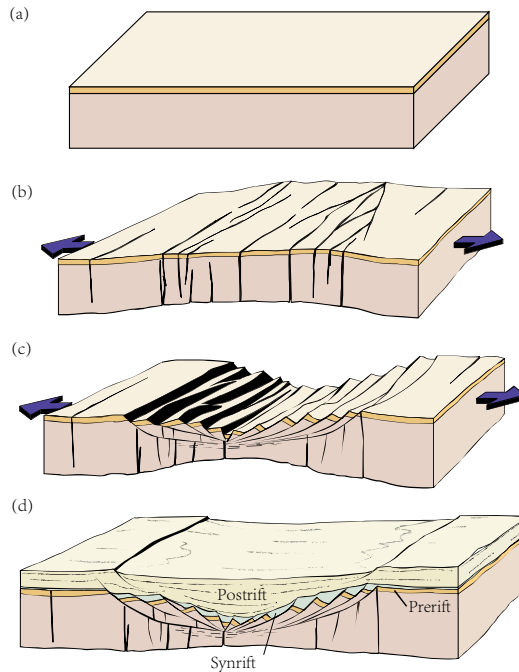


Figure 2.6: Schematic models of rift development: (a) pre-rift, (b) the onset of syn-rift, (c) the stretching phase of syn-rift and (d) post-rift (modified from Fossen, 2010).

2.4 Salt tectonics on passive margins

2.4.1 Salt basins on passive margins

Salt tectonics play a significant role in the formation and development of passive margins (Fig. 2.7). Examples include the Gulf of Mexico (e.g., Worrall and Snelson, 1989), offshore Angola (e.g., Mauduit et al., 1997), offshore Gabon (e.g., Dupré, et al., 2007, 2011; Beglinger et al., 2012), offshore Brazil (e.g., Demercian et al., 1993; Beglinger et al., 2012; Jackson et al., 2014), the North Sea (e.g., Bishop et al., 1995; Mannie et al., 2014), offshore northern Egypt (e.g., Gaullier et al., 2000; Loncke et al., 2006) and offshore Nova Scotia in eastern Canada (e.g., Keen and Potter, 1995; Hogg et al., 2001; Kidston et al., 2002). These areas generally display more complex morphologies than those in the absence of salt.

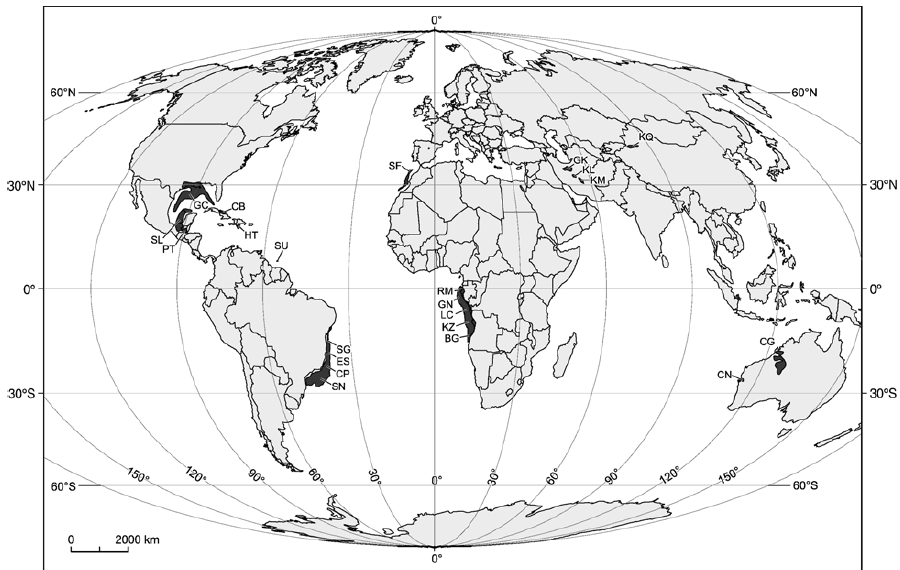


Figure 2.7: Map showing the distribution of salt basins on passive margins (from Hudec and Jackson, 2007). BG Benguela-Namibe; CB Cuban; CG Canning; CN Carnavon; CP Campos; ES Espírito Santo; GC Gulf Coast; GK Great Kavir-Garmsar-Qom; GN Gabon; HT Haitian; KL Kalut; KM North Kerman; KQ Kuqa; KZ Kwanza; LC Lower Congo; PT Petenciapas; RM Rio Muni; SF Safi; SG Sergipe-Alagoas; SL Salina-Sigsbee; SN Santos; SU Suriname.

Salt tectonics can operate during the entire geological time of passive margin formation and development or only parts thereof. According to the timing of salt deposition and the developing stage of passive margins (Fig. 2.8), salt-related basins on passive margins basically can be classified into three types, as prerift (e.g., North Iberian margin; Jammes et al. 2010; Roca et al. 2011), synrift (e.g., offshore Newfoundland, offshore Norway, offshore Senegal) and postrift (e.g., the Gulf of Mexico, offshore Brazil, offshore Angola) (Jackson and Vendeville, 1994; Tari et al.,

2003). More detailed models of passive margin evolution proposed by Peron-Pinvidic and Mantschal (2009) divide the developing process into stretching, thinning, exhumation and spreading stages. Correspondingly, salt basins on passive margins are sorted into prerift, syn-stretching, syn-thinning and syn-exhumation salt basins, according to the depositional time of salt (Rowan, 2014). Different types of salt basins have different governing mechanisms controlling the salt tectonics (Nilsen et al., 1995; Hudec and Jackson, 2004).

Major passive-margin salt basins, such as the Campos and Santos basins offshore Brazil (Demercian et al., 1993; Cobbold et al., 1995; Mohriak et al., 1995; Cobbold et al., 2001; Davison, 2007), the Lower Congo and Kwanza basins offshore West Africa (Duval et al. 1992; Spathopoulos, 1996; Cramez and Jackson, 2000; Marton et al., 2000; Tari et al., 2003; Rowan et al., 2004; Brun and Fort, 2004; Fort et al., 2004; Hudec and Jackson, 2004) and the Gulf of Mexico (Wu et al., 1990; Diegel et al., 1995; Peel et al., 1995; Rowan et al., 2000; Tari et al., 2002; Hall, 2002), belong to the post-rift type (Jackson and Vendeville, 1994) or the syn-exhumation type (Rowan, 2014). They usually have a broad salt distribution and formed after crustal thinning and extension ended but before the oceanic crust's final breakup and accretion, with little relief of the salt basement (Fig. 2.8; Rowan, 2014).

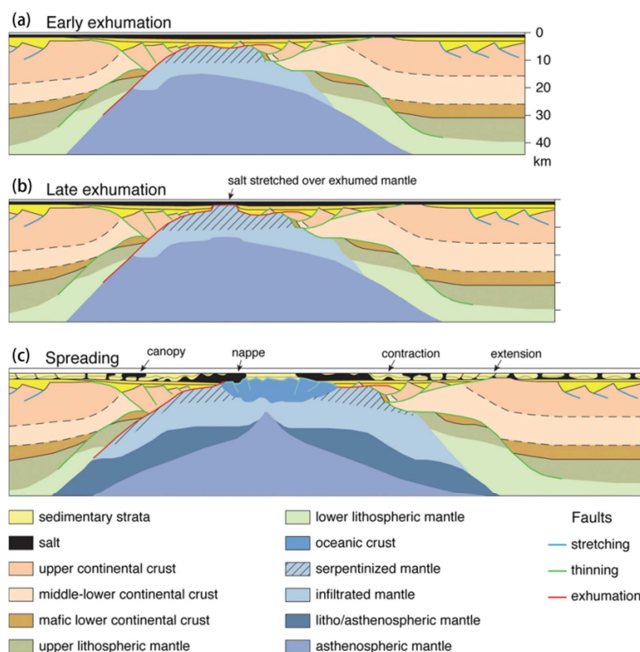


Figure 2.8: Syn-exhumation salt basin proposed by Rowan (2014): (a) early exhumation stage with deposition of a sag basin (orange) and salt after almost all crustal faulting has ceased, so that there is little offset of the base salt; (b) late exhumation stage with separation of synrift and sag sequences and salt attenuation over newly exhumed mantle; (c) spreading stage and development of thin-skinned deformation due to gravitational failure of the margin.

2.4.2 Gravity-driven salt tectonics on passive margins

Passive margins with syn-exhumation salt basins are closely associated with thin-skinned, gravity-driven salt tectonics, which are tectonically characterized by three zones, i) an extensional zone on the shelf and upper continental slope, ii) a transitional zone in the middle of the continental slope, and iii) a compressional zone on and in the front of the lower continental slope (Fig. 2.9; Cobbold and Szatmari, 1991; Fort et al., 2004; Vendeville, 2005; Krezsek et al., 2006). The proximal extensional zone is dominated by structures such as listric growth faults, grabens, rafts, salt diapirs and welds (Duval et al. 1992; Mauduit and Brun, 1998; Fort et al., 2004). Normal faults and grabens initiate the rise of salt diapirs by extensional thinning and faulting of the sedimentary overburden (Vendeville and Jackson, 1992a). The transitional zone is controlled by salt evacuation and diapirism (Fort et al., 2004). The distal compressional zone is characterized by folds, thrusts and squeezed diapirs, while allochthonous salt is commonly found on the newly formed oceanic crust (Tari et al., 2001; Brun and Fort, 2004; Rowan et al., 2004; Hudec and Jackson, 2006). Compressional salt structures in distal regions can modify preexisting salt diapirs formed in previous extensional settings (Vendeville and Nilsen, 1995; Rowan et al., 2000) or cause intrusion of salt nappes (Peel et al., 1995; Trudgill et al. 1999). In the absence of preexisting diapirs, salt acts as a detachment layer (Hudec and Jackson, 2007).

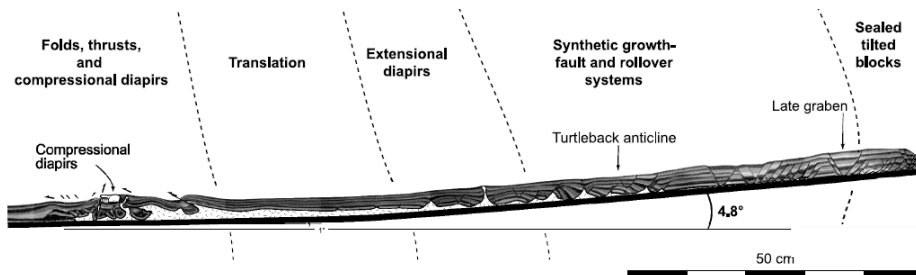


Figure 2.9: Cross section of an experimental model simulating salt tectonics and synsedimentary deformation on the Angolan margin (modified from Fort et al., 2004). Salt is shown in white.

2.4.3 Gravity gliding and spreading

This three-domain structural pattern of salt-tectonics on passive margins can be interpreted as the result of gravity spreading and gliding (Tari et al., 2003; Rowan et al., 2004). Gravity spreading and gravity gliding have similarities and differences in controlling gravity-driven salt tectonic systems. Both of them can express their influences on salt passive margins as three structural domains (extension, translation and contraction). However, they differ in their driving forces, initial conditions, the interaction of salt and sediment, and the structural styles in the same domains (Fig. 2.10; Rowan et al. 2004; Loncked et al., 2006; Brun and Fort, 2011; Rowan, 2014).

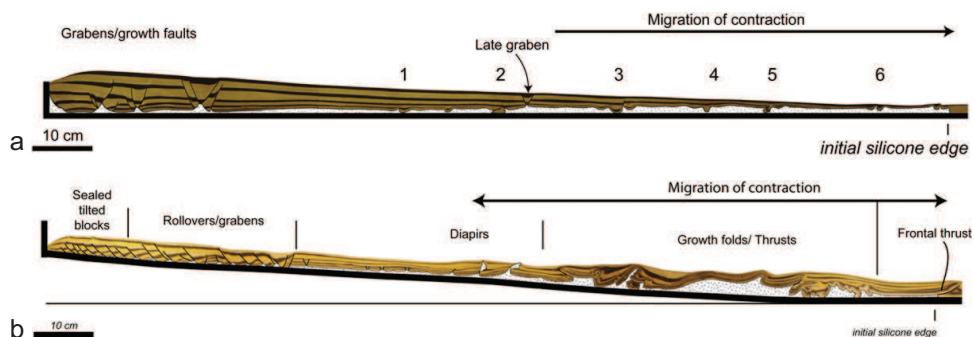


Figure 2.10: Experimental salt tectonic models of (a) pure spreading of sedimentary wedge on salt layer and (b) dominant gliding of margin tilting. From Brun and Fort (2011). Salt is shown in white.

Driving mechanism

Gravity spreading is induced by the seaward-thinning sediment wedge resulting from sediment influx from onshore regions (e.g., Koyi, 1996; Ge et al., 1997; Rowan et al., 2000; Vendeville, 2005), while gravity gliding is caused by the margin tilting basinward due to large-scaled processes like differential thermal subsidence and/or stretching of the salt during ongoing crustal extension beneath the salt (Brun and Fort, 2011; Hudec et al., 2013b). Rowan et al. (2004) defined gravity gliding and gravity spreading as follows: “The gravity gliding component of the deformation is the component controlled by any basinward slope of detachment, whereas the gravity spreading component is that controlled by the surficial slope of the seabed.” Thus the salt basement slope and salt overburden topography respectively control the salt tectonics in gravity gliding and gravity spreading.

Initiation requirements

Gravity spreading generated by differential sedimentary loading requires some conditions to initiate the whole process, which include a thick overburden, great water depth with a minimum value of 4500m, high sediment density, high pore fluid pressure and a seaward open boundary of the salt basin. Gravity gliding, by contrast, just needs a small margin tilt angle (lower than 1 degree), a basin width in the range of 200-600 km and a sedimentary overburden up to 1 km thick (Brun and Fort, 2011).

The role of salt and sediments

The role of the salt layer in these two processes is different (Rowan et al., 2004; Brun and Fort, 2011). In gravity gliding, the salt layer and sedimentary overburden together “automatically” slide down the slope with displacement vectors parallel to the detachment plane. The salt can be regarded as the driving component as well as the sedimentary overburden. New sediments following salt deformation tend to fill the salt-induced basins. In gravity spreading, the salt is “passively” expelled with

lateral spreading and vertical collapse in reaction to the pressure caused by the overburden weight (Brun and Fort, 2011; Rowan et al., 2004). Salt acts as the resisting component against the driving forces coming from sediment overburden, i.e., there is no salt deformation without uneven sedimentation (Brun and Fort, 2011).

Structural styles

In gravity spreading, the extensional domain is located in the area where the sedimentary wedge distributes or progrades. Wedge-shaped sediment makes overburden surface generally downdip. Nevertheless the strike of extensional normal faults can develop in multidirections due to local slope variations on the seafloor caused by uneven sediment thickness (Cobbold and Szatmari, 1991; Demercian et al., 1993) or landward tilting resulting from proximal loading subsidence (Rowan et al., 2004). Moreover, sedimentation rates can influence the types of extensional structures. For example, a low rate favors basinward listric growth-fault and rollover systems, while a high rate tends to produce landward listric growth-fault and rollover systems (Krezsek et al, 2007). Early extensional rafting can be regarded as an indicator only if the seaward boundary of the salt basin is free of sediment. The contractional domain is located at the wedge dip and frontal salt nappes form due to progressive intrusion. Both the extensional and contractional domains migrate seaward with the prograding sedimentary wedge (Fig. 2.10a; Brun and Fort, 2011).

In gravity gliding, the updip extensional domain is characterized by sealed tilted blocks (Brun and Fort, 2011), subparallel normal faults, and rollover systems (Mauduit and Brun, 1998). The downdip contractional domain is dominated by growth folds and thrusts formed prior to updip extensional structures, and further salt nappes form due to the abrupt failure of long-time distal contraction. If early extensional rafting in the proximal domain is coeval with distal contraction, such structural association can indicate gravity gliding. The migration direction of extension is seaward while that of contraction is landward (Fig. 2.10b; Brun and Fort, 2011).

Loncke et al. (2006) pointed out that where gravity gliding dominates, the structures tend to be cylindrical and perpendicular to the regional basal slope direction, while where gravity spreading dominates, radial and concentric extensional structures and along with polygonal and subcircular depocenters are present.

Controversy

It is hard to distinguish between gravity spreading and gravity gliding in reality (Schultz-Ela, 2001; Rowan et al., 2004), and therefore the dominant driving force (either gravity gliding or gravity spreading) controlling post-rift salt passive margins is often controversial.

Some researchers argue that post-rift salt passive margins generally are controlled by a dominant gliding (gliding-spreading) process driven by gravity because of the

evidence from seismic data and simulation experiments of “margin” tilting (e.g., Vendeville and Cobbold, 1987; Cobbold et al., 1989; Cobbold and Szatmari, 1991; Cobbold et al., 1995; Marton et al., 2000; Brun and Fort, 2004). In other words, gravity gliding plays a major role but involves to some extent gravity spreading (Brun and Merle, 1985). As margin tilting without a sedimentary wedge can initiate salt movement, the prograding sedimentary wedge just plays a secondary role (Brun and Fort, 2011). For example, an increasing sedimentation rate can contribute to an increase in deformation rate of the extensional and contractional domains (Mauduit et al., 1997).

Some other authors, such as Wu (1993), Vendeville (2005), Gaullier and Vendeville (2005) and Rowan et al. (2012) argue that post-rift long-lived salt-prone passive margins are controlled by gravity spreading generated by differential sedimentary loading. For example, the continued postsalt deformation and tectonics in the Mediterranean after thermal subsidence had ceased is driven by a sedimentary wedge prograding from onshore (Vendeville, 2005).

2.4.4 The northern Gulf of Mexico vs. offshore Angola

The northern Gulf of Mexico and offshore Angola are two well-known areas that have been widely investigated to determine the dominant driving forces, because of an abundance of hydrocarbon resources in their salt basins (e.g., the Kwanza and South Gabon basins of Africa). In addition, the similarity and difference between the Gulf of Mexico’s northern margin and the South Atlantic margins in terms of driving processes and structural patterns, have been discussed by many researchers (e.g., Tari et al., 2001; Fort and Brun, 2012; Rowan, 2014).

The northern Gulf of Mexico

The Gulf of Mexico is well-known for its spectacular platform lobate salt canopy, and its abundant and various minibasins formed on top of it (Fig. 2.11c). More noteworthy, the northern Gulf of Mexico displays distinctive features on its north (Louisiana) and northwest (Texas) margin. On the north-central margin (Fig. 2.11a), an extensional region presents short and curved normal faults dipping in various directions and a contractional region contains thick extrusive Sigsbee salt nappes with numerous Neogene minibasins on top of it (Peel et al. 1995). On the northwestern margin (Fig. 2.11b), a proximal extensional domain develops long and straight normal faults and a contractional domain the Perdido fold belt cored by ridges of the Middle Jurassic Louann Salt (Worrall and Snelson, 1989 in Brun and Fort, 2011).

Although there is still some uncertainty and controversy on the tectonic evolution of the Gulf of Mexico (Hudec et al., 2013b; Rowan, 2014), it is widely believed that prerift of the Gulf of Mexico began in the Late Triassic. Major rifting between the Yucatan block and the North American Plate occurred in the Middle Jurassic (Salvador, 1991; Pindell and Kenna, 2001, 2009; Stern et al., 2010; Huerta and Harry, 2012). The incipient Gulf of Mexico Basin was created above thinned transitional crust. Later the

bulk of upper crustal extension had decreased and even ceased in the latest synrift stage before the Louann salt started depositing during the late Middle Jurassic (Salvador, 1987; Buffler, 1991). During the Kimmeridgian to Tithonian, seafloor spreading occurred in the center of the basin and oceanic crust formed (Hudec et al., 2013b). During the Early Cretaceous, the Gulf of Mexico continued to expand and deepen by thermal subsidence and continuous crustal extension (Sawyer et al., 1991; Hudec et al., 2013b). Sediments were transported from onshore and deposited in the basin during the Late Cretaceous and the entire Cenozoic, resulting in a further deepening of the basin. Moreover, a continental shelf was constructed along the northwestern and northern margins of the Gulf of Mexico during the Cenozoic (Galloway, 2008).

It is commonly accepted that the dominant driving force in controlling postsalt deformation in the early postrift stage (the Late Jurassic-Cretaceous) is gravity gliding caused by thermal subsidence (e.g., Rowan et al., 2004; Fort and Brun, 2012) or due to stretching of the salt-sediment package during ongoing crustal extension (Hudec et al., 2013b). The consequent structural distribution is like that of the northwestern Gulf of Mexico where early-postrift extensional faults form at the landward edge of the basin, and coeval contractional deep salt nappes overlie the oceanic crust (Fig. 14 in Rowan, 2014). Small-wavelength deformation may start forming at the early postrift stage (Fig. 6b in Rowan et al., 2004).

However, the debate on the Cenozoic driving mechanism of salt initiation and postsalt deformation of the northern Gulf of Mexico is quite intense. Making use of seismic data, well logs, and experimental and numerical modelling (e.g., Talbot, 1992; Worrall and Snelson, 1989; Diegel et al., 1995; Rowan, 1995; Peel et al., 1995; Hall, 2002; Rowan et al., 2004; Vendeville, 2005; Gaullier and Vendeville, 2005; Gradmann et al. 2009; Rowan et al., 2012), numerous authors suggested that the dominant driving force for the Cenozoic salt tectonics in the Gulf of Mexico is gravity spreading driven by differential sedimentary loading, although some gravity gliding was caused by proximal uplift of the margin (Jackson et al., 2011; Dooley et al., 2013). For example, the Perdido fold belt cored by the Middle Jurassic Louann salt was first initiated by gravity gliding but then gravity spreading became dominant during the Latest Oligocene-Middle Miocene (Fig. 11 in Hudec et al., 2013a; Peel et al., 1995). Brun and Fort, however, insist that gravity gliding driven by margin tilting is the dominant reason for the Cenozoic presalt deformation supported by analogue modeling experiments, salt flow direction analysis and seismic data (Brun and Fort, 2011, 2012; Fort and Brun, 2012).

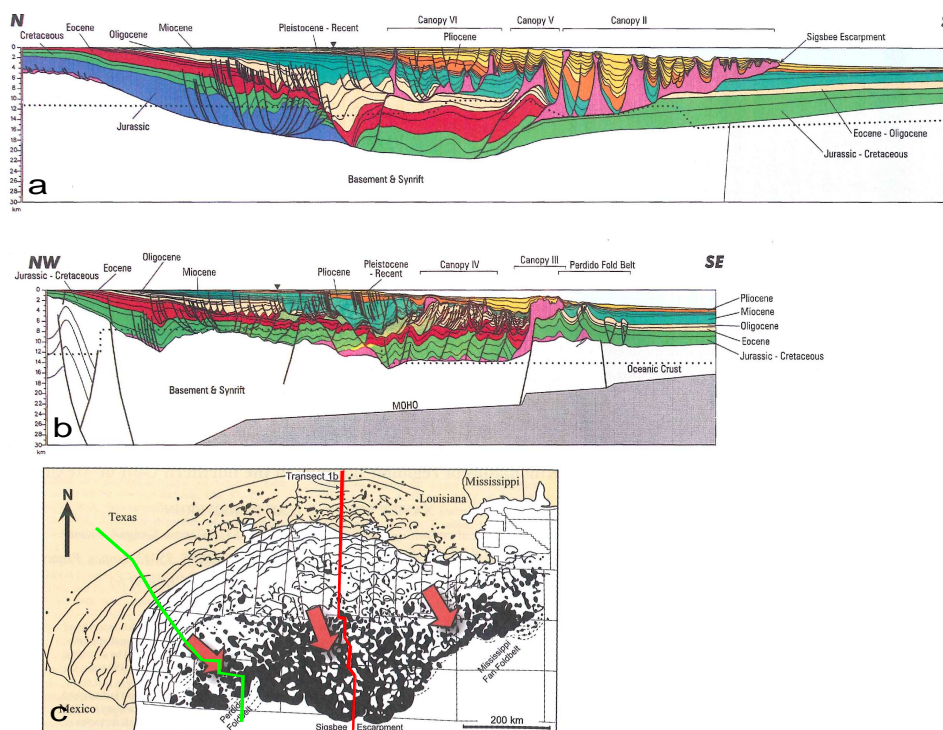


Figure 2.11: Schematic transects of the northern (a) and the northwestern (b) Gulf of Mexico (from Peel et al. 1995). See location in (c) and arrows showing the mean transport direction for the three spreading systems (modified from Peel et al., 1995 and Diegel et al., 1995 in Fort and Brun, 2012).

The central South Atlantic

The offshore Angola and offshore Brazil margins bound the central part of the South Atlantic. The important salt basins are the Campos and Santos salt basin offshore Brazil and the Lower Congo and Kwanza salt basin offshore Angola. The evolution of the South Atlantic is under controversy in many aspects such as the period of rift initiation (e.g., Meisling et al., 2001; Karner et al., 2003; Mohriak et al., 2008; Lentini et al., 2010; Unternehr et al., 2010; Quirk et al., 2013), the time of final separation of the continental crust (Jackson et al., 2000; Marton et al., 2000; Quirk et al., 2013; Meisling et al., 2001; Karner et al., 2003; Karner and Gamboa, 2007; Torsvik et al., 2009; Unternehr et al., 2010; Blaich et al., 2011; Mohriak and LeRoy, 2013) and the chronological order of salt deposition and final breakup (e.g. Jackson et al., 2000; Marton et al., 2000; Quirk et al., 2013; Karner et al., 2003; Karner and Gamboa, 2007; Mohriak et al., 2008; Unternehr et al., 2010; Blaich et al., 2011). For the central South Atlantic, the rifting did not seem to commence until the Berriasian to the early Barremian and the oceanic crust started forming during the late Early Cretaceous (the Barremian to Albian) (Rowan, 2014).

Rowan (2014) analyzed new seismic data and found their results to favor the models of Unternehr et al. (2010) and Zalan et al. (2011). The consensus in their models is that there is a period (the mid-Barrenmian to late Aptian) between the end of the bulk of rifting and final breakup of continental crust, during which a sag basin was first filled by sedimentary layers and then overlain by shallow marine Aptian salt evaporites. This means that the salt evaporite in Brazil and Africa was originally deposited within one presalt-sag basin underlain by the hyperextended crust, but then divided by the newly formed oceanic crust and the exhumed subcontinental mantle in the Albian (Fig. 2.12a, 2.13a). The Albian carbonate system developed in a shallow-marine environment. From the Late Cretaceous to the entire Cenozoic, the sedimentary system is dominated by basinward progressive siliciclastic deposition (Guerra and Underhill, 2012).

Postsalt deformation occurred during and mainly after salt deposition driven by gravitational failure (Davison et al., 2012; Quirk et al., 2012). The debate over the main driving mechanism between spreading-dominant by differential sedimentary loading (e.g., Spathopoulos, 1996; ; Ge et al., 1997; Marton et al., 2000; Cramez and Jackson, 2000; Kolla et al., 2001; Guerra and Underhill, 2012; Hudec and Jackson, 2002; Hudec and Jackson, 2004; Gremmer et al., 2005) or gliding-dominant by thermal subsidence of the newly-formed cooling oceanic crust (e.g., Cobbold and Szatmari, 1991; Demercian et al., 1993; Gaullier et al., 1993; Mauduit et al., 1997; Mauduit and Brun, 1998; Brun and Fort, 2011; Quirk et al., 2012) is still ongoing. In some cases, margin tilting can be regarded as the root cause for the salt displacement, and sediment loading as the direct reason. For example, thermal subsidence leads to a relatively rapid seaward sediment movement and causes the formation of salt in great thickness (e.g., Quirk et al., 2012). The structural analogue models triggered by “margin” tilting can produce salt structural styles and distributions that are more similar to the real case in the central South Atlantic (e.g., Brun and Fort, 2011) than models driven by gravity spreading.

The salt structures and distribution controlled by gravitational failure mainly include proximal extension and distal contraction. The upslope extension with basinward-dipping faults and tilted blocks, synthetic, antithetic rollover systems and ‘flip-flop’ salt walls (Fig. 2.12; Fig. 2.13). The Cabo Frio Fault is a large landward-dipping listric normal growth fault in the extensional domain of the Santos Basin with a spectacular area of 7700 km² (Quirk et al., 2005). Distal compressional structures include simple folds, thrust folds, squeezed diapirs, squeezed and inflated salt massifs, and thrust emplacement of allochthonous salt out over oceanic crust (Fig. 2.12; Fig. 2.13; Rowan, 2014). In the Santos Basin, multi-directional sediment supply leads to polygonal minibasins in the distal contractional domain (Guerra and Underhill, 2012). Allochthonous salt sheets or nappes are present but not of the impressive scale as those found in the Gulf of Mexico (Mohriak et al., 2012).

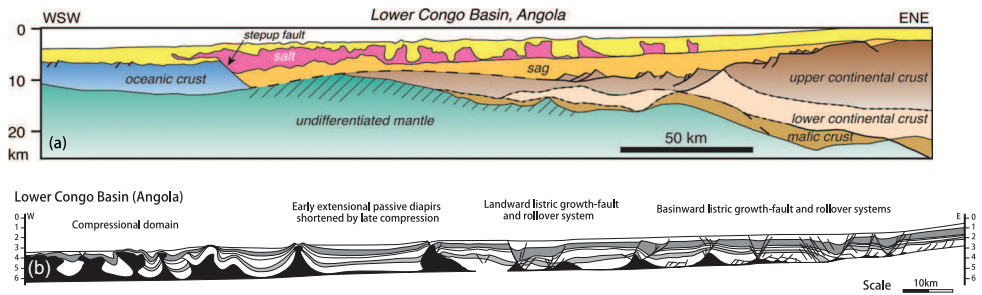


Figure 2.12: Interpreted seismic cross sections of the Lower Congo Basin on the Angolan margin. (a) cross section of the Angolan margin (from Rowan, 2014) and (b) cross section of salt structures of the Lower Congo Basin (modified from Fort et al., 2004 in Krezsek et al., 2007).

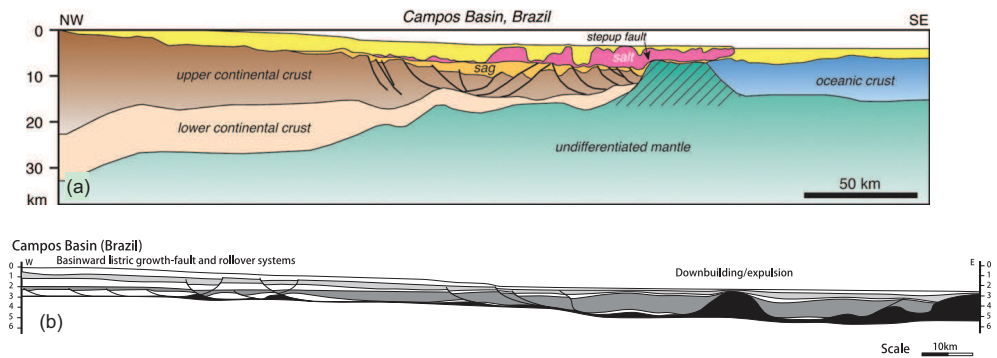


Figure 2.13: Interpreted seismic cross sections of the Campos Basin on the Brazilian margin. (a) cross section of the Brazilian margin (from Rowan, 2014) and (b) cross section of salt structures of the Campos Basin (from Guardado et al., 1989 and Cainelli and Mohriak, 1999 in Krezsek et al., 2007).

2.5 Study methods of salt passive margins

In order to investigate the evolution of salt-bearing passive margins, the mechanisms and kinematics of the salt tectonics, the salt-related structure styles and systems, and the relationship between salt tectonics and the associated sedimentary processes, some widely-adopted methods include outcrop studies, interpretation of seismic data and well logs, processed-based numerical simulation as well as analogue modelling experiments.

2.5.1 Outcrop

Outcrop studies allow direct observation and description of salt bodies and their associated structures in the field. It can be considered as the first door to enter the salt-tectonic world. Salt tectonics studies began with the first published description of a salt dome outcrop in the Saharan Altas of Algeria by Ville (1856). However, most salt-prone passive margins are submerged under sea level, and onshore outcrops are limited. Examples include the Great Kavir-Garmsar-Qom, Kalut and north Kerman basin in Iran (Jackson et al., 1990; Rahimpour-Bonab et al., 2007), the Carnarvon basin in Australia (Hocking et al., 1987), allochthonous salt in the eastern Willouran Ranges, South Australia (Hearon IV et al., 2014) and the Lansatine-Baouala salt canopy in the Tunisia passive margin (Masrouhi et al., 2013).

2.5.2 Subsurface data

Because of their close relationship with hydrocarbon resources, salt-bearing passive margins are investigated using subsurface data such as seismic data and well logs. Although there are some challenges of seismic imaging in salt-rich substrate, for example, the poor resolution and velocity control near salt diapir (e.g., Davison et al., 2000), a better understanding of salt tectonics on passive margins has been greatly improved by sequential restoration of the regional cross-sections based on the seismic interpretations (e.g., Diegel et al., 1995; Peel et al., 1995; Marton et al., 2000; Tari et al., 2003; Ferrer et al., 2012). With the ceaseless improvements of the geophysical techniques, various new salt structures and complicated combination styles are being increasingly revealed in several areas, and improved the previous explanations, for example, recognition of the superposed deformation in the basins offshore Angola (Cramez and Jackson, 2000; Zalan et al., 2011), flip-flop salt structures in the North Sea and South Atlantic (Quirk and Pilcher, 2005, 2012), new hypothesis for Jurassic Gulf of Mexico (Hudec et al., 2013b), new interpretation for presalt structure in salt basins offshore Brazil (Unternehrl et al., 2010), discovery of diffusion zone of pillow fold belt (Philippe et al., 2005; Dal et al., 2006; Guerin et al., 2006; Jackson et al., 2011; Hudec et al., 2013a).

2.5.3 Laboratory experiments

In last two decades, some groups have focused on simulating gravity-driven deformation of salt on passive margins in sand-silicone boxes. For example, Fort et al.

(2004) summarized three groups: Géoscience Rennes, CNRS, University of Rennes 1 (Vendeville, 1987; Vendeville and Cobbold, 1987; Cobbold et al., 1989; Cobbold and Szatmari, 1991; Gaullier et al., 1993; Mauduit et al., 1997; Mauduit and Brun, 1998), the Applied Geodynamics Laboratory, Bureau of Economic Geology, Austin, University of Texas (Vendeville and Jackson, 1992a, b; Jackson and Vendeville, 1994; Ge et al., 1997), and the Fault Dynamics Research Group, Royal Holloway, University of London (McClay et al., 1998).

Methods combining seismic data and modelling experiments, especially laboratory analogue experiments, are widely adopted by researchers. Some of them attempt to explain the mechanism of certain complicated salt structures formed in specific tectonic settings. For example, radial gliding (Cobbold and Szatmari, 1991), raft tectonics (Duval et al., 1992; Mauduit et al., 1997), rollover systems (Vendeville and Cobbold, 1987; Vendeville and Jackson, 1992b; Mauduit and Brun, 1998; Krezsek et al., 2007), extensional diapirism (Jackson and Vendeville, 1994), compressional structures (Letouzey et al., 1995; Cobbold et al., 1995; Ge et al., 1997; Brun and Fort, 2004; Rowan et al., 2004). Some of them aim to reconstruct the basin-scaled salt tectonic processes in the regional settings. For example, paradox structures in the Gulf of Mexico (Dooley et al., 2013), halokinesis of the Santos Basin (Guerra and Underhill, 2012), the salt-tectonic evolution of the Laurentian Basin in the Eastern Canada (Adam and Krezsek, 2012). Numerous geologists compare the different models' effects on controlling the structure styles and distributions at the margin scale. For example, different models for Kwanza Basin (Fort et al., 2004), progradation, aggradation and retrogradation of sedimentary loading (Ge et al., 1997; Cotton and Koyi, 2000; Vendeville, 2005), gravity spreading vs. gravity gliding (Brun and Fort, 2011, 2012; Rowan et al. 2012). These analogue models are not only used for explaining structures interpreted from seismic data, but also for predicting complicated finite deformations.

2.5.4 Numerical experiments

As supplement to interpretation of seismic data and physical experiments, numerical modelling of salt passive margins can help in validating the analytical and predictive models. For example, Last (1988) numerically simulated the movement of a package composed of a viscous sublayer with variable thickness and the elasto-plastic overburden on a gentle slope. His results are comparable with Lehner (1977)'s analytical model. Podladchikov et al. (1993) simulated the erosion-induced diapirism process and salt structures with different erosion rate. In their modelling, they just consider the vertical flow of salt and simple salt structures but without the internal deformation or horizontal movement of the sedimentary overburden. More complex processes and structures at the basin scale, such as folds and thrust salt nappes, also can be simulated by numerical modeling methods. They can help understand the velocity distribution, instantaneous strain rates and the evolving stages of stress (Gremmer et al., 2004). Recent finite numerical experiments related to salt-bearing passive margins focus on simulating the influence of differential sedimentary loading on a viscous substrate (e.g., Cohen and Hardy, 1996; Ings et al., 2004; Ings and Shimeld, 2006; Gremmer et al., 2005; Gradmann et al., 2009; Albertz and Ings, 2012).

Their results show the similarity to the analytical models of three structural domains (extensional, transition and contraction). However, some limitations like the oversimplification of the evaporites as uniform strata and limited consideration of gravitational failure in numerical models, hamper their capability to explain and predict basin-scaled salt tectonics in passive margins (Albertz and Ings, 2012).

CHAPTER 3

Experimental Modelling of Passive Margin Bathymetries under the Influence of Salt Tectonics

3.1 Introduction

To investigate the interaction between complex passive margins bearing salt and submarine turbidity currents, we use a numerical model to simulate turbidity currents flowing over the seabed of such passive margins. The seabed bathymetry is one of the most important input parameters of the model. Bathymetric seafloor data can be obtained in different ways, for instance by multibeam echosounding of the seafloor (e.g., Pratson and Haxby, 1996), from palaeobathymetric surfaces reconstructed from outcrop data (e.g., Aas et al., 2010a), from seismic data (e.g., Aas et al., 2010b; Albertão, 2010), or from analogue models by physical laboratory experiments (e.g., Athmer et al., 2009; Albertão, 2010). Sonar seafloor bathymetric surveys cannot, however, provide information of the tectonic evolution of the margins; outcrops are usually exposed in only two dimensions or within a limited area that is small compared to the length of the margin; tectonic information derived from subsurface data greatly depends on the data resolution and scientist's interpretation. By contrast, the approach of modeling tectonic analogues by physical experiments has the advantage of providing tectonic information in three- and even four-dimensions (e.g., Brun and Fort, 2004, 2011; Albertão, 2010). It is widely used to study salt tectonics on passive margins. In this thesis, we use analogue sandbox experiments in gravitational loading settings, combined with a laser tomographic scanner, to model

such passive margin topographies (Fig. 3.1). This down-scaled topography forms then the input for numerical simulations of turbidity currents flowing over it. The fundamental principles, set-up and results of the sandbox experiments are presented and discussed in this chapter.



Figure 3.1: Laboratory set-up of the analogue experiments in the ISES tectonic laboratory at the Vrije Universiteit Amsterdam. A computer controlled systems is installed over the sand-silicon model. This system combines a workstation computer for monitoring the experimental process, a laser scanner for collecting the bathymetric data, and a digital camera for taking top-view pictures during the experiments.

3.2 Laboratory modelling of passive margin bathymetries

“Sandbox” analogue experiments are widely used to model the evolution of a large variety of deformation types in structural geology and tectonics. For passive margins, especially for those with salt-induced deformations during late drifting stages, such as in the Gulf of Mexico and the South Atlantic margins, sand-silicon box experiments driven by gravitational forces have proven to be an effective method to study the deformation mechanisms (e.g., Vendeville and Cobbold, 1988; Cobbold and Szatmari, 1991; Vendeville and Jackson, 1992a, b; Demercian et al., 1993; Guerra and Szatmari, 2009; Brun and Fort, 2004, 2011). Such margins are characterized by a transition from upslope extension to downslope contraction caused by gravity sliding and spreading of the brittle-ductile package. In this study, the successful laboratory modeling of the Angolan margin conducted by Fort et al. (2004), Brun and Fort (2004, 2011) has been taken for reference, and therefore similar techniques are adopted here.

3.2.1 The natural prototype

During the drifting and early rifting stages the newly formed basins can get closed off from the open oceans and evaporites can form that may reach thicknesses of several

thousand meters. (Rouchy and Blanc-Balleron, 2006; Warren, 2006). Widths of salt basins can vary greatly: the Gulf of Mexico is in the range of 500 to 800 km (e.g., Worrall and Snelson, 1989), the salt basins in the South Atlantic are generally 200 to 400 km wide (e.g., Davison, 2007) while smaller ones such as offshore Nova Scotia are less than 100 km wide (Ings and Shimeld, 2006; Albertz et al., 2010). The initial geometry of salt basins is difficult to reconstruct due to the often poorly imaged salt bases on seismic surveys. In some modelling experiments, inclined tabular shapes and double-wedge shapes of silicone are used to simulate the salt geometries (e.g., Mauduti et al., 1997; Fort et al., 2004). Commonly, prekinematic sedimentary layers above the salt are up to a kilometer thick and drape the whole salt layer. The margin tilt angle can range from 1° to 4°, depending on the degree of thermal subsidence and waning rifting (Brun and Fort, 2011).

3.2.2 Model material and scaling considerations

In our analogue experiments in the ISES tectonic laboratory at the Vrije Universiteit Amsterdam, sand and silicone putty represent the prekinematic sediment and the salt respectively (e.g., Vendeville and Jackson, 1992a, b; Weijermars et al., 1993). A plastic sheet was placed under the silicone to represent a weak décollement layer (e.g., McClay, 1990; Allemand and Brun, 1991). The silicone putty used here is SGM-36 (manufactured by Dow Corning Europe, Senefte, Belgium) with a density of about 965 kg/m³ and a viscosity of 5×10⁴ Pa·s. A series of experiments conducted by Weijermars (1986a, b, 1993) has proven that SGM-36 is capable of providing a rheologically scaled analogue of salt. The overlying sand chosen here to represent the brittle sedimentary rocks has a mean grain size of 300 µm, a density of about 1500 kg/m³ (uncompacted and in air) and a coefficient of friction of 0.9 without significant cohesion (Willingshofer et al., 2005).

Laboratory experiments model the basin-scale natural analogue in a small-scale box. Therefore careful scaling considerations are necessary in the design of such modelling experiments in order to make the results comparable to nature. This requires a dynamic similarity between model and prototype in the distribution of stresses, rheologies and densities (Tab. 3.1) (Hubbert, 1937; Ramberg, 1981; Davy and Cobbold, 1991).

Assuming a density of the sedimentary overburden in nature in the range of 2300-2600 kg/m³ ($\rho_{overburden}$) and a salt density about 2200 kg/m³ (ρ_{salt}), the overburden-salt density ratio of the prototype is 1.05-1.18 (Weijermars et al., 1993). The corresponding density ratio in the model is about 1.55, which is higher than the prototype density ratio but is still considered acceptable because the density inversion between salt and its overburden is not the main driving force of the salt flow and deformation (Vendeville and Jackson, 1992a; see also chapter 2).

When the model-prototype ratios of stresses and lengths become approximately equal, the models follow the dynamic principle (Brun, 1999). The model-prototype ratios of stresses (σ^*) can be expressed as the equation:

$$\sigma^* = \rho^* g^* L^*$$

where ρ^* , g^* and L^* represent the ratio of density, gravity acceleration and typical length between the model and prototype. The gravity ratio g^* is 1 because the experiments are conducted under normal gravity. In our models, a silicone layer is covered by a sand layer of 0.01m thickness (L_{sand}) and the sand density (ρ_{sand}) is about 1500 kg/m³. Commonly the prekinematic overburden sediment is not more than 1 km in thickness ($L_{overburden}$). Hence $\rho^* = 0.58-0.65$ and $L^* \approx 10^{-5}$. Therefore in our model, σ^* can be calculated to be $5.8-6.5 \times 10^{-6}$, or, more generally, it lies in the range of 10^{-5} to 10^{-6} .

The geometric scaling factor L^* can be defined as

$$L^* = \frac{(C/\rho g)_{model}}{(C/\rho g)_{prototype}} = C^*/(\rho^* g^*) = C^*/\rho^*$$

(Hubbert, 1937; Lallemand et al., 1994; Schellart, 2002) where C is the cohesion and C^* is the ratio between model and prototype. C_{model} lies in the order of tens to over a hundred Pa (0-200 Pa according to Weijermars et al., 1993; 30-130 Pa according to Lohrmann et al., 2003, Panien et al., 2006, and Schellart, 2002) while $C_{prototype}$ is in the range of several to tens of MPa (0-60 Mpa according to Weijermars et al., 1993; 5-20 Mpa according to Jaeger and Cook, 1969, and Hoshino et al., 1972). C^* is thus about $3.3-6.5 \times 10^{-6}$ and ρ^* is between 0.44 to 0.65. Therefore, the geometric scaling factor L^* is in the range of 5.07×10^{-6} to 1.36×10^{-5} , which means that 1 cm in the model domain represents about 1 km in prototype.

Obviously, σ^* is nearly equal to L^* because the density of materials in the model and the density of the rocks in the prototype are approximately the same ($\rho^* \approx 1$), and since $g^* = 1$ it follows that $\sigma^* \approx L^*$ (see equation above) and thus the model is dynamically quite similar to the prototype (Brun, 1999).

The time scaling factor T^* is strongly influenced by the salt viscosity and the overburden loading with consideration of the density of model material, the material layer thickness, and the model size (Fort et al., 2004). T^* can be expressed as

$$T^* = \eta^*/(\rho^* L^*) = \eta^*/C^*$$

(Adam and Krezsek, 2012), where η^* is viscosity ratio between the model and prototype. The viscosity of salt in nature was taken as 2×10^{18} Pa·s (Weinberger et al., 2006) and since the silicone viscosity is 5×10^4 Pa·s, η^* becomes 2.5×10^{-14} . Since $C^* \approx 3.3-6.5 \times 10^{-6}$ as stated above, T^* accordingly is in the order of magnitude of 10^{-9} . If the experiment duration takes 72 hr, the simulated geological period can be expected to be about 1.86-2.11 Ma.

Table 3.1 Summary of the dynamic scaling properties of the experiments

| Property | Model | Prototype | Scaling factor | References |
|----------------------------------|--|---|--|---|
| Length | $L_{sand} = 1 \text{ cm}$ | $L_{overburden} = 1 \text{ km}$ | $L^* = \frac{(C/\rho g)_{model}}{(C/\rho g)_{prototype}} \quad (1)$ $L^* \approx 10^{-5}$ | (1) Hubbert, 1937; Lallemand et al., 1994; Schellart, 2002 |
| Cohesion | $C_{sand} = 0\text{-}200 \text{ Pa} \quad (2)$ $30\text{-}130 \text{ Pa} \quad (3)$ | $C_{overburden} = 0\text{-}60 \text{ MPa} \quad (2)$ $5\text{-}20 \text{ MPa} \quad (4)$ | $C^* = 3.3\text{-}6.5 \times 10^{-6}$ | |
| Density (sand/overburden) | $\rho_{sand} = 1500 \text{ kg/m}^3$ | $\rho_{overburden} = 2300\text{-}2600 \text{ kg/m}^3 \quad (2)$ | $\rho^* = 0.58\text{-}0.65$ | (2) Weijermars et al., 1993 |
| Density (silicone/salt) | $\rho_{silicone} = 965 \text{ kg/m}^3 \quad (2)$ | $\rho_{salt} = 2200 \text{ kg/m}^3 \quad (2)$ | $\rho^* = 0.44$ | (3) Lohrmann et al., 2003; Panien a et al., 2006; Schellart, 2002 |
| Stress | | | $\sigma^* = \rho^* g^* L^*$ $= 5.8\text{-}6.5 \times 10^{-6}$ $\approx 10^{-5}$ | (4) Jaeger and Cook, 1969; Hoshino et al., 1972 |
| Viscosity | $\eta_{silicone} = 5 \times 10^4 \text{ Pa}\cdot\text{s} \quad (2)$ | $\eta_{salt} = 2 \times 10^{18} \text{ Pa}\cdot\text{s} \quad (5)$ | $\eta^* = 2.5 \times 10^{-14}$ | (5) Weinberger et al., 2006 |
| Time | $T_{model} = 72 \text{ hr}$ | $T_{prototype} = 1.86\text{-}2.11 \text{ Ma}$ | $T^* = \eta^* / (\rho^* L^*) \quad (2)$ $\approx 3.8\text{-}4.3 \times 10^{-9}$ | |

3.2.3 Model setup

The setup is designed for modelling the deformation and structures formed by gravity sliding on passive margins with visco-elastic salt layers (Fig. 3.2). In total, four experiments were conducted. In these experiments, the model area is $50 \times 100\text{-}120 \text{ cm}^2$ and consists of a 8 mm thick layer of silicone overlain by a 10 mm thick layer of colored sand. The sand-silicone model originally rests on two horizontal plates (Plate 1 and 2) which divide the model into two parts (Fig. 3.2). The experiment is launched by tilting Plate 1 and Plate 2 to variable parts (e.g., Fort et al., 2004). While the experiment is conducted, additional sands are funneled at various time intervals to the newly-formed lower topographies caused by significant deformation. This process aims at simulating synkinematic sedimentation.

In the first experiment, the silicon layer has a tabular shape. The total length of the model is 1000 mm long, consisting of Plate 1 of 750 mm and Plate 2 of 250 mm. The model width is 500 mm. A metal bar is placed at the end of the model as a confining downslope boundary, while the metal bars are removed from the lateral boundaries to allow the model to move laterally when starting the experiment by tilting Plate 1 at an angle of 5° (Fig. 3.2a).

The setup of Models 2 and 3 has a tabular-shaped silicon layer underlying the sand layers confined within an area of about $50 \text{ cm} \times 120 \text{ cm}$. The experiments start by tilting Plate 1 by 4° (Fig. 3.2b and c). In the second experiment, the model is completely confined by the metal bars on each side of the model, and no additional sediments are added to the model. In the third experiment, at the end of Plate 2 there is a 150mm-wide zone without sand and thus the model is devoid of any confinement. Model 3 is used to simulate a situation where the prekinematic sedimentary deposits

have not completely covered the salt yet. Synkinematic sediments are supplied into the local depressions formed during the third experiment.

In the fourth model, a double-wedge-shaped model base simulates the salt basin, which is separated into two subbasins before the gravity gliding plays its role caused by salt deformation (e.g., Jackson et al. 2000; Marton et al., 2000). Originally, Plate 1 and Plate 2 form a V shape base by inclining in the opposite direction at angles of 1.72° and 3.43° respectively. A silicone layer fills the model with the maximum thickness of 1.4 cm at the juncture of the two plates. A 0.7 cm thick sand layer is sieved on top of the silicone as the prekinematic overburden deposit. A sand bar at the downslope boundary confines the far end of the model to simulate the newly-formed oceanic crust. The experiment starts by tilting Plate 2 to 1° (β) and Plate 1 to 4.8° (α) (Fig. 3.2d). Syntectonic sedimentary layers are provided by funneling colored sands in the newly-formed accommodation space.

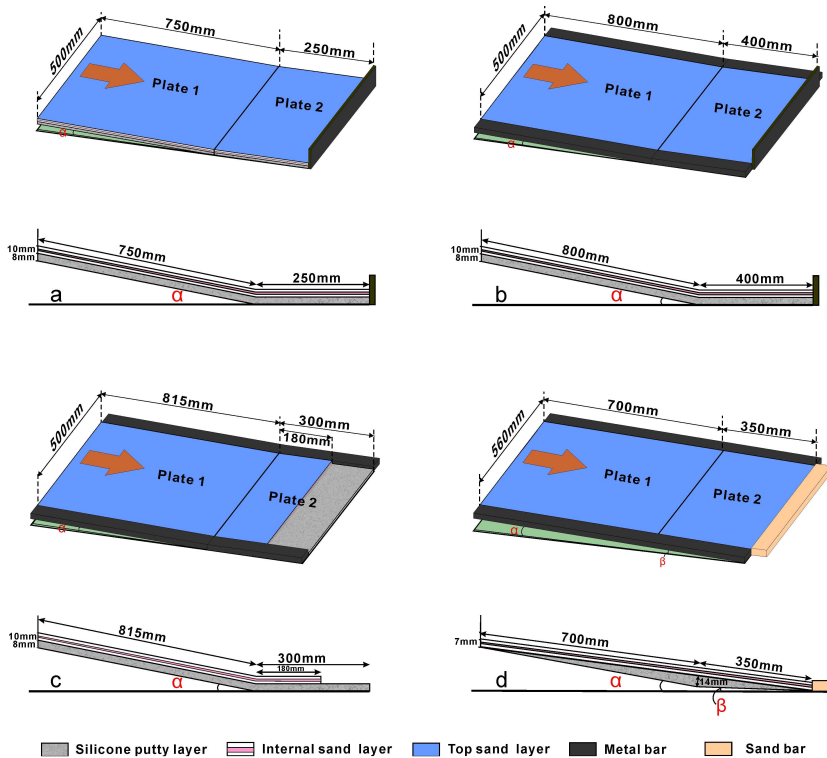


Figure 3.2: Setup of the sand-silicone experiments — (a) Model 1, (b) Model 2, (c) Model 3 and (d) Model 4. The oblique top views show the model size and the boundary confinements. Cross-sections of each model display the geometry of the model base and the thickness of the sand and salt layer. The experiments are initiated by tilting Plate 1 to angle α and Plate 2 to angle β . Orange arrows indicate the downslope direction of the model slope.

Table 3.2 Summary of set-up parameters of the four experiments

| Model No. | Size (cm ²) | Base shape | H _{sands} (mm) | H _{silicone} (mm) | α (°) | β (°) | Lateral boundary | Downslope boundary | Duration (hr) | Syn-kinematic sediments |
|-----------|-------------------------|----------------|-------------------------|----------------------------|--------------|-------------|-----------------------|--|---------------|-------------------------|
| 1 | 50× (75+25) | Tilted tabular | 10 | 8 | 5 | 0 | Free lateral boundary | Metal bar | 25 | Yes |
| 2 | 50× (80+40) | Tilted tabular | 10 | 8 | 4 | 0 | Metal bar | Metal bar | 68 | No |
| 3 | 50× (81.5+30) | Tilted tabular | 10 | 8 | 4 | 0 | Metal bar | 22cm uncovered silicon and free boundary | 69 | Yes |
| 4 | 56× (70+35) | Double wedge | 7 | 14 | 4.8 | 1 | Metal bar | Sand bar | 118 | Yes |

3.2.4 Results of the experiments

After launching the experiments, the ensuing deformation is driven entirely by gravity. The structural development during the experiments is influenced by the sand-silicone thickness ratio, the original geometry of the silicone layer and the basal slope angle, in addition to the intrinsic properties (density, coherence and viscosity) of the silicone (Weijermars et al., 1993). Thicker silicone layers have the potential to develop grabens instead of tilted blocks (Brun and Mauduit, 2008), while steeper slopes tend to result in more complex structural patterns (Fort et al., 2004). Considering all factors and parameters in the set-up, we limited the duration of the major experiments to 68-72 hours. During the experiment a digital 3D laser installed above the model scanned the evolving topography, which simulates the seafloor bathymetry, every 30 minutes, and a camera recorded the top view of the model surface structures. At the end of each experiment, the models are carefully wetted and cut into dip-parallel sections at regular intervals, in order to reveal the internal structures and to study their final geometry.

The experimental results of the four models are displayed by showing the top-view pictures of the structural evolution during the experiments, the 3D surface topography reconstructed by adopting the data collected by the laser scanner, or the dip-parallel cross sections showing the internal structures of the models.

Model 1

The top view of model 1 after 25 hours (Fig. 3.3c) shows that three distinctive structures form in the model from updip to downdip. Well-developed silicone diapirs and their associated normal faults and grabens form in the uppermost part of Plate 1, with a total width of about 3 cm and a length covering almost the entire model width. At the downslope side of these large structures, two relatively small grabens and their associated silicone diapirs develop, which can be considered as precursors of the

structures found updip. The traces of these extensional structures are almost parallel to each other and perpendicular to the downslope direction. Due to the free lateral boundaries of the model, sand and silicone have the potential to move sideward driven by gravitational and compactional effects. This results in a long and curved normal fault dipping towards the right side of simulation (looking downdip) nearly through the remainder of the model. This fault indicates that the sliding direction is oblique to the downslope direction, which is an unwanted effect uncommon in nature. Therefore, the experiment was ended and confined lateral boundaries were used in the following experiments.

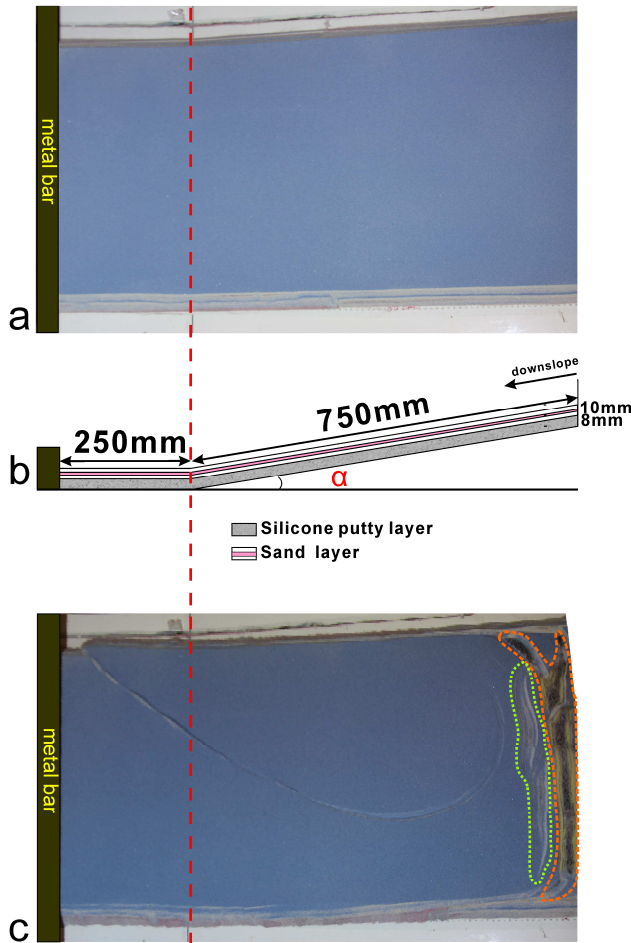


Figure 3.3: Initiation and final result of Model 1. (a) Top-view picture of the model at the beginning of the experiment; (b) side-view sketch of the model set up; (c) top-view picture of the model in the end of experiment. The red dashed line shows the joint of the two plates. The orange dashed polygon indicates the zone of the well-developed silicone diapirs, where the yellow sand was funneled into the topographic lows during the experiment. The green dashed polygon delineates two developing diapirs.

Model 2

Laterally confined boundaries are adopted in this model set-up and no additional sediments are supplied into the newly-formed topographic lows during this 68-hour experiment.

Fig. 3.4 shows the topographic evolution during this experiment. The first significant topographic change begins with a compressional fold at the toe of the inclined plate before updip extensional normal faults appear. Later the compressional structures evolve into more complex folds and thrusts with associated minibasins. Meanwhile, updip extensional structures occur in the form of faults, grabens and even diapirs. Most directions of the structures are parallel to each other and perpendicular to the slope.

The cross-section of the final result displays two distinctive structural domains: the extensional and compressional area (Fig. 3.12a). Because no synkinematic sediments were supplied during the experiment, no growth-fault and rollover systems formed in this model, and the only well-developed extensional structures are normal faults, grabens, minibasins, and diapirs between rafts (Fig. 3.5). The maturity of the diapirs generally decreases downdip, which suggests that the extensional structures in the upper slope area occur earlier than those further downdip and that the migration direction of extension is downdip. In the compressional domain, folds and thrusts are dominant and restricted to the toe of the slope; the contractional domain migrates in both the downdip as well as the updip direction, according to the prograding directions of the folds forming on both sides of the imbricated folds and thrusts (Fig. 3.6).

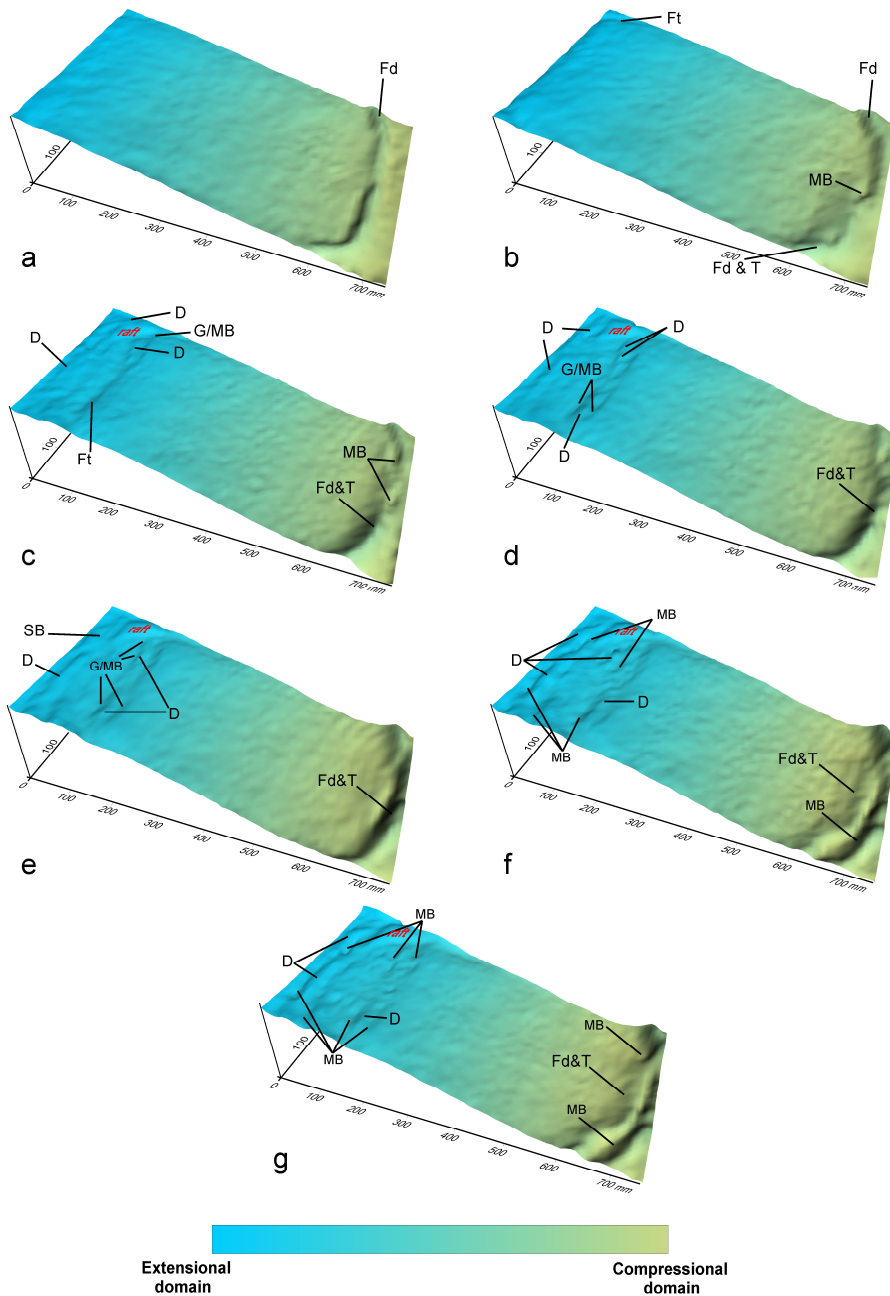


Figure 3.4: The temporal evolution of Model 2, visualized in 10-hour intervals by an artificially illuminated 3D surface. (a) 10 hr, (b) 20 hr, (c) 30 hr, (d) 40 hr, (e) 50 hr, (f) 60 hr and (g) 68 hr. Structural elements are interpreted and indicated on the surface; D: Diapir(s); Ft: Normal fault(s); Fd: Fold(s); Fd & T: Folds & thrusts; G: Graben(s); MB: Minibasin(s); SB: Silicone minibasin(s).

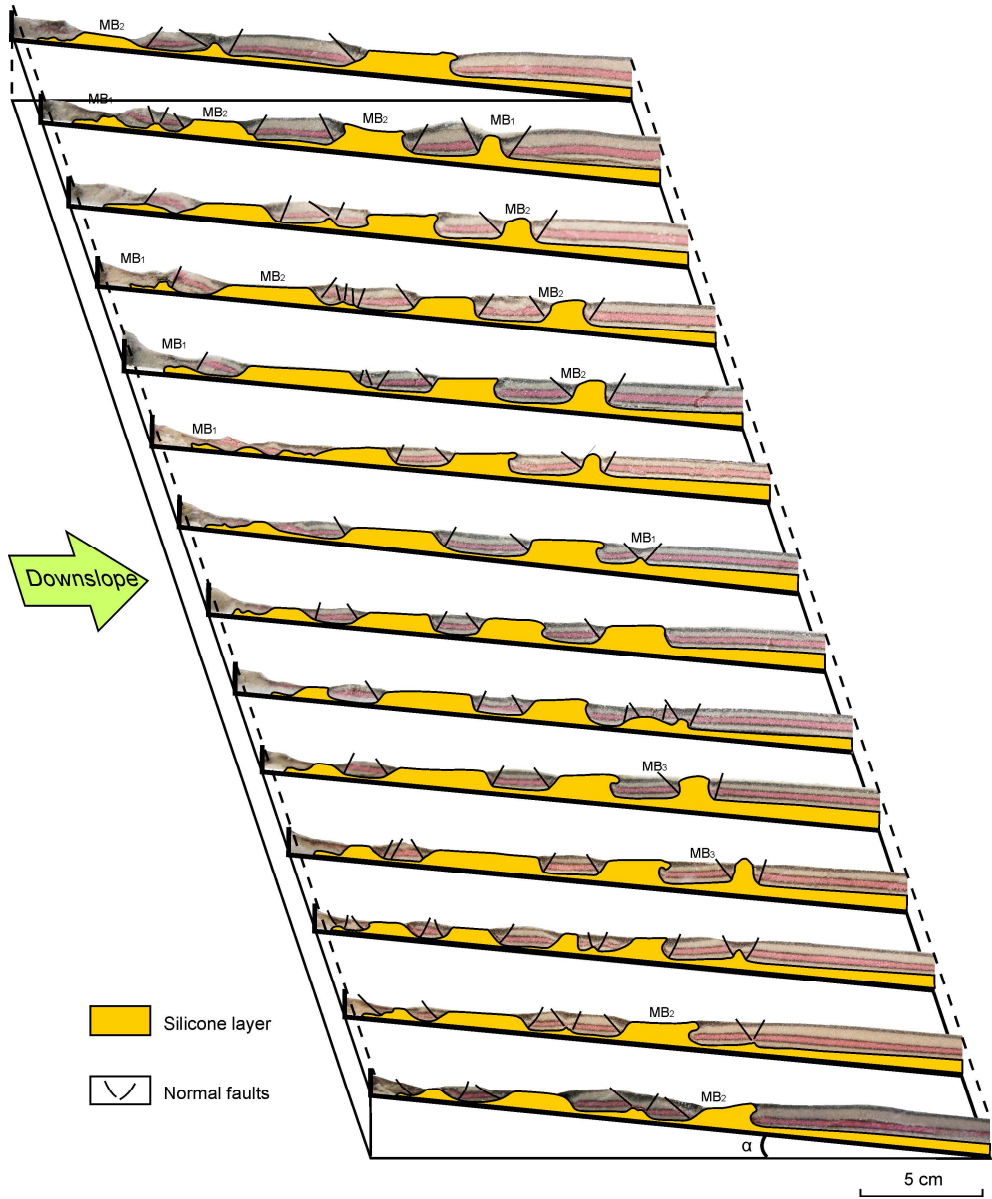


Figure 3.5: Serial dip-parallel cross sections showing the internal structures in the extensional domain of Model 2. The final result is sliced at intervals of 3.3 cm. Three types of minibasins are indicated, based on their boundary conditions, as MB₁ (with no direct contact with silicone), MB₂ (bounded by a silicone diapir or nappe and its adjacent rafts) and MB₃ (bounded by the adjacent silicone diapirs and with the basin center on the top of the prekinematic layer).

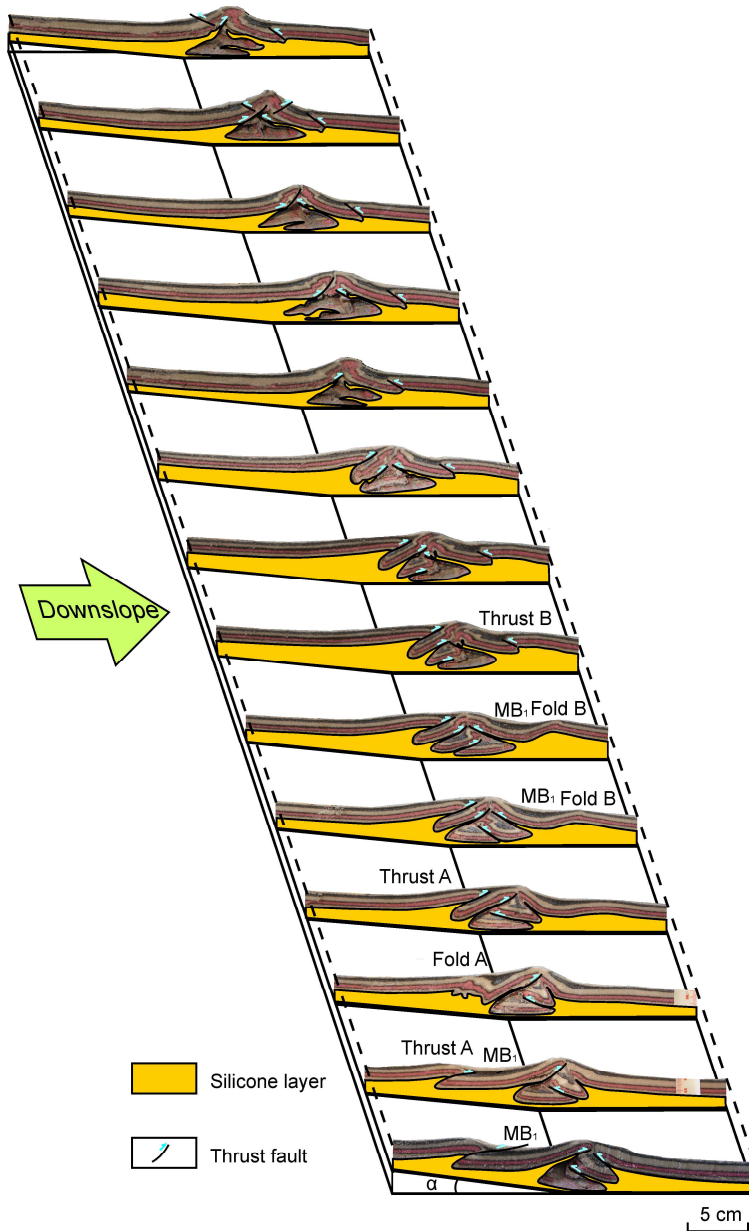


Figure 3.6: Serial down-dip cross-sections showing the internal structures in the compressional domain of Model 2. The final result is sliced at intervals of 3.3 cm. MB₁ indicates the minibasin with no direct contact with silicone.

Model 3

The downslope boundary of the third model is unconstrained and the sand layers do not completely cover the underlying silicone layer. During this experiment the newly-formed local depressions like grabens and minibasins are filled by synkinematic colored sands.

The package of silicone and sand moves and expands in the downdip direction, with the rate of the sands exceeding that of the silicone, resulting in the downslope boundary of the sand layer catching up with the silicone layer and almost covering it (Fig. 3.7). Only an extensional domain forms, in the updip part, with no distinct structures developing in the downslope area (Fig. 3.7; Fig. 3.12b). This is caused by the extensional forces being dominant in the upslope area and an absence of compressional stresses in the downslope area because of the free downslope terminal boundary. The extensional domain is characterized by normal faults, grabens, diapirs, rollovers and minibasins (Fig. 3.8). Major extensional diapirs are aligned along strike and are parallel to each other while some diapirs close to the lateral boundaries are parallel or oblique to the downslope direction (Fig. 3.7).

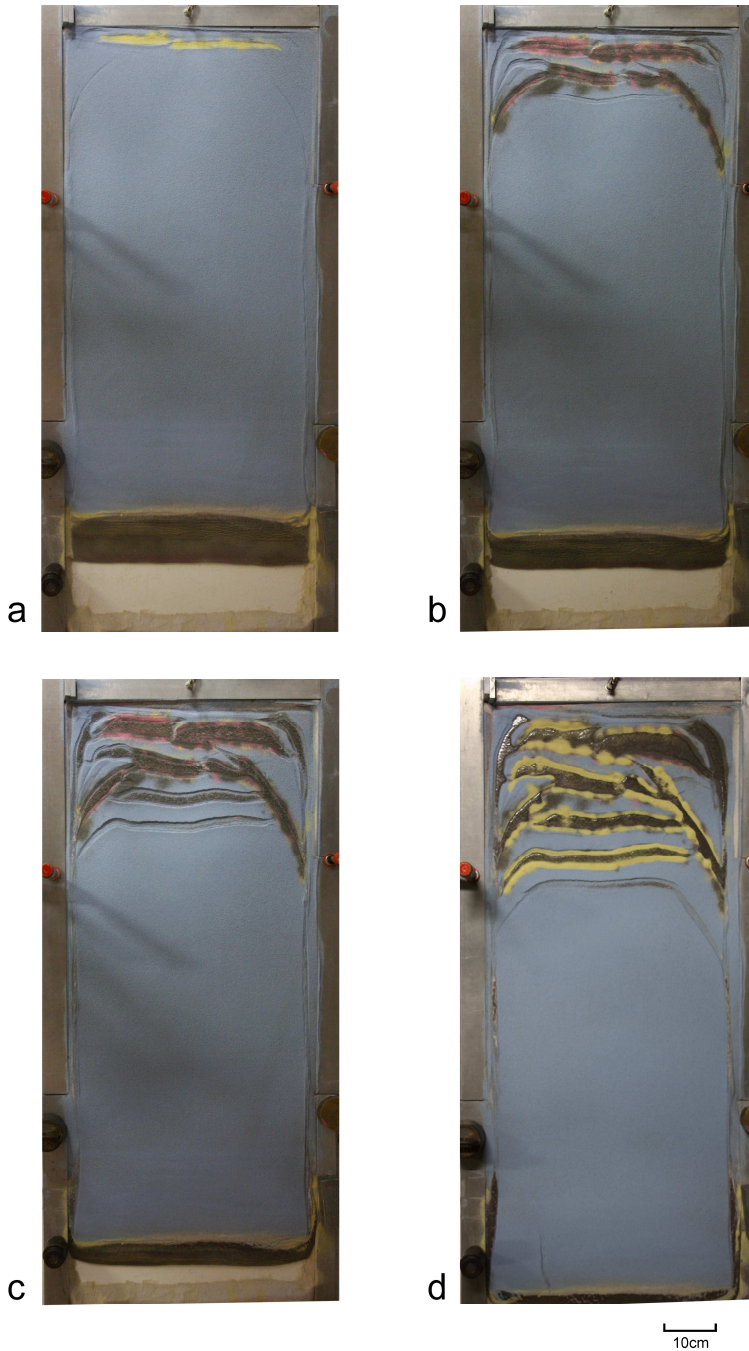


Figure 3.7: Top view of Model 3 showing the structural development after (a) 2h, (b) 11h, (c) 27h and (d) 48h. The pink and yellow sands are the synkinematic sediments added during the experiment.

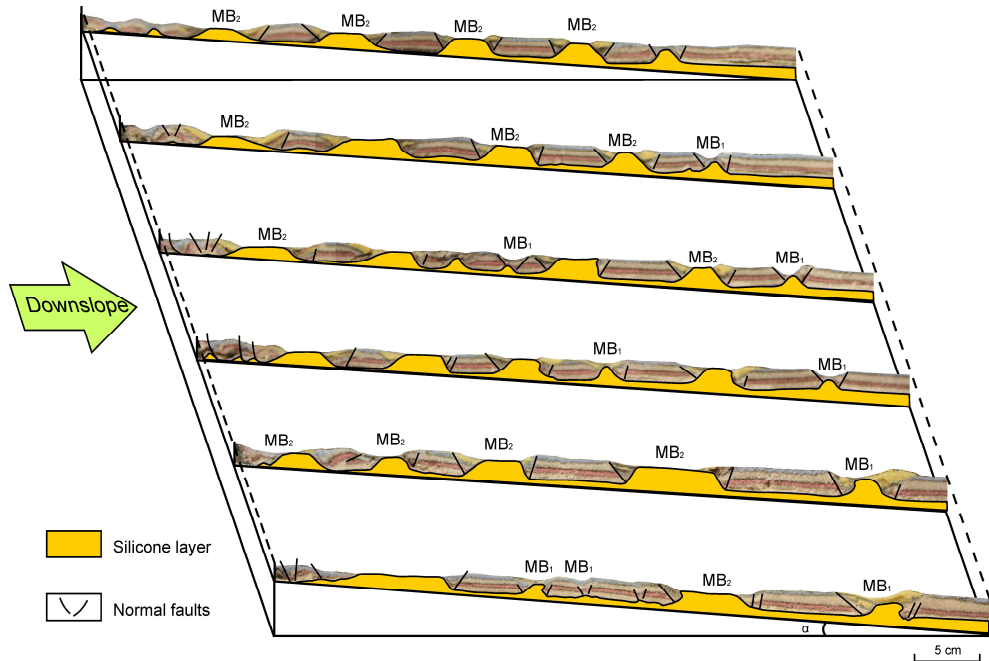


Figure 3.8: Serial downdip cross-sections showing the internal structures in the extensional domain of Model 3. The final result is sliced at intervals of 7.14 cm. Two types of minibasins (MB_1 and MB_2) develop in the extensional domain. Synkinematic layers of yellow sands can be observed in minibasins.

Model 4

In the fourth experiment the double-wedged silicone layer is bounded by a sand bar as the downslope boundary. The diapir type driven by erosionally differential loading is simulated in the later period of the experiment. The overlying sand above the silicone layer was removed in a small local area. During the rest of the experiment additional sand was funneled in the gap to simulate synkinematic sedimentation (pink sand in Fig. 3.9d).

The upslope extensional and the downslope compressional domains are the two major structural provinces in this model (Fig. 3.10, 3.11). They concomitantly develop during the experiment. The extensional diapirs in the upslope cross each other, resulting in minibasins in various polygonal shapes bounded by different structural elements (Fig. 3.9, 3.10). The compressional domain is characterised by two distinctive structures: a growth syncline (minibasin) located in a thrust footwall, and a thrust with a silicone detachment displaced onto the sand bar (Fig. 3.11). According to the prograding directions of these two structures, the dominant migration direction in the compressional domain is downslope. An erosional diapir ridge in the lower slope area upwells due to the differential sediment load on the silicone (Fig. 3.12c).

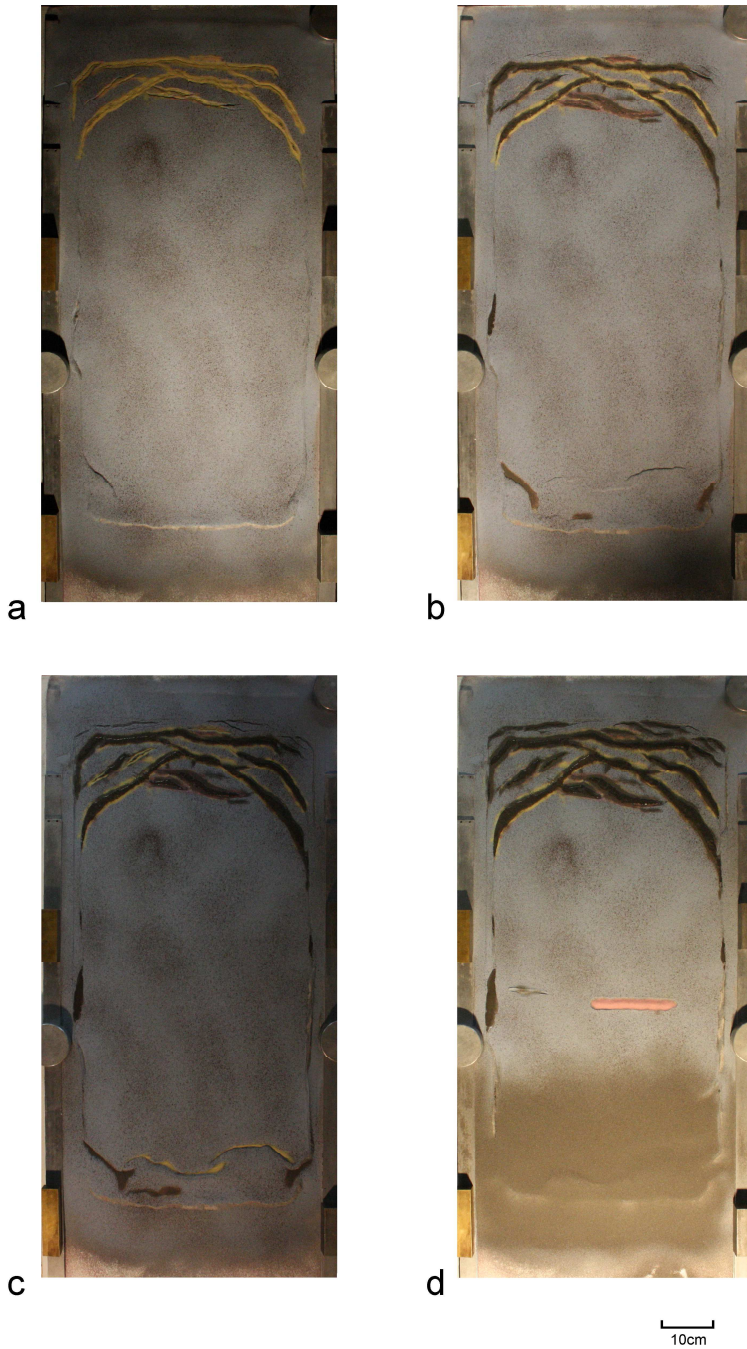


Figure 3.9: Top view of Model 4 showing the structural development after (a) 30h, (b) 60h, (c) 90h and (d) 118h. The pink and yellow sands are the synkinematic sediments added during the experiment.

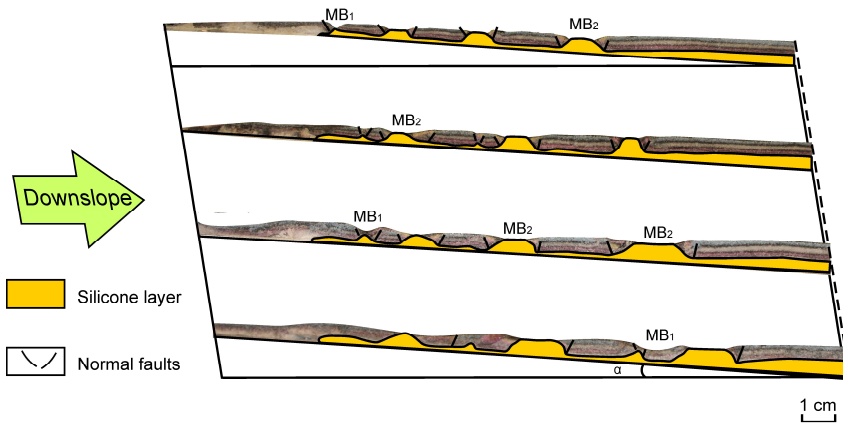


Figure 3.10: Four down-dip cross-sections showing the internal structures in the extensional domain of Model 4. The final result is sliced at intervals of 11.2 cm. Two types of minibasins (MB_1 and MB_2) develop here. Synkinematic layers of yellow sands can be observed in the minibasins.

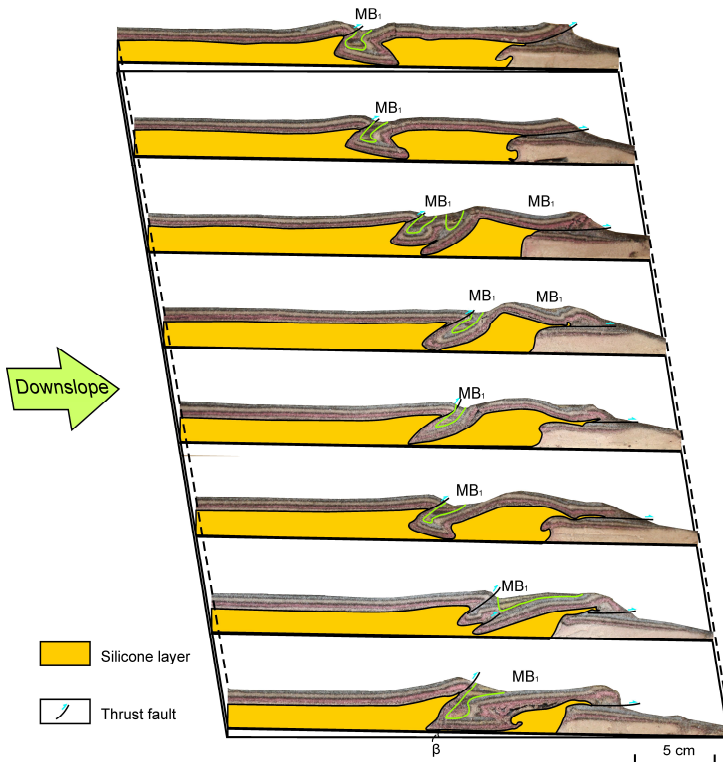


Figure 3.11: Serial down-dip cross-sections showing the internal structures in the extensional domain of Model 4. The final result is sliced at intervals of 6.2 cm. Only one type of minibasin (MB_1) develops in the compressional domain. The green lines outline the synkinematic layers in the growth syncline.

3.3 Comparison and discussion of experimental results

The results show that the set-ups with a free lateral boundary (Model 1) or a free downdip boundary (Model 3) (Fig. 3.12b) are not able to simulate the three structural zonations typical of passive margins influenced by salt movements. The fully confined models, i.e. Model 2 (Fig. 3.12a) and Model 4 (Fig. 3.12c), can develop these three domains: the upslope extensional, the middle transitional and the downslope compressional.

3.3.1 Extensional structures

The extensional structures in Model 2, 3 and 4 are quite similar and characterized by thin-skinned extensional structures like normal faults, grabens, rollovers, diapirs and their associated minibasins. The migration directions of these extensional structures are all downslope.

Rollovers and turtle structures

When comparing the extensional domains in our models with those of the dominant-gliding experiments conducted by Brun and Fort (2011) (Fig. 2.10b in chapter 2), it can be observed that the sealed tilted blocks and rollover systems are not very pronounced in the updips part of our experiments. Such structures require relatively high sedimentation rate (Fig. 7.18 in Brun and Fort, 2008), whereas in the present models the thickness of silicone is relatively greater and the sedimentation is lower or even zero, which does not allow any rollover structures to form. Only a few smaller features seem to be similar to fledgling rollover and turtle structures (Fig. 3.13).

Grabens and extensional diapirs

Due to the low sedimentation rates (in Model 3 and Model 4) or no sedimentation (in Model 2), the extensional diapirs developing from former grabens are unable to grow very high vertically. These diapirs experience stages of rise and fall.

At the initial stage, the upslope extension begins with formation of graben and of a small reactive diapir in the thinnest part of the graben (Fig. 3.14a). The graben later is amplified and the roof is thinned, allowing the active diapir to penetrate into (Fig. 3.14b) or even pierce the sand layer (Fig. 3.14c). At the rising stage, extensional strains act as driving forces for diapir upwelling whereas during the falling stage, extensional strains act as driving forces for the lateral movement of diapirs and therefore reduce the vertical flow. This increases the width of the older diapirs toward downslope but decreases their height (Fig. 3.14d-e), resulting in the formation of minibasins (MB₂). The driving gravity force causes the extensional zone to expand downslope and generates new grabens and diapirs in the downslope direction. Therefore, the downslope extensional diapirs are generally younger than the upslope ones (Fig. 3.5, 3.8 and 3.10).



Figure 3.12: Cross sections of Model 2 (a), Model 3 (b) and Model 4 (c) showing similarities and differences in structural zoning and styles.

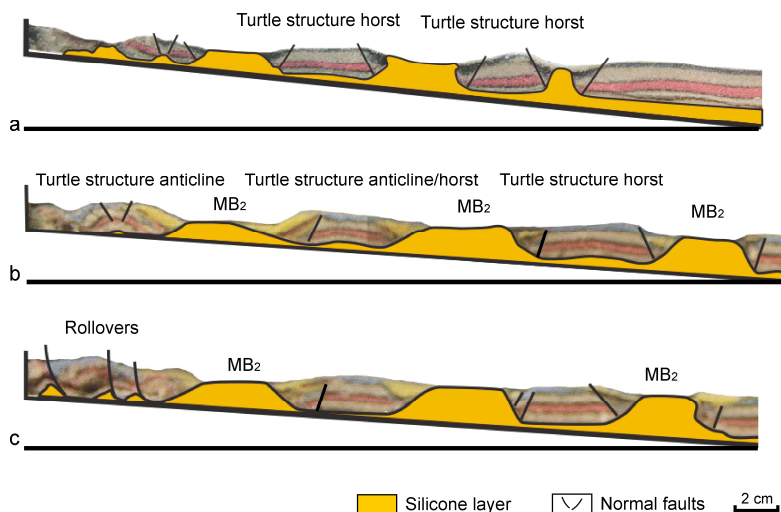


Figure 3.13: Turtle structures and rollovers displayed in the cross-sections of the extensional domains of Model 2 (a) and Model 3 (b, c). The yellow sand is synkinematic sediment. The MB₂ type of minibasins are indicated.

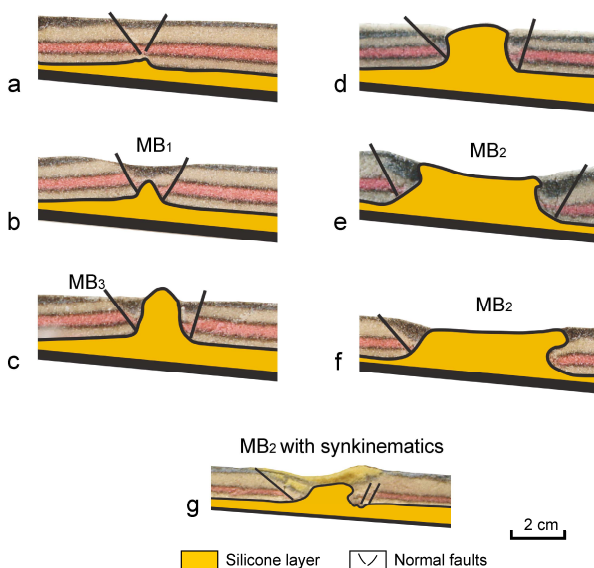


Figure 3.14: Cross-sections showing the stages of diapiric rise and fall. (a) A graben at the onset of extension (Model 2); (b) a reactive diapir rising in the graben (Model 2); (c) an active diapir penetrating the roof (Model 2); (d) a widened diapir (Model 2); (e) and (f) the falling of a continued widening diapir (Model 2); (g) synkinematic sediment filling in a MB₂ minibasin formed during the fall of a diapir (Model 3).

3.3.2 Compressional structures

According to the structural evolution in the Model 2 (Fig. 3.4) and Model 4 (Fig. 3.9), the downslope contraction occurs earlier than the upslope extension, in line with Brun and Fort's dominant-gliding model. They consider that this phenomenon is an important difference between dominant gliding and pure spreading, and thus compressional structures are the first basin-scaled deformation (Brun and Fort, 2011). However, the contractional structures migrate both downslope and upslope. In Model 2, the new compressional structures form on the both sides of the older ones (Fig. 3.6) while in Model 4 - although the new compressional structures form on the upslope side of the older ones - the existing and emerging structures both prograde downslope (Fig. 3.11). The silicone layer acts as a décollement layer in the compressional domain, which is common in the area as preexisting salt diapirs are lacking because the shortening thickens the overburden above the salt and therefore impedes the upwelling of salt (Hudec and Jackson, 2007). The compressional structures observed in the final stages include folds, thrusts, pinched synclines, growth synclines and pop-up silicone-cored anticlines.

Folds and thrusts

The folds observed here are usually the early stages of the later-to-be-formed thrusts. Folds A and B in Fig. 3.6 laterally (along-strike) develop to Thrust A and B which progrades downslope and upslope respectively. A relatively large thrust with silicone detachment develops on the downslope sand-bar boundary simulating the newly-formed oceanic crust, and some small folds can be found in its hanging wall in Model 4 (Fig. 3.11). The silicone body emplaced on the sand bar, to some extent, corresponds to the base salt ramping up basinward over the step-up fault and extending over oceanic crust as an allochthonous nappe in the South Atlantic (Fig. 16 in Rowan, 2014).

Pinched synclines and pod-like structures

In Models 2 and 4, pod-like structures are a particularly striking deformation feature in the compressional domain (Fig. 3.6, 3.11). Fig. 3.15a and c show the evolutionary stages of these structures. Two adjacent and oppositely vergent folds or thrusts confine a syncline (minibasin). As these two structures progressively prograde, the width of the syncline is decreasing with the vertical depth increasing. Continued pinching leads to the syncline becoming isolated from the source layer and getting incorporated into the silicone layer, creating a pod-like structures. The imbricated pod-like structure in Model 2 results from the multiple accumulations of these pinched synclines in the same location, and it becomes an anticline owing to its increasing height (Fig. 3.15c). The pinched growth syncline can be recognized in Model 4 because the synkinematic sediments are filled in this slowly decreasing accommodation space (Fig. 3.15d).

Pop-up anticlines

In Model 2 the thickening of the overburden above the silicone, due to the increasingly imbricated pinched synclines, retards the formation of compressional diapirs or even pop-up silicone-cored anticlines. Nevertheless, along with a pinched syncline, such a pop-up-type anticline can be found in Model 4.

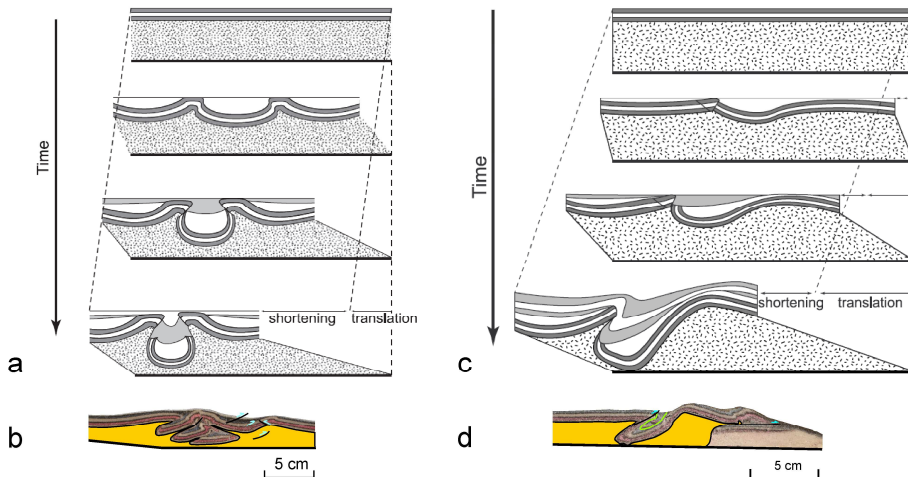


Figure 3.15: Pinched synclines, pod-like structures and pop-up anticlines. (a) and (c) Schematic diagrams summarizing the evolution of two types of pinched synclines (modified from Brun and Fort, 2004). (b) The imbricated pod-like structures in Model 2. (d) A pinched growth syncline and a pop-up anticline in Model 4.

3.3.3 Minibasins

Three types of minibasin are recognized in the results of all experiments based on their boundary contact relationships, regardless of whether they occur in the extensional or compressional domain. They are named here as MB₁, MB₂ and MB₃.

MB₁

The first type of minibasin has no contact with the silicone layer. It is bounded by the structures in the sand layers, in both the extensional or contractional domain. It can be a graben forming at the onset of extension (Fig. 3.14a), a syncline bounded by two folds or thrusts (Fig. 3.6), or a local depression bounded by the silicone-cored anticline and the fold in the hanging wall of the thrust fault (Fig. 3.11). Owing to the complexity of the compressional structures, the MB₁ forming in that domain have a larger variety of structural elements as boundaries than those formed in the extensional domain.

MB₂

This type of minibasin develops on top of a collapsed extensional diapir, with the diapir top surface as the minibasin's base. The previous space occupied by the rising diapirs is freed up to become a minibasin caused by the fall of the diapir; it is laterally confined by the adjacent higher prekinematic layers like the footwalls of normal faults (Fig. 3.14e, f). Subsequent sediment gradually fills in the minibasin of the type MB₂ as synkinematic layers (Fig. 3.14g). If the sedimentation rate is higher and the extension still continues, the diapir continues subsiding until its floor touches the subsilicone layer. The silicone layer thins to a weld and a mock turtle anticline might form in the minibasin during such an extreme fall of the diapir (Fig. 10 in Vendeville and Jackson, 1992b).

MB₃

This type of minibasin has the lower sediment layer as its base and the adjacent diapirs' flanks as its peripheral boundary (Fig. 3.5, 3.14c). MB₃ does not well develop in the experiments because the diapirs piercing through the sand layers here mostly have high maturity, i.e. they are in the stage of the diapiric fall, which are incapable of forming the high flank boundaries of the minibasin.

In conclusion, the experimental results compare well with the real passive-margin basins where salt tectonics play a role.

3.4 Digital elevation model

Considering the results of all models, the topographic data obtained from Model 2 is best suited as input data for the next-step, the numerical simulation of turbidity currents. Model 2 successfully simulates the typical structural characteristics of passive-margin basins with salt, i.e., their typical three structural domains. Moreover, the structures formed in a situation with no sedimentation produce more accommodation space in the form of minibasins than those under low sedimentation rates. This allows the accumulation of significant turbidite thicknesses in the numerical simulation experiments.

The scanned 3D topographic data of the uppermost, extensional domain (250 mm in the downdip direction) of Model 2 is used for the digital model. This partial topography is upscaled by a factor of 8×10^4 with a cell size of 250 m, in order to adjust the scale of the modelled minibasin to a few to tens of kilometers in diameter which are dimensions of typical minibasins in nature. To obtain a more realistic continental margin and to reduce the boundary effects, a shelf area with a width of 10 km and a gradient of less than 0.7° was added upslope by Kriging interpolation. Furthermore, an incised channel connecting the shelf to the mini-basin was manually created. The channel is moderately sinuous and has a U-shaped cross-section profile with a slope gradient of about 0.022 ($\theta \approx 1.25^\circ$). It is about 70 m deep, 3 km wide (with a 1.5 km wide thalweg) and 10 km long, which is approximately within the

average size of submarine canyons (depth of hundreds of meters and width of a few kilometers) (e.g. Mulder, 2010). The size of the digital elevation model is 40 km wide (along strike) and 30 km long (down dip) (Fig. 3.16).

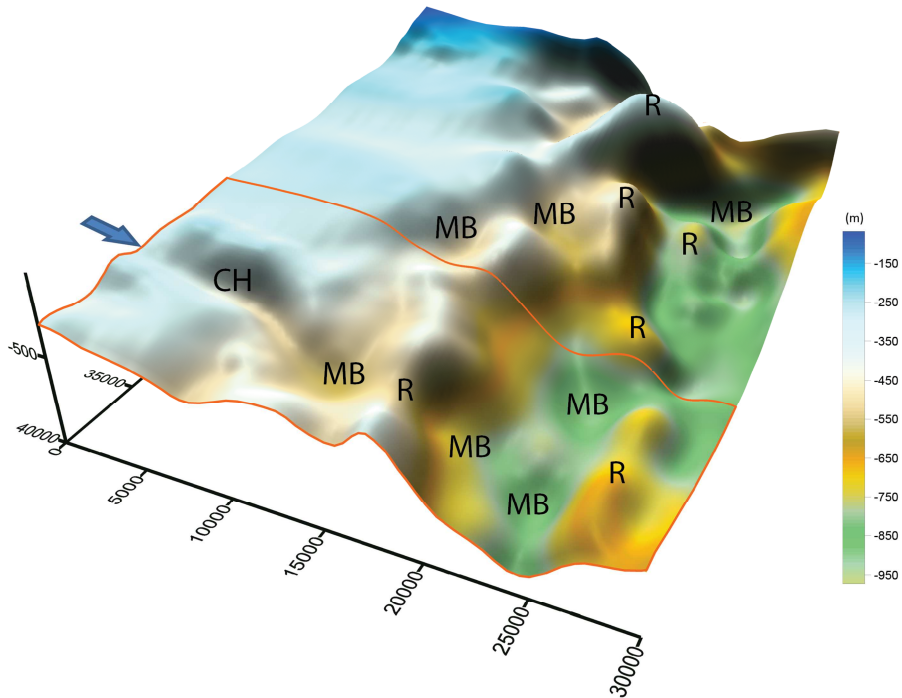


Figure 3.16: 3D view of the experimental analogue of sea-floor bathymetry with numerous tectonic ridges and mini-basins. The interesting topographic area is indicated by the orange line. Main geomorphological elements include an artificial incised channel (CH), minibasins (MB) and diapiric ridges (R). The blue arrow indicates the inflow point and the initial direction of the simulated turbidity currents.

CHAPTER 4

A Review of Subaqueous Turbidity Currents, Turbidites and Their Confined Systems

4.1 Introduction

Classic fan models of submarine turbidite systems are mostly based on the studies of basin-scaled submarine turbidite systems that simplify submarine reliefs as smooth seafloor topographies, especially on passive continental margins. However, several processes, including tectonic activity, can perturb smooth sediment transport profiles, which results in uneven submarine morphologies and a range of confined sedimentary settings. Slope physiography has a significant influence on turbidity current hydrodynamics, and therefore the location of erosion and deposition, and flow pathways.

This chapter first gives an introduction of the general understanding of density flows and sediment gravity flows, which have a direct relationship with turbidity currents. Then subaqueous turbidity currents (including initiation mechanisms, hydrodynamics), turbidites and classic fan models for deep-sea turbidite systems are reviewed in detail. Finally, the impact of confinement on the slope, in particular slope minibasins on passive margins, on subaqueous turbidity current behavior and depositional architecture, are discussed by reviewing the literature based on experimental modeling, outcrop studies, and subsurface data analysis.

4.2 Density flows and sediment gravity flows

Sediment can be transported via rivers, glaciers, wind, underground water, waves, seawater and so on. The spectrum of sediment-mixed fluids display their differences in terms of physical properties like the density contrast between them and the ambient fluid, the proportion of different grain sizes and densities in the mixture, and dynamic characteristics such as transportation capacities and sediment support mechanisms. The resulting deposit can possess diagnostic sedimentary sequences and structures. Two important flows regarding turbidity currents are first introduced. They are density flows and sediment gravity flows.

4.2.1 Density flows

Density flows are primarily horizontal flows that occur when a fluid of one density flows into another of a different density (Edwards, 1993). The density contrast between the flow and the ambient fluid (air and water) can be induced by the difference in temperature, salinity or the carried sediment. Four types of density flows are differentiated by the density difference, which are hypopycnal flows ($\rho_{flow} < \rho_{ambient\ fluid}$), homopycnal flows ($\rho_{flow} = \rho_{ambient\ fluid}$), mesopycnal flows (ρ_{flow} is between the densities of two layers in the stratified water column) and hyperpycnal flows ($\rho_{flow} > \rho_{ambient\ fluid}$) (Fig. 4.1) (Mulder and Alexander, 2001). Homopycnal and mesopycnal flows are less common in a deep water environment. The major density flows transporting a large amount of sediment to deep water are the hyperpycnal flows.

Mulder (2011) further divided hyperpycnal flows into two sub-types: suspended-load-dominanted hyperpycnal turbidity currents (hyperpycnal flows *sensu stricto*) (e.g., Mulder and Syvitski, 1995) and bedload-dominated hyperpycnal flows (e.g., inertia flows used by Bates, 1953; hyperpycnal flows used by Mutti et al., 1996). The first subtype can be considered as the quasi-steady low-density turbidity currents. The “hyperpycnal” here is used to mean “above a density threshold” but not simply “high density”. The second subtype of flows behave as hyperconcentrated and concentrated flows, often occur at the flooded-river mouths and flows along the steep basin slope in active tectonic settings. Now hyperpycnal flows are commonly referred to with a fluvial conception *sensu stricto* (Mulder and Alexander, 2001).

4.2.2 Sediment gravity flows

Sediment gravity flows are mixtures of particles/sediment and fluid that flow downslope because their density is greater than that of their ambient fluid. Gravity acting on the particles drives the mixture flowing downslope (Middleton and Hampton, 1973). The interstitial fluid between particles is a passive partner. Ideally, if the downslope component of the gravity exceeds the frictional resistance to flow and the grains are kept in suspension by the effective support mechanisms, sediment gravity flows are allowed to keep flowing down a slope. Their flow behavior is

determined by the density of the interstitial fluid, the density of the ambient fluid, the sediment type and concentration in the mixture, the clay content in the flow, and the gradient and confinement of topographic slope. On the basis of the dominant sediment support mechanisms, sediment gravity flows can be classified into four types: grain flows (supported by the interactions between cohesionless grains), liquefied/fluidized flows (supported by the upward escaping fluid), debris flows or mudflows (supported by the cohesive strength and buoyancy of the mud matrix), and turbidity currents (supported by fluid turbulence) (Middleton and Hampton, 1976).

Turbidity currents are part of a continuum of sediment gravity flows, in which grains are mainly supported by fluid turbulence (Middleton and Hampton, 1973; Lowe, 1982; Middleton, 1993; Simpson, 1997; Kneller and Buckee, 2000; Meiburg and Kneller, 2010). Turbidity currents can be found in subaerial and subaqueous environments and induced by natural and artificial causes. For example, flows of powder-snow avalanches triggered by mechanical failure in the snowpack, pyroclastic flows caused by volcano eruptions, submarine turbidity currents generated by oceanic earthquakes and volcanos, and even the flows due to the release of industrially polluted dense gas into air (Middleton, 1993; Simpson, 1997).

Grain flows, liquefied flows and debris flows are non-Newtonian flows while turbidity currents are Newtonian flows. In subaqueous settings, these four end-members can evolve into each other during their passage downslope and an individual sediment gravity flow can comprise several support mechanisms along their length.

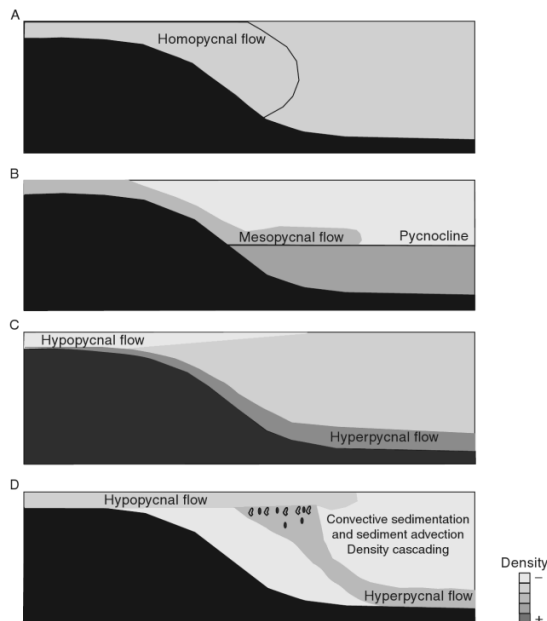


Figure 4.1: Classification of density flows (from Mulder, 2011).

4.3 Subaqueous turbidity currents and turbidites

In subaqueous settings, the ambient fluid is water. Subaqueous turbidity currents are a dilute end member of subaqueous sediment gravity flows, induced by the force of gravity acting on a turbid mixture of water and turbulence-suspended sediment, by virtue of the density difference between the mixture and the ambient water. “Dilute” means that subaqueous turbidity currents contain a relatively low threshold value of sediment volumetric concentration of about 9% (Bagnold, 1962). Subaqueous turbidity currents are also a type of subaqueous density flows because they have a density greater than that of the ambient water which results in the downslope flow (Middleton, 1993; Simpson, 1997).

4.3.1 Natural initiation and associated subaqueous turbidity currents

Subaqueous turbidity currents can be initiated by different triggers (e.g., river flood discharge, slope failures and storms) in different settings (e.g., freshwater lakes, marine delta fronts, canyons-fan systems fed by oceanographic systems and open continental slopes) (Talling, 2014). In submarine environments, initiations of turbidity currents can be basically categorized into two types: short events (e.g., earthquakes, volcanic eruptions, wave storms) on the shelf and marginal slope, or quasi-continuous events (e.g., perennial sediment input at river mouths of terrestrial streams). They can be transformed from the concentrated density flows or directly generated from hyperpycnal flows. All the mechanisms aim to decrease the shear strength of the sediment and liquefy sediment by increasing the pore pressure, in order to initiate the movement of mixed fluid.

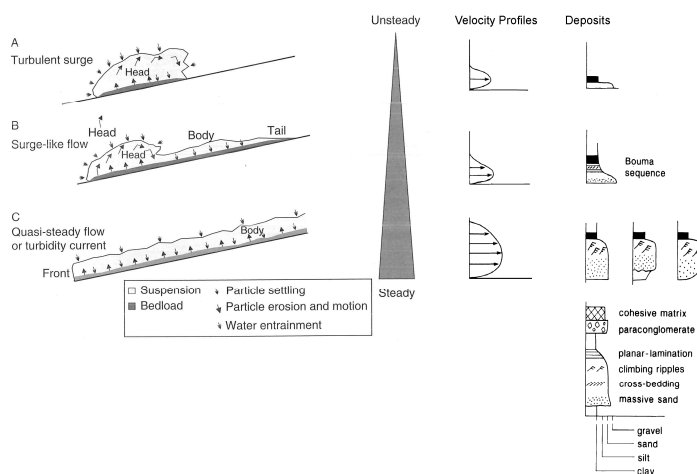


Figure 4.2: Classification of subaqueous turbulent flows and their representative velocity profiles and deposit sequences (modified from Mulder and Alexander, 2001; Mulder, 2011). Terminology adopted in the picture is used by Laval, 1988; Laval et al., 1988; Luthi, 1980; Pickering et al., 1989.

Sediment failure and surge-like flows

Subaqueous sediment failure can directly or indirectly generate turbidity currents. Failures are often related to sedimentary, weather and tectonic causes. The resulting turbidity currents undergo the processes of entrainment, retransportation and resedimentation of unconsolidated previous sediment. The interstitial fluid in such flows is the same as the ambient fluid.

In areas with high sedimentation rates or rapid progradation, deposit overloading or slope oversteepening are invoked as trigger mechanisms for sediment failure (Mulder, 2011). For example, at river mouths rapid progradation of bars lead to multiple sediment failures and associated low-concentration small-scaled surge-like turbidity currents (e.g., in British Columbia Fjord, Bornhold et al., 1994; in Itirbilung Fjord by Syvitski and Hein, 1991). Storm waves can resuspend previous deltaic deposits into suspension clouds and directly generate turbidity currents on a shelf (Prior et al. 1989; Mulder et al., 2001). Earthquake shaking and volcanic activity are tectonic mechanisms to trigger subaqueous failure. Such events can generate slumps and slides in the steep canyon head ($>15^\circ$) which gradually evolve into high concentration density flows on their gentler downslope path (3°), and finally produce the true surge-like turbidity currents (e.g., Unterseh, 1999). The most well-known example is the 1929 Grand Banks event, which caused submarine cables to be broken (Heezen and Ewing, 1952). Some earthquake-induced cases can be found, for example in the Marmara Sea (Beck et al., 2003), Algeria (Giresse et al., 2004) and Sumatra (Singh, 2005) (Mulder, 2011). Volcanic activities and tsunamis in Hawaii can also be causes (Carey and Schneider, 2011).

Failure-induced subaqueous turbidity currents are often surge-like flows (Fig. 4.2; Tab. 4.1). They often evolve from high concentration density flows. During the flow transformations, concentration and density both constantly decrease due to water entrainment and some of the members of this type of flow are regarded as the "**high-density turbidity currents**" of Nardin et al. (1979), Lowe (1982) and Mulder and Cochonat (1996) (Mulder, 2011). Surge-like turbidity currents have a noticeable head, a short body and a negligible tail (Fig. 4.2A, B). They display a strong vertical concentration gradient with concentrated flow at the base and turbulent flow at the top (Stacey and Bowen, 1987; Kneller and Buckee, 2000), and non-uniform velocity profiles along its whole length (Middleton, 1966a). They are unsteady flows with rapidly accelerating and decelerating rates encountering slope gradient variation. The sediments carried by surge-like turbidity currents are mainly sand grains and fines (Mulder and Alexander, 2001). Turbulence is the dominant particle support mechanism so there is no long-distance bedload transportation. Due to the short duration of the flows, sand can be rapidly deposited. Erosion of sand can happen at the flow base when the flows are reaccelerated on a steeper slope.

Surge-like turbidity currents are often related to short-time geological events so the period of sediment supply is temporary and limited. Therefore their capacity, duration and deposit greatly depend on the scale of the event. In large events related to

submarine earthquakes, the turbid surges progressively transform from the concentrated density flows, and can reach thicknesses of tens to hundreds of meters at a high speed (e.g., maximum of 19 m/s of the Grand Banks turbidity current; 20 m/s of the Nice Airport turbidity current on the continental slope) and may endure a few to tens of hours in the whole process (e.g., 600km in 13 hours of the Grand Banks turbidity current, Uchupi and Austin, 1979). Short-duration events and small-scale surge-like flows may only have thicknesses of centimeters to meters and may last for seconds to minutes. Some coalescent surge-like turbidity currents generated by retrogressive slides and slumps can endure for weeks to months, if their sediment supply is maintained for a sufficiently long time. This long duration is then similar to quasi-steady turbidity currents (Mulder, 2011).

Subaerial river continuation and quasi-steady flows

In contrast with the short-event triggers, another mechanism of generating subaqueous turbidity currents is the continuous flow of subaerial rivers debouching into receiving basins, like lakes and seas. For example, the river mouths of small to medium-size rivers (an average annual discharge < 380-460 m³/s) at high relief (Milliman and Syvitske, 1992); and the river mouths of fine-grained sediment-load rivers such as the Daling, Haile and Huanghe Rivers. The resulting turbidity currents are usually suspended-load-dominated hyperpycnal turbidity currents (Mulder, 2011).

In hyperpycnal flows, the initial internal fluid is fresh water, which reduces the density difference between the mixed fluids and their ambient water. So generally the average velocity of hyperpycnal flows is less than that of the surge-like flows on the same slope gradient (Alexander and Mulder, 2002). Their sediment concentration is also less than the transformed surge-like turbidity currents but it is still above the density threshold (Mulder et al. 1998). Along their way downslope, hyperpycnal flows keep their low density so that they are also termed "***low-density turbidity currents***" by Nardin et al. (1979), Lowe (1982) and Mulder and Cochonat (1996) (Mulder, 2011).

Hyperpycnal flows are quasi-steady flows (Fig. 4.2; Tab. 4.1) due to their prolonged input of sediment from a long-lived river, which means they have slowly accelerating and decelerating rates (Mulder and Syvitski, 1995). Quasi-steady turbidity currents have a longer duration of several days to weeks, depending on the flood duration at the river mouth (Skene et al., 1997; Mulder et al., 1998). For example, the hyperpycnal turbidity currents generated by the Var River in France lasted for 18 hours (Mulder et al. 2003). Such flows have an inconspicuous head and tail and a steady and longer body (Fig. 4.2C) with a more gradual vertical gradient of sediment concentration (Alexander and Mulder, 2002; Mulder and Alexander, 2001). Quasi-steady flows possess erosive and depositional abilities. The long body of long-duration quasi-steady flows can erode sand and transport it by bedload along considerable distances. It is rare that such flows can suspend coarse particles (Mulder, 2011). Turbidites produced by quasi-steady turbidity currents are variable as a consequence of the variation in sediment flux patterns between floods and between rivers, and the

variation in conditions with distance from a river mouth (Mulder and Alexander, 2001).

Table 4.1: The difference between quasi-steady flows and surge-like flows (modified from Mulder, 2011).

| | Quasi-steady flow | Surge |
|---|--|---|
| Minimum threshold of particle concentration for triggering | Yes | No |
| Initial concentration | 5-200 kg/m ³ | < 1-1500 kg/m ³ |
| Flow velocity | < 2 m/s | < 4 m/s to > 10m/s on steep slopes |
| Flow morphology | Front and body | Well-defined head + body+ tail |
| Flow structure | Quite homogeneous; bedload transport at the base of flow | Strong vertical gradient. Concentrated flow at the base and turbulent flow at the top |
| Flow behavior | Quasi-steady | Unsteady |
| Duration | Hours to weeks | Minutes to hours |
| Deposits | Hyperpycnites | Turbidites (Bouma sequence) |
| Bedload transport (single event) | Over long distance | Over short distance |

4.3.2 Experimental modelling and dynamics of subaqueous turbidity currents

In subaqueous environments, gravity processes associated with turbidity currents are difficult to observe and study directly, because of the catastrophic nature of large-scaled turbidity currents in nature (e.g., the cable breaks of the 1929 Grand Banks event, Heezen and Ewing, 1952). Therefore experimental and theoretical modelling of subaqueous turbidity currents in small scales are the main study methods to investigate the hydrodynamic characteristics of such flows. Subaqueous turbidity currents are modelled by injecting a denser fluid (e.g., salt water, clay suspensions or sediment-water mixture) into a standing fresh water tanks (e.g., Kuenen and Migliorini, 1950; Middleton, 1967; Luthi, 1980, 1981; García and Parker, 1989; García, 1994). However, laboratory-modelled turbidity currents differ from natural ones in the scaling of the flow parameters, the basin space and the process duration (Mulder, 2011). To make laboratory experiments comparable with natural cases, non-dimensional numbers are used, such as the Reynolds number (Re) and the Froude number (Fr). Currents that share the same values of Re and Fr are said to be dynamically similar (Kneller and Buckee, 2000).

The Reynolds number (Re) and turbulence

The Reynolds number is the ratio between inertial and viscous forces:

$$Re = \frac{\rho_f u h}{\mu} = \frac{u h}{\nu}$$

where ρ_f is the flow density, u is the flow velocity, h is the flow depth, μ is the dynamic viscosity of the flow, and ν is the kinematic viscosity of the flow. An empirical relation for the effective viscosity of clay-free sediment was given by Davidson et al. (1977) as:

$$\frac{\mu}{\mu_w} = (1 - 1.35C)^{-2.5}$$

where μ_w is the molecular viscosity of water and C is the sediment concentration.

The Reynolds number is used to define the flow regime: if $Re < 500$, i.e. viscous forces are dominant; such laminar flows occur in smooth, constant fluid motion; if $Re > 2000$ (Lowe and Guy, 2000), i.e. inertial forces are dominant; turbulent flows occur with chaotic eddies, vortices and other instabilities of flows; if $500 < Re < 2000$, transitional flows occur between the laminar and turbulent flow. Even in high-concentration cohesionless flows (45% by volume concentration), when the product of velocity and thickness exceeds $3 \times 10^{-2} \text{ m}^2/\text{s}$, the sediment can become rapidly fully suspended by turbulence (Kneller and Buckee, 2000). Increasing the flow density or the density contrast between a turbidity current and its ambient fluid, i.e., increasing Re , can help to increase the level of the turbulence in the head. The high instantaneous downstream velocity in the body also implies a relatively high turbulence.

When scaling laboratory experiments of subaqueous turbidity currents, it is very important to make sure that Re is sufficiently high to produce turbulence. Only in turbulent flows (high Re) is the Kelvin-Helmholtz vortex the primary entrainment mechanism (García and Parson, 1996; Parsons, 1998), which is a function of the densimetric Froude number (e.g., Ellison and Turner, 1959).

The Froude number (Fr) and hydraulic jumps

The Froude number is the ratio of inertial to gravitational forces acting on a fluid flow:

$$Fr = \frac{u}{\sqrt{gh}}$$

The Froude number defines the state of the flow: critical if $Fr = 1$, subcritical if $Fr < 1$ and supercritical if $Fr > 1$. In the subaqueous environment, due to the density difference between the flow and its ambient fluid, the apparent density ($\Delta\rho$) of a flow is

$$\Delta\rho = \rho_f - \rho_w$$

and accordingly the reduced gravitational acceleration is

$$g' = g \frac{\Delta\rho}{\rho_w} = gRC$$

where ρ_w is the density of the ambient water, R is the submerged specific gravity of the sediment and C is the volumetric sediment concentration in the flows. Therefore, the densimetric Froude number is expressed as

$$Fr_d = \frac{u}{\sqrt{g'h}} = \frac{u}{\sqrt{RgCh}}$$

A hydraulic jump is a phenomenon that occurs when the flow changes from supercritical to subcritical, passing through the stage of unity of the Froude number (Komar, 1971). It can happen when a high-velocity flow discharges into a low-velocity fluid. It can also occur in the situation that a supercritical turbidity current flowing downslope decelerates due to a significant decrease in the slope gradient or because of reduced confinement (Fig. 4.3; e.g., García and Parker, 1989; García, 1993; Lamb et al., 2004). The previously rapid flow is abruptly slowed down and increases in height, converting some of the flow's initial kinetic energy into an increase in potential energy, with some energy irreversibly lost through turbulence to heat. Suspended sediment will eventually deposit from the dying turbulence of the flow in the subcritical stage.

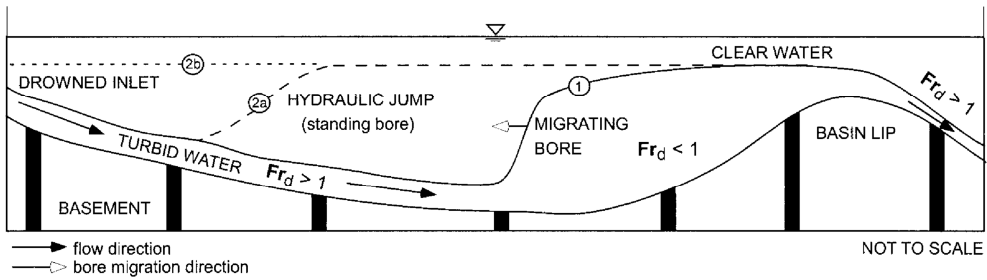


Figure 4.3: Schematic diagram showing a hydraulic jump in an experimental continuous turbidity current in a minibasin (from Lamb et al., 2004).

The Richardson number (Ri) and entrainment

Besides the Reynolds number and the Froude number, the Richardson number is also important in the dynamics of turbidity currents, which is a measure of stratification in the flow. The Richardson number is the ratio of potential to kinetic energy, expressed as

$$Ri = \frac{1}{Fr^2} = \frac{gh}{u^2}$$

This dimensionless number describes the stability of a flow interface and is used for quantification of the water entrainment within a flow. If Ri is much less than unity, buoyancy is unimportant in the flow. If it is much greater than unity, buoyancy is dominant, in the sense that there is insufficient kinetic energy to homogenize the fluids. If Ri is of the order of unity, the flow is likely to be buoyancy-driven: the energy of the flow derives from the potential energy in the system originally.

The densimetric Richardson number is

$$Ri_d = \frac{1}{Fr_d^2} = \frac{g'h}{u^2}$$

High values of Ri_d imply subcritical flows with weak water entrainment and stable density stratification while small values of Ri_d suggest supercritical flows with strong entrainment and less significant stratification. Entrainment caused by Kelvin-Helmholtz instabilities occurs when Ri_d is smaller than 0.25 (Simpson, 1997).

4.3.3 Anatomy

Regardless of surge or steady type of turbidity currents, they all start in the form of a surge which rapidly develops into a current with the longitudinal morphology of a head, a body and in some cases a tail (Fig. 4.2) (Edwards, 1993; Middleton, 1996a, b).

Head

A distinct bulge-shaped head develops in the very front part of subaqueous turbidity currents due to the strong mixing of the sediment and the ambient water. The head, as a boundary condition for the whole fluid, plays an important role in the dynamics (Simpson and Britter, 1979). The head is mainly erosional, often leaving structures like grooves and flute marks, and is therefore sedimentologically important (Allen, 1971; Middleton, 1993). It is the most concentrated part of the flow because the coarser grains can be suspended (e.g., Stow, 1986). Sediment can be entrained into the head of the flow. The fluid in the head circularly moves toward the front and the top (Mulder, 2011).

During its initiation and development, the head is subjected to forces such as the pressure caused by the density difference, the downslope component of the gravity force, bottom drag, interfacial frictions and buoyancy (e.g., Pratson et al., 2000). The balance between the driving and resistant forces controls its hydrodynamics, morphology, duration and sedimentation. The density-induced pressure and gravity drive the head movement. The bottom drag and interfacial friction increase the level of turbulence in the head. However, entrainment of the ambient fluid counteracts the above positive effect of the head. The instabilities caused by buoyancy lead to a no-slip condition at the lower boundary of the head, whereby the head has an overhanging nose (Fig. 4.4b). Due to such entrainment small reverse circulation can form in the lower part of the head. Friction-induced entrainment also occurs at the upper boundary, resulting in the Kelvin-Helmholtz (K-H) billows (Fig. 4.4b, c) (Britter and Simpson, 1978). These instabilities also cause the lobe and cleft structures in plan view (Fig. 4.4a).

An increase in the density difference between the current and the ambient fluid can reduce the height of the nose and enhance the extent of the overall turbulent mixing pattern of the flow (e.g., Simpson, 1997). Increasing the slope, however, provides a limited contribution to the velocity of the head, i.e., the head velocity is independent on low slopes ($< 2-3^\circ$) (e.g., Keulegan, 1957) and weakly dependent on steeper slope ($5^\circ-90^\circ$) (e.g., Britter and Linden, 1980). Although an increasing slope can lead to higher gravitational forces, it also can increase the frictional resistance at the upper boundary and buoyancy, resulting in increased entrainment (e.g., Siegenthaler and Buhler, 1985). The flow velocity tends to remain constant. The internal-wave velocity in the body increases with slope, and often exceeds the velocity of the head, such that with distance the head may expand in thickness due to the material feeding from the body and the increased entrainment of the dilute ambient water (e.g., Middleton, 1967; Simpson, 1997; Britter and Linden, 1980; Talling et al., 2001). The surge-type turbidity currents are dominated by the properties of the head, in contrast to the sustained or continuous underflows dominated by the body (Fig. 4.2).

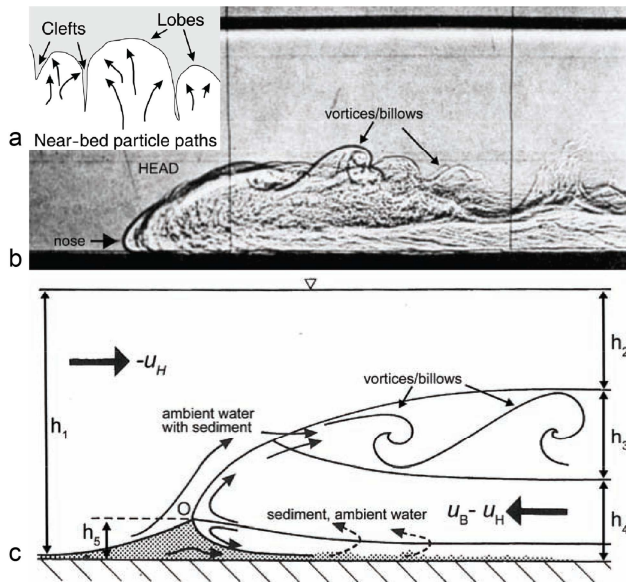


Figure 4.4: The head of an experimental turbidity current. (a) shows the schematic view of lobes and clefts seen from below (from Kneller and Buckee, 2000). (b) shows the side view of the head with the nose and the well-developed Kelvin-Helmholtz billows/vortices (modified from Britter and Simpson, 1978). (c) Schematic diagram of the water entrainment of the head (h_1 : the total height; h_2 : the height of the ambient fluid; h_3 : the height of the wake with vortices; h_4 : the height of the lower body; h_5 : the height of the nose; U_H : the velocity of the head; and U_B : the velocity of the body) (modified from Simpson, 1997).

Body

The body of the flow is behind the head, which the two are sometimes linked by a neck (Mulder, 2011). The sediment suspension is supported by the friction between the ambient water and the overriding bed (e.g., Stow et al., 1996). The body has an approximately constant flow thickness and structure, especially in the quasi-steady turbidity currents with internal-wave action. It vertically comprises two parts: a thin and dense layer in the lower part of the flow, and a less dense region in the upper part mixed with the ambient fluid (described as an ‘irregular succession of large eddies’ by Ellison and Turner, 1959) (e.g., Britter and Simpson, 1978; Simpson and Britter, 1979). Moreover, the K-H billows can transport sediment from the head back into the body. The high instantaneous downstream velocity (faster than the head) implies that the body may play a significant role in water and sediment entrainment via erosion (Kneller and Buckee, 2000).

Tail

The tail is the thin and diluted part of the flow behind the body (Mulder, 2011). The transported fine-grained sediment in the tail gradually settles due to energy loss during the downslope flow of subaqueous turbidity currents.

4.3.4 Stratification

The vertical morphology of turbidity currents indicates that they are stratified in velocity as well as density (Fig. 4.5; Fig. 4.6). Both of these parameters generally decrease upward. The flow velocity profile is characterized by a maximum value in the lower region of the flow. Stratification of turbidity currents can cause flow spilling and stripping on obstacles such as submarine channel levees (Kneller and McCaffrey, 1999; Mulder, 2011) and salt-induced topographic highs (Sinclair and Tomasso, 2002).

Lower and upper region

The mean velocity structure of a turbidity current comprises two regions: the lower and upper regions (Fig. 4.5). The lower region (near-wall region) is located in the lower part of turbidity currents with a positive velocity gradient, similar to a conventional turbulent boundary layer. The upper region (shear layer) is above the lower region and interfaces with the ambient fluid, with a negative velocity gradient. Generally, the upper region is 5 to 10 (or more) times thicker than the lower region (Stacey and Bowen, 1988). The height of the velocity maximum is controlled by the ratio of the drag forces at the upper and lower boundaries. Turbulent kinetic energy is close to zero at the height of the velocity maximum (Kneller et al. 1999; Kneller and Buckee, 2000; Gray et al., 2005; Leeder et al., 2005). This feature suggests that the dominance of turbulence by shear is related to the mean velocity profile (Meiburg and Kneller, 2010).

Concentration and density

Turbidity currents are density-stratified (Stacey and Bowen, 1988), which depends on the distribution of suspended sediment (concentration gradient). Their vertical concentration profile (Fig. 4.5) shows that the flow density decreases upward. Finer grains are mainly suspended in the less dense, uniformly mixed upper region, while coarser grains tend to be transported in the dense, less mixed basal layer of turbidity currents (e.g., García, 1994). Currents with different dynamics have different concentration or velocity profiles (Fig. 4.6). For example, low-concentration and weakly depositional currents (García, 1990, 1994; Altinkinar et al, 1996) have a smoother concentration profile than erosional currents (García, 1993) or currents with high rates of ambient fluid entrainment at the upper interfacial boundary (Peakall et al., 2000). The velocity profile of supercritical flows is acuter than that of subcritical flows (Sloff, 1977), i.e., the location of velocity maximum is lower in the current.

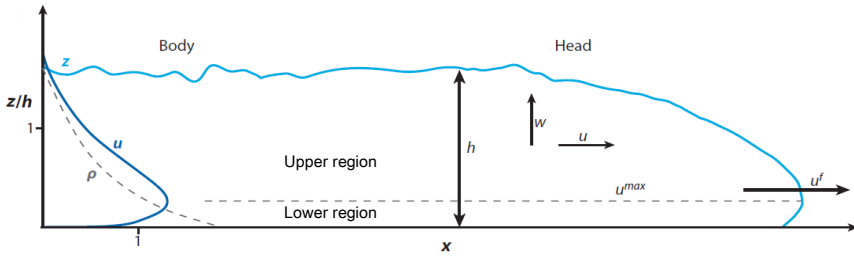


Figure 4.5: Stratification of a turbidity current (light blue line), with the generalized velocity (deep blue solid line) and density (black dashed line) profiles on the left side (modified from Meiburg and Kneller, 2010).

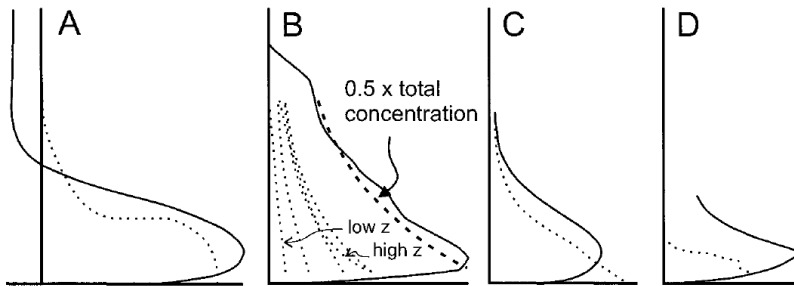


Figure 4.6: Velocity profiles (solid lines) and associated concentration profiles (dashed lines) for different types of experimental turbidity currents (from Peakall, et al., 2000). (A) Conceptual two-layer model of Middleton (1969, 1993) based on lock-exchange laboratory currents as indicated by return flow with corresponding negative velocities in the upper flow. (B) Continuous stratification observed in a strongly depositional subcritical flow (Garcia, 1994). Ordinary dashed lines show the concentration profiles of individual size classes from the polydisperse current (from left to right, 5, 8, 13, 20, and 32 μm); heavy dashed line shows the overall concentration profile (note different scale). (C) Nearly continuous sediment profile with a slight inflection at the velocity maximum, for a weakly depositional subcritical flow on low slopes (Altinakar, et al. 1996). (D) Strongly stepped grain-size profile for an erosional, saline, subcritical turbidity current that initially carried no suspended load (García and Parker, 1993).

4.3.5 Flow abilities and turbidite deposits

Under certain conditions a state of auto-suspension can occur where the sediment suspended by turbidity currents will not be deposited (Bagnold, 1962). However, in reality, if the sediment supply is exhausted or lower slope gradients are encountered, the driving force induced by gravity is gradually counteracted and therefore the flow decelerates. As the flow loses its capacity to carry sediments, grains will start settling out of suspension, mainly from the body and tail. First the coarser ones will be deposited and then successively finer ones, which results in a normally graded grain-size trend in a turbidite. Single-event turbidity currents can produce individual turbidite beds with thickness from millimeters to meters, but successive events of turbidity currents over a long geological term can construct submarine fan systems with thicknesses of tens to hundreds of meters.

Flow competence, capacity and efficiency

The ability of turbidity currents to transport sediment in suspension a certain distance is closely related to flow competence, which is the ability of a flow to transport the maximum grain size, to flow capacity, which is the total amount of sediment a flow can carry, and to flow efficiency, which is the ability of a flow to carry sediment according to its clay content (Mutti, 1979; Pickering et al., 1989). A turbidity current with high energy (competence, capacity and efficiency) can transport a large volume of sediment with a high proportion of coarser grains over a long distance and form well-sorted deposits. The sedimentation of a flow is mainly controlled by its deceleration.

Flow unsteadiness and non-uniformity

If the fluid properties (such as velocity) at every point of the flow do not change over time (i.e., it is constant with time), the flow is called steady. If a flow passing a given point becomes slower, it transfers to a waning flow; if it becomes faster, it transfers to a waxing flow (Fig. 4.7a) (McCaffrey and Kneller, 2001; Kneller and McCaffrey, 2003). If a flow has the same velocity at all points along a streamline at any given time (i.e., it is constant with distance), this flow is uniform with no spatial variation. Otherwise the flow is considered non-uniform flow (Fig. 4.7b). Flow non-uniformity depends mainly on changes of the slope gradient (McCaffrey and Kneller, 2001; Kneller and McCaffrey, 2003). When a flow is flowing above a concave-up slope profile or when it spreads at a channel mouth, it decelerates and becomes a depletive flow (Fig. 4.8a). Conversely, when a flow is flowing above a convex-up slope profile or confined by a channel, it accelerates and becomes an accumulative flow (Fig. 4.8b).

The velocity matrix

Kneller (1995) and Keller and Branney (1995) proposed a velocity matrix to predict the vertical trends of the grain size of a deposit, based on the velocity changes with both time and distance (i.e., flow unsteadiness and non-uniformity) (Fig. 4.9). Surge-type turbidity currents are mostly depletive waning flows which produce normally graded sequences. The distal turbidite beds are thinner and finer than the proximal. The classical Bouma sequence is characterized by such a vertical and longitudinal evolution. Depletive steady flows can result in massive sand beds without vertical grading in grain size. Longitudinally, the distal beds are also thinner and finer. Massive sand beds need a long-term and stable sediment supply, for example, perennial fluvial discharge. Quasi-steady hyperpycnal flows may be depletive waxing or depletive waning flows depending on the discharge (Mulder et al., 2003). Depletive waxing flows lead to deposits with coarsening-upward sequences which form the basal unit of hyperpycnites.

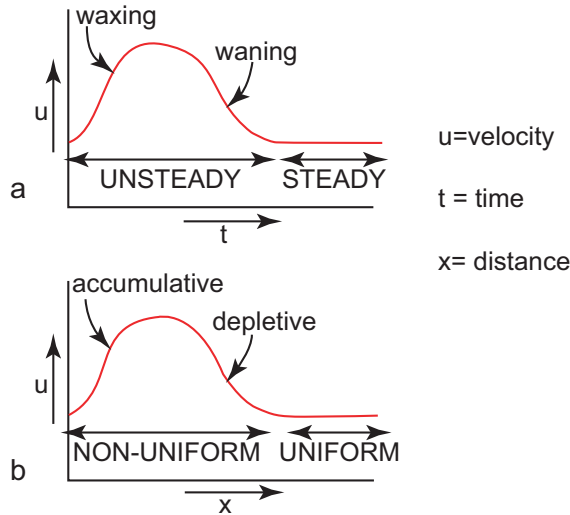


Figure 4.7: Graphs of time (t) vs. velocity (u) and distance (x) vs. velocity (u), showing different types of flow under a variety of conditions (from Weimer and Slatt, 2007; modified from Kneller, 1995). (a) Flow velocity first waxes, then wanes, then becomes steady over time. (b) Flow velocity first increases (accumulative), then decreases (depletive), then becomes uniform with downstream distance.

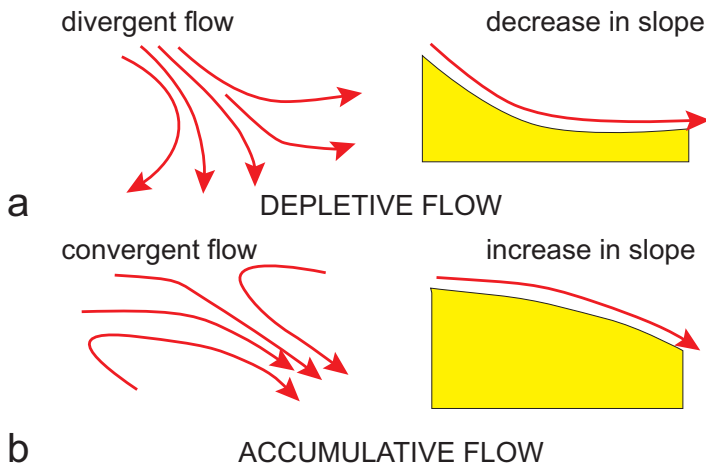


Figure 4.8: Diagram illustrating some causes of spatially depletive (downstream decrease in flow velocity) and spatially accumulative (downstream increase in flow velocity) sediment gravity flows (from Weimer and Slatt, 2007; modified from Kneller, 1995). (a) Plan view of a depletive flow resulting from divergent flow on the seafloor as the flow becomes unconfined, and a cross-section showing downstream decrease in flow velocity due to a reduction in slope gradient. (b) Plan view illustrating an accumulative flow resulting from convergence of the flow on the seafloor, and a cross-section illustrating an accumulative flow resulting from a downstream increase in the slope gradient of the seafloor.

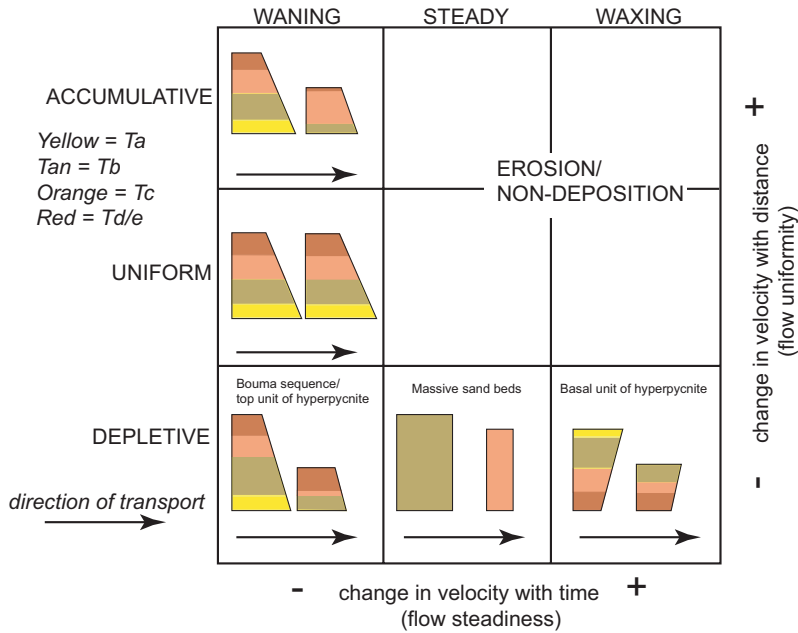


Figure 4.9: Velocity matrix showing the differently depositional sequences resulting from the changes in flow velocity with distance and with time (from Weimer and Slatt, 2007; modified from Kneller, 1995).

Bouma sequence

The Bouma sequence (Bouma, 1962) was the first idealized depositional sequence of a turbidity current deposit, which has been considered as the classical turbidite. A complete Bouma sequence is a normally graded bed, vertically (from bottom to top) consisting of five units (Fig. 4.10): Ta, a structureless or normally-graded, sandy division; Tb, a parallel laminated, sandy division; Tc, a ripple or climbing-ripple, laminated or convoluted, sandy division; Td, a parallel laminated to massive, silty division; and Te, a silt-clay, often microfaunal-rich division.

The vertical variations of grain size, thickness and sedimentary structures in divisions of the Bouma sequence reflect the changes in flow hydrodynamic conditions during deposition. Ta is the product of rapid deposition of the sediment and has erosional bedforms such as flute and tool marks formed at the head of the turbidity current. Tb and Tc are deposited by the traction of grains in the body along the seabed. Tb is deposited from the high-energy part of the body under upper flow regime conditions. Tc results from the deposition of the lower-energy part of the body under lower flow regime conditions. Td is attributed to sedimentation dominated by suspension fallout from the tail of the turbidity current. Te is a mixture of suspended fine-grained sediment (silt- and clay-sized particles) from both the tail of the current and the pelagic materials and it often contains shallow- and deep-marine microfauna.

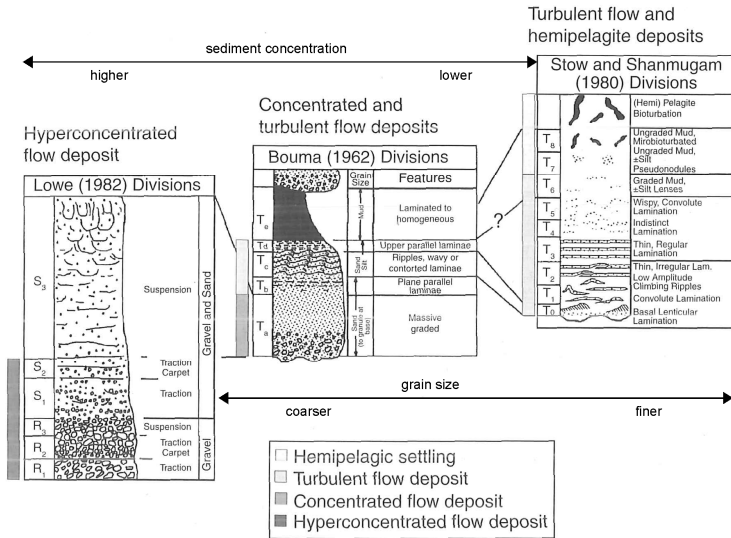


Figure 4.10: Typical vertical sequences of deposit from a hyperconcentrated flow (base of Lowe sequence: R₁-S₂), a concentrated flow (Lowe sequence S₃ and Bouma T_a) and a turbulent flow (turbidite) (Bouma T_b-e, and Stow and Shanmugam sequence) (modified from Mulder, 2011).

Other turbidite sequences

A complete Bouma sequence is rarely found in nature because the requirements in the grain sizes and flow conditions are difficult to satisfy within a single 1D expression of a deposit. The Bouma divisions are useful when describing deposits of waning turbidity currents, but many flows are non-uniform and unsteady. A high density turbidity current (Lowe, 1982) with a wide range of grain sizes probably can produce a complete Bouma sequence, while a low-density turbidity current without coarse grains is likely to produce a sequence lacking the T_a unit (Mutti et al, 1999). During the passage of a turbidity current, coarser sediment tends to deposit at the proximal region when the flow is dense, and the finer grains can be transported to the distal region when the flows are more dilute due to the water entrainment and energy loss (Bouma, 2000).

T_a is poorly graded because the basal part of a high-density turbidity current is concentrated, and turbulence can be dampened. This feature is similar to crude grading of a concentrated flow or no grading of a hyperconcentrated flow, corresponding to the S₂ unit of the *Lowe sequence* (Lowe, 1982) (Fig. 4.10). *Stow and Shanmugam* (1980) found that turbidite mudstones also exhibit a characteristic suite of waning-flow sedimentary structures and textures (Fig. 4.10). They subdivided Bouma T_c-T_e into T₀-T₈ based on variations in grain size and small-scale sedimentary structures (Fig. 4.10): Bouma T_c = Stow and Shanmugam T₀; Bouma T_d = Stow and Shanmugam T₁ and T₂; T_e = T₃-T₈.

Different trigger mechanisms can generate different initial flow conditions and therefore types of turbidity currents and deposition sequences. The deposit from a surge-like turbidity current with fine grain sizes (no larger than sand) is characterized by typical Bouma T_b - T_d facies (Fig. 4.2) (e.g., Mulder and Alexander, 2001). Small-scale surge-like flows with shorter durations are incapable of producing recognizable bedforms and structures due to their strongly unsteady flow body and insufficient settling time. Very-short-duration single surge-like flows are unable to produce thick deposits unless the scale of the flow is large or the flow is confined, but with a small ratio of bed thickness to bed length (Mulder and Alexander, 2001). Typical hyperpycnal deposits are thought to comprise a vertical sedimentary sequence with a lower coarsening-upward succession (from silt to fine sand) overlain by a fining-upward succession (from fine sand to silt) (Fig. 4.2C; Fig. 4.11). The lower succession is deposited during the rise of flood at river mouths when the flow is in the waxing phase (Fig. 4.9). Such a succession can be found in the Saguenay fjord in Canada (Syvitski and Shafer, 1996). Subsequently, the flow wanes and becomes accumulative at the river mouth or depletive at more distal areas, with the consequence that an upper normally graded succession is deposited (Fig. 4.9). The lower and upper unit of an individual hyperpycnite bed can be separated by an erosional or sediment-bypass surface if the flow power is sufficient to erode the underlying inversely graded deposit (Weimer and Slatt, 2007) (e.g., modern hyperpycnites in the central Japan Sea, Nakajima, 2006; the Cretaceous Dad Sandstone member of the Lewis Shale leveed-channel deposits, Soyinka and Slatt, 2004). Climbing ripples are a major feature of sedimentary structures of hyperpycnites. Land-derived organic material also can be found in hyperpycnites. A single flood peak may generate a flow with multiple pulses so that the deposit grading patterns may be more complex than simple inverse-to-normal grading (Talling, 2014).

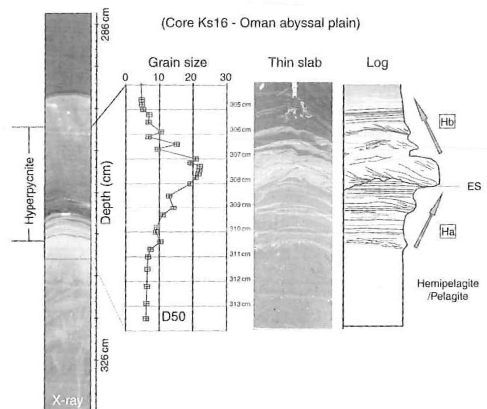


Figure 4.11: Vertical grain-size trend and thin-slab photograph of a hyperpycnite in the Oman Basin (from Bourget, 2009 in Mulder, 2011).

4.3.6 Classic models of turbidite systems

Commonly, subaqueous gravity flows including turbidity currents pass through submarine canyons and channels, and finally spread on the seafloor, forming a deep-sea turbidite system. The early fan models mainly focused on the morphological analysis of the system with the scales of architectural elements like valley and channels (e.g., Normark, 1970; Mutti and Ricci Lucchi, 1975).

The Walker model

Walker (1978), Mutti (1979), and Shanmugan and Moiola (1991) improved the Normark (1970) model into the first predictive model for deep-sea systems (deposits and their related flow types) at passive margins. Such a model has a progradational configuration (Fig. 4.12): Slumps or debris flows are generated in the proximal feeder channel of the upper slope; in the upper fan region, the coarse-grained hyperconcentrated-flow deposits develop in the feeder channels and fine-grained thin-bedded levee deposits are formed due to overspilling and flow stripping. The middle fan is characterized by distributary channels and lobes. Bouma-type turbidites develop in the lower fan.

The Walker model has limitations in its use because the suprafan definition of the Normark (1978) model is not consistent with the most recent data and the scale of fans that they studied for the model is not suitable for giant muddy fans on passive margins (Mulder, 2011).

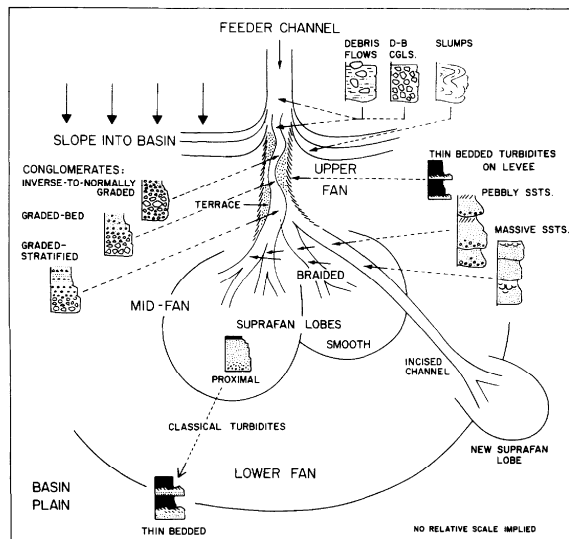


Figure 4.12: Walker's model of submarine turbidite systems showing fan morphology, depositional environment and facies distribution (from Walker, 1978).

Some sequence stratigraphic models later were proposed, with the consideration of basin-scale control factors such as the sedimentary supply, the tectonic context and the changes in eustacy. Such models attempt to combine the relationships between sedimentary environment, process and facies. Examples are the classifications of deep-marine turbidite systems published by Shanmugan et al. (1998) and Reading and Richards (1994).

The Shanmugan model

Based on the different geodynamic contexts of continental margins, they summarized two types of turbidite systems: passive-margin fans and active-margin fans (Fig. 4.13) (Shanmugan et al., 1988; Shanmugan and Muiola, 1988). Passive-margin fans include immature passive-margin fans (North Sea) having small sandy systems with well-developed lobes, and mature ones (Atlantic type) of Bally and Snelson (1980) having large muddy systems with small lobes. Active-margin fans include the Pacific-type active-margin fans showing small sandy systems with large lobes, and the mixed settings of Bally and Snelson (1980) such as the Bengal and Indus systems. However, some inconsistency exists in their models. For example, the Magdalena fan is on an active margin but shows the features of a passive-margin turbidite system (Mulder, 2011).

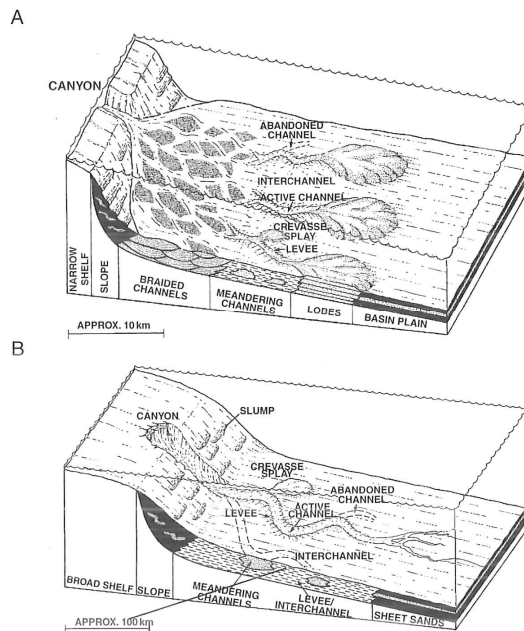


Figure 4.13: Shanmugan's model of deep-sea turbidite systems (from Shanmugan et al., 1988): (A) active-margin fan and (B) passive-margin fan.

The Reading and Richards model

Twelve models were proposed by Reading and Richards (1994) (Fig. 4.14), based on the relationship between the types of sediment source area and the dominant lithology. This provides a more elaborate classification of ancient and recent turbidite systems. The grain-size axis is divided into four types: mud-rich, sand-rich, mixed (mud/sand-rich) and gravel-rich. The sediment-source axis is divided into three types: point, linear or multiple source.

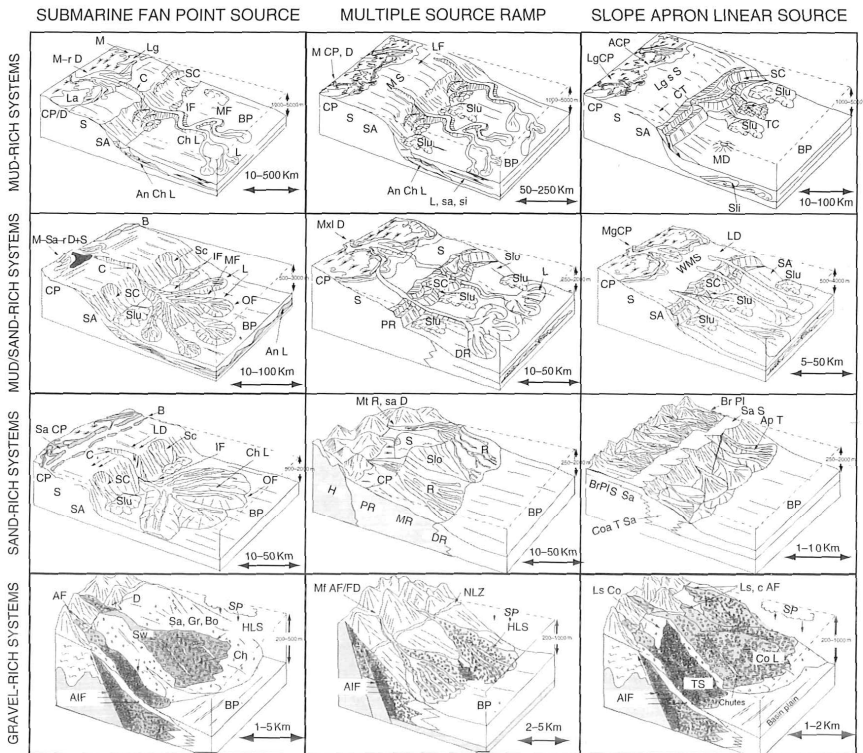


Figure 4.14: Reading and Richards' model of deep-sea turbidite systems (from Reading and Richards, 1994).

The Bouma model

Bouma (2000) proposed to differentiate between coarse-grained sand-rich fans, fine-grained sand-rich fans, and fine-grained mud-rich fans because ancient turbidite systems developed in once active tectonic settings (during the formation of active or passive margins), filling the sedimentary basins formed by tectonic extension or compression, were in confined settings, while modern fans develop on large passive margins without confinement. Bouma (2004) published two end models based on the

different relative distances from the sediment producing mountains to the coast, the relative width of the shelf, and the shape and location of the submarine fan (Fig. 4.15).

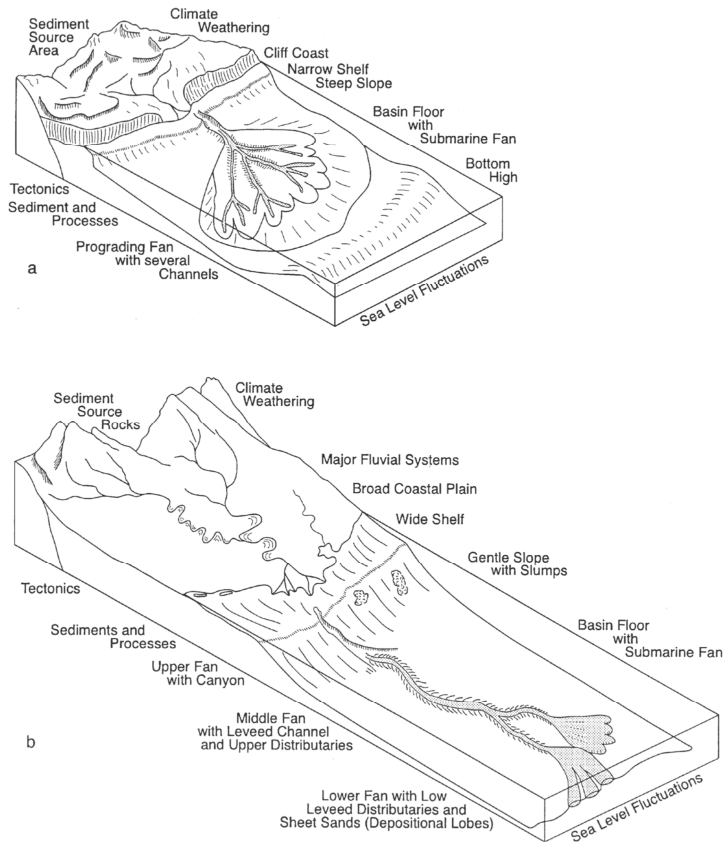


Figure 4.15: Bouma's model of submarine turbidite systems (from Bouma, 2004). (a) Typical situation for coarse-grained/sand-rich fans. (b) Typical situation for fine-grained/mud-rich fans. Major forces that produce, transport and deposit sediment are mentioned.

4.4 Confined turbidity currents and turbidites

Submarine turbidity currents and their associated turbidite systems are mainly controlled by key factors such as tectonics, climate, sediment supply, and eustatic fluctuations (Bouma, 2004; Mutti et al., 2009). These factors profoundly influence the flow condition of turbidity currents, sediment transportation and depositional processes, and hence the sediment distribution. Tectonics can affect the other control factors. On continental margins, tectonics can induce various topographic obstacles, reliefs and basins on a wide range of scales, which moderately or extremely confine the turbidity currents and turbidite systems within them. For example, the sub-basins or minibasins induced by salt tectonics on passive margins can partly or fully confine turbidity currents.

4.4.1 Turbidity currents encountering obstacles

The confinement of some topographic relief influences the pathway, behavior and deposition of a turbidity current. Flume experiments and ancient outcrop studies provide useful approaches to investigate the effects of an obstacle on a turbidity current. Effects, such as flow over-spilling, deflection and reflection, are dependent on the balance between flow energy and topographic highs (Kneller and McCaffrey, 1999). The parameters reflecting the flow energy include flow thickness, duration and acceleration, grain-size of the transported sediments, vertical movements due to turbulence, density stratification; the factors of the obstacle influencing the flow energy are mainly its height, geometry and orientation (e.g., Albertão et al., 2011).

Deflection, reflection and stripping

When a flow meets an obstacle which is much larger than the height of the flow head, it will run up and hence increase its height. For a relatively poorly stratified flow the maximum run-up height is probably determined by the bulk Froude number of the flow (Rottman et al., 1985 in Kneller and Buckee, 2000). Alexander and Morris (1994) proposed that if the height of the obstacle is twice or more the flow thickness, the flow will be reflected from the obstacle and a hydraulic jump may occur (Edwards, 1993; Pantin and Leeder, 1987). If the ratio between the obstacle height and the flow thickness is smaller than two, the flow will partly pass over the obstacle and partly be reflected and/or deflected. If the obstacle is too small compared with the flow thickness, there is little effect by the obstacle on the flow pathways but well on the sedimentary characteristics (e.g., Morris et al., 1998). For density-stratified flows, the maximum run-up height is a function of the velocity and density profiles and cannot be generalized in systems (Kneller and Buckee, 2000). The stripping of a stratified flow will happen even when encountering a small obstacle: the lower, denser part of the flow is likely to decelerate and rapidly deposit the carried sediments, or be reflected or deflected while the upper, dilute part of the flow tends to move up or over the obstacle. Flow stripping also occurs when a channeled subaqueous turbidity current travels across bends. The partial flow with finer sediment breaches the levees

into splays while the other partial flow with coarser particles remains within the channel (e.g., Peakall et al., 2000; Posamentier, 2001).

The internal Froude number (Fri), the dimensionless parameter which is a function of a flow velocity and the reciprocal of the flow height and the density stratification, can represent the kinetic flow energy. Lane-Serff et al. (1995) used the relation between Fri and the ratio Z/h between obstacle height (Z) and flow thickness (h) to predict the proportion of the flow that can continue over the obstacle (Fig. 4.16). For a flow with a particular value of Fri the threshold of Z/h , above which the flow will be entirely trapped, can be estimated. Kneller and McCaffrey (1999) described the joint effects of the dividing streamline and the degree of the topographic confinement (Fig. 4.17). A large Fri means the flow tends to act as a unity, completely overrunning or deflecting; while a small Fri implies flow stripping with a critical dividing streamline above which the partial flow is capable of running over or being reflected by the obstacle, and below which the partial flow is deflected.

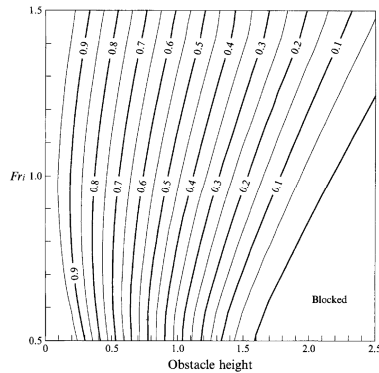


Figure 4.16: Proportion of the flow running over an obstacle as a function of the ratio (Z/h) between the obstacle height and the flow thickness, and the inertial Froude number (Fri) (from Lane-Serff et al., 1995).

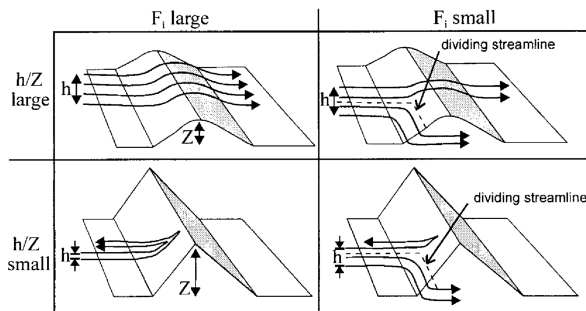


Figure 4.17: Schematic diagrams illustrating the joint effects of the dividing streamline (Fi) and the degree of topographical confinement, i.e., the ratio between flow thickness (h) and the obstacle height (Z) (from Kneller and McCaffrey, 1999).

Bores

The effect of confinement can lead to an internal bore migrating upstream (a phenomenon that the thickness of the downstream flow increases and the velocity decreases) (e.g., Edwards, 1993). The bore has some similarity with a hydraulic jump in the sense that there are changes in flow thickness. Although it is sometimes described as a moving internal hydraulic jump, the bore is not characterized by the transition from a supercritical flow to a subcritical flow (Kneller and Buckee, 2000). The velocities within the bore may be negative to be a reflecting current. Three types of bores are differentiated based on the ratio of the height of the bore to the thickness of the forward current through which it moves (Fig. 4.18). Type C is generated by the erosional head of a turbulent gravity current. Such a bore is strongest with strong entrainment of the ambient fluid at the upper interface. The strong bores might be associated with stronger stratification (Kneller and Buckee, 2000). Type A is characterized by a group of internal solitary waves, which may be responsible for the sedimentary structure of wave ripples in the associated deposits. Type B is an intermediate state between Type A and C.

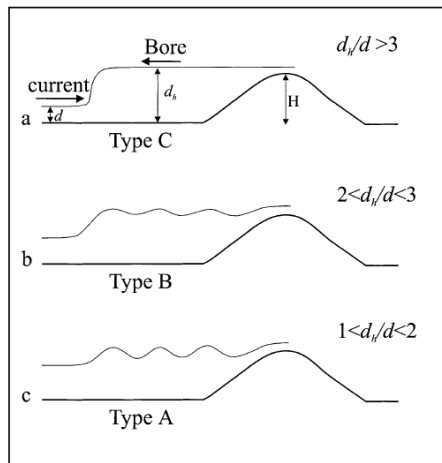


Figure 4.18: Nomenclature of three types of bores defined by Rottman and Simpson (1989). Here d is the flow thickness and d_b is the mean height of the bore waveform (from Kneller and Buckee, 2000).

Downslope effects of an obstacle

After running over an obstacle, the energy of the flow is reduced. Kneller and Buckee (2000) described four situations of downslope effects of an obstacle on the flow, according to the relationship between the internal Froude number, the velocity and the stratification degree of the flow (Fig. 4.19). For a weakly stratified flow with high velocity and Fri after encountering a very small obstacle, the flow will be divergent along the lee side of the obstacle (Fig. 4.19a). With an increase in the ratio of the obstacle height to the flow height, in the degree of stratification of the flow and in the

Fr_i value, and a decrease in the flow velocity, phenomena like vortex (Fig. 4.19b), oscillation (Fig. 4.19c) and even the hydraulic jump (Fig. 4.19d) occur on the lee side of the obstacle.

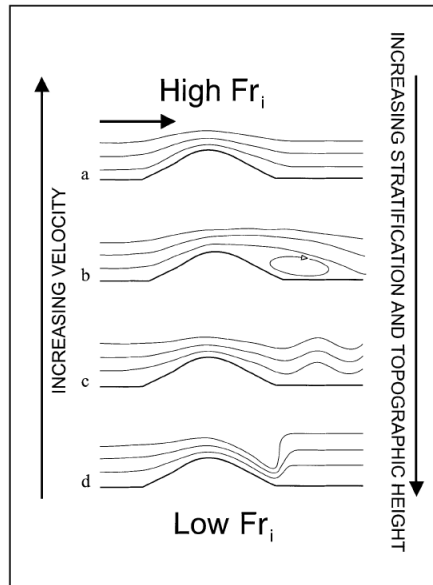


Figure 4.19: The effects on the downstream side of an obstacle on the flow (from Kneller and Buckee, 2000).

4.4.2 Turbidites under topographic controls

The hydrodynamic effects of a topographic relief on a turbidity current are important in controlling the pattern of sedimentation. Alexander and Morris (1994) summarized that effects on the flow include the generation and migration of hydraulic jumps on the counter-slope and lee-side of an obstacle, the reflection of solitary waves, the generation of the intensified mixing vortices at the margins of spreading currents and obstacles, the variations in spreading rate caused by gradient changes, and the restriction of lateral spreading by obstacles.

Upstream sedimentation and deposits

Large obstacles can result in a turbidity current being partly blocked by the obstacle and partly passing over the obstacle. The trapped flow accordingly decreases its competence and capacity to carry the sediment (Kneller and Buckee, 2000). Localized sedimentation often happens due to the occurrence of a non-migrating hydraulic jump or bore of a rapid waning current at the upstream side of an obstacle (Alexander and Morris, 1994, Kneller, 1995; Kneller and McCaffrey, 1995). Less localized deposits can

be associated with the upstream migration of bores or jumps in steady turbidity currents (Kneller and Buckee, 2000).

Some sedimentary structures and sequences in turbidites observed in the field have been explained as the result of the effects of topographic controls. Reflection and deflection of flows can cause a vertical repetition of grading sequences (inverse and normal grading) (e.g., Van Andel and Komar, 1969; Pickering and Hiscott, 1985; Porebski et al., 1991; Rothwell et al., 1992; Haughton, 1994, 2000; Kneller and McCaffrey, 1999). These repetitive sequences are often featured by the alternation of sand and mud, and climbing current-ripples with the flow direction opposed to the original flow direction which can be analyzed by load structures such as flute casts and sole marks (Marjanac, 1990; Kneller et al., 1991; Hodgson and Haughton 2004). These evidences can be found in turbidite outcrops in the field. For example, the Miocene turbidites ("Contessa" sandstones) in the northern Apennines (Ricci Lucchi and Valmori, 1980), the Cloridome Formation in Quebec, Canada (Pantin and Leeder, 1987) and the Annot Sandstone, France (Sinclair, 1994). Other evidences of reflection and deflection may include the thickening of the deposits along the way deviated from the main flow path (Marjanac, 1990; Porebski et al., 1991; Haughton, 2000), erosion or bypass on topographic highs (Thorngurg et al., 1990; Morris et al., 1998; Soreghan et al., 1999; Anderson et al., 2000; Burgess et al., 2000), distribution of coarse particles in the lows or at the slope toe, and finer ones on the highs (Thorngurg et al., 1990; Anderson et al., 2000; Burgess et al., 2000).

Downstream sedimentation and deposits

The downstream effects of an obstacle also can cause an abrupt thickening in the deposit on the lee side of an obstacle. The overspilling flow is reduced in its energy and separated over the whole downslope side of an obstacle. Sediments can be deposited from subcritical flows (Fig. 4.19b) along the pathway and the flow can cause scours and large bedforms such as the large-scale oscillatory dunes or gravel waves. Sediments also can be settled from supercritical flows (Fig 4.19c, d) and may produce upstream migration of mud-waves (e.g., the Var sedimentary ridges formed by turbidity current overspill from the adjacent fan valley; Sayoye, 1993 in Kneller and Buckee, 2000) or sediment waves (e.g., those on the right-hand levee of the Hueneme fan channel; Piper et al., 199b in Kneller and Buckee, 2000), and the occurrence of submarine plunge pools (Farre and Ryan, 1985; Aarseth et al., 1989).

4.4.3 Confinement of intraslope minibasins on passive margins

Topographic lows in different geological settings and scales have different effects on the turbidity current. Gaumet et al. (2003) distinguished four scales of topographic confinement of flows: i) basin-scale (several hundreds of kilometers in length), for example, in foreland basins on active margins; ii) sub-basin scale (tens of kilometers in length), for example, as various minibasins (extensional and compressional) generated by salt movement and faulting systems on passive margin; iii) “local” scale (several kilometers in width), for example channels and canyons; and iv) bed scale (several hundred meters in width).

The turbidite systems on passive margins are greatly influenced by the topographic controls induced by salt tectonics, such as diapirism and withdrawal (discussed in Chapter 2; Fig. 4.20) and the faulting systems (discussed in Chapter 2; Fig. 4.21). Typically, the slopes of passive continental margins are characterized by two types of above-graded slope topographies (e.g., the Gulf of Mexico; Prather et al. 1998; offshore Brazil and Angola; Smith, 2004): the ponded intraslope basins (minibasins) (Prather, 2003) or silled sub-basins (Smith, 2004), and the stepped bathymetric profiles (Prather, 2003) or connected tortuous corridors (Smith, 2004), due to the high subsidence rates of salt withdrawal minibasins.

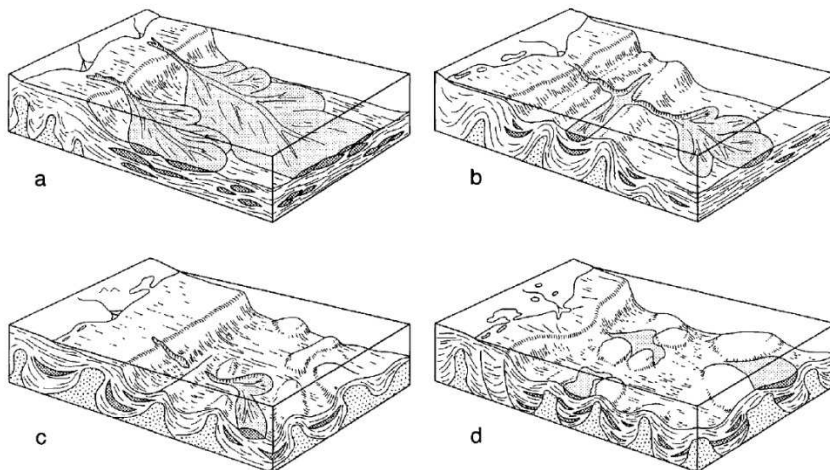


Figure 4.20: Schematic sketches of the interaction between diapirism and fan deposition proposed by Bouma (2004). (a) No direct interaction between the diapirs and the shelf and the turbidite fan; (b) diapiric ridges form troughs that are claimed to have to be filled first (two directional fills) before overflow to a next trough can take place; (c) continuous diapiric activity, likely during a high-stand systems tract, breaks a turbidite system into two parts; (d) breaking apart of a fan by diapiric activity. The sediment source at the delta front was either not active when the diapirs moved upwards, or the delta switched to another location. (c) and (d) can happen when the fan is still exposed, but it is more common when they are buried (from Bouma, 2004).

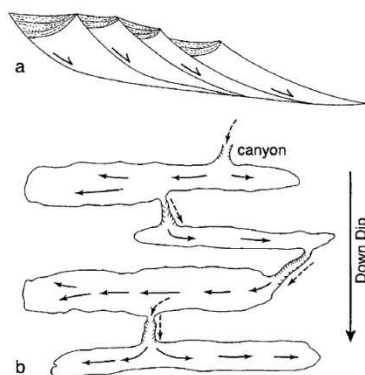


Figure 4.21: Schematic dip section (a) and plan view (b) of adjacent turbidite sub-basins resulting from individual tilting of faulted blocks (from Bouma, 2004). Spillover is claimed only to occur once the updip basin is filled. The location of the lowest spot in the outside wall of an individual sub-basin, and the gradients in each sub-basin, can result in one or two transport and filling directions into the next sub-basin.

Ponded slope/ silled sub-basins

Smith (2004) termed a closed topographic depression on a slope that has a topographic barrier at its downdip margin a silled sub-basin. If the volume of a subaqueous flow is much smaller than the scale of the silled sub-basin, the flow spreads out on the sub-basin floor and is not capable of reaching the bounding margin of the sub-basin (Fig. 4.22A). This scenario cannot be considered as ponding. When the flow volume is relatively large enough to sustain the flow to reach the bounding slope, the flow can be partly or fully trapped by the bounding slope (Fig. 4.22B).

The ***'fill-and-spill'*** model was suggested for the filling history of linked ponded minibasins on the slope of the Gulf of Mexico (Fig. 4.23; Prather et al., 1998; Prather, 2000). The sediment is captured in ponded accommodation created by salt withdrawal (Fig. 4.23A). As the fans successively fill this minibasin (4.23B), turbidity currents spill over the bounding slope to the downslope minibasin once the sill separating successive basins is overtopped (Fig. 4.23C). During the overspill process, as the equilibrium profile adjusts to the downslope basin, a localized truncation surface can be generated by erosion of the upslope basin margin (Fig. 4.23D). The accommodation between the truncation surface and the local equilibrium profile is backfilled as turbidity currents flow into the downslope basin (Fig. 4.23E). Finally, the basins are draped by muddy turbidites or hemipelagic deposits (Fig. 4.23F). Although this 2D model is often adopted in the stratigraphic evolution of successive intraslope minibasins, the filling history described in this model is incapable of explaining all scenarios of filling processes in such settings.

Badalini et al. (2000) proposed a model which emphasizes that the basins could fill coevally, but with partitioning of sand and mud among basins due to flow stratification. This model is often referred to as ***'flow-stripping'*** model. Based on flume and outcrop studies, Sinclair and Tommaso (2002) elaborated four phases of this

model: (1) flow ponding, where flows are completely confined in the upper basin, with deposition of thick sheet-like sand and mud couplets (Fig. 4.24A); (2) flow stripping, where finer sediments of the flow spill over the bounding slope of the upper basin and the coarser sediments are retained within this basin (Fig. 4.24B); (3) flow bypass, where flows either traverse the filled upper basin, resulting in channel incision, or switch the location of feeder channels, leading to abandonment of the upper basin (Fig. 4.24Ci, Cii); (4) blanketing, where backfilling in the interbasinal canyon results in base-level rise and channel-levee systems with low sand/mud ratios develop over basins (Fig. 4.24D).

In summary, during these processes, topography and deposition interact with each other. A sill initially prevents the current from flowing downslope and at least ponds the denser portion of the flow within the upslope minibasin. However, the accumulation of ponded deposit smoothes the topographic relief, therefore the sill allows more volume of the stripped flow to pass over into the lower minibasin and acts as the linking passage connecting the successive sub-basins (Fig. 4.25; Smith, 2004).

Smith (2004) also pointed out that 1) at the initial sub-basin entry point, the gradient reduction and the lateral spreading at the slope break result in the rapid deposition in front of the incised slope channel that feeds the sub-basin; 2) during the filling stage, the turbidite systems accumulate in the form of aggradation and progradation to the spill point of the sub-basin; 3) downslope steeper gradients lead to incisions of an outlet channel during overspill of large turbidity currents; 4) the overall profile of flow paths is altered with time due to incision of the steeper segments above and below the sub-basin and by deposition on the lower gradients in the area of the sub-basin.

Based on seismic and well data, more complicated turbidite models are recognized for silled sub-basins. For example, three end-member scenarios of proximal area (sand-rich fan lobe, leveed channel complex and mud-rich mass transport complexes) and three end-member situations for the distal part (a high sill, a low sill and an incised channel) proposed by Winker and Booth (2000); the vertical stacking sequence (mass transport complexes at the base, sand-rich distributary channel/lobe complexes in the middle, and channel-levee complexes and hemipelagic drapes at the top) by Beaubouef and Friedman (2000).

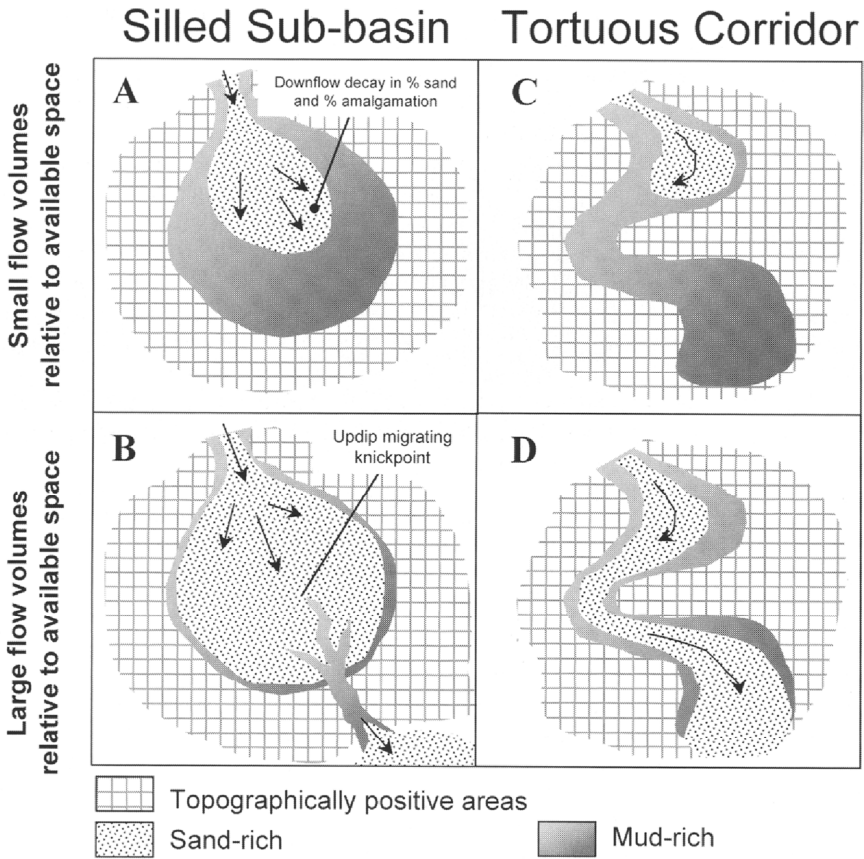


Figure 4.22: Schematic diagrams illustrating the relationship between the areal extent of sediment gravity flows and the areas of receiving depressions. (A) Silled sub-basin in which sand-transporting flows are small in volume relative to the scale of the receiving space. (B) Silled sub-basin in which sand-transporting flows are large in volume relative to the scale of the receiving space. The diagram shows spill to the next sub-basin downslope with associated incision and bypass in the upper sub-basin. (C) Connected tortuous corridor in which sand-transporting flows are small in volume relative to the potential flow path. (D) Connected tortuous corridor in which sand-transporting flows are large in volume relative to the potential flow path. From Smith (2004).

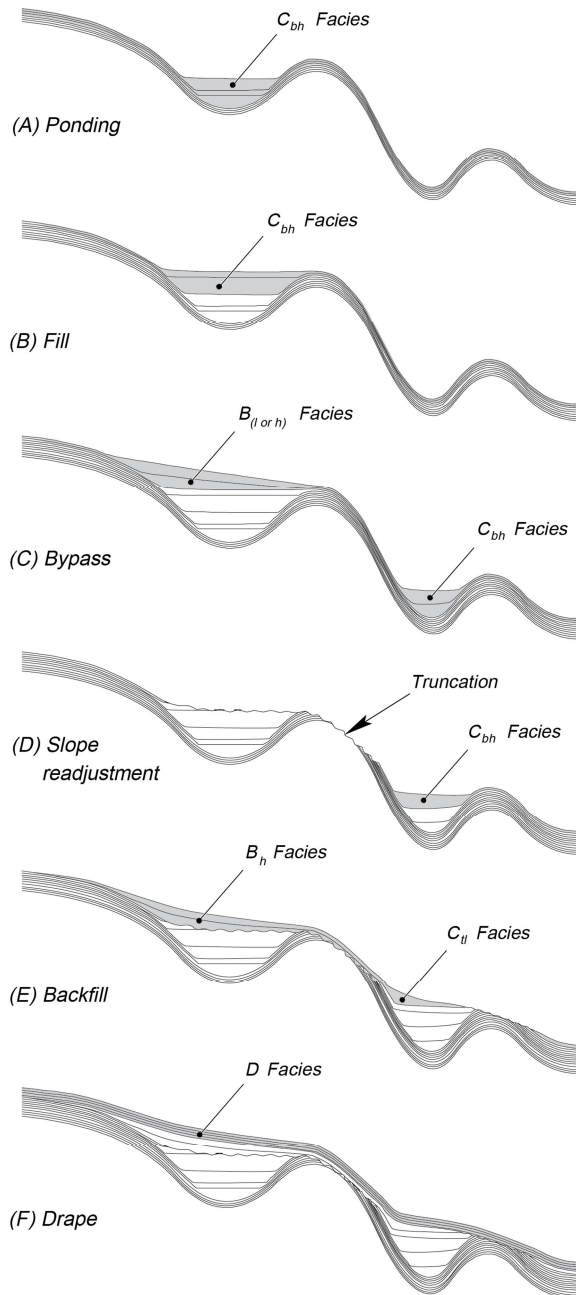


Figure 4.23: Evolution of an idealized ponded depositional sequence (from Prather et al., 1998). See text for description.

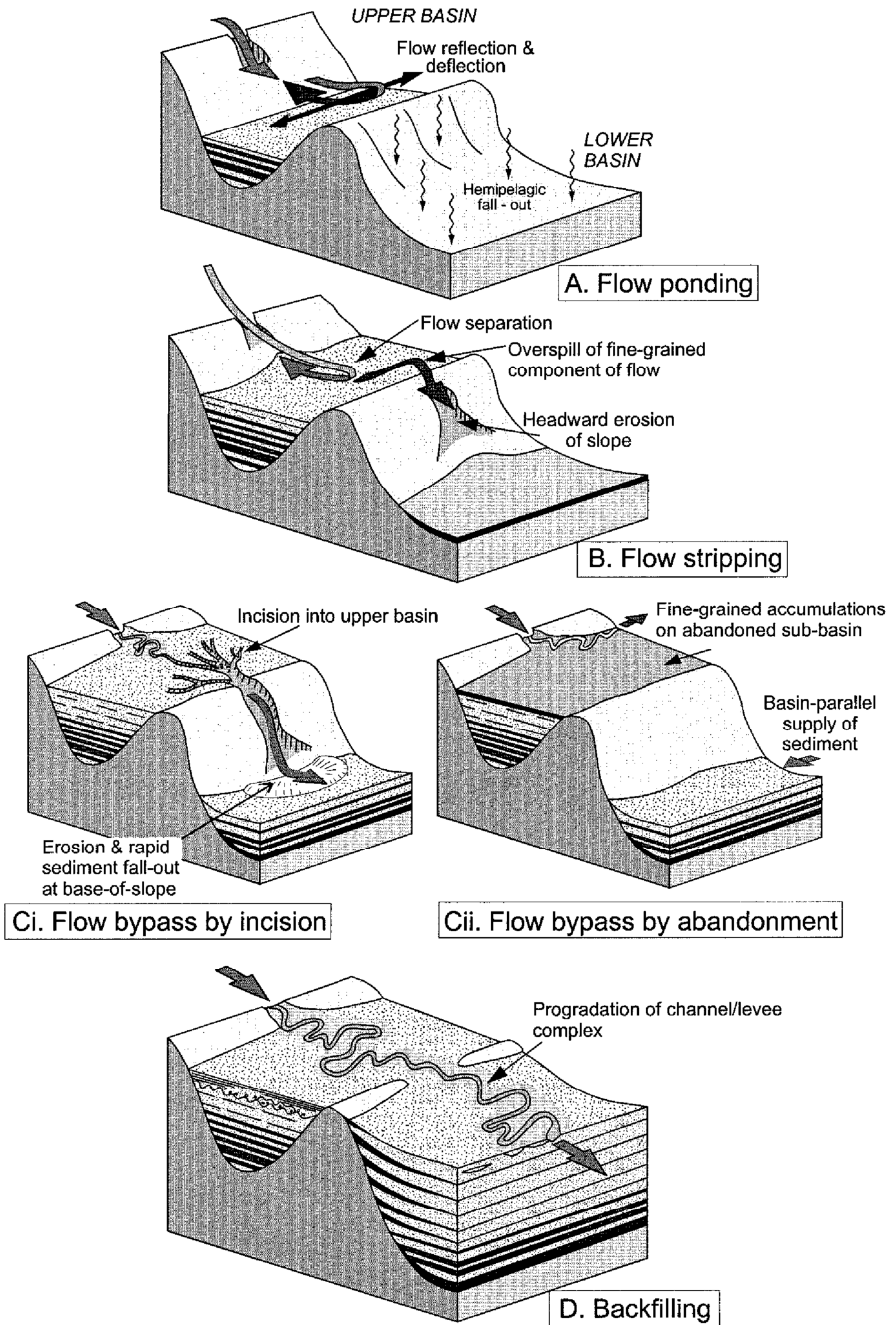


Figure 4.24: Depositional model for the progressive infill of a confined turbidite basin and associated deposits at the base of the slope of a lower basin. See text for descriptions of the four stages. From Sinclair and Tomasso (2002).

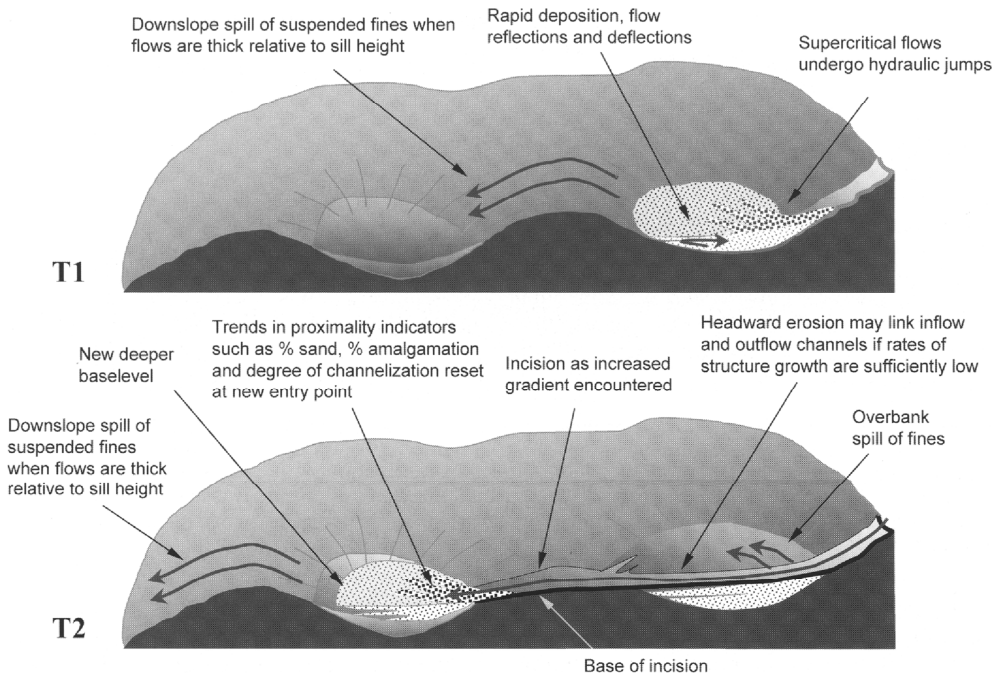


Figure 4.25: Schematic diagrams illustrating elements of the fill and spill model for two adjacent sub-basins (from Smith, 2004).

Stepped slope/ connected tortuous corridor

Well data and three-dimensional data show that the most common case of complex slope topographies are connected tortuous corridors (Fig. 4.22C, D; Fig. 4.26) rather than isolated silled sub-basins (Smith, 2004). The silled sub-basins recognized on 2D seismic imaging are probably connected by corridors which can be revealed in 3D view. The connected tortuous corridors can vary in their geometries. For example, an elongate, tortuous and laterally confined depression. Subaqueous flows can be guided and funneled along the corridors. Erosion and deposition of the flow can occur due to gradient changes caused by topographic reliefs along the flow pathway (e.g., slopes in West Africa and Brazil; Smith, 2004). Fan lobes are deposited in subtle depressions or at local breaks in slope. In addition, erosional conduits containing mud-rich channel-levee deposits are also observed. Amalgamated sand-rich turbidite channels have been observed in erosionally modified fault-controlled troughs in the Campos Basin (Moraes et al., 2000 in Smith, 2004).

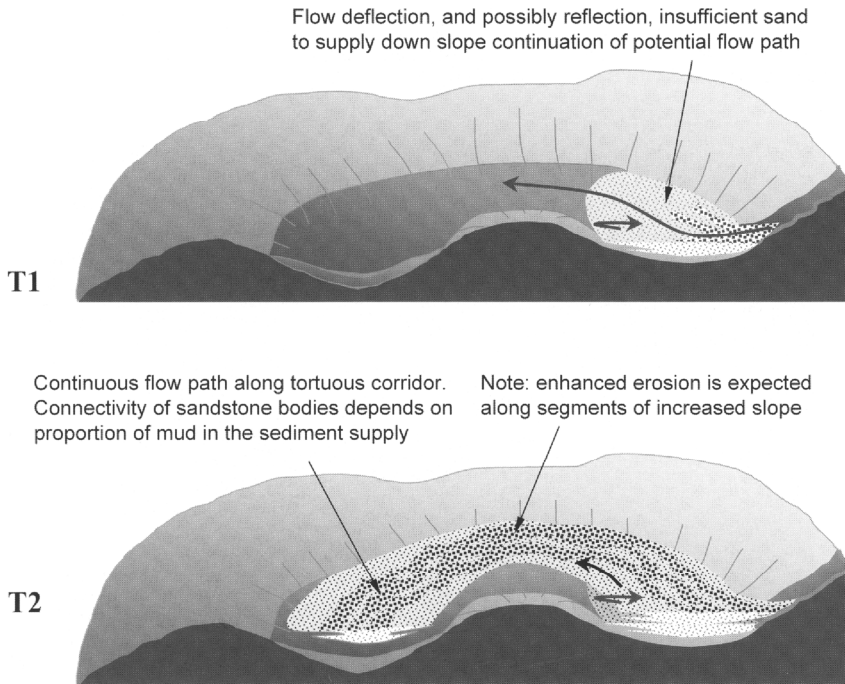


Figure 4.26: Schematic diagrams of the connected tortuous corridor model showing a case with small flow volume (from Smith, 2004).

The depositional processes and sedimentary systems for both models are mainly controlled by factors such as the ratio between the flow scale and the basin scale, the proportion of grain sizes of sediments, and the ratio between the rate of topographic growth and the rate of depositional smoothing (Smith, 2004). If the scale of the flow is small relative to the scale of the minibasin, the flow is not able to reach the bounding slope. The resulting deposition is limited at the entry point and the basin center and passive downlap occurs. If the flow is sufficiently large to reach the bounding slope, the corresponding effects such as the deflection and reflection of the flow can be recorded in the deposits. If the sediment of the flow is poor in mud, the resulting mud-poor systems at the entry points are characterized by sand-on-sand erosional contact, while for the mud-rich systems at the entry points, channel-overbank complexes are dominant. Hydraulic jumps can occur at the slope break and lead to rapid deposition. If the elevation difference between the ridge or the sill and the basal floor (uplifted by the accumulation of sediment) of the updip minibasin is small, a sand-rich backfill of the conduits connecting the successive minibasins can occur.

Smith (2004) proposed some criteria to distinguish the silled sub-basins model from the connected tortuous corridor model: In successively silled sub-basins, deposits in downslope basins tend to be younger than those in upslope basins; proximal-distal facies trends should be reset in each successive sub-basin; incision, bypass and fine-grained filling should be found during flow spilling over the updip silled sub-basin;

flow reflection is more common in silled sub-basins; and thick mud caps on top of individual turbidites may indicate that flows are fully ponded in silled sub-basins.

4.4.4 Confinement of depositional topographies

Topographic confinement can also be caused by depositional causes. For example, Mutti (1985) and Mutti et al. (1994) recognized a type of turbidite systems (Type I) where the stacking pattern is influenced by the local subtle depositional relief produced by active sand deposition. The subsequent turbidity currents are deflected by this relief, producing a self-maintaining cyclic process that leads to the formation of cycles of thickening-upwards sequences (Mutti and Sonnino (1981) in Albertão, (2010)). The internal architecture affected by the compensation of depositional relief may be found in many outcrops in collisional basins of the Northern Apennines, the Tertiary Piedmont Basin and the south-central Pyrenees (Mutti et al. (1994) in Albertão (2010)).

Based on the outcrop study of Miocene Cingoz Foramtion of southern Turkey, Satur et al. (2000) recognized three types of sandstone bodies that are topographically controlled by previous deposits. For example, the previous deposition in the area of transition between the canyon and the regions of linear tongue-shaped sandbodies reduces the topographic gradient and confinement, allowing lobate sandstone bodies to form during retrogradation.

In the Golo turbidity systems (Gervais et al., 2004, 2006), the three-dimensional geometry of the lobe is directly controlled by the pre-existing depositional morphology. In the upstream parts, strong confinement of the previous deposits is responsible for major deposition at the toe of the lateral slope and force the lateral migration of subsequent deposits (Fig. 4.27a). Longitudinally, the confinement of the previous deposits is expressed as aggradation and retrogradation of deposits instead of progradation (Fig. 4.27b).

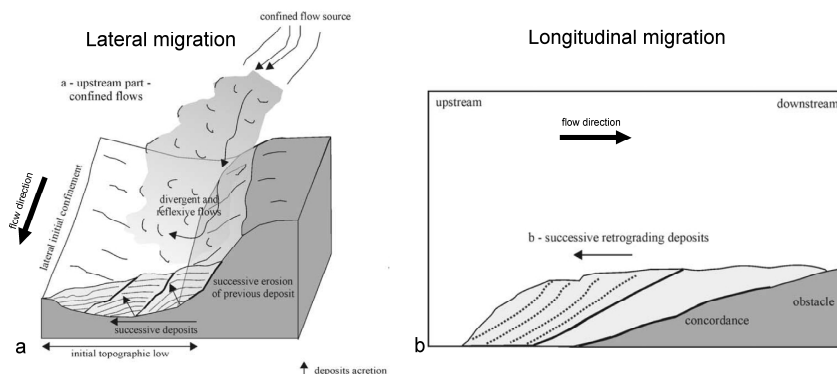


Figure 4.27: Schematic diagrams showing the impact of a lateral slope on lateral migration (a) and of a frontal slope on longitudinal migration (b). Modified from Gervais et al., 2006.

The depositional control on turbidity currents can also be found in the leveed systems, such as flank levees (e.g., Var turbidite systems, Migeon et al., 2000, 2001) and terraced morphologies of deep-sea channels (e.g., Golo turbidite systems; Ferry et al., 2004; Gulf of Lions; Jouet et al., 2006). They have resulted from depositional processes and influence the subsequent turbidity currents and associated deposits in return.

In conclusion, topographic confinement is an indispensable factor in controlling the flow pathways and behavior of turbidity currents, sediment dispersal and geometries of turbidite systems. The balance between the topographic scale, the flow scale and energy controls the effects of the confinement.

CHAPTER 5

Numerical Modelling of Turbidity Currents and Depositional Stratigraphy in Slope Minibasins

5.1 Introduction

Numerical simulation experiments of turbidity currents traversing a subaqueous topography (bathymetry) of channels and minibasins were conducted in order to investigate the interaction between these flows, their deposits and the changing bathymetries. This chapter first introduces the methods adopted in the numerical simulations. The experimental results are then presented and compared with the flow parameters, the flow evolutions, the flow-deposit interactions as well as the internal architectures and stacking patterns of the deposits. The results are compared with data from published literature, which are found to provide valuable support to our results.

5.2 Methodology

In order to develop conceptual models to simulate the dispersal patterns of turbidity currents and stacking patterns of their deposits in diapiric minibasins on passive margins, we integrate results from the experimental analogue seabed bathymetry and numerical flow simulation software “FanBuilder”. First, the digital topographic data originally obtained from analogue tectonic experiments in the laboratory was upscaled to realistic dimensions that occur in nature; additionally, an entrenched channel was added on the shelf and the shelf break to serve as point source for the flows (see chapter 3). Subsequently, the FanBuilder software was employed to model low-density turbidity currents that flow from the incised channel down into the minibasins on the synthetic continental margin. Both equilibrium and non-equilibrium turbidity currents at the source were modeled. A set of parameters within ranges expected to occur in nature was used in the flow simulation experiments. Multiple flow events with the same input parameters from the same point source were run, whereby the deposits were stacked on top of each other, usually until the first minibasin is filled to spill. The resulting sedimentary deposits were then analyzed in 3-D, typically in a series of strike and dip sections.

5.2.1 FanBuilder

FanBuilder is a three-dimensional process-based model that simulates turbidity current hydrodynamics and sedimentation on an arbitrary bathymetry for a specified number of flow events (Groenenberg, 2007; Groenenberg et al., 2009). In contrast to other three-dimensional numerical models including Delft 3D, Flow-3D and Sedflux 2.0, FanBuilder possesses the following two important characteristics for this study: (1) it is specially designed to simulate low-density turbidity currents and (2) geomorphic features and processes such as channelization, channel aggradation, avulsion and lobe switching in the resulting deposits can be observed in real-time.

The model is essentially based on five depth-averaged mathematical equations proposed by Parker et al. (1986). These five equations ensure the maintenance of flow momentum in the streamwise and transverse directions as well as flow mass and sediment mass conservation during one flow event. It permits the simulation of the hydrodynamic evolution of a turbidity current and its resulting deposit in three dimensions above an arbitrary bathymetry (Bradford et al., 1997; Bradford and Katopodes, 1999). A convection-diffusion equation is combined into this model to govern sediment transport. The model supports sediment transport of multiple grain-size classes and sediment exchange through erosion and deposition. The input parameters for the model include the initial bathymetry of the receiving basin, the grain size distribution of the sediment, the magnitude-frequency distribution of the flows, and the initial volume concentration of the sediment in the flows. By adjusting these parameters, their impact on the long-term stratigraphic evolution of turbidite deposits can be simulated and studied by this model. The evolution of the flows and the resulting stratigraphy (mostly the thickness and the mean grain size) is instantaneously visible in three dimensions during simulation.

To ensure that FanBuilder is sufficiently effective to simulate turbidity currents flow behavior and their depositional processes, Groenenberg (2007) conducted two sets of validation experiments based on data from laboratory experiments, including those of turbidity currents on a constant and smooth ramp by Luthi (1980, 1981) and a series of experiments of turbidity currents encountering various shapes of obstacles by Kneller and McCaffrey (1995). Qualitatively and partially quantitatively comparing results from numerical simulations and those from their correspondent physical experiments in terms of depositional geometries and distribution of thickness and grain size, the authors felt that deviations between the physical and the numerical flows are small. FanBuilder, they concluded, is thus a reliable flow simulation application for low-density turbidity currents flowing over different types of topographies. It is applicable primarily to simulating fully-developed low-density turbidity currents with volumetric sediment concentrations not exceeding 7% (Groenenberg, 2007; Groenenberg et al., 2009).

Further applications of FanBuilder to simulating large-scaled turbidity currents behavior in submarine sedimentary systems were realized subsequently, including testing conceptual submarine lobe models based on the data from outcrops exposed in the Karoo basin, South Africa (Groenenberg et al., 2010) and predictive models of the impact of relay ramps on turbidity currents with different inflow angles (Athmer et al., 2010). These successful applications of FanBuilder for modelling low-density turbidity currents at different scales over diverse topographic surfaces, and particularly the study of Athmer et al. (2010), provide important incentives for using FanBuilder to conduct studies on the impact of salt-induced complex topographies on low-density flows..

5.2.2 Input topography: seabed bathymetry

Experimental salt-bearing passive margins with various minibasins were successfully modelled in the tectonic laboratory (see Chapter 3). The digital topographic surface obtained from the extensional domain of Model 2 was found to be best suited for the simulation because the minibasins that developed in this model produce relatively large accommodation for the turbidity currents. The method of upscaling and modification of the chosen bathymetry is explained in Chapter 3. The specific location of the interest is indicated by the orange line in Fig. 3.16. The topographic area of interest (15 km × 30 km; Fig. 5.1) consists of a channel on the outer part of the shelf (average dip ~ 0.7°), several successive minibasins and two associated significant tectonic ridges on the slope (average dip ~ 4°). The channel is moderately sinuous and has a U-shaped cross-section profile with a slope gradient of about 0.022 ($\theta \approx 1.25^\circ$). It is about 70 m deep, 3 km wide (with a 1.5 km wide thalweg) and 10 km long, and it connects to a 5 km wide confined minibasin with a downstream bounding edge slope gradient of about 0.021 (~ 1.20°) as a spillover point that is about 60 m higher than the minibasin center (Fig. 5.2). Beyond this ridge is the lee-side slope with a gradient of about 0.0454 (~ 2.60°) and two smaller, poorly-confined minibasins (about 2.5 km in diameter) adjacent to each other in the distal part of the interest area.

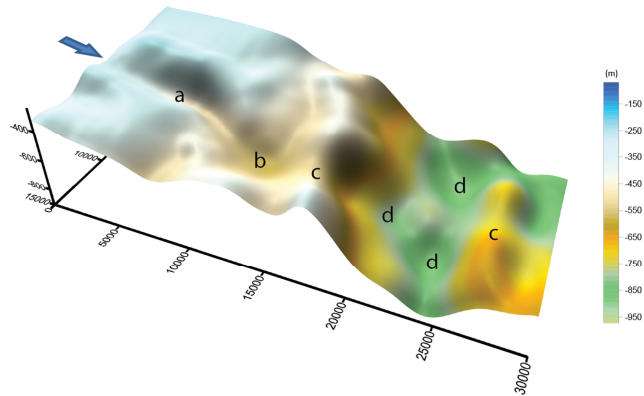


Figure 5.1: 3D view of the topographic area used in this study as the seabed bathymetry analogue. The main geomorphological elements include (a) a leveed channel, (b) a well-confined minibasin, (c) diapiric ridges and (d) three poorly-confined minibasins. The shelf-to-slope channel (a) acts as sediment supply corridor and extends into the first mini-basin (b). The ridges (c) act as obstacles for the currents flowing downslope. Open minibasins (d) offer the potential sedimentary accommodation space for spill-over flows over the ridges. The blue arrow indicates the inflow point and the initial direction of the simulated turbidity currents.

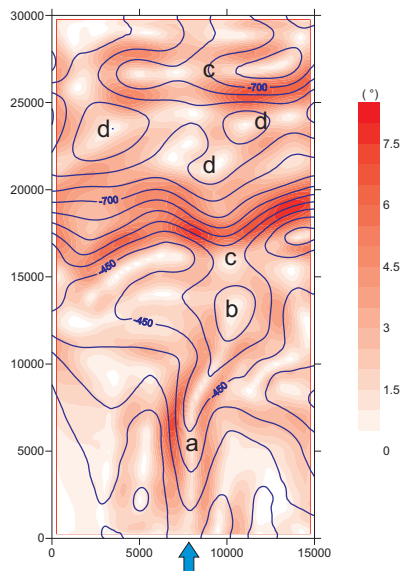


Figure 5.2: Terrain slope contour map with red hues indicating the slopes, superimposed onto the elevation contour map (blue lines) of the study area. The terrain slope angle is shown in degrees as the steepest descent or ascent at any grid node on the surface. The blue arrow indicates the inflow point. Areas marked (a) to (d) are consistent with those in Fig. 5.1.

5.2.3 Flow parameters

Both non-equilibrium and equilibrium initial flows (i.e. released at the source point) are simulated in multiple events. To determine whether the initial flows are in the equilibrium state or not the densiometric Froude number of the inflow is compared to the Froude number for an equilibrium flow under a given parameter setting.

The densiometric Froude number (see Chapter 2) is defined as

$$Fr_d = \frac{u}{\sqrt{g'h}} = \frac{u}{\sqrt{RgCh}}$$

Where u is the flow velocity, C is the flow concentration (volumetric percentage), h is the flow depth or height, g is the gravitational acceleration, and R is a dimensionless number, defined as the ratio between the sediment-seawater density difference and the seawater density ($R = (\rho_s - \rho_w) / \rho_w$). Here we take $\rho_s = 2650 \text{ kg/m}^3$ and $\rho_w = 1027 \text{ kg/m}^3$, and therefore $R = 1.58$.

The shear velocity measures the effect of the flow on the bed. In the absence of bedforms, it is assumed to be proportional to the square of the layer-averaged velocity of the flow. Due to the existence of the channel slope in the simulation scenario, the velocity is modified and simplified using the following equation, based on the Chézy equation for open channel flow (Middleton and Southard, 1984)

$$u^3 = \frac{FluxRg\beta}{C_D}$$

where $Flux = uCh$, β is the sine of the downstream slope and C_D is a dimensionless drag coefficient which scales with the intensity of the turbulence in the flow and varies with the ratio between bedform height and the flow depth. Parker et al. (1996) adopted a C_D value range of between 0.002 and 0.06 in their models, depending on the scale of the simulated flow. FanBuilder treats the value of C_D as a constant during the simulation, and this value greatly influences the depositional geometry of the unobstructed flow at its inflow point (Groenenberg, 2007). Therefore, it is important to impose an appropriate C_D value for the scale of the modelled flows and the purpose of the simulation experiments.

For equilibrium flows, the required densiometric Froude number can be derived as

$$Fr_d^* = \sqrt{\frac{\beta}{C_D}}$$

If $Fr_d \approx Fr_d^*$, we consider the initial flows as being in equilibrium, and if not, the initial flows are considered as non-equilibrium. Regardless of the initial state (equilibrium or

non-equilibrium) of the inflow, the characteristics of flow vary and evolve with time under the influence of the seabed bathymetry after entering the channel.

Table 5.1 Summary of the main inflow parameters considered in the numerical simulation flows.

| Non-equilibrium flows | | | | | | | | | | | | | |
|-----------------------------------|---------------------|--------------------|-----------------------------------|----------------|----------------|-------------------------------|---|-------------|------------------|------|------|----------|--------------|
| Sediment volume (m ³) | Flow velocity (m/s) | Flow concentration | Flow density (kg/m ³) | Flow depth (m) | Flow width (m) | Flow flux (m ² /s) | Grain size component | Slope angle | Drag coefficient | Fra | Fra* | Re | Event number |
| 10E+07 | 15 | 0.04 | 1091.92 | 50 | 500 | 30 | 250 µm 60% 100 µm 40% | 1.25° | 0.005 | 2.69 | 2.10 | 8.19E+08 | 65 |
| Equilibrium flows | | | | | | | | | | | | | |
| <i>Supercritical inflows</i> | | | | | | | | | | | | | |
| 5E+06 | 5 | 0.02 | 1059.46 | 50 | 500 | 5 | 250 µm 60% 100 µm 40% | 1.25° | 0.0136 | 1.27 | 1.27 | 2.65E+08 | 100 |
| <i>Subcritical inflows</i> | | | | | | | | | | | | | |
| 5E+06 | 3 | 0.01 | 1043.23 | 79.18 | 500 | 2.375 | 250 µm 60% 100 µm 40% | 1.25° | 0.03 | 0.86 | 0.86 | 2.48E+08 | 2 |
| 5E+06 | 3 | 0.02 | 1059.46 | 39.59 | 500 | 2.375 | 250 µm 60% 100 µm 40% | 1.25° | 0.03 | 0.86 | 0.86 | 1.26E+08 | 2 |
| 5E+06 | 3 | 0.03 | 1075.69 | 26.39 | 500 | 2.375 | 250 µm 60% 100 µm 40% | 1.25° | 0.03 | 0.86 | 0.86 | 8.52E+07 | 2 |
| 2E+06 | 2 | 0.01 | 1043.23 | 35.19 | 500 | 0.7 | 100 µm 30% 80 µm 40% 60 µm 27% 3 µm 3% | 1.25° | 0.03 | 0.86 | 0.86 | 9.8E+07 | 2 |
| 2E+06 | 2 | 0.02 | 1059.46 | 17.60 | 500 | 0.7 | 100 µm 30% 80 µm 40% 60 µm 27% 3 µm 3% | 1.25° | 0.03 | 0.86 | 0.86 | 4.97E+07 | 2 |
| 2E+06 | 2 | 0.03 | 1075.69 | 11.73 | 500 | 0.7 | 100 µm 30% 80 µm 40% 60 µm 27% 3 µm 3% | 1.25° | 0.03 | 0.86 | 0.86 | 3.36E+07 | 2 |

The parameters considered in setting up the initial condition mainly include the flow velocity, concentration, depth and width, released sediment volume, sediment grain size, drag coefficient, flow event number and so on (Tab. 5.1). These parameters are constrained within the range of magnitudes published from the few turbidity currents that have been measured in nature, and through consideration of software stability and computational efficiency. For example, turbidity currents on the Mid-Atlantic Ridge with a flow thickness of 30 m, a flow velocity of 1.5-40 m/s and a concentration of 0.03-0.12 (Van Andel and Komar, 1969); turbidity currents in the incised channel (without spillover lobes) of Bute Inlet with a flow thickness of 30-40 m, a slope degree of 1.5°, a flow velocity of 3.35 m/s, a flow concentration of 0.005-0.01 and a maximum grain size of 480 µm (Zeng et al., 1991); four turbidity currents measured by Xu et al. (2004) with a flow-body thickness of 50 m and a maximum head velocity of 5-12 m/s along the canyon (e.g., Zeng and Lowe, 1997; Mulder and Alexander, 2001). We aim to limit the negative effects of the boundary conditions in order to allow sufficient flow numbers to reach the minibasins.

Three sets of numerical simulations were modeled and analyzed:

- i) A set of non-equilibrium-flow simulations of highly supercritical turbidity currents with 65 successive events (Section 5.3);
- ii) A set of equilibrium-flow simulations that were initially supercritical flows with a densimetric Froude number of 1.27 is modelled with 100 flow events (Section 5.4);

iii) Two sets of subcritical equilibrium inflows with the same densimetric Froude number of 0.86, but different in sediment volume, flow velocity and grain size components, are simulated with two flow events. Each group of equilibrium subcritical inflows has three sets of parameters which are only different in their flow concentrations, flow density and flow heights, but have the same flow flux (Tab. 5.1). The comparison between the results within one group can serve as sensitivity tests for the applied parameters, for example by varying the flow concentration and height, and keep the other parameters constant.

5.3 Non-equilibrium inflows

Sixty-five point-sourced flow events of highly supercritical turbidity currents are simulated in this scenario. The flow parameters are kept identical in all these events (Tab. 5.1). During each flow experiment, the evolution of the flow characteristics in the channel and the minibasins can be monitored in real-time. At the end of this set of experiments the data of the depositional thicknesses and of mean grain sizes is saved. The mean grain size reflects the proportion of the two initial components (100 μm and 250 μm). A higher mean grain size means a higher proportion of coarser grains. Furthermore, the internal architecture of the deposits within the minibasins can be analyzed in order to investigate the interplay between the pre-existing bathymetry and sedimentation.

5.3.1 Flow evolution

The results of the 65 successive flow events show that the pre-existing bathymetry profoundly influences the flow pathway and flow behaviors of the traversing turbidity currents. The real-time variations of the flow hydrodynamic parameters (flow thickness, flow concentration and densimetric Froude number) illustrate the temporal evolution in flow characteristics.

Full ponding stage (flow event 1)

In event 1, the surging turbidity current is fully confined within the upper minibasin without any overspilling (Fig. 5.3; Fig. 5.4). Although the initial flow has a high speed of 15m/s, once the flow was completely released into the channel and funneled by the channel corridor (after about 2000s), the maximum flow velocity decreased to about 8m/s with a maximum concentration of 4.5% (Fig. 5.3a, b, c). When entering the upper minibasin, the flow began to spread within the whole basin (Fig. 5.3d, e, f). As a part of the flow encountered the ridge-shaped bounding slope, the flow velocity decreased and the flow thickness increased dramatically (Fig. 5.3g, h, i). At this stage the flow became partially supercritical and partially subcritical. Flow deflections and reflections occurred on the up-dip facing intrabasinal slope until the flow energy diminished within the basin (Fig. 5.4). As this flow's deposit is entirely confined to the minibasin it is a true ponded event.

Fill-and-spill stage (flow event 2-44)

At this stage, the turbidity currents are mostly confined within the upper minibasin but partially spill over the bounding ridge downslope into the smaller distal minibasins. This occurs from event 2 to event 44 in the non-equilibrium set of simulation experiments. Flow event 25 is described as an example (Fig. 5.5; Fig. 5.6). Although its energy was reduced due to the occurrence of flow spreading in the upper minibasin and flow resistance at the downstream ridge (Fig. 5.5a, b, c), part of the flow was capable of surmounting the lowest point of the bounding ridge (Fig. 5.5d, e, f). Part of the flow that spilled over continued with a higher velocity along the lee slope into the two smaller down-dip minibasins (Fig. 5.5g, h, i). There, the flows that partially spilled over the ridge experienced deflections due to the poorly-confined bathymetry with a significant lateral spread (Fig. 5.6).

Trapping stage (flow event 45-65)

For the remaining events the turbidity currents are no longer able to spill over the ridge bounding the upper minibasin. They are completely trapped in the area of the upper minibasin because the ridge built up depositional relief and the minibasin depocenter retrograded. Figure 5.7 illustrates the event-45 evolution after the flow completely expanded within the upper minibasin (at about 4000s). The area of flow spreading within the minibasin is relatively larger than that of the former two stages. Although there is no flow spilling over the bounding slope, the flow can reach as far as the ridge top (Fig. 5.7a, b, c). The plan view of the flow morphology shows that the turbidity current evolved from a fan shape to a pronounced shape of a pedate leaf (Fig. 5.7d, e, f). When the flow velocity is diminished sufficiently all sediment settles out onto the floor of the minibasin (Fig. 5.7g, h, i).

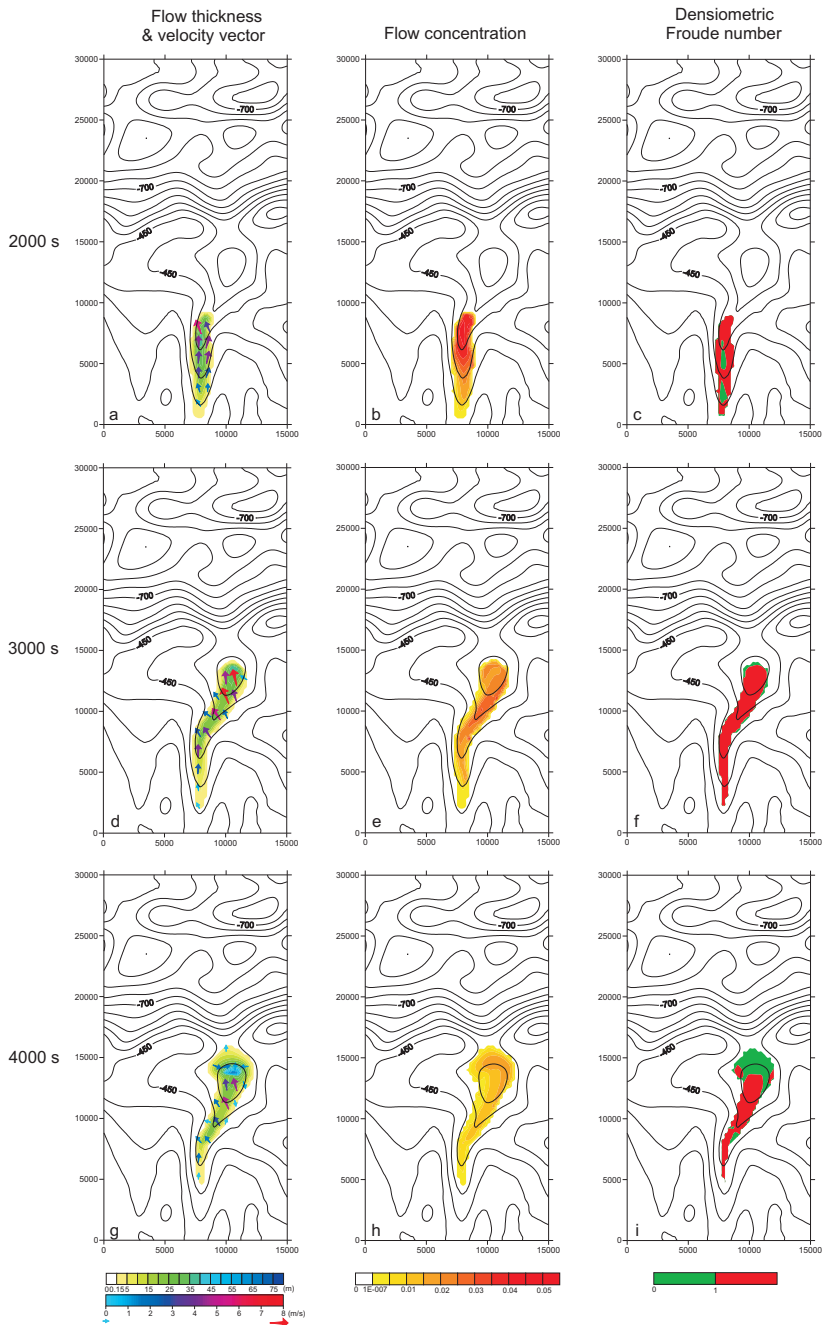


Figure 5.3: Flow evolution of event 1 (at 2000s, 3000s and 4000s) of supercritical non-equilibrium inflows is displayed as maps of flow thickness, velocity vectors, concentration and the densimetric Froude number distribution. All maps are superposed onto the contour map of the original bathymetry.

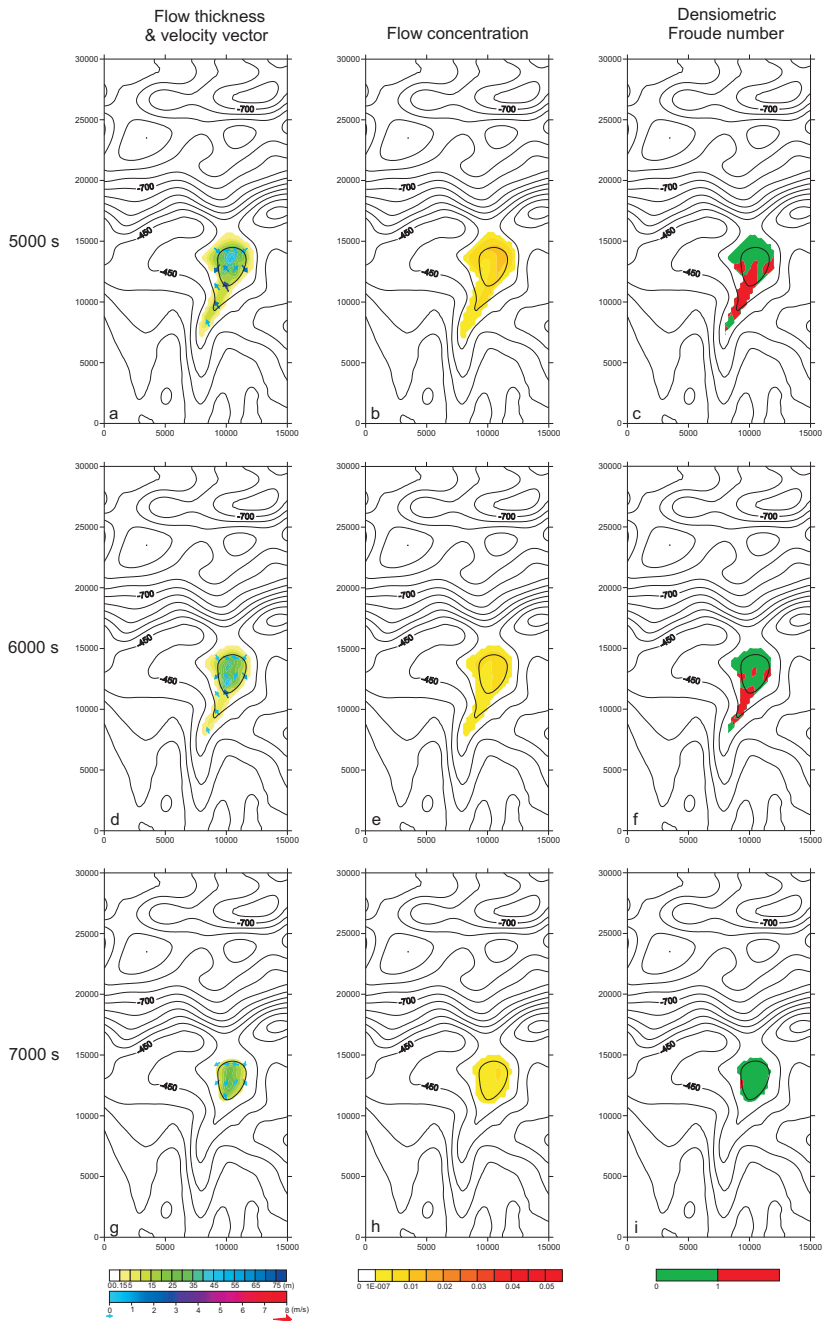


Figure 5.4: Flow evolution of event 1 (at 5000s, 6000s and 7000s) of supercritical non-equilibrium inflows is displayed as maps of flow thickness, velocity vectors, concentration and the densimetric Froude number distribution. All maps are superposed onto the contour map of the original bathymetry.

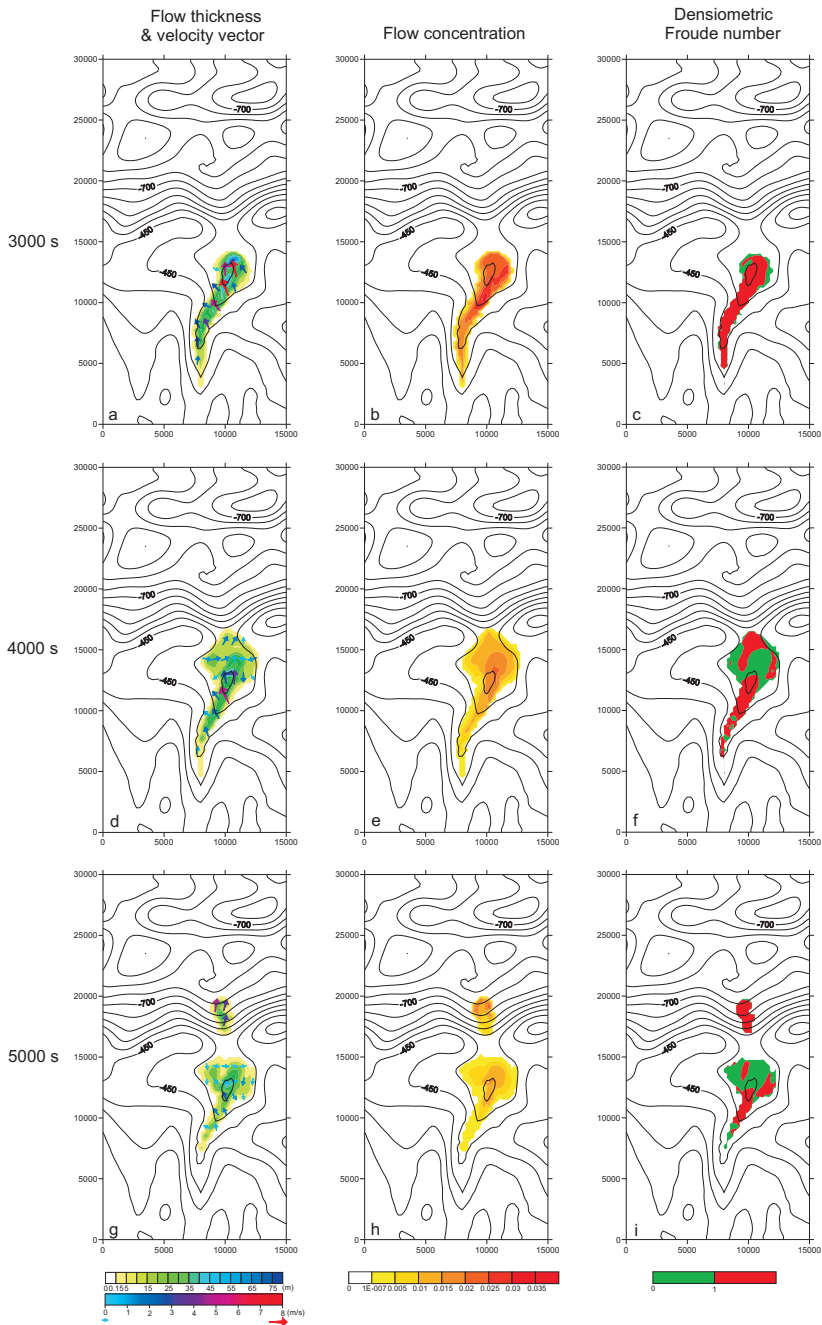


Figure 5.5: Flow evolution of event 25 (at 3000s, 4000s and 5000s) of supercritical non-equilibrium inflows is displayed as maps of flow thickness, velocity vectors, concentration and the densiometric Froude number distribution. All maps are superposed onto the contour map of the bathymetry after event 24.

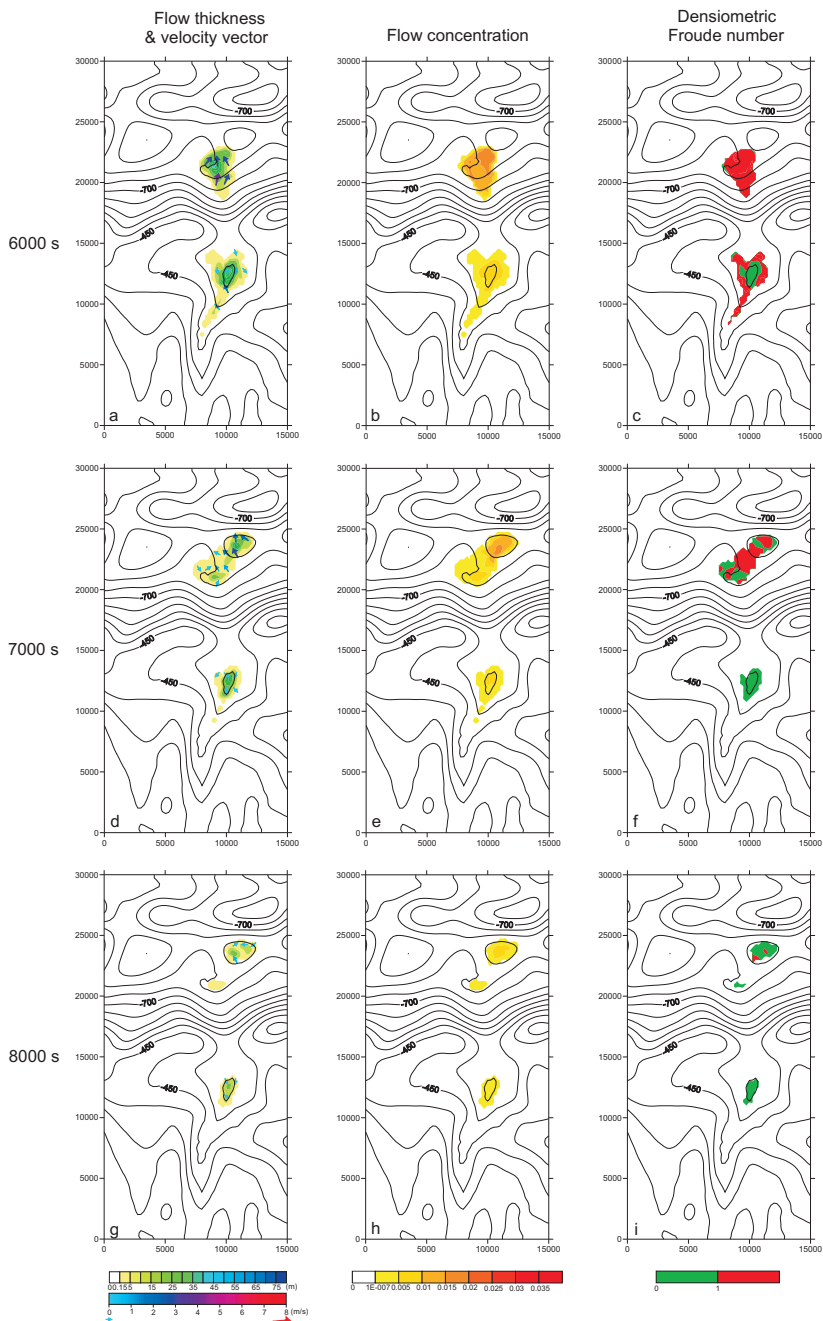


Figure 5.6: Flow evolution of event 25 (at 6000s, 7000s and 8000s) of supercritical non-equilibrium inflows is displayed as maps of flow thickness, velocity vectors, concentration and the densimetric Froude number distribution. All maps are superposed onto the contour map of the bathymetry after event 24.

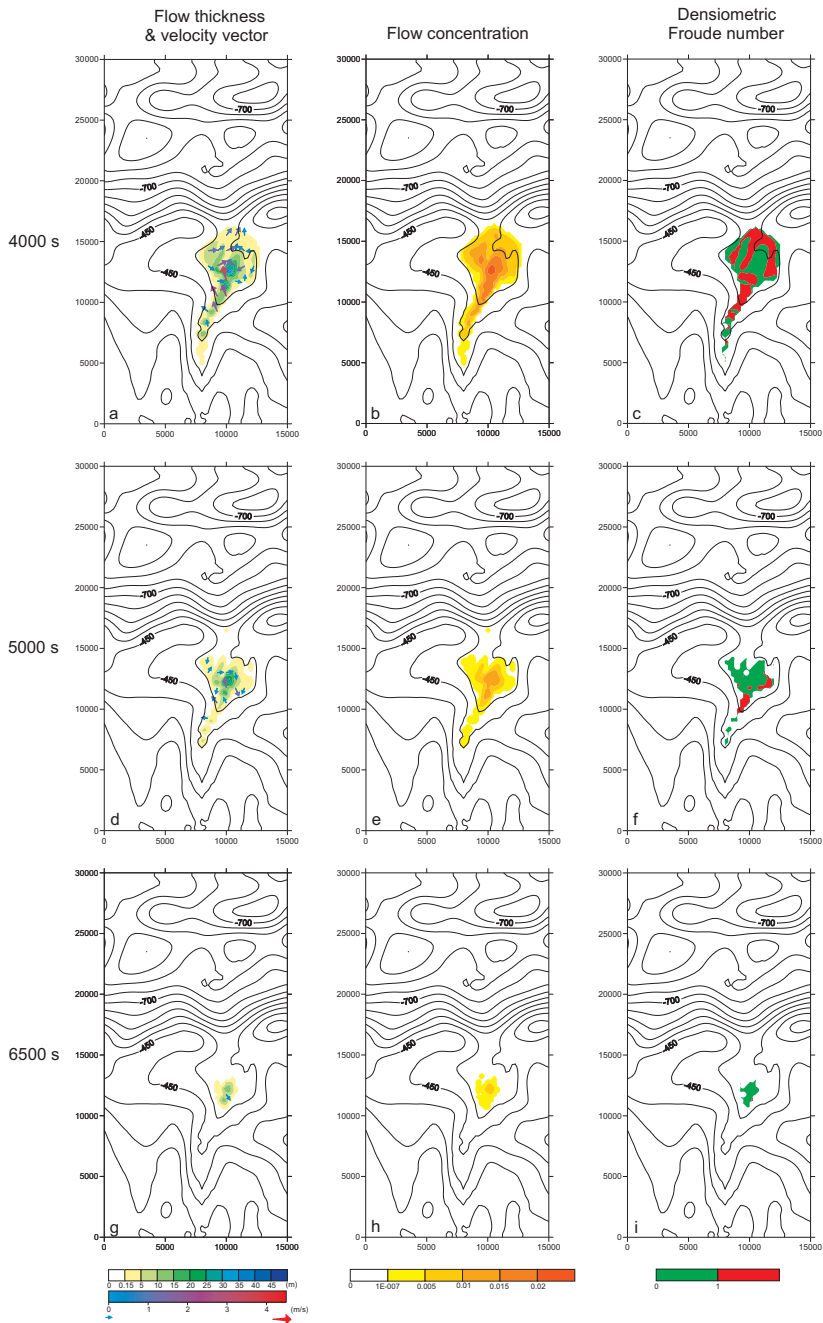


Figure 5.7: Flow evolution of event 45 (at 4000s, 5000s and 6500s) of supercritical non-equilibrium inflows is displayed as maps of flow thickness, velocity vectors, concentration and the densimetric Froude number distribution. All maps are superposed onto the contour map of the bathymetry after event 44.

5.3.2 Flow-deposit interaction

The turbidity current deposits from the numerical simulations lead to an evolving bathymetric template that influences subsequent flow behavior. Here we describe the interaction between bathymetry, flow characteristics and deposits in terms of the distribution of thickness and grain size, as well as the significant bathymetric changes during the three stages (ponding, fill-and-spill and trapping).

Deposit and mean grain size

Among all 65 depositional beds, the maximum thickness of a single bed is found to be 2.25 m. The depositional thickness map of bed 1 (Fig. 5.8a) indicates that significant deposition took place on the counterslope of the upper minibasin. Its maximum deposit thickness is about 1.90 m. Small amounts of finer sediment is deposited in the upstream slope area of the basin. The corresponding mean grain size distribution shows that the thicker deposits have larger mean grain sizes, i.e. greater portions of coarser grains (Fig. 5.8b). The contour profile of the mean grain size strongly resembles that of the deposit thickness (Fig. 5.8a).

Individual beds that formed in the stage of fill-and-spill (flow events 2-44) are distributed over three minibasins. The maximum deposit thickness is about 1.76 m. Due to the currents' spill-over and flowing down the lee slope, erosion occurs along the slope. Figure 5.8c and d display the deposit thickness and grain size distribution of bed 2, with small amounts of finer sediment deposited in the poorly confined down-dip minibasins while the thickest deposits are located in the well-confined upper minibasin. At later stages, coarser grains are also delivered over the upper minibasin ridge into the down-dip minibasins (Fig. 5.8f, h). The thickest deposits in the upper minibasin are concentrated close to the original minibasin center (Fig. 5.8e, g). Moreover, minimal amounts of erosion (less than 0.1 m; indicate in blue on the thickness maps) can be found at the entrance into the upper minibasin, on the bounding ridge and on the small obstacle between the smaller down-dip minibasins. Figure 5.8i and j show that during the late fill-and-spill stage the depositional extents of the spilling flows become smaller but still contain some coarser grains.

In the trapping stage (flow events 45-65), the depositional extent in the upper minibasin is larger than that of bed 1 (Fig. 5.8k, m, o). The thickest deposits occur not only in the upper minibasin, whose depocenters continuously shift upstream, but individual beds in the channel progressively form depositional bars. The mean grain size distribution in the upper minibasin displays an increasingly complicated pattern due to these bathymetric irregularities (Fig. 5.8l, n, p).

The thickness distribution of the total deposit in the fill-and-spill stage and the trapping stage are displayed in Figure 5.9a and b. The maximum thickness of all 65 beds is found to be 85 m, located in the center of the upper minibasin (Fig. 5.9c).

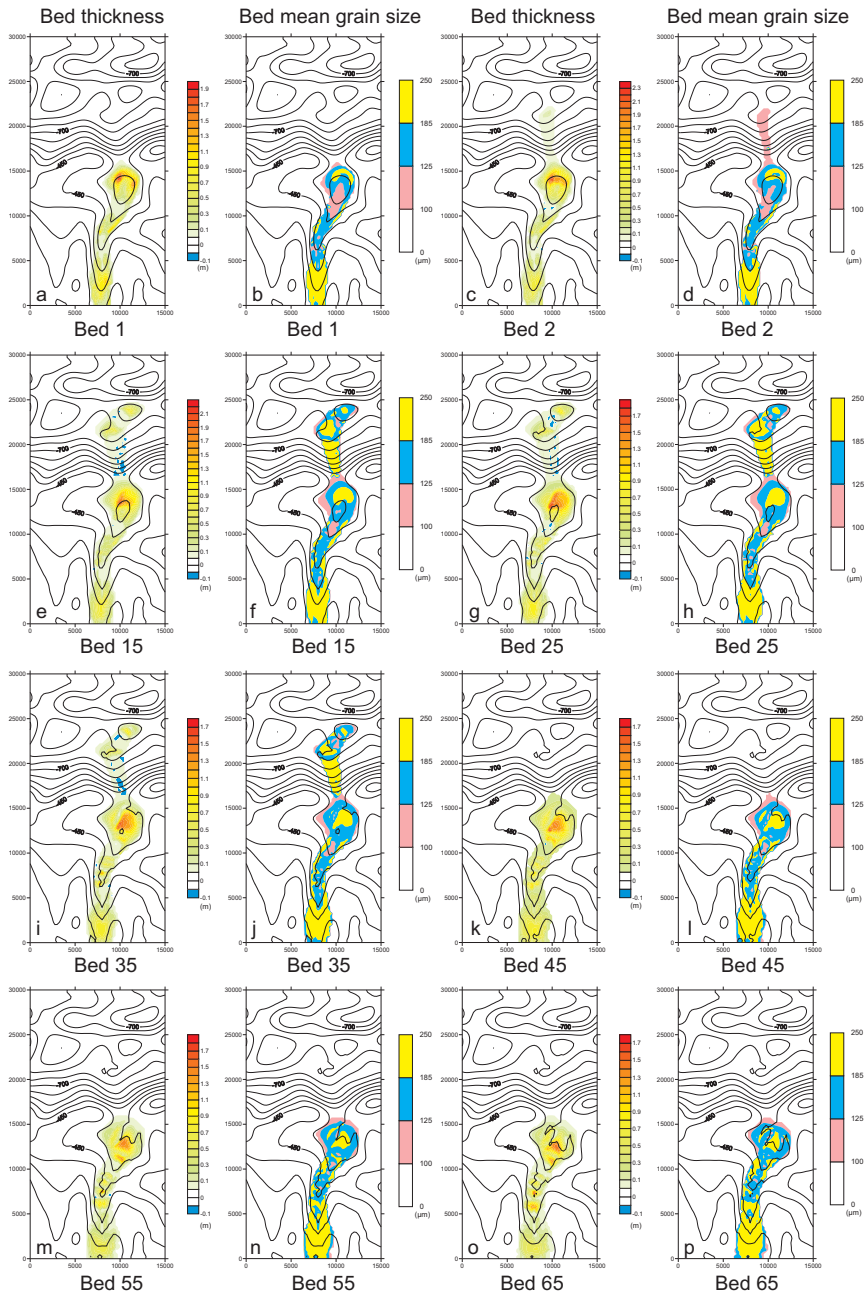


Figure 5.8: Maps showing the deposit and erosion thickness and the grain-size distribution of the individual beds formed in event 1, 2, 15, 25, 35, 45, 55 and 65 (supercritical non-equilibrium inflows). Each map is superposed on the pre-existing bathymetric map.

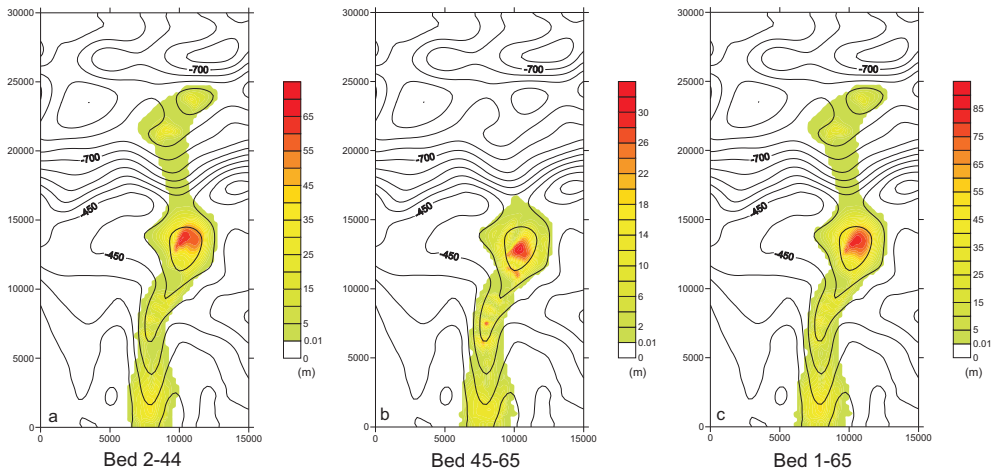


Figure 5.9: Maps showing the deposit thickness of the beds formed in event 2-44 (a), event 45-65 (b) and event 1-65 (c) (supercritical non-equilibrium inflows). All thickness maps are superposed on the elevation contour map of original bathymetry.

Bathymetric changes

The ongoing accumulation of the deposits from the 65 flows leads to continuous changes in the bathymetric template, i.e. the depositional relief combined with the original bathymetry. Conversely, these bathymetric changes influence the pathways of the turbidity currents and the location and geometry of their deposits. This evolution of the bathymetry is displayed in Figure 5.10.

During the fill-and-spill stage, a subtle depositional ridge initially develops around the counterslope of the upper minibasin (Fig. 5.10a, b). It then grows in height and moves towards the upstream direction to form a more pronounced ridge-shape above the original basin center (Fig. 5.10c). The volume of the initial minibasin gradually decreases, while a new, rather subtle ridge forms on the basinward side of the original depositional ridge (Fig. 5.10d, e). Eventually, the limited accommodation is segmented by the depositional ridges into a finger-like geometry (Fig 5.10f) while the deposit in the upper minibasin forms a gentle ramp between the remaining accommodation and the basin edge (Fig. 5.10g). In this cross section, the basin accommodation after event 65 has considerably decreased compared to the original bathymetry and the basin center and “spill-over point” have migrated a significant distance upstream.

By determining the gradient of the counterslope of the upper minibasin in increments of ten flow events, one obtains a general trend of the gradient changes (Fig. 5.10h). After an initial decrease it increased and then decreased, but was still higher after 65 flow events than the original gradient. This to some extent contributes to the three evolutionary stages of flow behaviour and basin infill.

Numerical Modelling of Turbidity Currents and Depositional Stratigraphy in Slope Minibasins

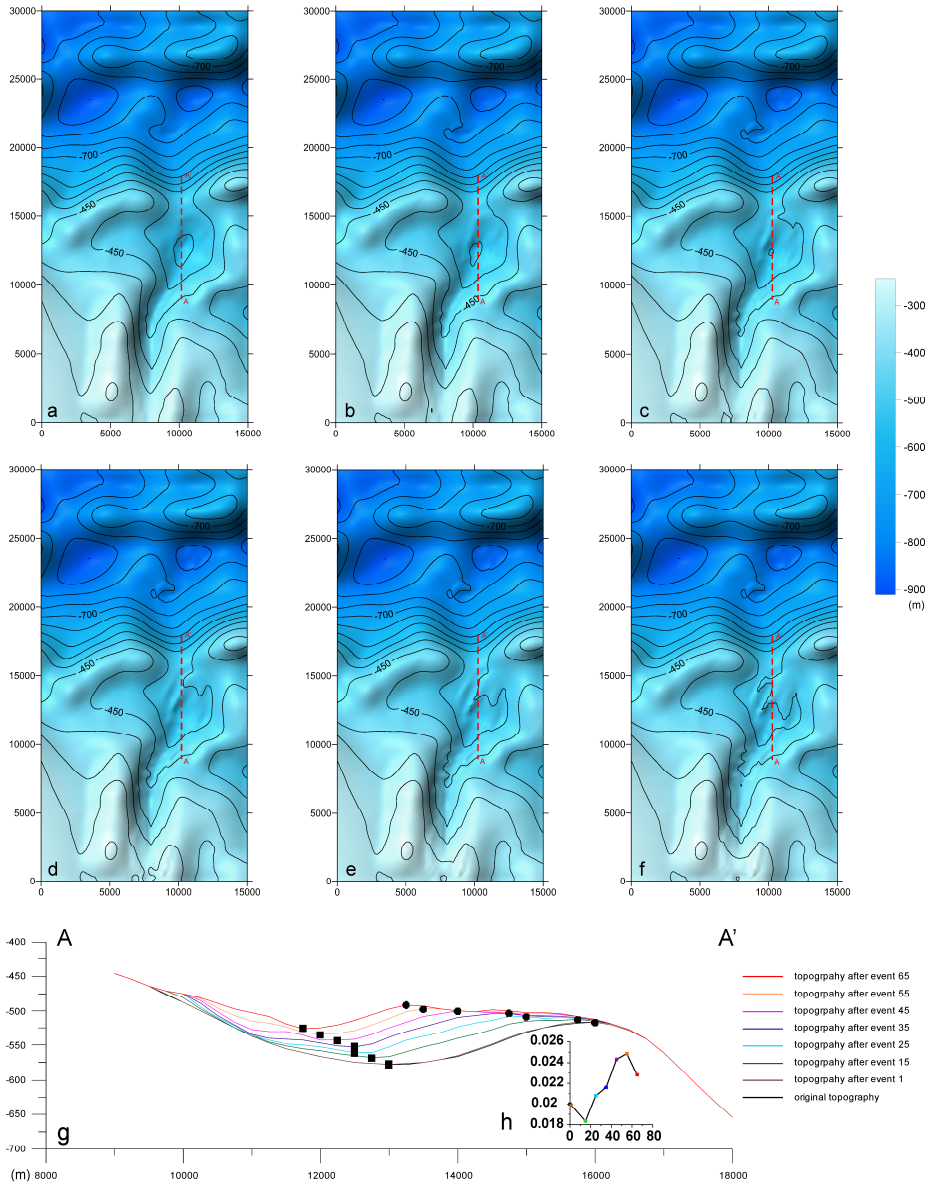


Figure 5.10: Maps showing the topographical changes after event 15 (a), 25 (b), 35 (c), 45 (d), 55 (e) and 65 (f) (supercritical non-equilibrium inflows). The corresponding changes in longitudinal cross-section profiles of the upper minibasin are shown in (g), with the location of the sections indicated in the maps by red dashed lines. The black round dots indicate the location of the potential “spill-over points” of the upper minibasin. The black square dots show the locations of the lowest points in the sections – not to be confused with the depocenter. The changes in the counterslope gradient (from the lowest point to “spill-over point”) of each topography are illustrated in (h).

5.3.3 Depositional architecture

A stratigraphy of the 65 beds is established by using the data of the depositional thickness and the lithofacies. This helps to reflect how the flow-deposit interaction influences the internal architecture and stacking pattern of the depositional system. Flow overspill is an important phenomenon in our simulation experiments and the depositional characteristics in the distal minibasins directly indicate the confinement of the upper minibasin. Thus, based on a comprehensive analysis of the flow pathways and the spatial trends of the bed depocenters and mean grain size, six groups of bed sequences that share similar characteristics are distinguished.

Group 1 (G1)

Group 1 consists of only bed 1, which is not present in the down-dip minibasins because the flow is fully confined by the bounding ridge of the upper minibasin. About 50% of the sediment is deposited within this minibasin (Fig. 5.11). Both longitudinal (parallel to stream direction) (Fig. 5.12) and lateral (perpendicular to stream direction) (Fig. 5.13) cross-sections show that the deposit around the minibasin is thicker and coarser-grained than that in its center. The depocenter of this group lies on the counterslope (Fig. 5.14).

Group 2 (G2)

Group 2 is composed of the beds formed from event 2 to event 14. More than 50% of the sediment volume is ponded in the upper minibasin, nearly 10% of the sediment is transported to two lower minibasins and less than 40% of the sediment is deposited in the channel (Fig. 5.11). The beds of Group 2 in the upper minibasin longitudinally have a bigger thickness on the counterslope of the previous depositional relief (topography after event 1) (Fig. 5.12). Laterally, the deposits in the basin center and the counterslope grow faster than that on the basin flank (Fig. 5.13). The beds of Group 2 in the first lower minibasin show first a thickening-upward and then a thinning-upward trend, while the mean grain size has a coarsening-up profile. The depocenter of Group 2 in the first lower minibasin is on the counterslope of its underlying bathymetry, as seen in the longitudinal cross section (Fig. 5.15a), and on the higher basin flank as seen in the lateral cross section (Fig. 5.15b).

The depocenter of the entire group 2 is on the counterslope of the relief formed after event 1. The depocenter moves upstream relative to the depocenter of Group 1 (Fig. 5.14a) and laterally towards the minibasin center (Fig. 5.14b). Consequently, the new depositional relief formed by Group 2 has a greater slope gradient on its new counterslope.

Group 3 (G3)

Group 3 is distinguished by the recognition of a new sequence (bed 15 – bed 25) in the first lower minibasin. More than 10% of the total sediment volume is deposited in

the down-dip minibasins. In this sequence, the bed thickness in the first lower minibasin generally stabilizes at about 0.8 m. Its average bed thickness is smaller than that of Group 2. A similar thickness profile also exists in the second lower minibasin. The shifting trend of the group depocenter in the first lower minibasin is vertically upward on the counterslope (Fig. 5.15a, b).

The sedimentation rate of Group 3 in column C in Figure 5.12 and Figure 5.13 is higher than elsewhere in the cross sections. The depocenter of Group 3 longitudinally remains on the counterslope of the topography formed after event 14 (Fig. 14a), while it laterally shifts from one side of the basin to the other side (still not in the basin center) (Fig. 14b). The newly-formed depositional bathymetry has a lowest point and counterslope that shifted upstream.

Group 4 (G4)

Beds 26 to 44 comprise this group. Here the amount of sediment transported to the lower minibasins is considerably reduced (Fig. 5.11). Consequently, the bed thickness and mean grain size gradually decrease upwards (Fig. 5.12). Moreover, the group depocenter in the first lower minibasin migrates to its basin center (Fig. 5.14). The beds of Group 4 in the upper minibasin have a more pronounced thickness on the counterslope of the depositional relief formed by Group 3 (vertically it is in the center of the original minibasin), although the bed thickness on the upstream slope is increasing. Less sediment is deposited on the D and E locations (Fig. 5.12). The group depocenter in the upper minibasin migrates towards the original minibasin center, but is, however, still on the counterslope of the relief developed after event 25 (Fig. 5.14a). The lateral cross-section shows that it moves vertically upward on the basin side-slope (Fig. 5.14b). The gradient of the counterslope of the newly formed relief (i.e. the top surface of bed 44) is larger than that of Group 3.

Group 5 (G5)

This group is composed of the beds deposited from event 45 to event 51. Because the flow is trapped in the upper minibasin again, there is no sediment in the down-dip minibasins. In this group, the sedimentation rate on the counterslope of the top surface of Group 4 (vertically atop the original minibasin center) is dominant, while little sediment is deposited on the basin margins (Fig. 5.12). Due to the imbalance of the rate of deposition on the side-slope of the previous depositional topography, local depressions form (Fig. 5.13). The vortices developing at the margins of the flow transport sediment backwards to the minibasin entrance (Fig. 5.7). The depocenter of Group 5 continues to migrate longitudinally towards the upstream direction and laterally towards the original basin center (Fig. 5.14).

Group 6 (G6)

The remaining beds (from bed 52 to bed 65) constitute Group 6. Figure 5.12 shows that the original minibasin center (column C) has a thicker deposit. The beds there

form a thinning upward succession, while the beds on the upstream slope (column B) thicken- and coarsen- upwards. Similar trends also can be found in the lateral cross-section (Fig. 5.13). The thickest deposit is still above the location of the original minibasin center while the bed thickness of one basin flank increases greatly. Consequently, the group depocenter is further moving towards the original minibasin center longitudinally and laterally (Fig. 5.14).

In summary, significant deposition takes place on the counterslope of the bounding relief (the ridges) rather than the minibasin centers. The lowest points and “spill-over points” are shifted upstream with a continuous decrease in accommodation, which leads to changes in the slope gradient of the newly-formed depositional relief. This greatly influences the flow pathways and the geometry and internal stacking pattern of the system. The main minibasin is back-filled by successive deposits, which results in an internal architecture whose local depocenter migrates upstream longitudinally and towards the original minibasin center laterally (Fig. 5.16). During the infill, the formation of a local depositional depression can be observed.

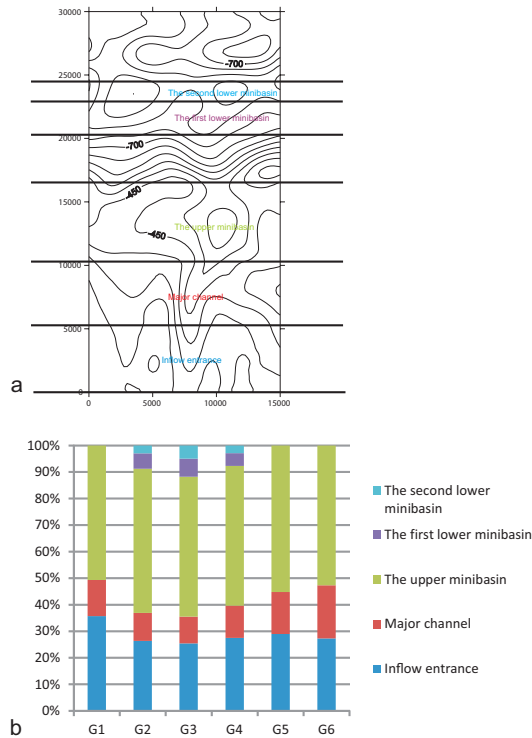


Figure 5.11: (a) The spatial division of the topography into five areas. (b) Proportion of the sediment volumes in the five areas for the six groups (supercritical non-equilibrium inflows).

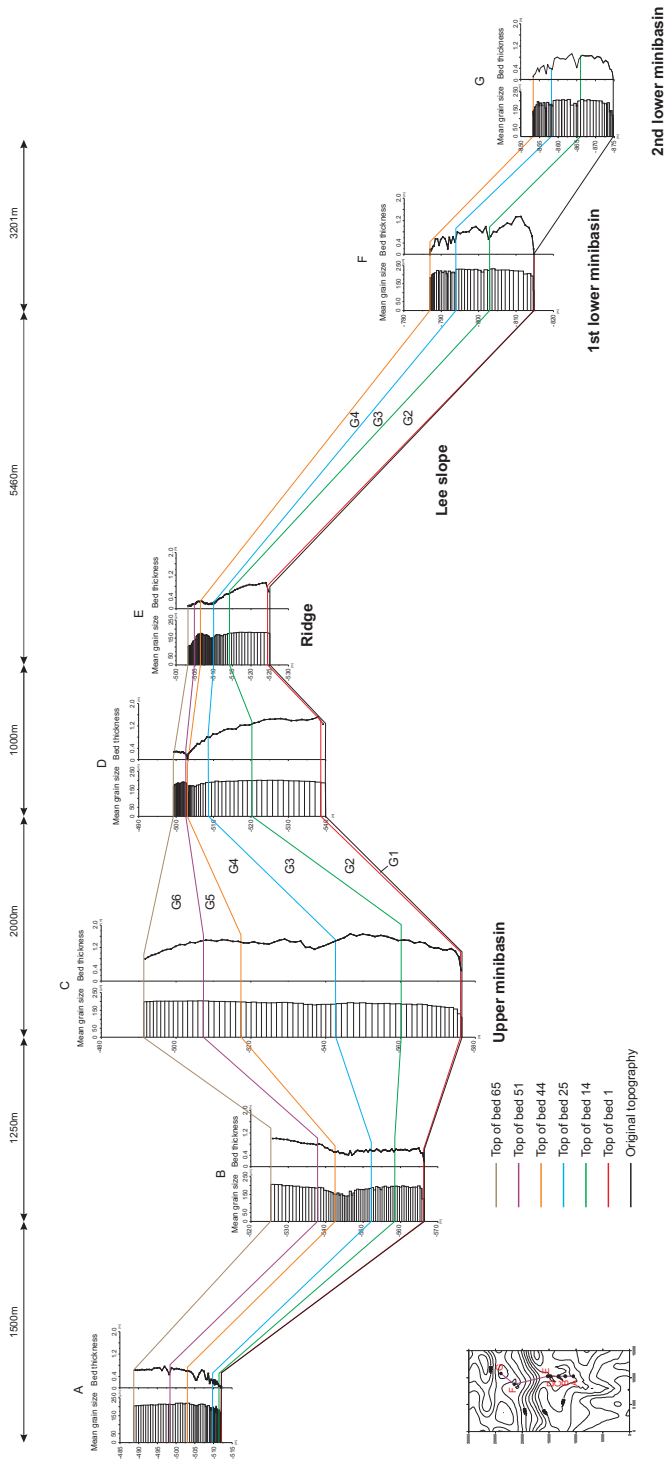


Figure 5.12: Cross-section showing the longitudinal isochronous correlation of the stratigraphy (supercritical non-equilibrium inflows) in the three minibasins. Seven spots (A-G) are selected to display the mean grain-size column and layer thickness profile. Spots A, B, C and D are along the central longitudinal axis of the upper well-confined minibasin, spot F is located at the thickest deposit of the first lower minibasin, and spot G is in the second lower minibasin (see the map showing these locations). Six stratigraphic groups are recognized (G1, G2, G3, G4, G5 and G6). For detailed explanations see text.

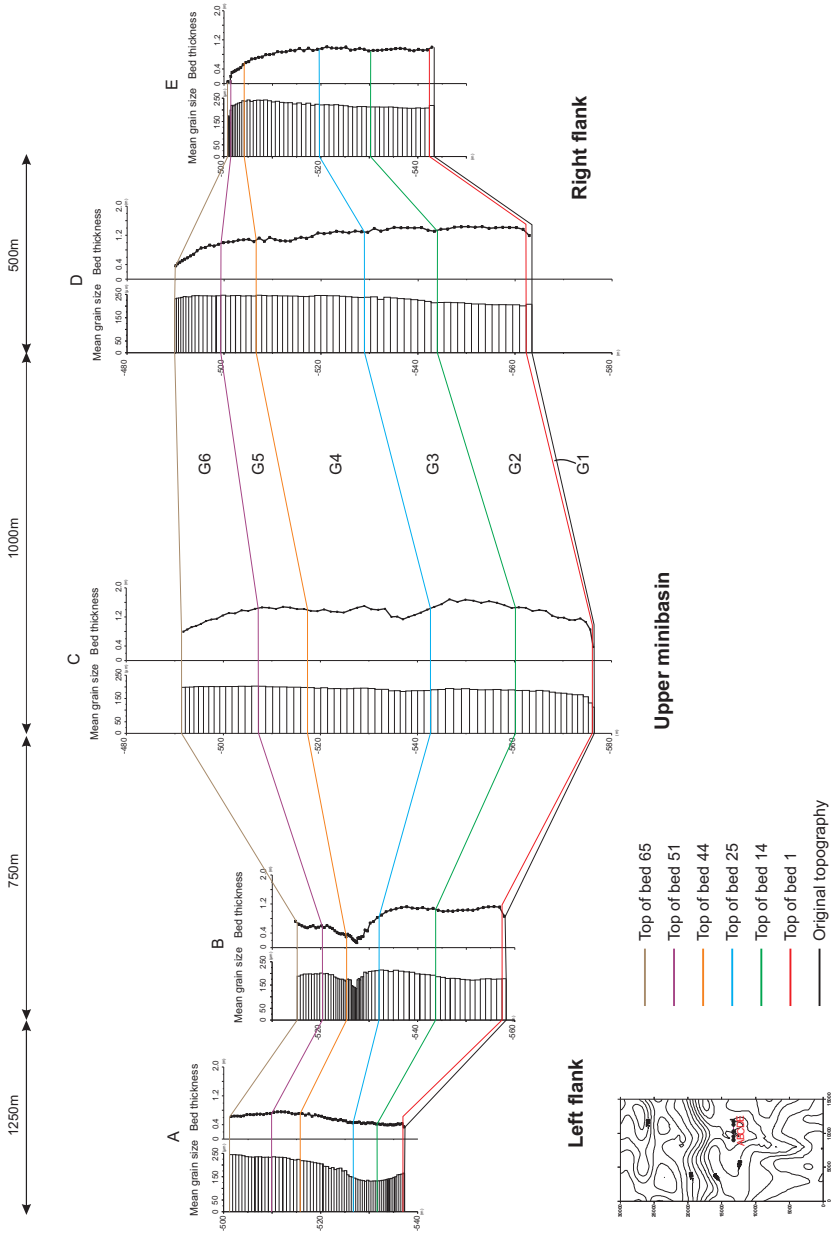


Figure 5.13: Cross-section showing the lateral isochronous correlation of the stratigraphy (supercritical non-equilibrium flows) in the upper minibasin. Five spots are selected to display their mean grain-size column and layer thickness profile. Spot A, B, C and D are along the central lateral axis of the upper well-confined minibasin (see the map showing these locations). Six stratigraphic groups are recognized (G1, G2, G3, G4, G5 and G6). For detailed explanations see text.

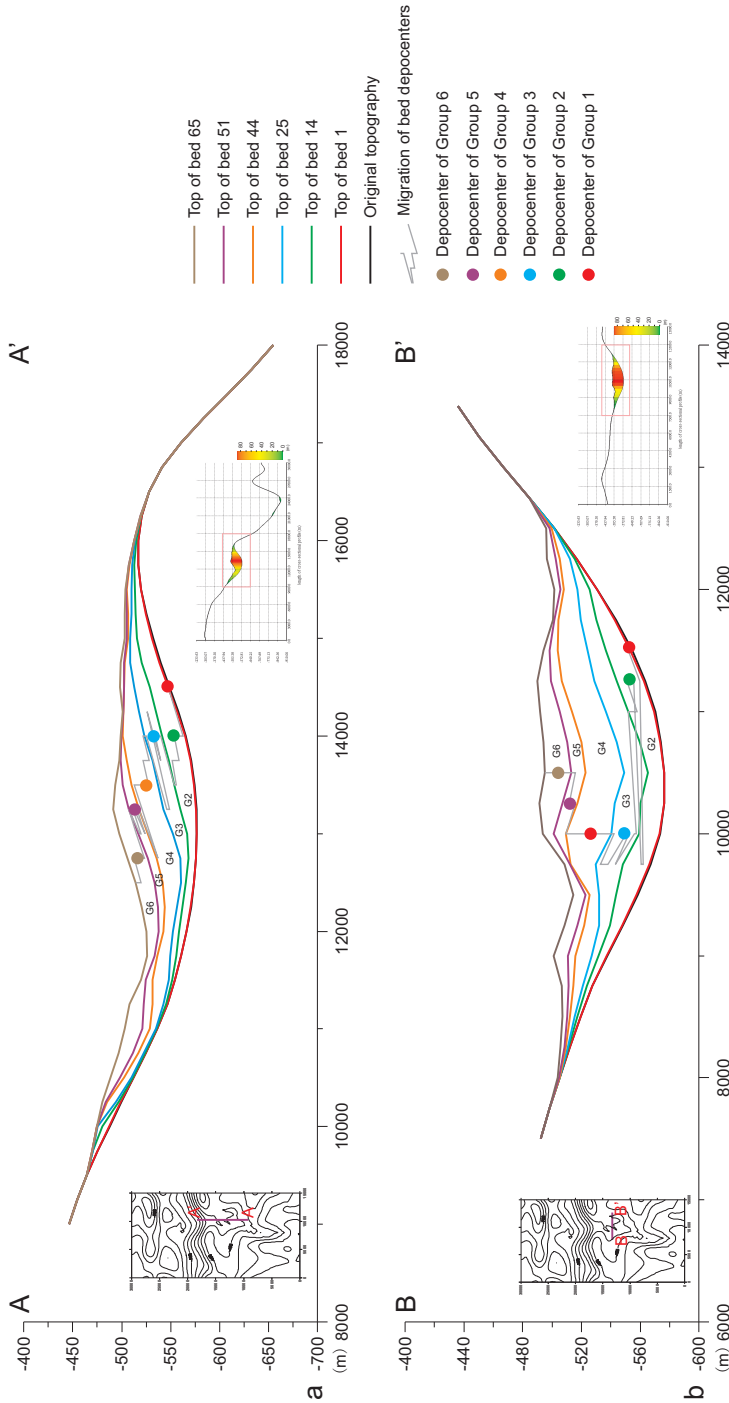


Figure 5.14: Longitudinal (a) and lateral (b) migrational trends of group depocenters (supercritical non-equilibrium inflows) in the upper minibasin. The colored dots indicate the spatial locations of the group depocenters in the cross section. Six stratigraphic groups are recognized (G1, G2, G3, G4, G5 and G6). For detailed explanations see text. The total deposit thickness of the sections is displayed in colored scale.

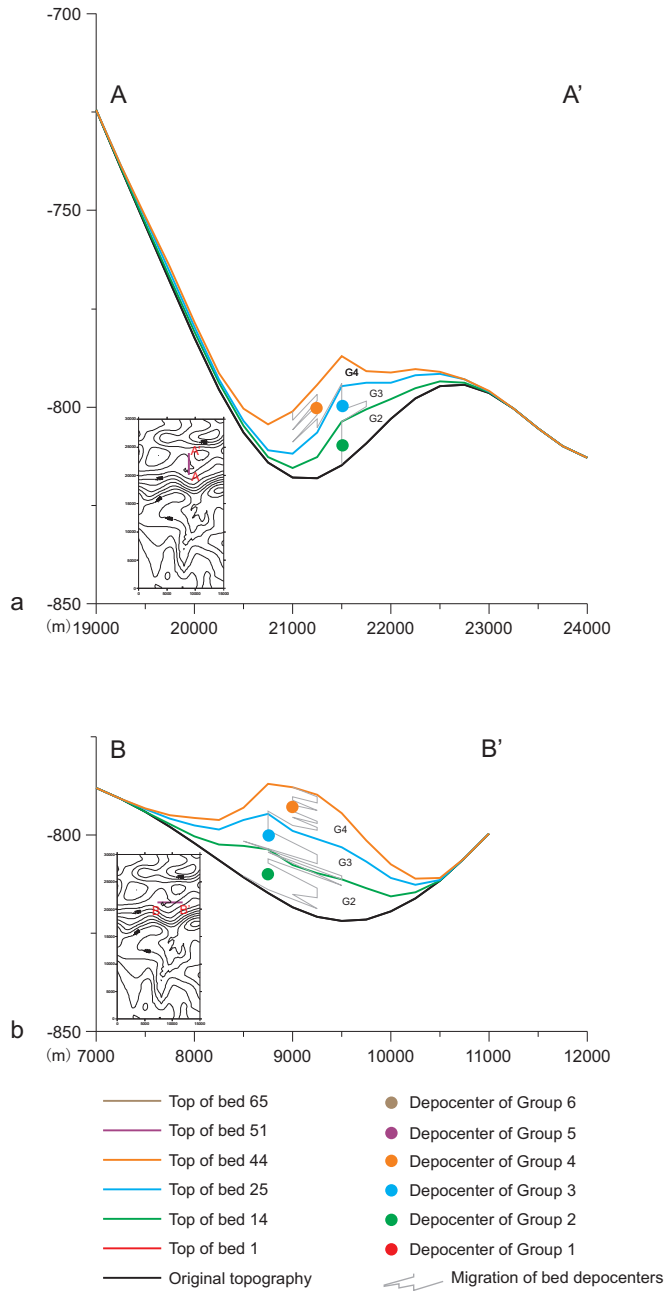


Figure 5.15: Longitudinal (a) and lateral (b) trends of group depocenter migration (supercritical non-equilibrium inflows) in the first lower minibasin. The colored dots indicate the spatial locations of group depocenters in the cross section. Six stratigraphic groups are recognized (G1, G2, G3, G4, G5 and G6). For detailed explanations see text.

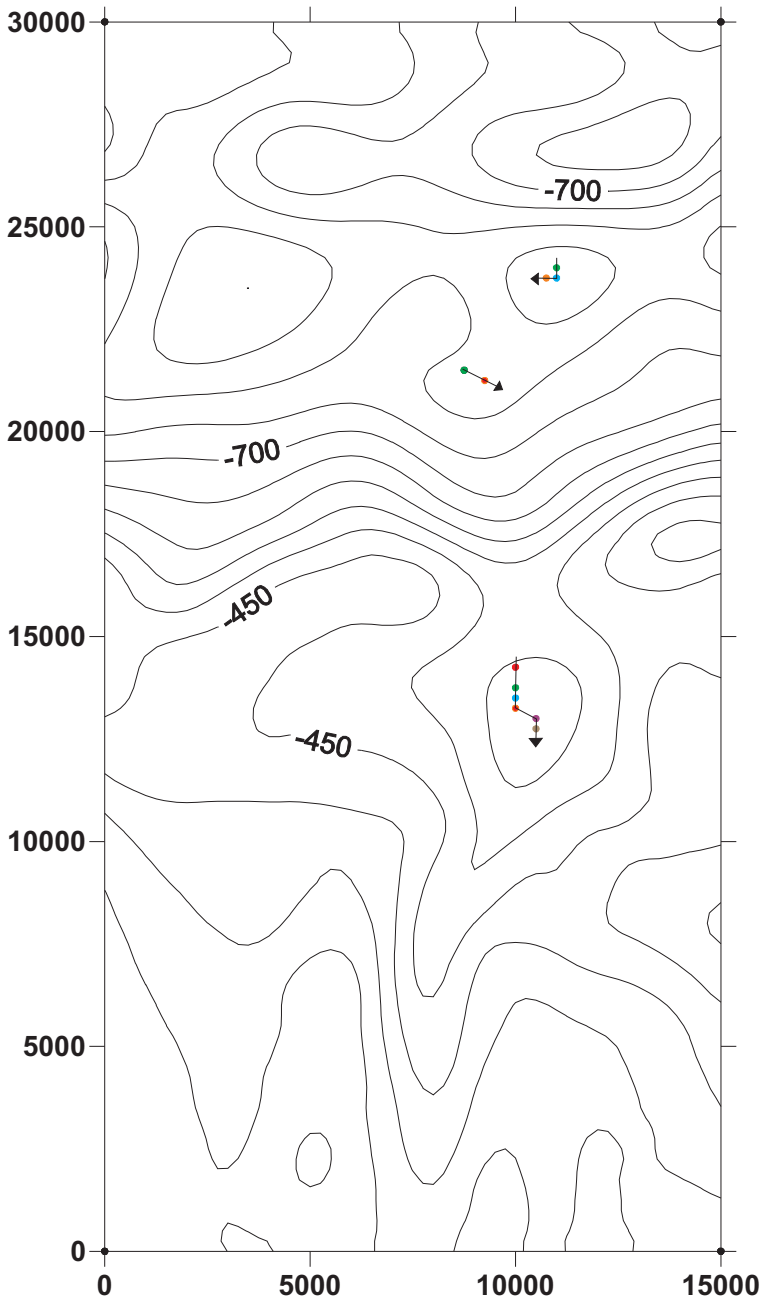


Figure 5.16: Plan view of the depocenter migrations in the three minibasins based on the spatial location of the maximum depositional thickness of each group (supercritical non-equilibrium inflows). The lines with arrows indicate the general shifting directions. The color of dots shows the six groups as in Fig. 5.14 to Fig. 5.15.

5.4 Supercritical equilibrium inflows

One set of constant parameters is used to simulate 100 turbidity current events with supercritical equilibrium inflows. The sediment volume is $5e+06 \text{ m}^3$, the initial flow velocity 5 m/s, the flow concentration 2%, the flow density 1059.46 kg/m^3 , the grain size with components of $250 \mu\text{m}$ (60%) and $100\mu\text{m}$ (40%), the flow depth 50 m, the drag coefficient 0.0136, and the densimetric Froude number 1.27. In the following, the results of the flow evolution, the depositional distribution and the internal architecture are analyzed.

5.4.1 Flow evolution

The results of the 100 successive flow events show that the pre-existing topography profoundly influences the flow pathways and flow behavior of the turbidity currents traversing it. The real-time variations of the hydrodynamic parameters of the flows (flow thickness, flow concentration and the densimetric Froude number) are used to illustrate the evolution of the flow characteristics. Here, four different stages are distinguished.

Full ponding stage (flow event 1)

In event 1, the surged turbidity current is fully confined within the upper minibasin without spill-over, although it reaches the top of the bounding slope (Fig. 5.17; Fig. 5.18). After about 3000s, the flow volume is completely released into the channel and starts to enter the upper minibasin with a maximum flow velocity of about 5 m/s (Fig. 5.17d). When reaching the upper minibasin center (Fig. 5.17g, h, i), the flow begins to expand across the whole basin. Meanwhile the velocity and energy of the flow head decreases but its height is largely increased due to the resistance of the downstream bounding slope and a concurrent hydraulic jump (Fig. 5.18a, b, c). Accordingly, the flow is divided into supercritical and subcritical zones (Fig. 5.18c, f, i). Later, the tail of the flow wanes (Fig. 5.18d, g). Flow deflection and reflection occur within the upper minibasin until the flow energy diminishes (Fig. 5.18).

Fill-and-spill stage (flow event 2-31)

At this stage, the turbidity currents are mostly confined within the upper minibasin but partially spill over the bounding ridge to flow downslope into the distal and smaller mini-basins (Fig. 5.19). Taking flow event 25 as an example, the flow is seen to expand in the upper minibasin (Fig. 5.19a, b, c) and the major part of the flow is confined within this basin. Part of the turbidity current, however, is capable of surmounting the lowest point of the bounding ridge, becoming supercritical along the lee slope before flowing into the two smaller minibasins down-dip (Fig. 5.19d, e, f). After the sediment has settled down in all three minibasins the flow energy is completely dissipated (Fig. 5.19g, h, i).

Transitional stage (flow event 32-40)

This stage is characterized by alternating spill-over and minibasin confinement. Spill-over only happens in flow events 34, 36, 37 and 40 while in the remaining flows confinement prevails. This stage is therefore transitional between the previous and the subsequent stage.

Trapping stage (flow event 41-100)

For the remaining flow events the turbidity currents are not able to spill over and remain trapped in the first minibasin. Figure 5.20 shows that flow event 45 flow has a similar evolutionary process as event 1 but with a more complex flow energy distribution within the upper minibasin caused by internal bars, similar to the non-equilibrium flows discussed above.

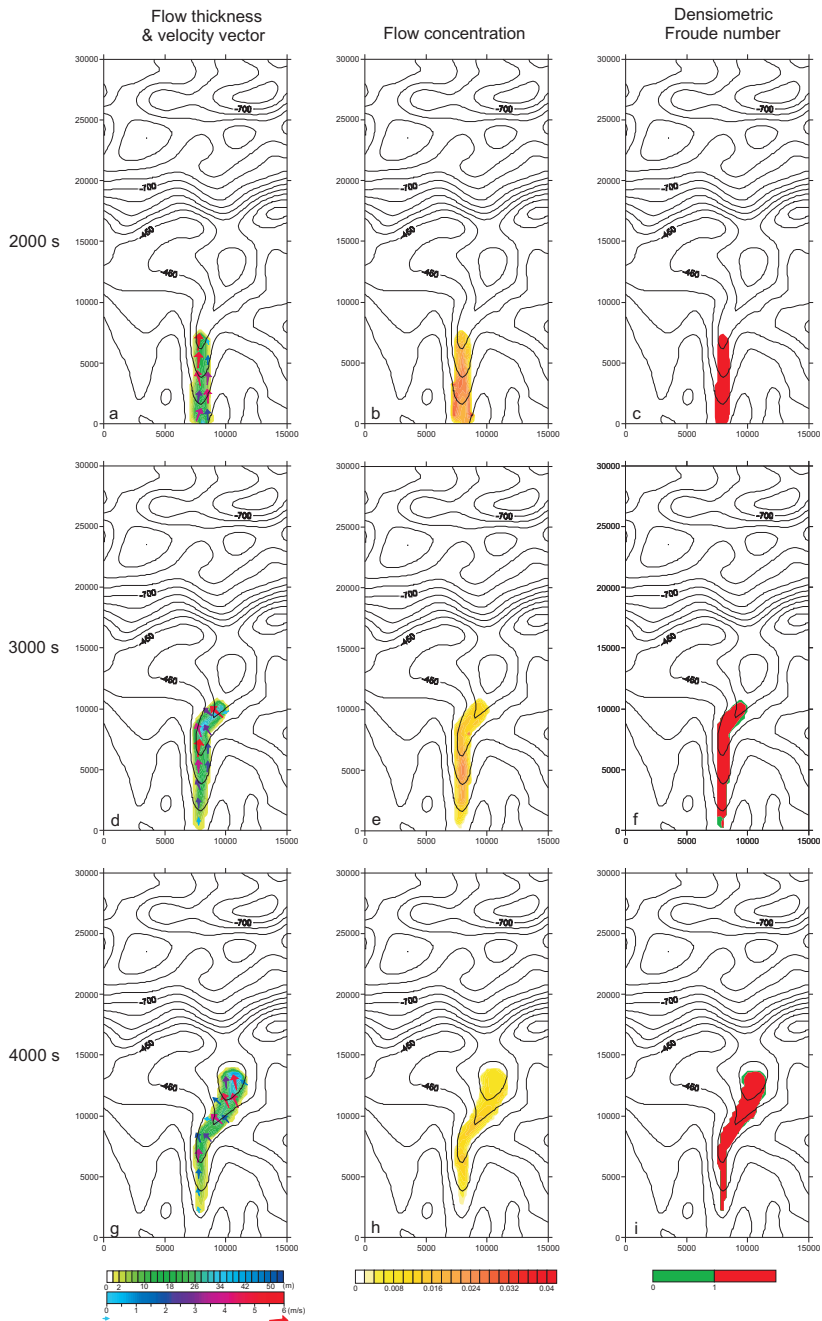


Figure 5.17: Flow evolution of event 1 (at 2000s, 3000s and 4000s) of supercritical equilibrium inflows is displayed as maps of flow thickness, velocity vectors, concentration and the densimetric Froude number. All maps are superposed on the elevation contour maps of the original bathymetry.

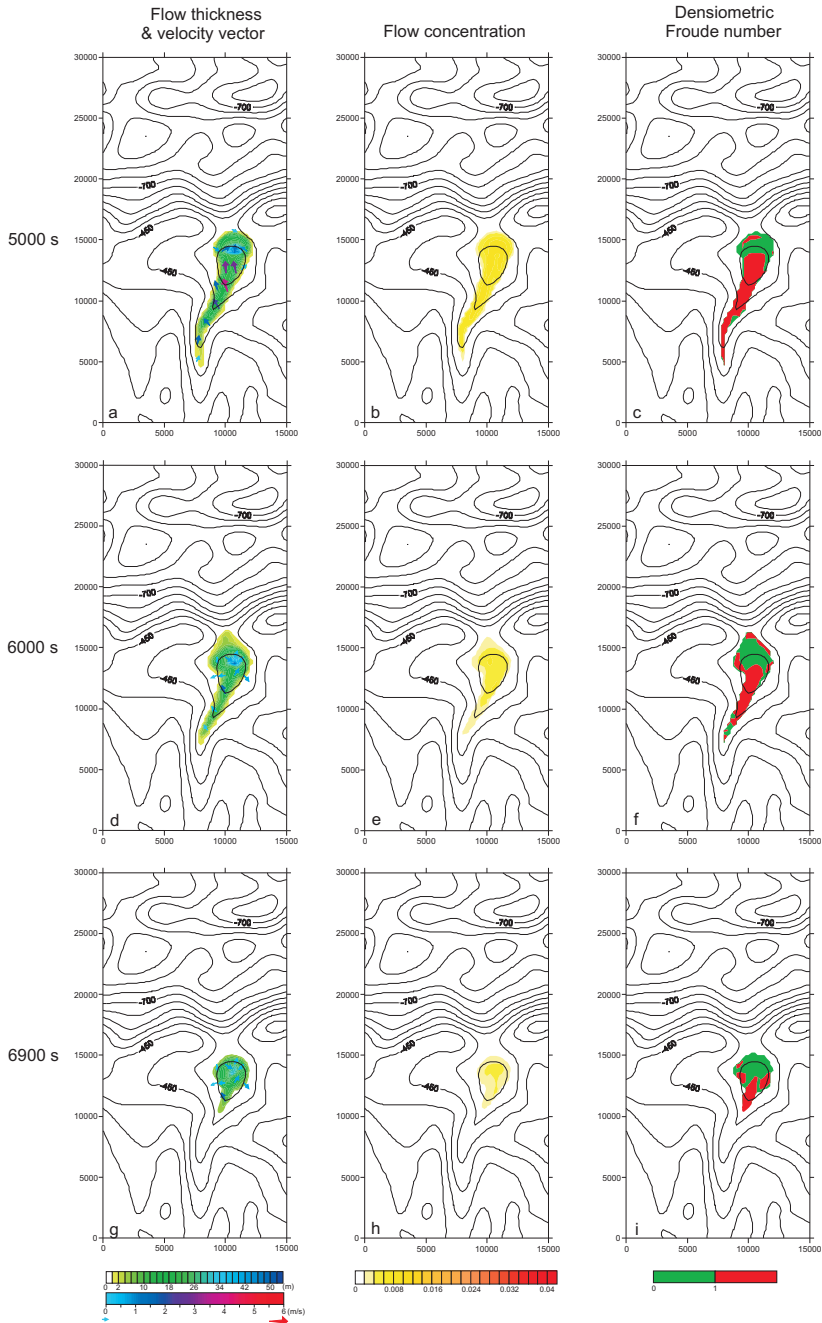


Figure 5.18: Flow evolution of event 1 (at 5000s, 6000s and 6900s) of supercritical equilibrium inflows is displayed as maps of flow thickness, velocity vectors, concentration and the densiometric Froude number. All maps are superposed on the elevation contour maps of the original bathymetry.

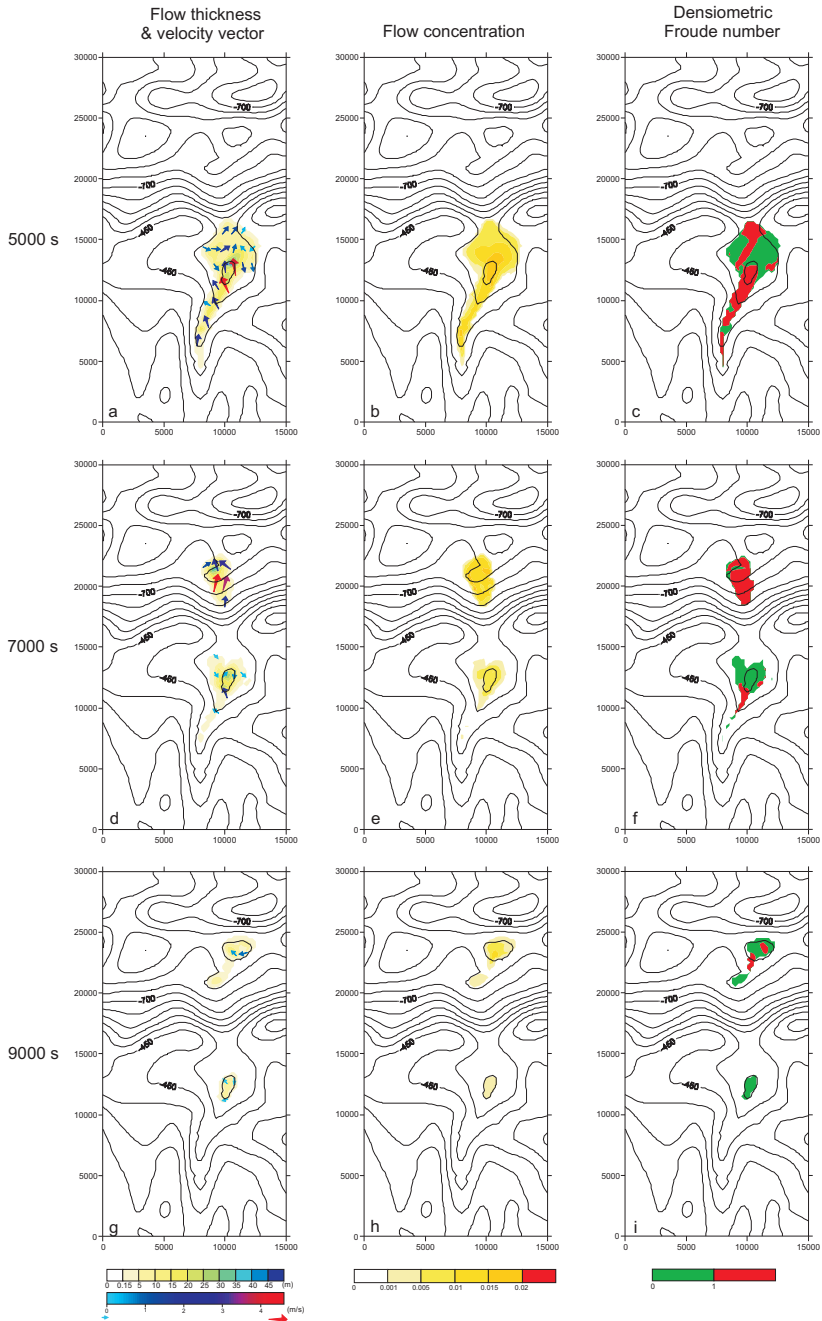


Figure 5.19: Flow evolution of event 25 (at 5000s, 7000s and 9000s) of supercritical equilibrium inflows is displayed as maps of flow thickness, velocity vectors, concentration and the densimetric Froude number. All maps are superposed on the elevation contour map of the bathymetry formed after event 24.

Numerical Modelling of Turbidity Currents and Depositional Stratigraphy in Slope Minibasins

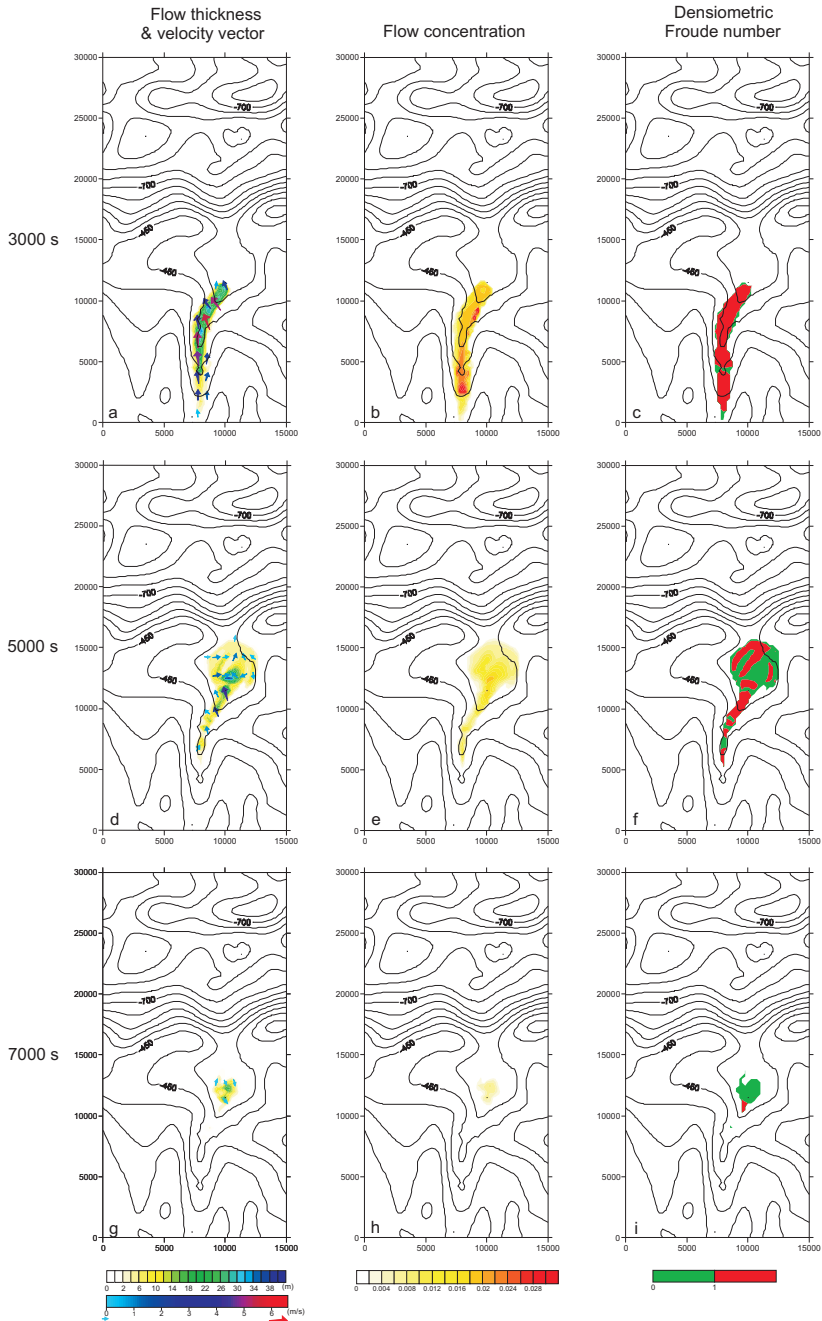


Figure 5.20: Flow evolution of event 45 (at 3000s, 5000s and 7000s) of supercritical equilibrium inflows is displayed as maps of flow thickness, velocity vectors, concentration and the densimetric Froude number. All maps are superposed on the elevation contour map of the bathymetry formed after event 44.

5.4.2 Flow-deposit interaction

The resulting turbidites from the numerical simulation form a dynamic bathymetry that influences subsequent flow behavior. Here we describe the interaction between bathymetry, flow and deposits in terms of the distribution of thickness and grain size, as well as the significant bathymetric changes during the three stages (ponding, fill-and-spill and trapping).

Deposit and mean grain size

The depositional thickness map of bed 1 (Fig. 5.21a) indicates two sites of significant deposition. One is the inflow entry where a levee-shaped deposit is formed with a maximum thickness of about 1.80 m. The other one is on the counterslope of the upper minibasin with a maximum thickness of about 1 m. Both locations also have the coarsest mean grain size (Fig. 5.21b).

The beds formed at the fill-and-spill stage are distributed over three minibasins. The thickest sediment is located in the upper well-confined minibasin. Erosion occurs on the lee-side of the bounding ridge (blue in Fig. 5.21). In the early phase of this stage, merely finer grains are transported to the distal minibasins by the spillover flows (Fig. 5.21c, d). Afterwards, the flows carry increasingly coarser grains over the bounding ridges to the lower minibasins, accompanied by stronger erosion on the downstream slope of the ridge (Fig. 5.21e, f, g, h). Coarser grains can be found on the counterslopes of three minibasins and the lee-side of the bounding ridge.

At the transitional stage, the spill-over becomes less frequent. Moreover, the sediment volume and the grain size of the spilling flows gradually decrease (Fig. 5.21i, j). The maximum total thickness of the beds from 2 to 40 (the fill-and-spill and transitional stages) is about 70 m (Fig. 5.22a).

At the trapping stage, no deposition takes place in the distal minibasins. The total thickness map of the beds from 41 to 100 shows that significant deposition happens in the channel and the original minibasin center (Fig. 5.22b). The depositional area in the upper minibasin is constantly shrinking (Fig. 5.21k, m, o). The depocenter of the individual bed in the remaining space of the upper minibasin is still located on its corresponding topographic counterslope (Fig. 5.21k, m). Coarser sediments are deposited in the channel by the flows on their way to the upper minibasin (Fig. 5.21l, n, p) and some minor erosion can be found on the lee sides of the depositional bars in the channel (Fig. 5.21k, m, o). In the last event, only sediments with fine-to-medium mean grain sizes are dominant in the decreasing accommodation of the upper minibasin due to the increasingly significant deposition of coarser grains in the channel (Fig. 5.21p).

The thickness distribution of the entire 100-bed sequence is displayed in Figure 5.22c. The depocenter of the total deposit is exactly in the original minibasin center with a maximum thickness of about 90 m.

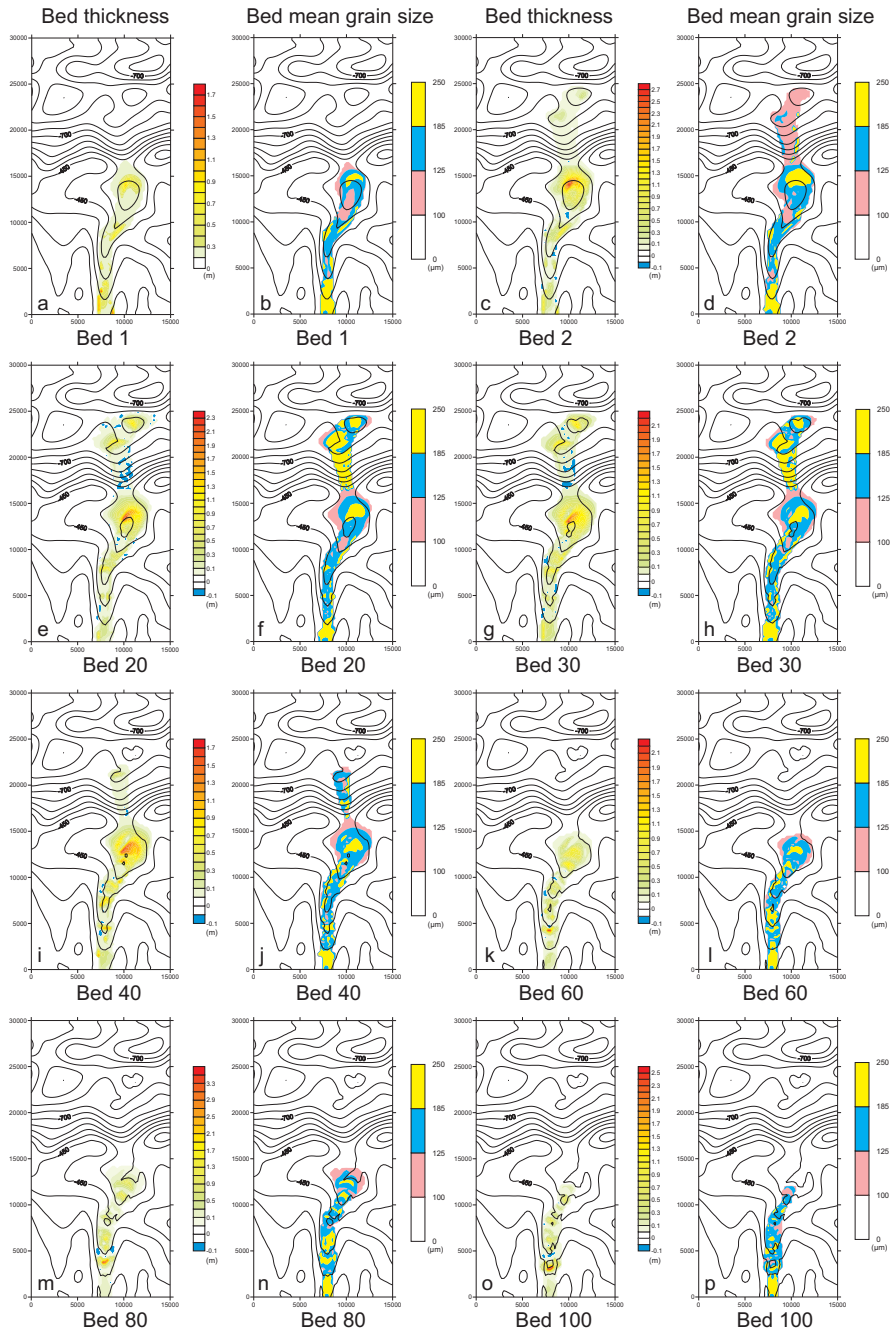


Figure 5.21: Maps showing the depositional and erosional thicknesses and the grain-size distribution of the individual beds formed by flow events 1, 2, 20, 30, 40, 60, 80 and 100 (supercritical equilibrium inflows). Each map is superposed on the pre-existing bathymetric map.

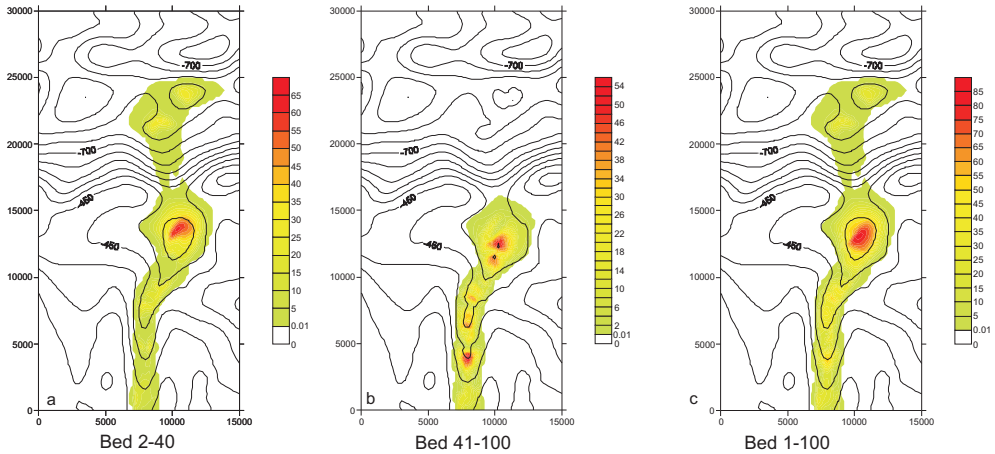


Figure 5.22: Maps showing the depositional thickness of the beds formed by events 2-40 (a), events 41-100 (b) and events 1-100 (c) (supercritical equilibrium inflows).

Bathymetric changes

The depositional relief developed by the 100 beds influence the flows and their deposits. The evolution of the bathymetry is displayed in Figure 5.23.

During the fill-and-spill stage, depositional ridges develop around the counterslope of the upper minibasin (Fig. 5.23a). At the trapping stage, more depositional ridges form and divide the limited accommodation space into small segments. Similarly, the depositional bars in the channel became more pronounced (Fig. 5.23b, c).

This evolution can also be observed in the longitudinal cross-sections. Figure 5.23d displays two small local depositional depressions formed on the final topography after event 100. In this cross-section one can also notice that the basin accommodation has decreased through time. Moreover, the “spill point” and the lowest point of the topographies have both shifted continuously upstream.

Further, we determined the gradient of the counterslope of the upper minibasin in step of 10 events. A general trend of the gradient change is obtained (Fig. 5.23e) and shows that it first decreased in the first 40 events, then greatly increased from event 41 to event 50, and gradually decreased again. Comparing the flow evolution with the slope gradient changes, there is a certain corresponding relationship between them: The fill-and-spill and transitional stages *versus* the first gradient decrease, and the beginning of trapping stage *versus* the abrupt gradient increase.

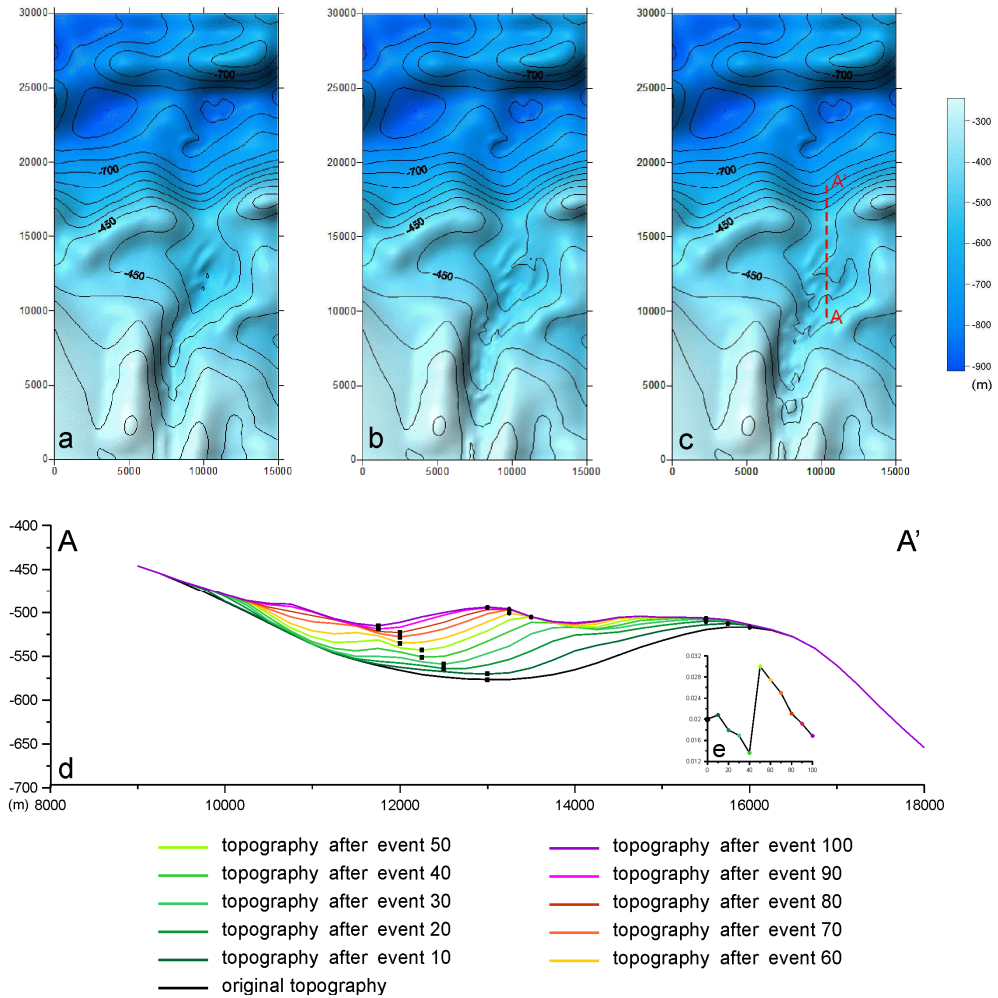


Figure 5.23: Maps showing the topographical changes after events 40 (a), 70 (b) and 100 (c) (supercritical equilibrium inflows). The topographic changes are shown in longitudinal cross-section profiles of the upper minibasin (d). The locations of the sections are indicated in the plan maps by red dashed lines. The black round dots indicate the locations of the potential “spill point” of the upper minibasin. The black block dots show the location of the lowest points in the sections – not to be confused with the depocenter. The variation of the counterslope gradient (from the lowest point to the “spill-over point”) is illustrated in (e).

5.4.3 Depositional architecture

Based on the flow pathways and the spatial trends of the bed depocenters and mean grain size, six groups of bed sequences are distinguished.

Group 1 (G1)

Group 1 consists of bed 1 which is confined to the upper minibasin in which about 50% of the sediment is deposited (Fig. 5.24). Both longitudinal (parallel to the stream direction) (Fig. 5.25a) and lateral (perpendicular to the stream direction) (Fig. 5.25b) cross-sections show that the depocenter of this group is on the counterslope (Fig. 5.25).

Group 2 (G2)

Group 2 is composed of the beds formed by events 2 to 20. More than 50% of the sediment volume is ponded in the upper minibasin, while nearly 10% of the sediment is transported to the two lower minibasins (Fig. 5.24). The depocenters of Group 2 in both the upper minibasin and the first lower minibasin are on the counterslopes of their corresponding previous topography in the longitudinal cross section (Fig. 5.25a; Fig. 5.26a) and on the basin flank in the lateral cross section (Fig. 5.25b; Fig. 5.26b).

Group 3 (G3)

Group 3 is distinguished by the recognition of a new sequence (beds 21 to 31) in the first lower minibasin. More than 10% of the total sediment volume is deposited in the down-dip minibasins. The depocenter of Group 3 in the upper minibasin longitudinally remains on the counterslope of the topography formed after event 20 (Fig. 5.25a), while it laterally shifts closer to the original minibasin center (Fig. 5.25b). This results in a newly-formed depositional topography whose lowest point and counterslope were shifted in the upstream direction. The depocenter in the first lower minibasin exhibits a similar trend (Fig. 5.26).

Group 4 (G4)

Beds 32 to 40 comprise this group in which the flow evolution is at a transitional stage. The volume of sediment transported to the lower minibasins is considerably decreased (Fig. 5.24). The group depocenter in the upper minibasin migrates towards the original minibasin center, however it is still on the counterslope of the topography developed after event 31 (Fig. 5.25a). The lateral cross-section shows that it moves slightly to the basin flank (Fig. 5.25b). Due to the imbalance of the depositional rates on the previous relief, local depositional depressions are forming (Fig. 5.25b). The depocenter of Group 4 in the first lower minibasin moves vertically upwards but is still located on the counterslope/flank of the basin (Fig. 5.26).

Group 5 (G5)

This group is composed of the beds deposited from event 41 to event 70. Because the flow is now trapped in the upper minibasin again, there is no sediment in the down-dip minibasins. The depocenter of Group 5 continues to migrate longitudinally towards in the upstream direction and laterally towards the original basin center (Fig. 5.25).

Group 6 (G6)

The remaining beds (from bed 71 to 100) constitute Group 6. The sedimentation in the channel becomes stronger (see also Fig. 5.22b), as some form of backfilling process, which results in a decreasing sediment volume in the upper minibasin (Fig. 5.24). The group depocenter longitudinally moves further upstream (Fig. 5.25a) and laterally towards the newly formed local depression (Fig. 5.25b).

In summary, the most significant deposition occurs on the counterslope of the bounding slopes. The thickest deposits in the upper minibasin have the coarsest mean grain size. The depositional relief and slope gradient greatly change in the entire evolution, which results in the depocenter migrating upstream (Fig. 5.27) in a backfilling pattern within the minibasin.

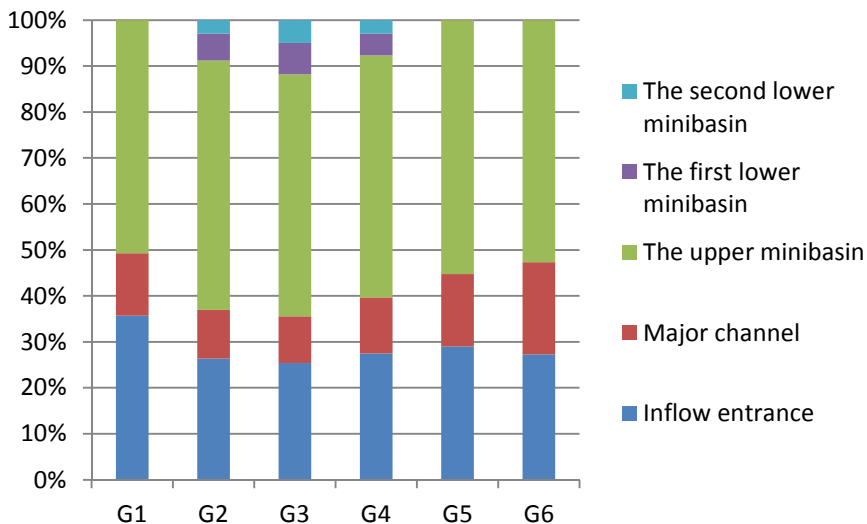


Figure 5.24: Proportion of the sediment volume (supercritical equilibrium inflows) in the five different areas for the six groups. The division of the five zones is shown in Fig. 5.11a.

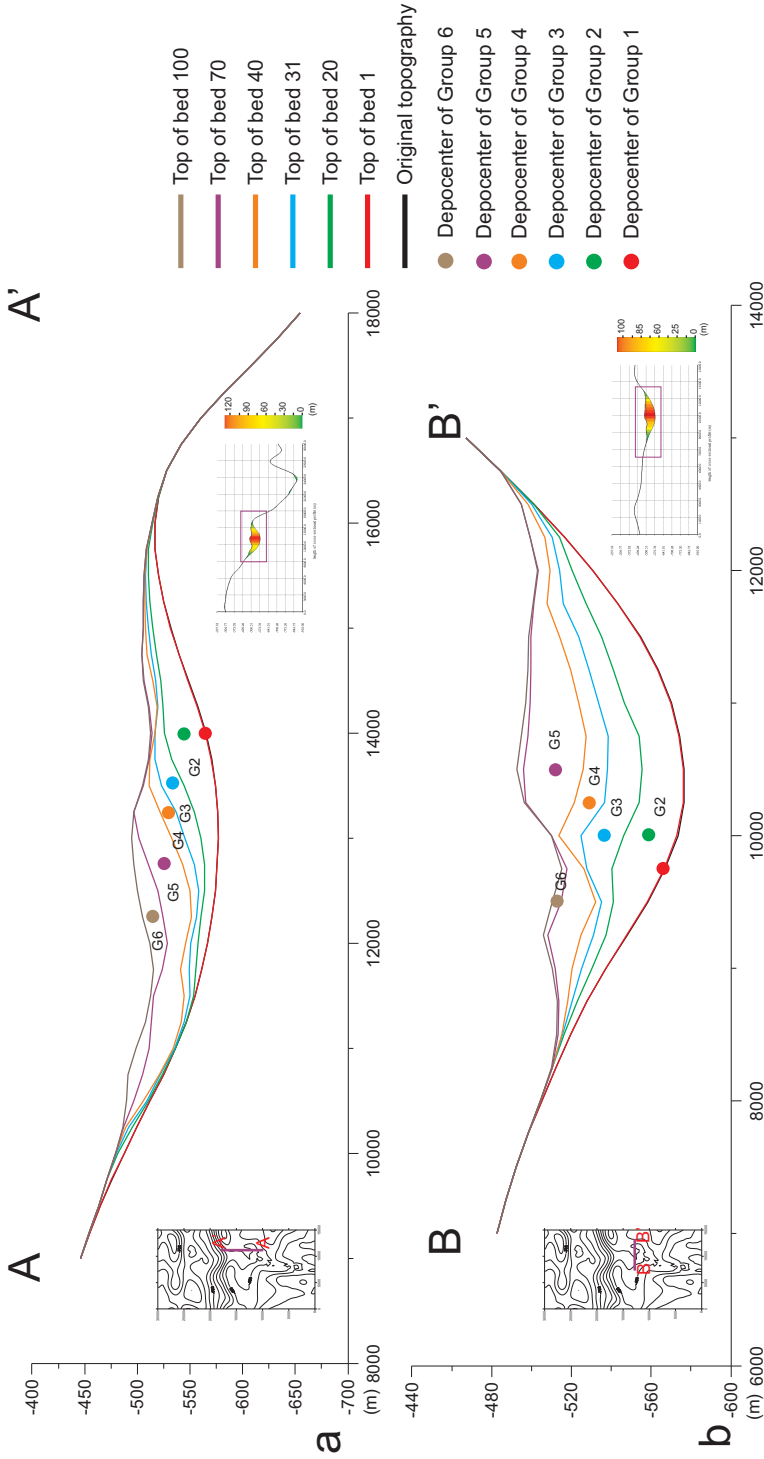


Figure 5.25: Longitudinal (a) and lateral (b) trends of group depocenter migration (supercritical equilibrium inflows) in the upper minibasin. The colored dots indicate the spatial locations of the group depocenters in the cross section. Six stratigraphic groups are recognized (G1, G2, G3, G4, G5 and G6). For detailed explanations see text. The total deposit thickness of the sections is displayed in colored scale.

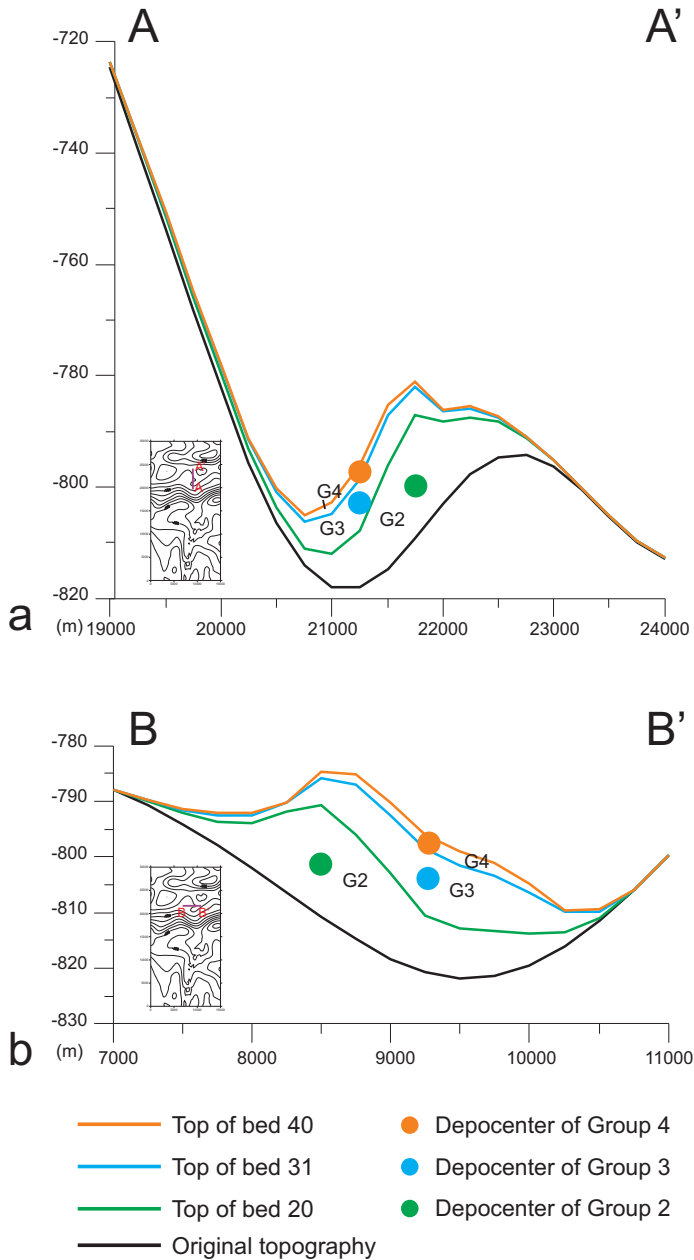


Figure 5.26: Longitudinal (a) and lateral (b) trends of group depocenter migration (supercritical equilibrium inflows) in the first lower minibasin. The colored dots indicate the spatial locations of group depocenters in the cross section. Six stratigraphic groups are recognized (G1, G2, G3, G4, G5 and G6). For detailed explanations see text.

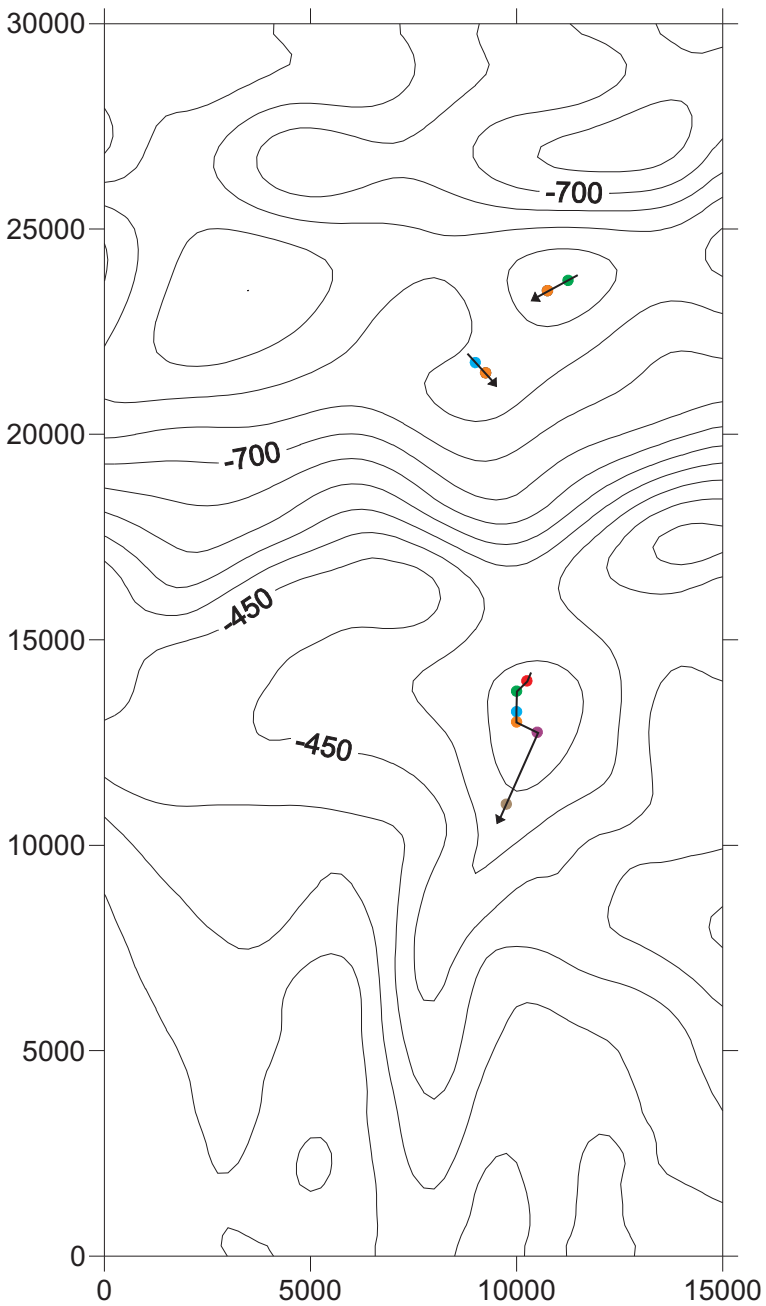


Figure 5.27: Plan view of the depocenter migrations in the three minibasins based on the spatial location of the maximum depositional thickness of each group (supercritical equilibrium inflows). The lines with arrows indicate the general shifting directions. The color of dots shows the six groups as in Fig. 5.25 to Fig. 5.26.

5.5 Subcritical equilibrium inflows

One group of three sets of subcritical equilibrium inflows with the same flow velocity of 3 m/s and an inflow flux of 0.7 m²/s but at different flow concentrations (1%, 2% and 3%) and flow heights (79.18m, 39.59m and 26.39m) are simulated, each by two events (Tab. 5.1), and subsequently their flow behavior and resulting deposit are compared. A second group of three sets of parameters are then performed with a similar strategy, but with a smaller sediment volume, flow velocity and finer grains (Tab. 5.1). All flows have a subcritical densimetric Froude number of 0.86 at the inflow point. Also here, the resulting deposit distributions are compared..

5.5.1 Flow evolution

The first group of equilibrium subcritical inflows can serve as an example to describe the major differences in the evolution of the flows as a function of the different concentrations and flow heights. These two parameters are inversely proportional in order to keep the densimetric Froude number the same. Although the inflows are all subcritical in the channel, the flows evolve rapidly into supercritical conditions but become subcritical in various parts of the minibasins (Fig. 5.30).

In general, the inflows with lower concentrations and higher flow heights are more likely to spill over the bounding ridge of the minibasin and expand into the wider downslope area. The inflows with a concentration of 3% are fully confined within the upper minibasin without any spill-over and with a shorter flow life. The velocities of the three flows entering the minibasin are almost the same (about 5m/s). However, the inflow with a concentration of 1% has a higher flow height when encountering the bounding slope than the other two scenarios (Fig. 5.28) and a larger flow volume spills over into the next minibasin. The inflow with highest concentration tends to maintain the high concentration for a longer time (Fig. 5.29) but stays confined to the upper minibasin.

5.5.2 Deposit

The distribution of deposit thickness of the two groups indicates the major differences in deposit geometry at the entry point. The inflows with the concentration of 1% and 2% have levee-like margins in the vicinity of the entry point into the channel (Fig. 5.31a, b; Fig. 5.33a, b). But their specific locations are different: The rim of the flow of 1% is farther from the entry point than that in the flow of 2%. The inflows with a concentration of 3% have significant deposition at their entry points (Fig. 5.31c; Fig. 5.33c). For the sediment deposited within the upper minibasin, the depocenters in all scenarios are on the counterslopes of their bounding slopes (Fig. 5.31; Fig. 5.33).

In the first group the coarser grains (125 µm to 250 µm) are mainly confined to the channel and the upper minibasin, while the finer grains (100 µm to 125 µm) can be transported over the ridge downslope (Fig. 5.32). In the second group, due to the

constituent grains having much smaller sizes than the first group, different trends of the grain size distribution are found. For the inflow with a 1% concentration, the (relatively) coarser grains with a mean grain size between 80 μm and 90 μm can be carried to distal areas. With an increase of the inflow concentration, more coarser grains are confined within the upper minibasin and hence the mean grain size of the sediment transported by the spill-over flows decreases (Fig. 5.34).

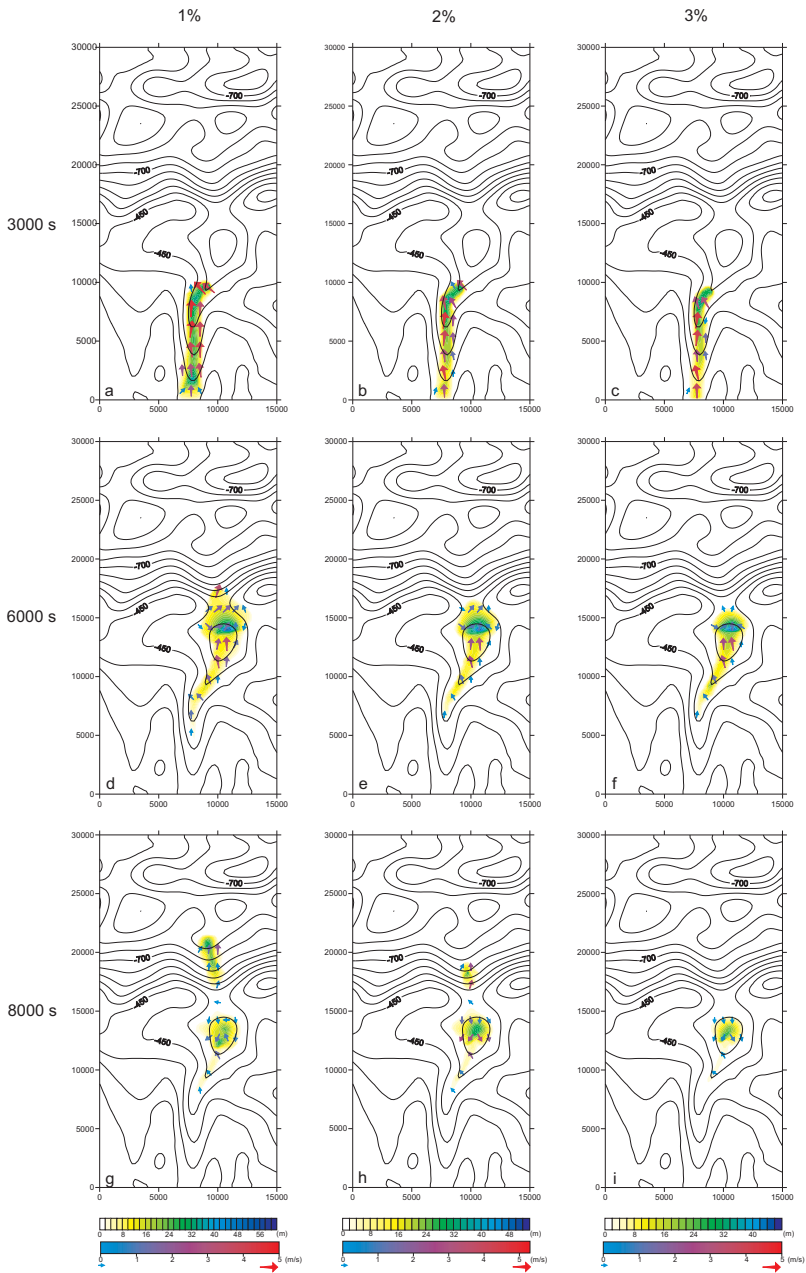


Figure 5.28: Flow thickness evolution of event 2 (at 3000s, 6000s and 8000s) of the first group of subcritical equilibrium inflows (1%, 2% and 3%) together with the flow vectors. All maps are superposed onto the original bathymetric contour map.

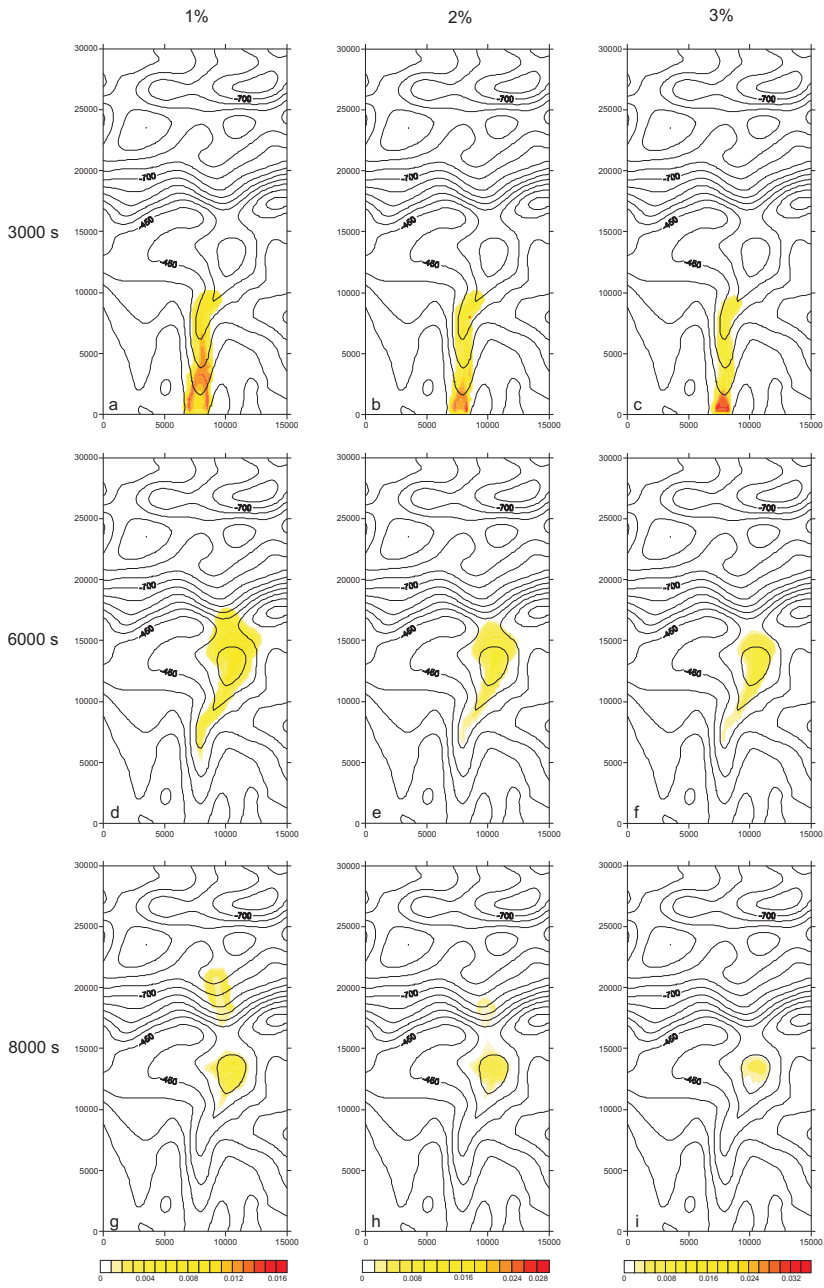


Figure 5.29: Flow concentration evolution of event 2 (at 3000s, 6000s and 8000s) of the first group of subcritical equilibrium inflows (1%, 2% and 3%). All maps are superposed onto the elevation contour map of the original topography. Notice the differences in scale of the concentrations.

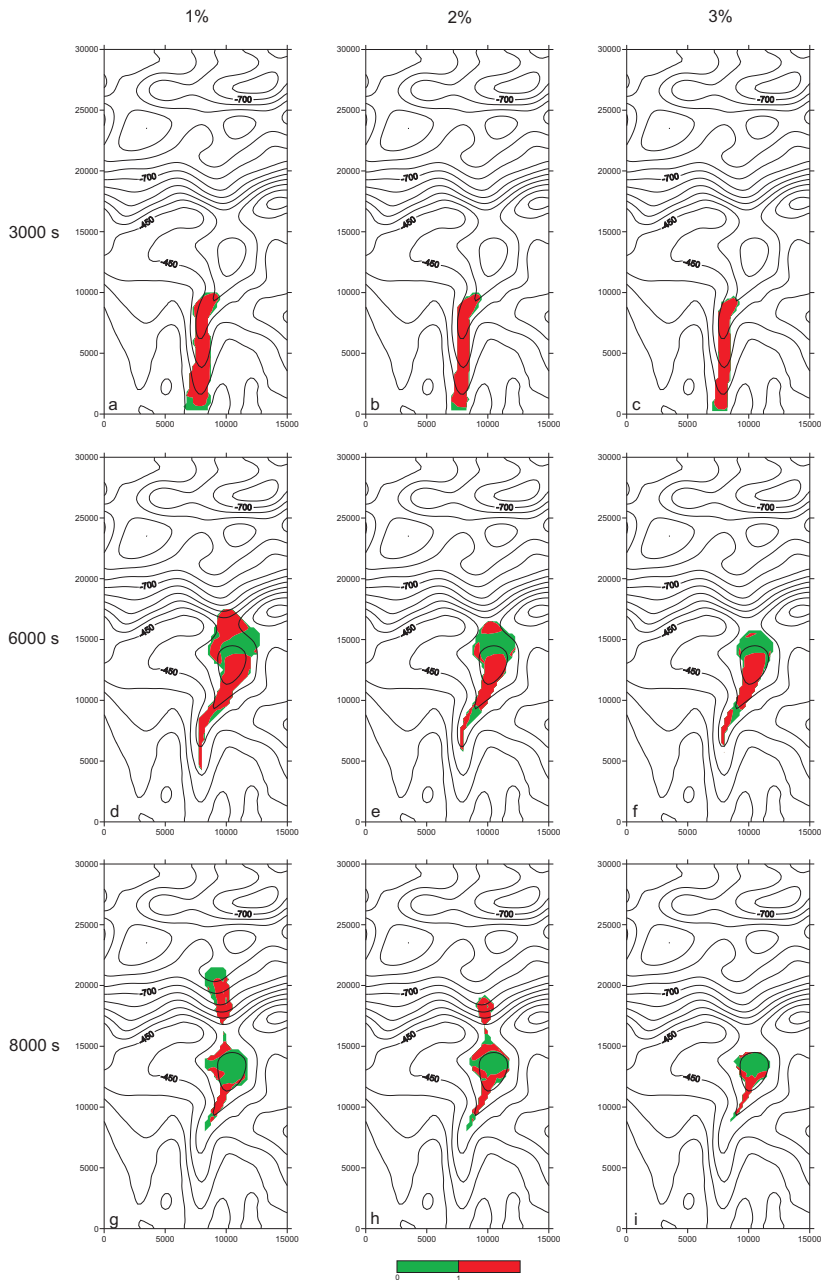


Figure 5.30: Densimetric Froude number evolution of event 2 (at 3000s, 6000s and 8000s) of the first group of subcritical equilibrium inflows (1%, 2% and 3%). All maps are superposed onto the elevation contour map of the original topography.

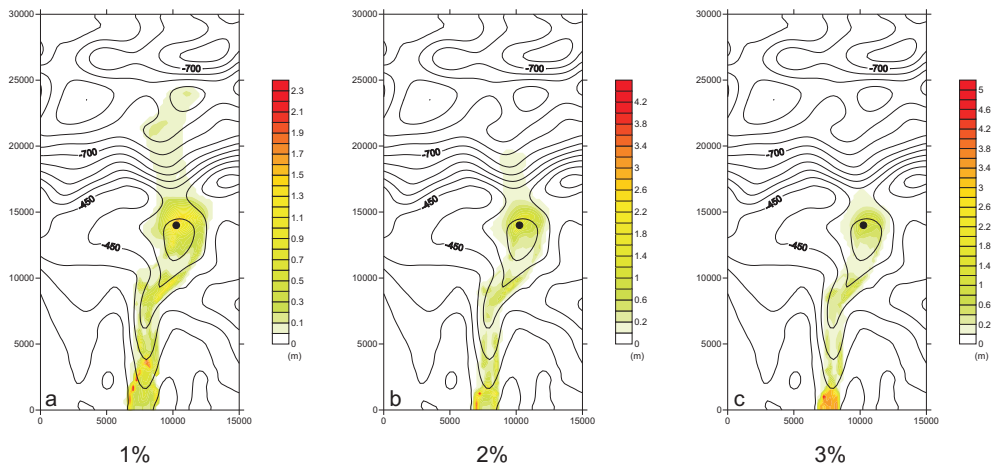


Figure 5.31: Maps of the total deposit thickness after event 2 (the first group of subcritical equilibrium inflows). The black dots indicate the depocenter in the upper minibusin with the respective maximum thickness of 1.84 m at 1% (a), 1.83 m at 2% (b) and 1.55 m at 3% (c) initial concentration.

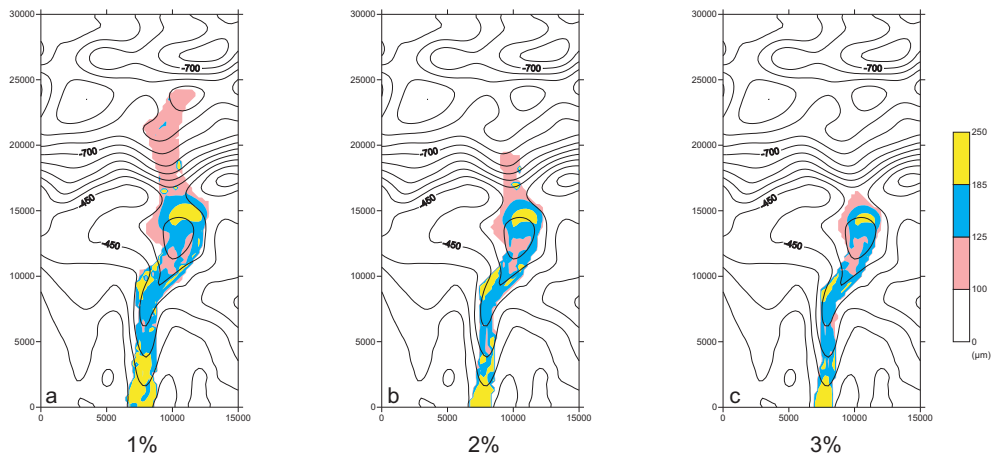


Figure 5.32: Maps of the mean grain sizes of bed 2 (the first group of subcritical equilibrium inflows).

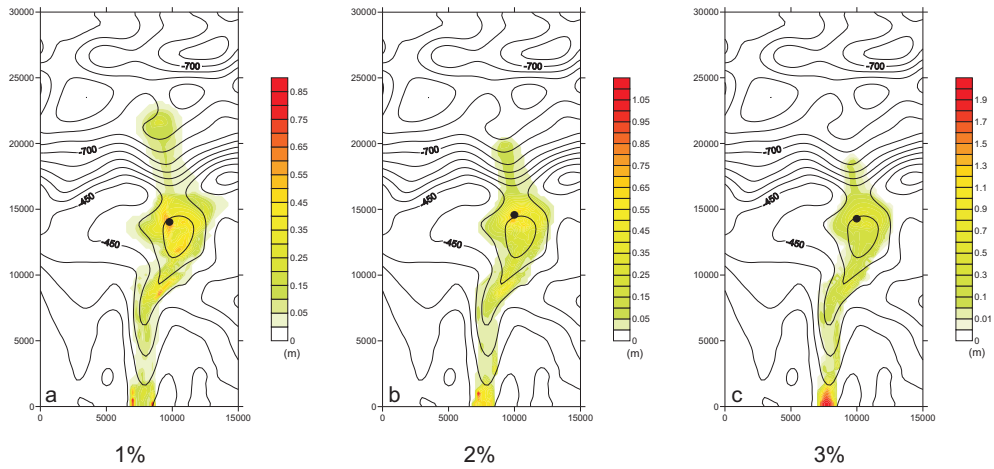


Figure 5.33: Maps of total deposit thickness after event 2 (the second group of subcritical equilibrium inflows). The black dots indicate the depocenter in the upper minibasin with the respective maximum thickness of 0.60 m at 1% (a), 0.70 m at 2% (b) and 0.66 m at 3% (c) initial concentration.

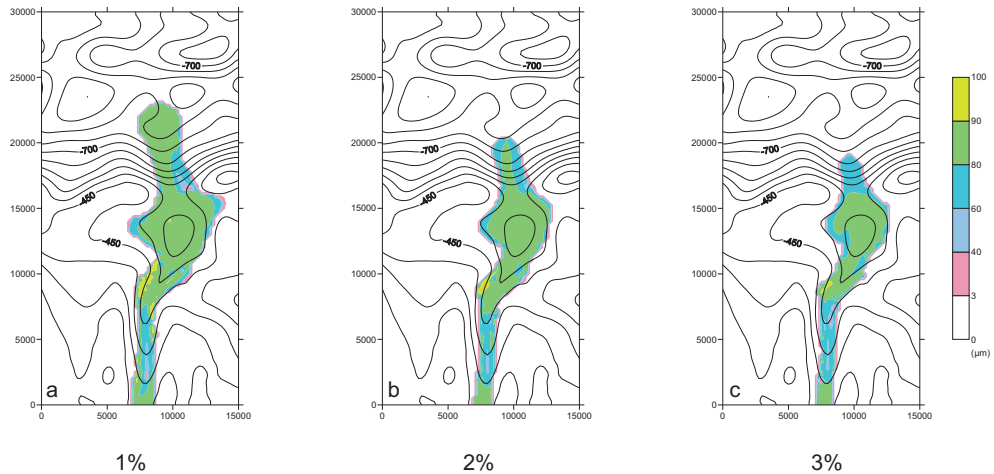


Figure 5.34: Maps of the distribution of the mean grain sizes of bed 2 (the second group of subcritical equilibrium inflows).

5.6 Discussion

5.6.1 Comparison of experimental results

The experimental results of the flows simulated with different parameter settings exhibit some similarities and some differences in their flow behaviors, flow pathways, flow-deposit interactions and internal stacking patterns.

Boundary conditions

Regardless of whether there is supercritical or subcritical inflow, after being released into the feeder channel all flows evolve into supercritical condition as they are funneled down into the upper minibasin (Fig. 5.30). Nevertheless, inflows with different concentrations produce diverse depositional geometries at the inflow area. Both supercritical non-equilibrium (4% concentration) and subcritical equilibrium inflows (3%) accumulate a lobe-like geometry of the deposit at the entry point (Fig. 5.8a; Fig. 5.31c; Fig. 5.33c), while the less dense inflows (1% and 2%) produce levee-like rims at the entry area (Fig. 5.21a; Fig. 5.31a, b; Fig. 5.33a, b). The rims formed by 1%-concentration inflows are located farther from the entry point than those formed by the 2%-concentration inflows. In two sets of experiments of successive flows (65 flow events and 100 flow events), about 30% volume of the sediment is deposited at the entry area (Fig. 5.11; Fig. 5.24).

While the flows travel in the channel, they invariably discharge some amount of sediment within the channel. Several depositional bars are formed in most parts of the channel, and with increasing numbers of flows these bars become more and more pronounced (Fig. 5.9; Fig. 5.22). In the later trapping stage, up to 20% volume of sediment is found to settle there (Fig. 5.11; Fig. 5.24).

Hydraulic jump

The flows entering the upper minibasin initially expand laterally and when they reach the counterslope, the ponding of flows upstream of the bounding slope results in flow head thickening and deceleration on the counterslope. Meanwhile the flow energy in the minibasin center remains high due to the continued high-velocity incoming flow. The flow is mostly supercritical and becomes partly subcritical in the minibasin, i.e. forming a hydraulic jump related to the topographic changes (e.g., Komar, 1971; Kneller and Branney 1995; Lamb et al., 2004). The counterslope ridge can cause deflection of the flow from the counterslope sideways, with flow velocity decreasing. Therefore the bulk of the coarser grains are first deposited on the counterslope and the sides of the upper minibasin as the flow decreases in sediment-carrying capacity due to the decreasing velocity. The finer grains finally settle down at the entry and center region of the minibasin. All simulation results indicate that the depocenters are located on the counterslope of the depositional topographies that the flows encounter.

Capability of overspilling

The simulated flows with different initial conditions differ in their capabilities of flowing over the bounding ridge of the upper minibasin. Although the supercritical equilibrium inflows are smaller in scale relative to the supercritical non-equilibrium flows, both are able to surmount this ridge-shaped obstacle delimiting the upper minibasin, usually starting from the second event (Fig. 5.8; Fig. 5.21). In the first several events, the coarser grains are ponded in the upper minibasin while the finer ones can be spilled over into the lower minibasins (Fig. 5.8; Fig. 5.21). For the much smaller-scaled subcritical flows, the inflows with higher initial height, lower initial concentration and finer grain sizes possess a stronger ability to spill over the bounding slope and transport coarser sediment downslope (Fig. 5.34a). In other words, more dilute, less dense and thicker turbidity currents find it easier to cross the confinement of the bounding ridge.

Flow-deposit-topography interaction

The experimental results of two sets of subcritical inflows shows a strong relationship between the flow pathways, the depositional characteristics, and the evolving bathymetry. Both sets of flows mainly exhibit fill-and-spill and trapping behaviour.

At the fill-and-spill stage, due to the confinement by the bounding ridge, the bulk of the flow is confined to the upper minibasin and a small portion of the flow overspills the obstacle. The resulting deposit displays a strong grain size partitioning between the upper and lower minibasins. Coarser materials are found mainly on the counterslope of the upper minibasin, while the finer ones are in the center of the upper minibasin and the down-dip area beyond the ridge. Initially the deposits in the upper minibasin initially smoothen (reduce) the slope gradient of the basin counterslope so that the effective confinement of the ridge is reduced and more volume with more coarse grains is allowed to reach the distal area.

After the fill-and-spill stage, the accumulated deposits on the counterslope develop into a pronounced high that causes the spill point to aggrade vertically and migrate upstream. The counterslope gradient becomes higher and the increasing confinement gradually decreases the amount and grain size of the sediment that can be carried by the spillover flows. A transitional stage may occur with a reduced frequency of overspilling, but eventually no more spilling occurs and full trapping in the upper minibasin ensues.

At the trapping stage, it is worth noticing that although both the accommodation volume in the upper minibasin and the counterslope gradient have decreased by successive deposits, this effect is counteracted by the increasingly stronger deposition in the channel as a form of backfilling, resulting in a decreasing volume of sediment being transported into the upper minibasin.

Spill point

In the present study, the spill point and its migration is important to indicate the degree of confinement by the bounding ridge. The spill point is the topographic peak in the axial (longitudinal) section of the upper minibasin, which is initially located at the lowest point on the ridge crest. With the evolution of the depositional relief, the topographically highest point is converted into the top of the increasingly growing relief. Combining the cross-section and plan view of the changing topography, a gentle ramp zone is first formed between the depositional ridge and the original bounding ridge due to backfilling of the deposit (Fig. 5.10). This ramp evolves into a small local depression at a later stage (Fig. 5.23). Although the flows in the trapping stage are not capable of spilling over the bounding ridge of the original minibasin, they can spill over the newly formed “spill point” of the depositional relief and spread out on that ramp zone or in small local depressions by settling down the finer grain size (Fig 5.21n).

Internal architecture and stacking patterns

The thicknesses of the total deposits indicate that the depocenter of the original minibasin comes to lie eventually in the basin center. From the detailed stratigraphic framework one can determine the backward-stacking fill pattern of the entire system through analysis of the group or bed depocenters. This architecture is fundamentally controlled by deposition of the individual flows on the underlying and continually evolving bathymetry. Therefore, the upper minibasin shows different bed characteristics at different locations (Fig. 5.12; Fig. 5.13). The area near the ridge top and the side slope are characterized by fining- and thinning-upwards cycles. In the basin center, two cycles of coarsening-thickening- to fining-thinning-upward sequences are developed. The downstream slope exhibits a coarsening- and thickening-upward sequence. The deposits in the local depositional depressions are usually found to grow upward both in terms of thickness and grain size.

The stratigraphic sequences show that the lower minibasins undergo a three-phase evolution of progradation, aggradation and retrogradation (respectively corresponding to Group 2, 3 and 4 in the non-equilibrium flows), as seen in basin floor fans in the Tanqua-Karoo Basin, South Africa (Hodgson et al., 2006). The sequence profiles generally have a bottom-to-top trend that consists of a cycle of coarsening- and thickening-upwards, followed by a cycle of stable bed thicknesses and mean grain sizes, and finally capped by a cycle of fining- and thinning-upward (Fig. 5.12).

5.6.2 Comparison with other studies

Some aspects of the interaction between flow, deposit and bathymetry discussed in this thesis can be compared to results by previous studies, either field work, laboratory experiments or numerical simulations.

Filling history

It is widely believed that bathymetries play a significant role in controlling turbidity current behavior and the resulting sediment distribution (e.g., Pickering and Hiscott, 1985; Haughton, 1994, 2000, 2001; Martinsen et al., 2003; Hodgson and Haughton 2004; Joseph and Lomas, 2004; Gee et al., 2007; Albertao et al., 2011; Oluboyo et al., 2014). Smith (2004) classified the slope bathymetric styles into three types based on the degree of confinement: (i) silled sub-basins, (ii) partially silled basins with lateral escape paths, and (iii) tectonically-induced bounding slopes that guide but do not block flow paths. More detailed conceptual ***fill-spill-bypass*** models for successive mini-basins downslope were described and modified by numerous researchers (Winker, 1996; Weimer et al., 1998; Beaubouef and Friedman, 2000; Badalini et al., 2000; Sinclair and Tomasso 2002; Covault and Romans, 2009). The upstream minibasin is thought to be progressively filled with sediment to its spill points and the subsequent bypassing flows transport sediments to the downdip minibasins (Prather et al., 1998). A ***flow-stripping*** model proposed by Badalini et al. (2000) suggests that minibasins could fill coevally. Sinclair and Tomasso (2002) described the four phases comprising this model as flow ponding, flow stripping, flow bypass and blanketing, based on flume experiments and outcrop studies.

In our models, the turbidity currents were initially ponded in the up-dip minibasin, and later partially confined within the upstream minibasin and partially spilled over the bounding slope into the downstream minibasins. However, due to the bathymetric changes in the minibasin and the considerable amount of sediment deposited in the channel zone, at the later stage no bypassing flows occurred any more. Our results deviate therefore from the above-mentioned models in several important aspects.

Grain size partitioning

The non-uniformity of flows is influenced by the basin topography (e.g., Kneller and McCaffrey, 1999; Peakall et al., 2000; Amy et al., 2005). In the fill-and-spill stage of our numerical experiments, for the initial flow events, spatial partitioning of the grain size occurs between the linked minibasins. Coarser grains are deposited in the upper minibasin and finer grains can be carried over the separating lip downslope into the distal minibasins. This phenomenon is also documented in the ***flow-stripping*** model (Badalini et al., 2000; Sinclair and Tomasso, 2002), laboratory experiments (e.g., Brunt et al., 2004) and numerical simulations (e.g., Aas et al., 2010). Moreover, the studies of Brunt et al. (2004) and Aas et al. (2010, 2014) also show that with the decreasing effective confinement of the upstream basin (generated by the deposition within it), progressively greater proportions of coarser-grained material is by-passed

downstream into the subsequent basin. This is in accordance with the coarsening-upward sequence trend of Group 2 in the lower minibasins in our experiments. Brunt et al. (2004) pointed out that increased deposition in the channel leads to a decrease of the grain size in the minibasins.

Significant deposition on the counterslope

Kubo (2004) adopted both laboratory experiments and numerical simulations to model particle-driven density currents traversing a series of humps. Such a topography can be regarded as small linked minibasins. Although Kubo (2004) did not measure the sediment grain size, he found that the deposit thickness on the distal humps is smaller than the one of the proximal humps, and an increase in deposition occurs on the upslope side of the humps, which is in agreement with our result of significant deposition on the counterslope of the minibasin.

Internal architecture and stacking pattern

The detailed depositional architectures in confined turbidite systems could be used to unravel the impact of pre-existing topographies on sediment dispersal. For this, well-exposed 3D outcrops or high-resolution seismic data would be required. Most outcrops are exposed essentially in two dimensions and thus offer only partial information on the sedimentary architecture (Shanmugam and Moiola, 1991; Shanmugam, 2000; Satur et al., 2000). Due to inherent limitations of geophysical techniques, most seismic data is inadequate to resolve the desired sedimentary details and small-scale stacking patterns. A typical seismic section of a salt-withdrawal minibasin of the Gulf of Mexico merely shows an overall aggradational sequence in the minibasin center (e.g., Winker, 1996). Moreover, surface and subsurface layers often experience post-depositional processes such as compaction and tectonic deformations that change their original geometry and architecture. Only few case studies document high quality data that are required for a detailed one-to-one comparison with our results (e.g. Gervais et al., 2006; Moody et al., 2012).

Moody et al. (2012) examined the outcrops of the Morillo Formation of the Ainsa Basin, (Spain) for its spatial and stratigraphic variations (longitudinally and vertically) in geometry and dimensions of the channel elements in weakly confined channel systems. They found that the axial downdip area has the highest net sand content in this system. Although no channel elements develop in our confined minibasin system, the depositional distribution in our models shows that the coarser and thicker deposits in the upper minibasin are also mainly in the axial-downdip area within the basin.

Direct seismic evidence has not yet been found in the minibasins of the Gulf of Mexico to support the back-filling stacking patterns suggested by our models. Prather et al. (2012) documented the stratigraphic evolution of linked intraslope basins in the Brazos-Trinity depositional systems, the western Gulf of Mexico, based on recent coring results and 3D seismic data. They focused on distinguishing the different

aprons (low-relief ponded, high-relief ponded and perched aprons) in these minibasins. Nevertheless, by carefully recognizing and tracing the depocenters of series 20-70 in basins II and IV, a general trend of upstream migration can be obtained, which to some extent supports the landward-stacking patterns of deposits in our modeling results (Fig. 5.35).

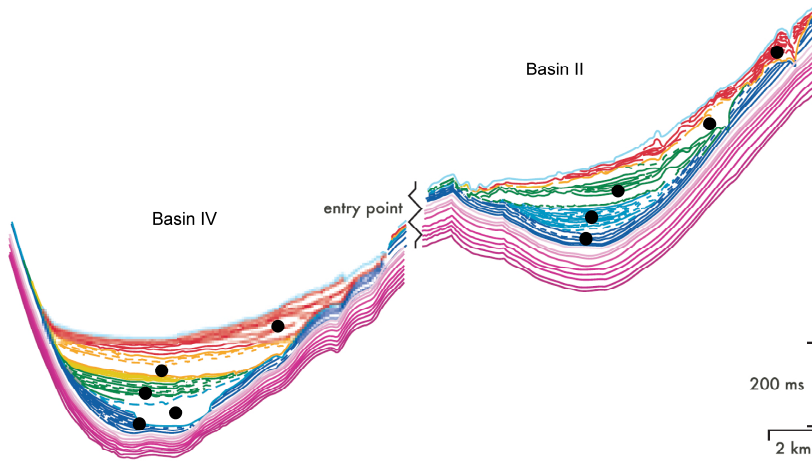


Figure 5.35: Stratigraphic evolution of basin II and IV in the Brazos-Trinity depositional system, modified from Fig. 24F in Prather et al., 2012. Pink lines show Series 10, dark blue Series 20, light blue lines Series 30, green lines Series 40, yellow lines Series 50 and 60, and red lines Series 70. Black dots indicate our interpreted depocenters of each series. During deposition of Series 10, salt withdrawal creates shallowly ponded accommodation (<60 m) in Basin IV while the Basin II has not formed yet. Subsidence starting with Series 20 brought the slope close to its present structural configuration (creating Basin II and increasing the accommodation of basin IV).

Furthermore, Amy et al. (2007) also found a landward shift in the proximal depositional facies of a sub-basin of the Alpine foreland in the Grès de Peïra Cava (SE France). A similar stacking pattern was modelled by process-based simulation of turbidity currents over the recreated seabed bathymetry of the Peïra Cava turbidite system (Aas et al., 2010, 2014). They offered two reasons that might contribute to this back-stepping pattern (Fig. 5.36): (1) a net decline in sediment supply as a result of allogenic processes, and/or (2) a landward migration of the slope break. They verified the second hypothesis by evidence of an upward decrease of the slope-related facies. The first hypothesis is well supported by our models in that the sediment transported into the upper minibasin decreases due to a significant early deposition in the feeding channel.

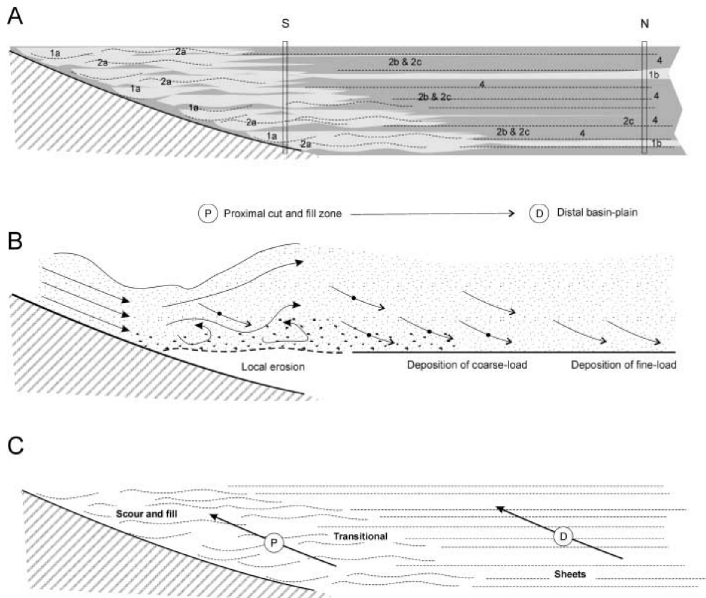


Figure 5.36: (a) Summary diagram of the sedimentary architecture in relatively proximal and distal environments of the Grès de Peira Cava showing the distribution of elements. Process model proposed to explain the development of different facies types (b) and the backward migration of depositional environments (c). It should be noted that this model does not take into account allogenic factors, which could overprint this basin-specific 'generic' style of sediment accumulation. From Amy et al., 2007.

Our experiments use a static initial bathymetry and there was no tectonic subsidence or uplift during the numerical flow simulations. Therefore, turbidite systems in relatively stable confined minibasins or local depressions bounded by a depositional relief should be taken for reference. Using high-resolution seismic data, Gervais et al. (2006) recognized retrograding units on the depositional relief of the previous deposits in a distal lobe of the Golo confined turbidite system (latest Pleistocene, offshore Corsica). The hydrodynamic reasons for this retrogradation suggested by them are similar to ours. Flows are erosive in the low in front of the obstacle, whereas the ponded flows are reflected by and spreading along the whole slope, with sediment being deposited on it (Fig. 5.37a). Progressively, deposition creates new frontal slope and generates landward stacking deposits (Fig. 5.37b).

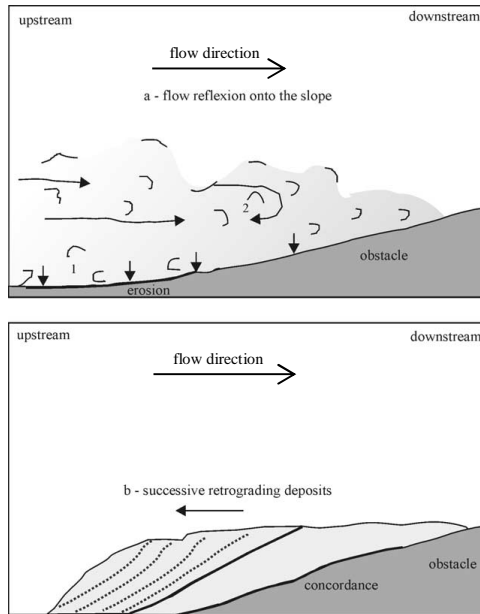


Figure 5.37: Schematic diagram showing the impact of a frontal slope on longitudinal migrations generating forced retrograding deposits (modified from Gervais et al., 2006). Flow direction is from left to right. (a): Flows are erosive in front of the obstacle, but depositional on the counterslope of the obstacle. (b): Successive deposits on the newly-formed counterslope form the retrograding migration unit.

Therefore, it is suggested that the flow-deposit-topography interactions observed in our study can be analogous to the flow processes, the depositional dispersal and the stacking patterns in a specific type of a confined turbidite system, which can be reasonably expected to exist in certain modern and ancient systems.

CHAPTER 6

Conclusions and Recommendations

6.1 Main conclusions

- Tectonics, including salt tectonics, on passive continental margins results in complicated seabed bathymetries along the slope between the shelf-edge break and the continental rise. A diverse range of salt diapirs and walls, and the related salt withdrawal minibasins, exists. Similar intraslope minibasins can be bounded by fold-and-fault systems without direct contact with salt bodies. For example, small-scale graben in the overburden of a rising salt diapir, and local depressions located between adjacent anticlines/folds of sedimentary layers cored by squeezed salt diapir ridges. As a unique structural style of salt tectonics, salt-withdrawal minibasins form and develop in allochthonous or autochthonous salt bodies.
- The sandbox analogue experiments (Chapter 3), which are driven by gravity gliding, can successfully model the evolution and structural styles in extensional and compressional zones of salt tectonism on passive margins. Three types of minibasins are recognized in the results based on their boundary contact relationships: MB1 (no contact with the silicone layer), MB2 (the silicone layer as the basin base) and MB3 (the silicone diapir as the basin flank).

- The pre-existing minibasins on passive margins greatly affect the behavior of turbidity currents and the sedimentation of turbidites. Moreover, the interaction between flow, deposit and the dynamic topography has a paramount influence on the stratigraphy and architecture of confined turbidite systems. In order to better understand these interactions, models for predicting the confined minibasin systems have been attempted in order to establish, by means of seismic interpretation, field studies, laboratory experiments and numerical simulation.
- The method that integrates laboratory tectonic modelling (successive-minibasin topography) and numerical flow simulation (multiple turbidity-current events) is proved to be effective (Chapter 5). The investigations of flow-deposit-bathymetry interactions, through the analysis of real-time variations in flow properties, the flow pathway, the sediment distribution (thickness and mean grain size), and the internal stacking patterns of the turbidite systems under different flow conditions can be applied to better predict the distribution of reservoir sands in the subsurface.
- The interaction between the flows, deposits and bathymetries analyzed from the results of sets of numerical simulation demonstrate the following:

Flow evolution

Modelled turbidity currents experience the fully ponding, fill-and-spill and trapping stages. In the fully ponding stage, the turbidity currents are completely confined within the up-dip minibasin without downstream overspill. In the fill-and-spill stage, turbidity currents are partially restricted within the up-dip minibasins and partially spilled over the bounding slope flowing to the down-dip minibasins. In the trapping stage, turbidity currents are limited in the domain of the original up-dip minibasin and spilling no longer happens.

Grain size partitioning

In the early stage of fill-and-spill stage, only finer grains can be transported by the spilling flows. Subsequently with the topographic changes within the up-dip minibasin, a higher portion of coarser grains are able to be carried over the bounding ridge into the distal minibasins by increasing the volume of spilling flows. With the continuous evolution of depositional relief, spilling flows decrease in volume and grain size. Perhaps after a transitional stage (the alternation of spilling and no spilling), eventually the spilling process ends.

Flow-deposit-topography interaction

A significant proportion of the deposition within the minibasins (the up-dip and down-dip minibasins) takes place on the counterslopes of the bathymetry that is changing after every flow. This is the fundamental reason for the associated changes in the bathymetric template and the upstream migration of the spill point.

The flow pathway and evolution depend much on the volume of flow reaching the up-dip minibasin, the remaining accommodation space and the bathymetric configuration (geometry, gradient, and aspect). Deposition on the counterslope first smoothes the gradient and decreases the accommodation space so that the subsequent flows can partially surmount and spill over the bounding ridge. Later, the deposition in the channel becomes stronger, resulting in a decrease in the volume of the flow entering the up-dip minibasin. Moreover, the depositional relief builds up and new local depressions form, thus the effect of the decrease in the accommodation space of the original minibasin is counteracted. With the upstream migration of the spill point, the possibility of a flow to overspill diminishes.

Internal architecture and stacking pattern

The flow evolution and pathway, the sediment dispersal patterns, and the topographic changes together result in the internal architecture and stacking pattern. By correlating the stratigraphic framework through the autogenic evolution of flows, we observe that the entire system experiences a progradation, aggradation and retrogradation stacking pattern. In other studies this stacking pattern has been attributed to allogenic forcing through waxing and waning sediment supply (Hodgson et al. 2006). A sequence of coarsening- and thickening- upwards trend is dominant in the down-dip minibasins. The upper minibasin shows different stratigraphic packages in different locations. The depocenters in all three minibasins migrate upstream longitudinally and towards the minibasin center laterally, which results in a back-filling stacking pattern.

6.2 Recommendations for further work

- The conceptual model established in this thesis based on the numerical simulation needs to be further validated and modified by careful mapping of high-quality 3D reflection seismic data and/or the three-dimensional field outcrop. There is a rich future in research on the dynamic interactions of flow-deposit-bathymetry in the successive minibasins but “solid” data is needed to test the exportability of concepts derived from integrated physical and numerical modelling.
- In this thesis, although the basal minibasin topography is formed by tectonics, during the numerical simulations the initial basal topography does not change.

Therefore, syn-tectonic sedimentation is not under consideration. However, syn-sedimentary tectonics or syn-tectonic sedimentation is important during the formation and development of the intraslope minibasins on passive margins. Therefore, a logical future step would be to conduct the associated numerical simulation based on the real-case model in such settings.

- Commonly, confined turbidite systems contain a wide grain-size range. It is necessary in future work to combine the high-density sediment gravity flows such as high-density turbidity currents, debris flows and mud flows in the numerical simulations to capture the full range of processes in these settings. This requires a new numerical simulator that integrates the flow modules for different end members of sediment gravity flows, since FanBuilder is designed for low density turbidity currents only.

References

- Aarseth, I.A., Lønne, O., Giskeødegaard, O., 1989. Submarine slides in glaciomarine sediments in some western Norwegian fjords. *Marine Geology* 88, 1–21.
- Aas, T.E., Basani, R., Howell, J., Hansen, E., 2014. Forward modelling as a method for predicting the distribution of deep-marine sands: an example from the Peira Cava Sub-Basin. In: Martinius, A.W., Howell, J.A., Good, T.R. (Eds.), *Sediment-Body Geometry and heterogeneity: Analogue Studies for Modelling the Subsurface*. Geological Society, London, Special Publication 387, pp. 247–269.
- Aas, T.E., Howell, J.A., Janocko, M., Midtkandal, I., 2010a. Re-created Early Oligocene seabed bathymetry and process-based simulations of the Peira Cava turbidite system. *Journal of the Geological Society, London*, 67, 857–875.
- Aas, T.E., Howell, J.A., Janocko, M., Jackson, C.A.-L., 2010b. Control of Aptian palaeobathymetry on turbidite distribution in the Buchan Graben, Outer Moray Firth, Central North Sea. *Marine and Petroleum Geology* 27, 412–434.
- Abd El-Gawad, S. M., Pirmez, C., Cantelli, A., Minisini, D., Sylvester, Z., Imran, J., 2012. 3-D numerical simulation of turbidity currents in submarine canyons off the Niger Delta. *Marine Geology* 326–328, 55–66.
- Adam, J., Krezsek, C., 2012. Basin-scaled salt tectonic processes of the Laurentian Basin, Eastern Canada: insight from integrated regional 2D seismic interpretation and 4D physical experiments. In: Alsop, G.I., Archer, S.G., Hartley, A.J., Grant N.T., Hodgkinson, R. (Eds.), *Salt Tectonics, Sediments, Prospectivity*. Geol. Soc. London Spec. Publ. 363, pp. 331–360.
- Albertão, G.A., 2010. Control of the submarine palaeotopography on the turbidite system architecture: an approach combining structural restorations and sedimentary process-based numerical modeling, applied to a Brazilian offshore case study Vol. I. Ph.D. thesis. Université Bordeaux 1, Talence, France.
- Albertão, G.A., Eschard, R., Mulder, T., Teles, V., Chauveau, B., Joseph, P. 2014. Modelling the deposition of turbidite systems with Cellular Automata numerical simulations: a case study in the Brazilian offshore. *Marine and Petroleum Geology*. DOI: 10.1016/j.marpetgeo.2014.07.010
- Albertão, G.A., Mulder, T., Eschard, R. 2011. Impact of salt-related palaeotopography on the distribution of turbidite reservoirs: Evidence from well-seismic analysis and

- structural restorations in Brazilian offshore. *Marine and Petroleum Geology* 28, 1023–1044.
- Albertz, M., Beaumont, C., Shimeld, J.W., Ings, S.J., Gradmann, S., 2010. An investigation of salt tectonics structural styles in the Scotian Basin, offshore Atlantic Canada: Paper 1, comparison of observations with geometrically simple numerical models. *Tectonics* 29, TC4017. Doi:10.1029/2009TC002539, 29 pp.
- Albertz, M., Ings, S.J., 2012. Some consequences of mechanical stratification in basin-scale numerical models of passive-margin salt tectonics. In: Alsop, G.I., Archer, S.G., Hartley, A.J., Grant N.T., Hodgkinson, R. (Eds.), *Salt Tectonics, Sediments, Prospectivity*. *Geol. Soc. London Spec. Publ.* 363, pp. 303–330.
- Alexander, J., Morris, S.A., 1994. Observations on experimental, nonchannelized, high-concentration turbidity currents and variations in deposit around obstacles. *Journal of Sedimentary research* A64, 899–909.
- Alexander, J., Mulder, T., 2002. Experimental quasi-steady density currents. *Marine Geology* 186, 195–210.
- Allemand, P., Brun, J.P., 1991. Width of continental rifts and rheological layering of the lithosphere. *Tectonophysics* 188, 63–69.
- Allen, J.R.L., 1971. Mixing at turbidity-current heads, and its geological implications. *Journal of Sedimentary Petrology* 41, 97–113.
- Allen, P.A., Allen, J.R., 2005. *Basin Analysis: Principles and Applications*. 2nd ed., Blackwell Publishing, 549 p.
- Altınakar, M.S., Graf, W.H., Hopfinger, E.J., 1996. Flow structure in turbidity currents. *Journal of Hydraulic Research* 34, 713–718.
- Amy, L.A., Kneller, B.C., McCaffrey, W.D., 2007. Facies architecture of the Gres de Peira Cava, SE France: landward stacking patterns in ponded turbiditic basins. *Journal of the Geological Society* 164, 143–162.
- Amy, L.A., Peakall, J., Talling, P.J., 2005. Evolution of density- and viscosity-stratified gravity currents: insight from physical experiments and implications for submarine flow deposits. *Sedimentary Geology* 179, 5–29.
- Anderson, J.E., Cartwright, J., Drysdall, S.J., Vivian, N., 2000. Controls on turbidite sand deposition during gravity-driven extension of a passive margin: examples from Miocene sediments in Block 4, Angola. *Marine and Petroleum Geology* 17, 1165–1203.
- Athmer, W., Groenenberg, R.M., Luthi, S.M., Donselaar, M.E., Sokoutis, D., Willigshofer, E., 2009. Relay ramps as pathways for turbidity currents: a study combining analogue sandbox experiments and numerical flow simulations. *Sedimentology* 57, 806–823.
- Badalini, G., Kneller, B., Winker, C.D., 2000. Architecture and processes in the Late Pleistocene Brazos-Trinity turbidite system, Gulf of Mexico Continental slope. In: Weimer, P., Slatt, R.M., Coleman, J., Rosen, N.C., Nelson, H., Bouma, A.H., Styzen, M. J., Lawrence, D.T. (Eds.), *Deep-water reservoirs of the world*, GCSSEPM. 20th Annual Bob F. Perkins Research Conference, pp. 304–317.
- Bagnold, R.A., 1962. Auto-suspension of transported sediment: turbidity currents. *Proc. Roy. Soc. London* A265, 315–319.
- Balkwill, H.R., Legall, F.D., 1989. Whale Basin, offshore Newfoundland: Extension and salt diapirism. In: Tankard, A.J., Balkwill, H.R. (Eds.), *Extension Tectonics and*

- stratigraphy of the North Atlantic margins. *American Association of Petroleum Geologists Memoir* 46, pp. 233–245.
- Bally, A.W., Snelson, S., 1980. Realms of subsidence. In: Miall, A.D. (Ed.), *Fact and principles of word petroleum occurrence*. Canadian Society of Petroleum Geologists Memoir 6, pp. 9–94.
- Barde, J.P., Gralla, P., Harwijanto, J., Marsky, J., 2002. Exploration at the eastern edge of the Precaspian basin: Impact of data integration on Upper Permian and Triassic prospectivity. *American Association of Petroleum Geologists Bulletin* 86, 399–415.
- Bates, C.C., 1953. Rational theory of delta formation. *AAPG Bull.* 37, 2119–2162.
- Beaubouef, R.T., Friedmann, S.J., 2000. High resolution seismic/sequence stratigraphic framework for the evolution of Pleistocene intraslope basins, western Gulf of Mexico: Depositional models and reservoir analogs. In: Weimer, P., Slatt, R.M., Coleman, J., Rossen, N.C., Nelson, H., Bouma, A.H., Styzen, M.J., and Lawrence, D.T., (Eds.), *Deep-water reservoirs of the world*. 20th Annual Research Conference Proceedings, Houston, Texas, Society of Economic Paleontologist and Mineralogists, Gulf Coast Section, pp. 40–60.
- Beck, C., Schneider, J-L., Cremer, M., MercierdeLepinay, B., Cagatay, N., Labeyrie, L, et al., 2003. Late Pleistocene major sedimentary reworking event (homogeneite) in Marnara Sea Central basin: preliminary results of giant piston-coring and high-resolution seismic reflection. EGS-AGU joint meeting 6-11 April, 2003, Nice, France.
- Beglinger, S.E., Corver, M.P., Doust, H., Cloetingh, S., Thurmond, A.K., 2012. A new approach of relating petroleum system and play development to Basin evolution: An application to the conjugate margin Gabon coastal and Almada-Camamu Basins. *AAPG bulletin*, 96, 953–982.
- Beglinger, S.E., van Wees, J-D., Cloetingh, S., Doust, H., 2012. Tectonic subsidence history and source-rock maturation in the Campos Basin, Brazil. *Petroleum Geoscience*, 18, 153–172.
- Bishop, D.J., Buchanan, P.G., Bishop, C.J., 1995. Gravity driven thin-skinned extension above Zechstein Group evaporites in the western central North Sea: an application of computer-aided section restoration techniques. *Marine and Petroleum Geology* 12, 115–135.
- Blaich, O.A., Faleide, J.I., Tsikalas, F., 2011. Crustal breakup and continent-ocean transition at South Atlantic conjugate margins. *J. Geophys. Res.*, 116, B01042, Doi: 10.1029/2010JB007686.
- Bornhold, B.D., Ren, P., Prior, D.B., 1994. High-frequency turbidity currents in British Columbia Fjords. *Geo-Mar. Lett.* 14, 238–243.
- Bouma, A.H., 1962. *Sedimentology of some flysch deposits: a graphic approach to facies interpretation*. Elsevier, Amsterdam, 168p.
- Bouma, A.H., 1982, Intraslope basins in northwest Gulf of Mexico: key to ancient submarine canyons and fans. In: Watkins, J.S., Drake, C.L. (Eds.), *Geologic Evolution of Continental Margins*. American Association of Petroleum Geologists Memoir 43, pp. 567–581.
- Bouma, A.H., 2000. Fine-grained, mud-rich turbidite systems: model and comparison with coarse-grained, sand-rich systems. In: Bouma, A.H., Stone, C.G. (Eds.), *Fine-Grained Turbidite Systems*. AAPG Memoir 72 / SEPM Special Publication No. 68,

- The American Association of Petroleum Geologists and SEPM (Society of Sedimentary Geology), Tulsa, pp. 9–20.
- Bouma, A.H., 2004. Key controls on the characteristics of turbidite systems. In: Lomas, S.A., Joseph, P. (Eds.), *Confined Turbidite Systems*. Geological Society, London, Special Publications, vol. 222, pp. 9–22.
- Bouma, A.H., Smith, L.B., Sidner, B.R., McKee, T.R., 1978. Intraslope basin in northwest Gulf of Mexico. In: Bouma, A.H., Moore, G.T., Coleman, J.M. (Eds.), *Framework, facies, and oil-trapping characteristics of the upper continental margin*. American Association of Petroleum Geologists, *Studies in Geology* 7, pp. 289–302.
- Bradford, S.F., Katapodes, N.D., 1999. Hydrodynamics of turbid underflows II: aggradation, avulsion, and channelization. *Journal of Hydraulic Engineering, ASCE* 125, 1016–1028.
- Bradford, S.F., Katapodes, N.D., Parker, G., 1997. Characteristic analysis of turbid underflows. *Journal of Hydraulic Engineering, ASCE* 123(5), 420–431.
- Britter, R.E., Linden, P.F., 1980. The motion of the front of a gravity current down an incline. *Journal of Fluid Mechanics* 91, 531–543.
- Britter, R.E., Simpson, J.E., 1978. Experiments on the dynamics of a gravity current head. *J. Fluid Mech.* 88, 223–9652.
- Brun, J.P., 1999. Narrow rifts versus wide rifts: Interferences for the mechanics of rifting from laboratory experiments. *Philosophical Transactions of the Royal Society of London* 357, 695– 712.
- Brun, J.P., Mauduit, T.P.O., 2008. Rollovers in salt tectonics: the inadequacy of the listric fault model. *Tectonophysics* 457, 1–11.
- Brun, J.P., Merle, O., 1985. Strain patterns in models of spreading-gliding nappes. *Tectonics* 4, 705–719.
- Brun, J.P., Fort, X., 2004. Compressional salt tectonics (Angolan margin). *Tectonophysics* 382, 129–150.
- Brun, J.P., Fort, X., 2008. Entre sel et terre. Structures et mécanismes de la tectonique salifère. Collection «Interactions». Vuibert, Paris.
- Brun, J.P., Fort, X., 2011. Salt tectonics at passive margins: geology versus models. *Marine and Petroleum Geology* 28, 1123–1145.
- Brun, J.P., Fort, X., 2012. Salt tectonics at passive margins: Geology versus models – Reply. *Marine and Petroleum Geology* 37, 195–208.
- Brunt, R.L., McCaffrey, W.D., Kneller, B., 2004. Experimental modeling of the spatial distribution of grain size developed in a fill-and-spill mini-basin setting. *Journal of sedimentary Research* 74, 438–446.
- Buffler, R.T., 1991. Early Evolution of the Gulf of Mexico Basin. In: Goldthwaite, D. (Ed.), *Introduction to Central Gulf Coast Geology*. New Orleans Geological Society, New Orleans, Louisiana, pp. 1–15.
- Burgess, P.M., Flint, S., Johnson, S., 2000. Sequence stratigraphic interpretation of turbiditic strata: An example from Jurassic strata of the Neuquén basin, Argentina. *Geological Society of America Bulletin* 112, 1650–1666.
- Cainelli, C., Mohriak, W.U., 1999. Some remarks on the evolution of sedimentary basins along the eastern Brazilian continental margin. *Episodes*, 22/3, 206–216.

- Carey, S.N., Schneider, J.-L., 2011. Volcaniclastic processes and deposits in the deep-sea. In: Hüneke, H. Mulder, T. (Eds.), *Deep-Sea Sediments. Development in Sedimentology*, Elsevier, Amsterdam, vol. 63, pp. 457–515.
- Cloetingh, S., Kooi, H., 1992. Intraplate Stresses and Dynamic Aspects of Rifted Basins. *Tectonophysics* 215, 167–185.
- Cloetingh, S., Ziegler, P.A., 2007. Tectonic models for the evolution of sedimentary basins. *Treatise on Geophysics* 6, 485–611.
- Cloetingh, S., Burov, E., Matenco, L., Beekman, F., Roure, F., Ziegler, P.A., 2013. The Moho in extensional tectonic settings: insights from thermo-mechanical models. *Tectonophysics* 609, 558–604.
- Cobbold, P.R., Meisling, K.E., Mont, V.S., 2001. Reactivation of an obliquely rifted margin, Campos and Santos basins, southeastern Brazil. *American Association of Petroleum Geologist Bulletin* 85, 1925–1944.
- Cobbold, P.R., Rossello, E., Vendeville, B.C., 1989. Some experiments on interacting sedimentation and deformation above salt horizons: *Bulletin de la Société Géologique de France, Série 8*, v. 5, pp. 453–460.
- Cobbold, P.R., Szatmari, P., 1991. Radial gravitational gliding on passive margins. *Tectonophysics* 188, 249–289.
- Cobbold, P.R., Szatmari, P., Demercian, L.S., Coelho, D., Rossello, E.A., 1995. Seismic and experimental evidence for thin-skinned horizontal shortening by convergent radial gliding on evaporites, deep-water Santos Basin, Brazil. In: Jackson, M.P.A., Roberts, D.G., Snelson, S. (Eds.), *Salt tectonics: A global perspective. American Association of Petroleum Geologists Memoir* 65, pp. 305–321.
- Cohen, H.A., Hardy, S., 1996. Numerical modelling of stratal architectures resulting from differential loading of a mobile substrate. In: Alsop, G.I., Blundel, D.J., Davison, J. (Eds.), *Salt Tectonics. Geol. Soc. London Spec. Publ.* 100, pp. 265–274.
- Colletta, B., Letouzey, J., Pinedo, R., Ballard, J.F., Balé, P., 1991. Computerized X-ray tomography analysis of sandbox models: Examples of thin-skinned thrust systems. *Geology* 19, 1063–1067.
- Cotton, J.T., Koyi, H.A., 2000. Modeling of thrust fronts above ductile and frictional detachments: application to structures in the Salt Range and Potwar Plateau, Pakistan. *Geological Society of America Bulletin* 112, 351–363.
- Covault, J.A., Romans, B.W., 2009. Growth patterns of deep-sea fans revisited: turbidite system morphology in confined basins on the Quaternary California Borderland. *Marine Geology* 265, 51–66.
- Coward, M., Stewart, S., 1995. Salt-influenced structures in the Mesozoic–Tertiary cover of the southern North Sea, U.K. In: Jackson, M.P.A., Roberts, D.G., Snelson, S. (Eds.), *Salt tectonics: a global perspective. AAPG Memoir* 65, pp. 229–250.
- Cramez, C., Jackson, M.P.A., 2000. Superposed deformation straddling the continental – oceanic transition in deep-water Angola. *Marine and Petroleum Geology* 17, 1095–1109.
- Dailly, G.C., 1976. A possible mechanism relating progradation, growth faulting, clay diapirism and overthrusting in a regressive sequence of sediments. *Bulletin of Canadian Petroleum Geology* 24, 92–116.

- Dal, J.-A., Guerin, G., Mather, J., 2006, The Paleocene – Eocene of the Gulf of Mexico: A 350-mile-long salt gravity-driven sliding system. AAPG Search and Discovery article 90052, accessed April 15, 2013.
http://www.searchanddiscovery.com/documents/2006/06088houston_abs/abstracts/dal.htm.
- Dan, G., Sultan, N., Savoye, B., 2007. The 1979 Nice harbour catastrophe revisited: Trigger mechanism inferred from geotechnical measurements and numerical modelling. *Marine Geology* 245, 40–64.
- Davison, I., 2007. Geology and tectonics of the South Atlantic Brazilian salt basins. In: Ries, A., Butler, R., Graham, R. (Eds.), *Deformation of the Continental Crust: The Legacy of Mike Coward*. Geol. Soc. Spec. Publ. 272, pp. 345–359.
- Davidson, J.F., Harrison, D., Carvalho, G.D., 1977. On the liquid-like behaviour of fluidized beds. *Annual Review of Fluid Mechanics* 9, 55–86.
- Davison, I., Anderson, L., Nuttall, P., 2012. Salt deposition, loading and gravity drainage in the Campos and Santos Salt basins. In: Alsop, G.I., Archer, S.G., Hartley, A.J., Grant N.T., Hodgkinson, R. (Eds.), *Salt Tectonics, Sediments, Prospectivity*. Geol. Soc. London Spec. Publ. 363, pp. 157–172.
- Davy, P., Cobbold, P.R., 1991. Experiments in shortening of a 4-layer model of the continental lithosphere. *Tectonophysics* 188, 1–25.
- Demercian, S., Szatmari, P., Cobbold, P.R., 1993. Style and pattern of salt diapirs due to thin-skinned gravitational gliding, Campos and Santos Basins, offshore Brazil. *Tectonophysics* 228, 393–433.
- Demyttenaere, R., Tromp, J.P., Ibrahim, A., Allman-Ward, P., Meckel, T., 2000. Brunei deep water exploration: from sea floor images and shallow seismic analogues to depositional models in a slope turbidite setting. In: Weimer, P., Slatt, R.M., Coleman, J., Rosen, N.C., Nelson, H., Bouma, A.H., Styzen, M. J., Lawrence, D.T. (Eds.), *Deep-water reservoirs of the world, GCS-SEPM. 20th Annual Bob F. Perkins Research Conference*, pp. 304–317.
- Diegel, F.A., Karlo, J.F., Schuster, D.C., Shoup, R.C., Tauvers P.R., 1995. Cenozoic structural evolution and tectonostratigraphic framework of the northern Gulf Coast continental margin. In: Jackson, M.P. A., Roberts, D. G., Snelson, S. (Eds.), *Salt tectonics: a global perspective: AAPG Memoir* 65, pp. 109–151.
- Dooley, T.P., Jackson, M.P.A., Hudec, M.R., 2013. Coeval extension and shortening above and below salt canopies on an uplifted, divergent, continental margin: the northern Gulf of Mexico. *AAPG Bull.* 10, 1737–1764.
- Dupré, S., Bertotti, G., Cloetingh, S., 2007. Tectonic history along the South Gabon Basin: Anomalous early post-rift subsidence. *Marine and Petroleum Geology*, 24, 151–172.
- Dupré, S., Cloetingh, S., Bertotti, G., 2011. Structure of the Gabon Margin from integrated seismic reflection and gravity data. *Tectonophysics* 506, 31–45.
- Duval, B., Cramez, C., Jackson, M.P.A., 1992. Raft tectonics in the Kwanza Basin, Angola. *Marine and Petroleum Geology* 9, 389–404.
- Dyson, I.A., 1999. The Beltana Diapir—A salt withdrawal minibasin in the northern Flinders Ranges. *Mines and Energy South Australia Journal* 15, 40–46.
- Edwards, D.A., 1993. *Turbidity Currents: Dynamics, Deposits and Reversals*. Springer, Berlin Heidelberg, 173 p.

- Ellison, T.H., Turner, J.S., 1959. Turbulent entrainment in stratified flows. *Journal of Fluid Mechanics* 6, 423–448.
- Farre, J.A., Ryan, W.B.F., 1985. 3-D view of erosional scars on U.S. mid-Atlantic continental margin. *AAPG bulletin* 69, 923–932.
- Ferrer, O., Jackson, M.P.A., Roca, E., Brubinat, M., 2012. Evolution of salt structures during extension and inversion of the offshore parentis basin (Eastern Bay of Biscay). In: Alsop, G.I., Archer, S.G., Hartley, A.J., Grant N.T., Hodgkinson, R. (Eds.), *Salt Tectonics, Sediments, Prospectivity*. *Geol. Soc. London Spec. Publ.* 363, pp. 361–379.
- Ferry, J.-N., Babonneau, N., Mulder, T., Parize, O., Raillard, S., 2004. Morphogenesis of Congo submarine canyon and valley: implications about the theories of the canyons formation. *Geodynamica Acta* 17, 241–251.
- Fort, X., Brun, J.P., 2012. Kinematics of regional salt flow in the northern Gulf of Mexico. In: Alsop, G.I., Archer, S.G., Hartley, A.J., Grant, N.T., Hodgkinson, R. (Eds.), *Salt Tectonics, Sediments and Prospectivity*. *Geol. Soc. London Spec. Publ.* 363, pp. 265–287.
- Fort, X., Brun, J.P., Chauvel, F., 2004. Salt tectonics on the Angolan margin, synsedimentary deformation processes. *AAPG Bull.* 88, 1523–1544.
- Fossen, H., 2010. *Structural Geology*. Cambridge University Press, Cambridge, United Kingdom.
- Galloway, W.E., 2008. Depositional evolution of the Gulf of Mexico sedimentary basin. In: Hsu, K.J. (Ed.), *The Sedimentary Basins of the United States and Canada. Sedimentary Basins of the World*, vol. 5, pp. 505–549.
- García, M.H., 1990. *Depositing and Eroding Sediment-driven Flows: Turbidity Currents*. University of Minnesota, St. Anthony Falls Hydraulic Laboratory, Report 306, 179 p.
- García, M.H., 1993. Hydraulic jumps in sediment-driven bottom currents. *Journal of Hydraulic Engineering* 119, 1094–1117.
- García, M.H., 1994. Depositional turbidity currents laden with poorly sorted sediment. *Journal of Hydraulic Engineering* 120, 1240–1263.
- García, M.H., Parker, G., 1989. Experiments on hydraulic jumps in turbidity currents near a canyon-fan transition. *Science* 245, 393–396.
- García, M.H., Parker, G., 1993. Experiments on the entrainment of sediment into suspension by a dense bottom current. *Journal of Geophysical Research* 98, 4793–4807.
- García, M.H., Parsons, J.D., 1996. Mixing at the front of gravity currents. *Dynamic Atmosphere and Oceans* 24, 197–205.
- Gaullier, V., Brun, J.-P., Guerin, G., Lecanu, H., 1993. Raft tectonics: the effects of residual topography below a salt décollement. *Tectonophysics* 228, 363–381.
- Gaullier, V., Mart, Y., Bellaiche G., Mascle, J., Vendeville, B.C., Zitter, T., Second leg of the PRISMED II Scientific Party, 2000. Salt tectonics in and around the Nile Deep-Sea Fan: Insights from the “PRISMED II” cruise. In: Vendeville, B.C., Mart, Y., Vigneresse J.L. (Eds.), *Salt, shale, and igneous diapirs in and around Europe*. *Geol. Soc. London Spec. Publ.* 174, pp. 111–129.
- Gaullier, V., Vendeville, B.C., 2005. Salt tectonics driven by sediment progradation: Part II–Radial spreading of sedimentary lobes prograding above salt. *American Association of Petroleum Geologists Bulletin* 89, 1081–1089.

- Gaumet, F., Joseph, P., Eschard, R., 2003. Thin turbidite Reservoirs: Reservoir characterization and uncertainty estimation. IFP/Petrobras project "Thin Turbidite Reservoirs". Institut Français du Pétrole, IFP Internal Report Ref. 57800. 104p.
- Gawthorpe, R.L., Hurst, J.M., 1993. Transfer zones in extensional basins: Their structural style and influence on drainage development and stratigraphy. *Journal of the Geological Society, London*, 150, 1137–1152.
- Ge, H., Jackson, M.P.A., Vendeville, B.C., Maler, M.O., Handschy, J.W., 1997. Deformation of prograding wedges over a ductile layer—applications of physical models to geologic examples. *Gulf Coast Assoc. Geol. Soc. Trans.* 47, 177–184.
- Gee, M.J.R., Gawthorpe, R.L., Bakke, K., Friedmann, S.J., 2007. Seismic geomorphology and evolution of submarine channels from the Angolan continental margin. *Journal of Sedimentary Research* 77, 433–446.
- Gemmer, L., Beaumont, C., Ings, S.J., 2005. Dynamic modelling of passive margin salt tectonics: effects of water loading, sediment properties and sedimentation pattern. *Basin Research* 17, 383–402.
- Gemmer, L., Ings, S.J., Medvedev, S., Beaumont, C., 2004. Salt tectonics driven by differential sediment loading: stability analysis and finite-element experiments. *Basin Research* 16, 199–218.
- Gervais, A., Savoye, B., Mulder, T., Gonthier, E. 2006. Sandy modern turbidite lobes: A new insight from high resolution seismic data. *Marine and Petroleum Geology* 23, 485–502.
- Gervais, A., Savoye, B., Piper, D.J.W., Mulder, T., Cremer, M., Pichevin, L., 2004. Present morphology and depositional architecture of a sandy confined submarine system: the Golo turbidite system (eastern margin of Corsica). In: Lomas, S.A., Joseph P., (Eds.), *Confined Turbidite Systems*. Geological Society, London, Special Publication. Geological Society, London, Special Publication 222, pp. 59–89.
- Giresse, P., Pauc, H., Deverchère, J., Savoye, B., the MARADJA Scientific Party, 2004. Gravity-induced transport on the Algerian margin. EGU 1st meeting Nice, France, 25–30, April, 2004.
- Gradmann, S., Beaumont, C., Albertz, M., 2009. Factors controlling the evolution of the Perdido Fold Belt, northwestern Gulf of Mexico, determined from numerical models. *Tectonics* 28, pp. 1–28.
- Gray, T.E., Alexander, J., Leeder, M.R., 2005. Quantifying velocity and turbulence structure in depositing sustained turbidity currents across breaks in slope. *Sedimentology* 52, 467–488.
- Groenenberg, R.M., 2007. Process-based modelling of turbidity-current hydrodynamics and sedimentation. 200 p., Delft University of Technology, Delft, Ph.D. thesis.
- Groenenberg, R.M., Hodgson, D.M., Prelat, A., Luthi, S.M., Flint, S., 2010. Flow-deposit interactions in submarine lobes: insights from outcrop observations and realizations of a process-based numerical model. *J. Sed. Res.* 80, 252–267.
- Groenenberg, R.M., Sloff, C.J., Weltje, G.J., 2009. A high-resolution 2-DH numerical scheme for process-based modelling of 3-D turbidite fan stratigraphy. *Computers and Geosciences* 35, 1686–1700.

- Guardado, L.R., Gamboa, L.A.P., Lucchesi, C.F., 1989. Petroleum geology of the Campos Basin, Brazil. A model for a producing Atlantic-type basin. In: Edwards, J.D., Santogrossi, P. A. (Eds.), *Divergent/Passive Margin Basins*. American Association of Petroleum Geologists Memoir, 48, Tulsa, 3–79.
- Guerin, G., Philippe, Y., Dal, J.-A., 2006. Impact of amount of gravity-driven compression and intermediate décollement levels on the Sigsbee Salt Canopy Formation, Gulf of Mexico. AAPG Search and Discovery article 9005, accessed April 15, 2013, http://www.searchanddiscovery.com/documents/2006/06088houston_abs/abstracts/guerin.htm.
- Guerra, M., Szatmari, P., 2009. Modelagem física de processos halocinéticos. In: Mohriak, W., Szatmari, P., Dos Anjos, S.M.C. (Eds.), *Sal: geologia e tectonônica - exemplos nas bacias brasileiras*. Petrobras – Editora Beca, São Paulo, 2ª ed., pp. 167–179.
- Guerra, M.C.M., Underhill, J.R., 2012. Role of Halokinesis in controlling structural styles and sediment dispersal in the Santos basin, offshore Brazil. In: Alsop, G.I., Archer, S.G., Hartley, A.J., Grant N.T., Hodgkinson, R. (Eds.), *Salt Tectonics, Sediments, Prospectivity*. Geol. Soc. London Spec. Publ. 363, pp. 363–206.
- Hall, S.H., 2002. The role of autochthonous salt inflation and deflation in the northern Gulf of Mexico. *Marine and Petroleum Geology* 19, 649–682.
- Harrison, T.S., 1927. Colorado-Utah salt domes. AAPG Bull. 11, 111–133.
- Harrison, J.C., Jackson, M.P.A., 2014. Exposed evaporite diapirs and minibasins above a canopy in central Sverdrup Basin, Axel Heiberg Island, Arctic Canada. *Basin Research* 26, 567–596.
- Haughton, P.D.W., 1994. Evolving turbidite systems on a deforming basin floor, Tabernas, SE Spain. *Sedimentology* 47, 497–518.
- Haughton, P.D.W., 2000. Deposits of deflected and ponded turbidity currents, Sorbas Basin, southeast Spain. *Journal of Sedimentary Petrology* A64, 2, 233–246.
- Haughton, P.D.W., 2001. Contained turbidites used to track sea bed deformation and basin migration, Sorbas Basin, south-east Spain. *Basin Research* 13, 117–139.
- Hayward, A.B., Graham, R.H., 1989. Some geometrical characteristics of inversion. *Geological Society Special Publication* 44, 17–39.
- Heaton, R.C., Jackson, M.P.A., Bamahmoud, M., Nani, A.S.O., 1995. Superposed Neogene extension, contraction, and salt canopy emplacement in the Yemeni Red Sea. In: Jackson, M.P.A., Roberts, D.G., Snelson, S. (Eds.), *Salt tectonics: A global perspective*. American Association of Petroleum Geologists Memoir 65, pp. 333–351.
- Hearton IV, T.E., Rowan, M.G., Lawton, T.F., Hannah, P.T., Giles, K.A., 2014. Geology and tectonics of Neoproterozoic salt diapirs and salt sheets in the eastern Willouran Ranges, South Australian. *Basin Research*. DOI: 10.1111/bre.12067.
- Heezen, B.C., 1974. Atlantic-type continental margins. In: Burk, C.A., Drake, C.L. (Eds.), *The geology of continental margins*. Springer, Berlin Heidelberg, pp. 13–24.
- Heezen, B.C., Ewing, M., 1952. Turbidity currents and submarine slumps, and the 1929 Grand-Banks earthquake. *American Journal of Science* 250, 849–873.
- Heezen, B.C., Ewing, M., Ericson, D.B., 1954. Reconnaissance survey of the abyssal plain south of Newfoundland. *Deep-sea Res.* 2, 122–188.

- Hocking, R.M., Moors, H.T., Van de Graaff, W.J.E., 1987. Geology of the Carnarvon Basin western Australia, Department of Mines Western Australia.
- Hodgson, D.M., Flint, S.S., Hodgetts, D., Drinkwater, N.J., Johannessen, E.P., Luthi, S.M., 2006. Stratigraphic evolution of fine-grained submarine fan systems, Tanqua depocenter, Karoo Basin, South Africa. *Journal of Sedimentary Research* 76, 20–40.
- Hodgson, D.M., Houghton, P.D.W., 2004. Impact of syndepositional faulting on gravity current behavior and deep-water stratigraphy: Tabernas-Sorbas Basin, SE Spain. In: Lomas, S.A., Joseph, P. (Eds), *Confined Turbidites Systems*. Geological Society, London, Special Publications, vol. 222, pp. 135–158.
- Hogg, J.R., Dolph, D.A., Mackidd, D., Michel, K., 2001. Petroleum systems of the deep water Scotian Salt Province, offshore Nova Scotia, Canada. GCSSEPM Foundation 21th Annual Research Conference, 23–34.
- Hoshino, K., Koide, H., Inami, K., Iwamura, S., Mitsui, S. 1972. Mechanical Properties of Tertiary Sedimentary Rocks under High Confining Pressure. Geological Survey of Japan, Kawasaki, Report 244.
- Hubbert, M.K., 1937. Theory of scale models as applied to the study of geologic structures. *Geological Society of America Bulletin* 48, 1459– 1520.
- Hudec, M.R., Jackson, M.P.A., 2002. Structural segmentation, inversion, and salt tectonics on a passive margin: Evolution of the inner Kwanza Basin, Angola: *Geological Society of America Bulletin* 114, 1222– 1244.
- Hudec, M.R., Jackson, M.P.A., 2004. Regional restoration across the Kwanza Basin, Angola: Salt tectonics triggered by repeated uplift of a metastable passive margin *American Association of Petroleum Geologist Bulletin* 88, 971–990.
- Hudec, M.R., Jackson, M.P.A., 2006. Advance of allochthonous salt sheets in passive margins and orogens. *AAPG Bull.* 90, 1535–1564.
- Hudec, M.R., Jackson, M.P.A., 2007. Terra infirma: Understanding salt tectonics. *Earth-Science Reviews* 82, 1–28.
- Hudec, M.R., Jackson, M.P.A., Peel, F.J., 2013a. Influence of deep Louann structure on the evolution of the northern Gulf of Mexico. *AAPG Bulletin* 10, 1711–1735.
- Hudec, M.R., Jackson, M.P.A., Schultz-Ela, D.D., 2009. The paradox of minibasin subsidence into salt: clues to the evolution of crustal basins. *Geological Society of America Bulletin* 121, 201–221.
- Hudec, M.R., Norton, I.O., Jackson, M.P.A., Peel, F.J., 2013b. Jurassic evolution of the Gulf of Mexico Salt Basin. *AAPG Bull.* 97, 1683–1710.
- Huerta, A.D., Harry, D.L., 2012. Wilson cycles, tectonic inheritance, and rifting of the North American Gulf of Mexico continental margin. *Geosphere* 8, 374 pp.
- Humphris, C.C., Jr., 1978. Salt movement on continental slope, northern Gulf of Mexico. In: Bouma, A.H., Moore, G.T., Coleman, J.M. (Eds.), *Framework, facies, and oil-trapping characteristics of the upper continental margin*. American Association of Petroleum Geologists, *Studies in Geology* 7, pp. 69–86.
- Humphris, C.C., Jr., 1979. Salt movement in continental slope, northern Gulf of Mexico: *American Association of Petroleum Geologists Bulletin* 63, 782–798.
- Ings, S.J., Beaumont, C., Gemmer, L., 2004. Numerical modeling of salt tectonics on passive continental margins: preliminary assessment of the effects of sediment loading, buoyancy, margin tilt, and isostasy. In: Post, P.J., Olson, D.L., Lyons, K.T., Palmes, S.L., Harrison, P.F., Rosen, N.C. (Eds.), *Salt-Sediment Interactions and*

- Hydrocarbon Prospectivity: Concepts, Applications and Case Studies for the 21st Century. 24 Annual GCSSEPM Foundation Bob F. Perkins Research Conference Proceedings, Houston, 5-8 December, pp. 36–68.
- Ings, S.J., Shimeld, J.W., 2006. A new conceptual model for the structural evolution of a regional salt detachment on the northeast Scotian margin, offshore Eastern Canada. *American Association of Petroleum Geologists Bulletin* 90, 1407–1423.
- Ismail-Zadeh, A., Tsepelev, I., Talbot, C., Korotkii, A., 2004. Three-dimensional forward and backward modeling of diapirism: Numerical approach and its applicability to the evolution of salt structures in the Pricaspian basin. *Tectonophysics* 387, 81–103.
- Jackson, C.A.L., Jackson, M.P.A., Hudec, M.R., Rodriguez, C., 2014. Internal structure, kinematics, and growth of a salt wall: Insight from 3-D seismic data. *Geology* 42, 307–310.
- Jackson, C.A.L., Gawthorpe, R.L., Leppard, C.W., Sharp, I.R., 2006. Rift-initiation development of normal fault blocks: insight from the Hammam Fauraun fault block, Suez Rift, Egypt. *Journal of the Geological Society, London*, 163, 165–183.
- Jackson, M.P.A., 1995. Retrospective salt tectonics. In: Jackson, M.P.A., Roberts, D.G., Snelson, S. (Eds.), *Salt Tectonics: a Global Perspective*. AAPG Memoir 65, pp. 1–28.
- Jackson, M.P.A., Cornelius, R.R., Craig, C.R., Gansser, A., Stöcklin, J., Talbot, C.J., 1990. Salt diapirs of the Great Kavir, Central Iran. *GSA Memoir* 177, 139 pp.
- Jackson, M.P.A., Cramez, C., Fonck, J.-M., 2000. Role of subaerial volcanic rocks and mantle plumes in creation of South Atlantic margins: implications for salt tectonics and source rocks. *Mar. Petrol. Geol.* 17, 477–498.
- Jackson, M.P.A., Dooley, T.P., Hudec, M.R., McDonnell, A.I., 2011. The pillow fold belt: a key subsalt structural province in the northern Gulf of Mexico. *AAPG Search Discov. Article* (#10329), 21 pp.
- Jackson, M.P.A., Harrison, J.C., 2006. An allochthonous salt canopy on Axel Heiberg Island, Sverdrup Basin, Arctic Canada. *Geology* 34, 1045–1048.
- Jackson, M.P.A., Talbot, C.J., 1986. External shapes, strain rates, and dynamics of salt structures. *Geological Society of America Bulletin* 97, 305–323.
- Jackson, M.P.A., Talbot, C.J., 1991. A glossary of salt tectonics. In: *Geological Circular*, 91-4. The University of Texas at Austin, Bureau of Economic Geology (44 pp.).
- Jackson, M.P.A., Vendeville, B.C., 1994. Regional extension as a geologic trigger for diapirism. *Geological Society of America Bulletin* 106, 57–73.
- Jaeger, J.C., Cook, N.G.W., 1969. *Fundamentals of Rock Mechanics*. Methuen, London.
- Jammes, S., Manatschal, G., Lavier, L., 2010. Interaction between prerift salt and detachment faulting in hyperextended rift systems: the example of the Parentis and Mauléon basins (Bay of Biscay and western Pyrenees). *AAPG Bull.* 94, 957–975.
- Joseph, P., Lomas, S.A., 2004. Deep-water sedimentation in the Alpine Foreland Basin of SE France: new perspectives on the Grès d'Annot and related turbidite systems: an introduction. In: Joseph, P., Lomas, S.A. (Eds.), *Deep-Water Sedimentation in the Alpine Foreland Basin of SE France: New Perspectives on the Grès d'Annot and Related Systems*. Geological Society, London, Special Publications 221, pp. 1–17.
- Jouet, G., Berné, S., Rabineau, M., Basseti, M.A., Bernier, P., Dennielou, B., Sierro, F.J., Flores, J.A., Taviani, M., 2006. Shoreface migrations at the shelf edge and sea-level

- changes around the Last Glacial Maximum (Gulf of Lions, NW Mediterranean). *Marine Geology* 234, 21–42.
- Karner, G.D., Driscoll, N.W., Barker, H.N., 2003. Synrift regional subsidence across the West African continental margin: the role of lower plate ductile extension. In: Arthur, T.J., MacGregor, D.S., Cameron, N.R. (Eds.), *Petroleum Geology of Africa: New Themes and Developing Technologies*. Geol. Soc. London Spec. Publ., vol. 207, pp. 105–129.
- Karner, G.D., Gamboa, L.A.P., 2007. Timing and origin of the South Atlantic pre-salt sag basins and their capping evaporites. In: Schreiber, B.C., Lugli, S., Bazbel, M. (Eds.), *Evaporites through Space and Time*. Geol. Soc. London Spec. Publ., vol. 285, pp. 15–35.
- Keen, C.E., Potter, D.P., 1995. Formation and evolution of the Nova Scotian rifted margin: evidence from deep seismic reflection data. *Tectonics* 14, 918–932.
- Keulegan, G.H., 1957. An experimental study of the motion of saline water from locks into fresh-water channels. US. Natl. Bur. Stand., Report 5168.
- Kidston, A.G., Brown, D.E., Altheim, B., Smith, B.M., 2002. Hydrocarbon potential of the deep-water Scotian slope. Canada-Nova Scotia Offshore Petroleum Board. Annual Report.
http://www.cnsopb.ns.ca/pdfs/Slope_Report_Exec_Summary.pdf
- Kneller, B.C., 1995. Beyond the turbidite paradigm: physical models for deposition of turbidites and their implications for reservoir predictions. In: Hartley, A.J., Prosser, D.J. (Eds.), *Characterization of Deep Marine Clastic Systems*. Geological Society, London, pp. 31–49.
- Kneller, B.C., Bennett, S.J., McCaffrey, W.D., 1999. Velocity structure, turbulence and fluid stresses in experimental gravity currents. *J. Geophys. Res. Oceans* 104, 5381–5391.
- Kneller, B.C., Branney, M.J., 1995. Sustained high-density turbidity currents and the deposition of thick massive beds. *Sedimentology* 42, 607–616.
- Kneller, B.C., Buckee, C., 2000. The structure and fluid mechanics of turbidity currents: a review of some recent studies and their geological implications. *Sedimentology* 47 (Suppl.1), 62–94.
- Kneller, B.C., Edwards, D., McCaffrey, W., Moore, R., 1991. Oblique reflection of turbidity currents. *Geology* 19, 250–252.
- Kneller, B.C., McCaffrey, W.D., 1995. Modelling the effects of salt-induced topography on deposition from turbidity currents. In: Travis, C.S., Harrison, H., Hudec, M.R., Vendeville, B.C., Peel, F.S., Perkins, B.E. (Eds.), *Salt, Sediment and Hydrocarbons*. Proceedings of GCSSEPM (SEPM Gulf Coast Section) 16th. Annual Research Conference Houston, pp. 137–145.
- Kneller, B.C., McCaffrey, W.D., 1999. Depositional effects of flow non-uniformity and stratification within turbidity currents approaching a bounding slope: deflection, reflection and facies variation. *Journal of Sedimentary Research* 69, 980–991.
- Kneller B.C., McCaffrey, W.D., 2003. The interpretation of vertical sequences in turbidite beds: the influence of longitudinal flow structure. *Journal of Sedimentary Research*. 73, 706–713.

- Kneller, E.A., Johnson, C.A., 2011. Plate kinematics of the Gulf of Mexico based on integrated observations from the Central and South Atlantic. *Gulf Coast Assoc. Geol. Soc. Trans.*, 61, 283–299.
- Kockel, F., 1998. Salt problems in Northwest Germany and the German North Sea sector. In: Kockel, F., Marschall, R. (Eds.), *Geology and Geophysics of Salt Structures. Journal of Seismic Exploration*, vol. 7, pp. 219–235.
- Kolla, V., Bourges, P., Urruty, J.M., Safa, P., 2001. Evolution of deepwater Tertiary sinuous channels offshore, Angola (West Africa) and implications to reservoir architecture. *American Association of Petroleum Geologists, Bulletin* 85, 1373–1405.
- Komar, P.D., 1971. Hydraulic jumps in turbidity currents. *Geological Society of American Bulletin* 82, 1477–1481.
- Koyi, H., 1988. Experimental modeling of role of gravity and lateral shortening in Zagros mountain belt. *AAPG Bulletin* 72, 1381–1394.
- Koyi, H., 1996. Salt flow by aggrading and prograding overburdens. In: Alsop, G.I., Blundell, D.J., Davison, I. (Eds.), *Salt Tectonics. Geol. Soc. Special Publ.* 100, pp. 243–258.
- Krezsek, C., Adam, J., Grujic, D., 2007. Mechanics of fault and expulsion rollover systems developed on passive margins detached on salt: insights from analogue modelling and optical strain monitoring. In: Jolley, S.J., Barr, D., Walsh, J.J., Knipe, R.J. (Eds.), *Structurally Complex Reservoirs. Geological Society, London, Special Publications* 292, pp. 103–121.
- Krezsek, C., Adam, J., King, S., Grujic, D., 2006. 3D Gravity Spreading of Passive Margins: insights from Analogue Modeling and Particle Image Velocimetry Analysis, *Geophysical Research Abstracts* 8, 09170.
- Kubo, Y., 2004. Experimental and numerical study of topographic effects on deposition from two-dimensional, particle-driven density currents. *Sedimentary Geology* 164, 311–326.
- Kuenen, P.H., Migliorini, C.I., 1950. Turbidity currents as a cause of graded bedding. *Journal of Geology* 58, 91–127.
- Lallemand, S.E., Schnuerle, P., Malavieille, J., 1994. Coulomb theory applied to accretionary and nonaccretionary wedges; possible cause for tectonic erosion and/or frontal accretion. *Journal of geophysical research, B, Solid Earth and Planets*, 99, 12033–12055.
- Lamb, M., Hickson, T., Sheets, B., Marr, J., Paola, C., Parker, G., 2004. Surging versus continuous turbidity currents: flow dynamics and deposits in an experimental intraslope minibasin. *Journal of Sedimentary Research* 74, 148–155.
- Lamb, M.P., Toniolo, H., Parker, G., 2006. Trapping of sustained turbidity currents by intraslope minibasins. *Sedimentology* 53, 147–160.
- Lane-Serff, G.F., Beal, L.M., Hadfield, T.D., 1995. Gravity current flow over obstacles. *Journal of Fluid mechanics* 292, 39–53.
- Last, N.C., 1988. Deformation of a sedimentary overburden on a slowly creeping substratum. In: Swoboda, G.S. (Eds.), *Numerical Methods in Geomechanics. Balkema, Rotterdam*, pp. 577–585.

- Laval, A., 1988. Modélisation d'écoulements de type bouffée de densité. Application à l'interprétation des dépôts turbiditiques. Unpubl. Ph.D. thesis, Univ. Bordeaux I, 262.
- Laval, A., Cremer, M., Beghin, P., Ravenne, C., 1988. Density surges: two-dimensional experiments. *Sedimentology* 35, 73–84.
- Leeder, M.R., Gawthorpe, R.L., 1987. Sedimentary models for extensional tiltblock/half-graben basins. In: Coward, M.P., Dewey, J.F., Hancock, P.L. (Eds.), *Continental Extensional Tectonics*. Geological Society Special Publication 28, pp. 139–152.
- Leeder, M.R., Gray, T.E., Alexander, J., 2005. Sediment suspension dynamics and a new criterion for the maintenance of turbulent suspensions. *Sedimentology* 52, 683–691.
- Lehner, P., 1969. Salt tectonics and Pleistocene stratigraphy on continental slope of northern Gulf of Mexico. *American Association of Petroleum Geologists Bulletin* 53, 2431–2479, doi: 10.1306/5D25C945-16C1-11D7-8645000102C1865D.
- Lehner, F.K., 1977. A theory of substratal creep under varying overburden with applications to tectonics. AGU Spring Meeting, Washington DC. EOS Abstr. 58, pp. 508.
- Lentini, M.R., Fraser, S.I., Sumner, H.S., Davies, R.J., 2010. Geodynamics of the central South Atlantic conjugate margins: implications for hydrocarbon potential. *Petrol. Geosci.* 16, 217–229.
- Letouzey, J., B. Colletta, R. Vially, and J. C. Chermette, 1995, Evolution of salt-related structures in compressional settings. In: Jackson, M.P.A., Roberts, D.G., Snelson, S. (Eds.), *Salt Tectonics: A Global Perspective*. AAPG Memoir 65, pp. 41–60.
- Liro, L.M., Coen, R., 1995. Salt deformation history and postsalt structural trends, offshore southern Gabon, west Africa. In: Jackson, M.P.A., Roberts, D.G., Snelson, S. (Eds.), *Salt Tectonics: A Global Perspective*. AAPG Memoir 65, pp. 323–331.
- Lohrmann, J., Kukowski, N., Adam, J., Oncken, O., 2003. The impact of analogue material parameters on the geometry, kinematics, and dynamics of convergent sand wedges. *Journal of structural geology* 25, 1691–1711.
- Loncke, L., Gaullier, V., Mascle, J., Vendeville, B., Camera, L., 2006. The Nile deep-sea fan: an example of interacting sedimentation, salt tectonics, and inherited subsalt paleotopographic features. *Marine and Petroleum Geology* 23, 297–315.
- Lowe, D.R., 1982. Sediment gravity flows: II, Depositional models with special reference to the deposits of high-density turbidity currents. *J. Sed. Petrol.* 52, 279–297.
- Lowe, D.R., Guy, M. 2000. Slurry-flow deposits in the Britannia Formation (Lower Cretaceous), North sea: a new perspective on the turbidity current and debris flow problem. *Sedimentology* 47, 31–70.
- Luth, S., Willingshofer, E., Sokoutis, D., Cloetingh, S., 2013. Does subduction polarity changes below the Apls? Inferences from analogue modelling? *Tectonophysics* 582, 140–161.
- Luthi, S.M., 1980. Some new aspects of two-dimensional turbidity currents. *Sedimentology* 28, 97–105.
- Luthi, S.M., 1981. Experiments on non-channelized turbidity currents and their deposits. *Marine Geology* 40, M59–M68.

- Maharaj, V.T., 2012. The effects of confining minibasin topography on turbidity current dynamics and deposit architecture. Ph.D. Dissertation. The University of Texas at Austin.
- Mannie, A.S., Jackson, C.A.-L., Hampson, G.J., 2014. Structural controls on the stratigraphic architecture of net-transgressive shallow-marine strata in a salt-influence rift basin: Middle-to-Upper Jurassic Egersund Basin, Norwegian North Sea. *Basin Research* 26, 675–700.
- Marjanac, T., 1990. Reflected sediment gravity flow and their deposits in flysch of Middle Dalmatia, Yugoslavia. *Sedimentology* 37, 921–929.
- Martinsen, O.J., Lien, T., Walker, R.G., Collinson, J.D., 2003. Facies and sequential organisation of a mudstone-dominated slope and basin floor succession: the Gull Island Formation, Shannon Basin, Western Ireland. *Marine and Petroleum Geology* 20, 789–807.
- Marion, L.G., Tari, G.C., Lehmann, C.T., 2000. Evolution of the Angolan passive margin, West Africa, with emphasis on post-salt structural styles. In: Mohriak, W.U., Talwani, M. (Eds.), *Atlantic rifts and continental margins*. American Geophysical Union Geophysical Monograph 115, pp. 129–149.
- Masrouhi, A., Bellier, O., Koyis, H., Vila, J.-M., Ghanmi M., 2013. The evolution of the Lansarine-Baouala salt canopy in the North African Cretaceous passive margin in Tunisia. *Geol. Mag.*, 150, 835–861.
- Matthews, W.J., Hampson, G.J., Trudgill, B.D., Underhill, J.R., 2007. Controls on fluviolacustrine reservoir distribution and architecture in passive salt-diapir provinces: Insights from outcrop analogs. *American Association of Petroleum Geologists Bulletin* 91, 1367–1403.
- Mauduit, T., Brun, J.P., 1998. Growth fault/rollover systems: birth, growth, and decay. *Journal of Geophysical Research*, 103, 18119–18136.
- Mauduit, T., Guérin, G., Brun, J.P., Lecanu, H., 1997. Raft tectonics: the effects of basal slope value and sedimentation rate on progressive extension. *Journal of Structural Geology* 19, 1219–1230.
- McCaffrey, W.D., Kneller, B.C., 2001. Process controls on the development of trap potential on the margins of confined turbidite systems and aid to reservoir evaluation. *AAPG Bulletin* 85, 971–988.
- McClay, K.R., 1990. Extensional fault systems in sedimentary basins: a review of analogue model studies. *Marine and Petroleum Geology* 7, 206–233.
- McClay, K.R., Dooley, T., Lewis, G., 1998. Analog modeling of progradational delta systems. *Geology* 26, 771–774.
- Meiburg, E., Kneller, B., 2010. Turbidity currents and their deposits. *Annu. Rev. Fluid Mech.* 42, 135–156.
- Meisling, K.E., Cobbold, P.R., Mount, V.S., 2001. Segmentation of an obliquely rifted margin, Campos and Santos basins, southeastern Brazil. *AAPG Bull.* 85, 1903–1924.
- Middleton, G.V., 1966a. Experiments on density and turbidity currents I. Motion of the head. *Canadian Journal of Earth Sciences* 3, 523–546.
- Middleton, G.V., 1966b. Experiments on density and turbidity currents II. Uniform flow of density currents. *Canadian Journal of Earth Sciences* 3, 627–637.

- Middleton, G.V., 1967. Experiments on density and turbidity currents III. Deposition of sediment. *Canadian Journal of Earth Sciences* 4, 475–505.
- Middleton, G.V., 1969. Turbidity currents. In: Stanley, D.J. (Ed.), *The New Concepts of Continental Margin Sedimentation: Application to the Geological Record*. American Geological Institute, short course, Lecture 10.
- Middleton, G.V., 1993. Sediment deposition from turbidity currents. *Annual Review of Earth and Planetary Sciences* 21, 89–114.
- Middleton, G.V., Hampton, M.A., 1973. Sediment gravity flows: mechanics of flow and deposition. In: Middleton, G.V., Bouma A.H. (Eds.), *Turbidity and Deep Water Sedimentation*. SEPM, Pacific Section, Short Course Lecture Notes, Anaheim, pp. 1–38.
- Middleton, G.V., Hampton, M.A., 1976. Subaqueous sediment transport and deposition of sediment gravity flows. In: *Marine Sediment Transport and Environmental Management*. Wiley, New York, pp. 197–218.
- Middleton, G.V., Southard, J.B., 1984. *Mechanics of sediment movement*. SEPM, Short Course 3, 401 pp.
- Migeon, S., Savoye, B., Faugères, J.-C., 2000. Quaternary development of migrating sediment waves in the Var deep-sea fan: distribution, growth pattern, and implication for levee evolution. *Sedimentary Geology* 133, 265–293.
- Migeon, S., Savoye, B., Zanella, E., Mulder, T., Faugères, J.-C., Weber, O., 2001. Detailed seismic-reflection and sedimentary study of turbidite sediment waves on the Var Sedimentary Ridge (SE France): significance for sediment transport and deposition and for the mechanism of sediment-wave construction. *Marine and Petroleum Geology* 18, 179–208.
- Milliman, J.D., Syvitski, J.P.M., 1992. Geomorphic/tectonic control of sediment discharge to the ocean: the importance of small mountainous rivers. *J. Geol.* 100, 525–544.
- Mohr, M., Kukla, P.A., Urai, J.L., Bresser, G., 2005. Multiphase salt tectonic evolution in NW Germany. Seismic interpretation and retro-deformation. *International Journal of Earth Sciences* 94, 917–940.
- Mohriak, W.U., Azatmari, P., Anjos, S., 2012. Salt: geology and tectonics of selected Brazilian basins in their global context. In: Alsop, G.I., Archer, S.G., Hartley, A.J., Grant, N.T., Hodgkinson, R. (Eds.), *Salt Tectonics, Sediments, Prospectivity*. Geol. Soc. London Spec. Publ. 363, pp. 131–158.
- Mohriak, W.U., Leroy, S., 2013. Architecture of rifted continental margins and break-up evolution: insights from the South Atlantic, North Atlantic and Red Sea–Gulf of Aden conjugate margins. In: Mohriak, W.U., Danforth, A., Post, P.J., Brown, D.E., Tari, G.C., Nemcok, M., Sinha, S.T. (Eds.), *Conjugate Divergent Margins*. Geol. Soc. London Spec. Publ. 369, pp. 497–535.
- Mohriak, W.U., Macedo, J.M., Castellani, R.T., Rangel, H.D., Barros, A.Z.N., Latge, M.A., Ricci, J.A., Mizusaki, A.M., Szatmari, P., Demercian, L.S., Rizzo, J.G., Aires, J.R., 1995. Salt tectonics and structural styles in the deep water province of the Cabo Frio Region, Rio de Janeiro, Brazil. In: Jackson, M.P.A., Roberts, D.G., Snelson, S. (Eds.), *Salt Tectonics: A Global Perspective*. AAPG Memoir 65, pp. 305–321.
- Mohriak, W.U., Nemcok, M., Enciso, G., 2008. South Atlantic divergent margin evolution: rift-border uplift and salt tectonics in the basins of SE Brazil. In: Pankhurst, R.J.,

- Trouw, R.A.J., Brito Neves, B.B., de Wit, M.J. (Eds.), West Gondwana Pre-Cenozoic Correlations across the South Atlantic Region. *Geol. Soc. London Spec. Publ.* 294, pp. 365–398.
- Moody, J.D., Pyles, D.R., Clark, J., Bouroulec, R., 2012. Quantitative outcrop characterization of an analog to weakly confined submarine channel systems: Morillo 1 Member, Ainsa Basin, Spain. *American Association of Petroleum Geologists Bulletin* 96, 1813–1841.
- Moraes, M.A.S., Becker, M.R., Monteiro, M.C., Netto, S.L.A., 2000. Using outcrop analogues to improve 3D heterogeneity modelling of Brazilian sand-rich turbidite reservoirs. Gulf-coast section SEPM Foundation Seventeenth Annual Research Conference, 587–605.
- Morelock, J., 2004. Margin Structure. *Geological Oceanography*.
<http://geology.uprm.edu/Morelock/margstruct.htm>
- Morris, S.A., Alexander, J., Kenyon, N.H., Limonov, A.F., 1998. Turbidites around an active fault scarp on the Lower Valencia Fan, northwest Mediterranean. *Geo-Marine Letters* 18, 165–171.
- Mulder, T., 2011. Gravity processes and deposits on continental slope, rise and abyssal plains. In: Huneke, H., Mulder, T. (Eds.), *Deep-Sea Sediments. Developments in Sedimentology*, Elsevier, Amsterdam, Vol. 63, pp. 24–148.
- Mulder, T., Alexander, J., 2001. The physical character of sedimentary density currents and their deposits. *Sedimentology* 48, 269–299.
- Mulder, T., Cochonat, P., 1996. Classification of offshore mass movements. *J. Sed. Res.* 66, 43–57.
- Mulder, T., Syvitski, J.P.M., 1995. Turbidity currents generated at river mouths during exceptional discharges to the world oceans. *J. Geol.* 103, 285–299.
- Mulder, T., Syvitski, J.P.M., Migeon, S., Faugeres, J.-C., Savoye, B., 2003, Marine hyperphycnal flows: initiation, behavior and related deposits. A review. *Marine and Petroleum Geology* 20, 861–882.
- Mulder, T., Syvitski, J.P.M., Skene, K.I., 1998. Modelling of erosion and deposition by turbidity currents generated at river mouths. *J. Sed. Res.* 68, 124–137.
- Mulder, T., Weber, O., Anschutz, P., Jorissen, F.J., Jouanneau, J.-M., 2001. A few months-old storm-generated turbidite deposited in the Capbreton Canyon (Bay of Biscay, S-W France). *Geo-Mar. Lett.* 21, 149–156.
- Mutti, E., 1979. Turbidites et cônes sous-marins profonds. In: Homewood, P (Ed.), *Sédimentation Détritique (Fluviatile, Littorale et Marine)*, Short Course. Fribourg, Institut de Geologie de l'Université de Fribourg, pp. 353–419.
- Mutti, E. 1985. Turbidite systems and their relations to depositional sequences. In: Zuffa, G.G. (Ed.), *Provenance of arenites*. NATO-ASI Series, Reidel Publishing Company, pp. 65–93.
- Mutti, E., Bernoulli, D., Ricci Lucchi, F., Tinterri, R., 2009. Turbidites and turbidity currents from Alpine 'flysch' to the exploration of continental margins. *Sedimentology* 56, 267–318.
- Mutti, E., Davoli, G., Mora, S., Papani, L., 1994. Internal stacking patterns of ancient turbidite systems from collisional basins. GCSSEPM Foundation 15th Annual Research Conference Submarine Fans and Turbidite Systems, 257–268.

- Mutti, E., Davoli, G., Tinterri, R. and Zavala, C., 1996. The importance of ancient fluvio-deltaic systems dominated by catastrophic flooding in tectonically active basins. *Sci. Geol. Mem.* 48, 233–291.
- Mutti, E., Ricci Lucchi, F., 1975. Turbidite facies and facies association. Field Trip All. 9th Int. Sed. Congr., Nice, 21–36.
- Mutti, E., Sonnino, M., 1981. Compensation cycles: a diagnostic feature of sandstone lobes. International Association of Sedimentologists, 2nd European Meeting, Bologna, 120–123.
- Mutti, E., Tinterri, R., Ramacha, E., Mavilla, N., Angella, S., Fava, L., 1999. An introduction to the analysis of ancient turbidite basins from an outcrop perspective. AAPG course notes. 39, 93 p.
- Nakajima, T., 2006. Hyperpycnites deposited 700 km away from river mouths in the central Japan Sea. *Journal of Sedimentary Research* 76, 59–72.
- Nardin, T.R., Hein, F.J., Gorsline, D.S., Edwards, B.D., 1979. A review of mass movement processes, sediment and acoustic characteristics, and contrasts in slope and base-of-slope systems versus canyon-fan-basin floor systems. In: Doyle, L.J., Pilkey, O.H. (Eds.), *Geology of Continental Slopes*. SEPM Spec. Publ. 27, pp. 61–73.
- Nettleton, L.L., 1995. History of concepts of Gulf Coast salt-dome formation. AAPG Bull. 39, 2373–2383.
- Nilsen, K.T., Vendeville, B.C., Johansen, J.-T., 1995. Influence of regional tectonics on halokinesis in the Nordkapp Basin, Barents Sea. In: Jackson, M.P.A., Roberts, D.G., Snelson, S. (Eds.), *Salt Tectonics: A Global Perspective*. AAPG Memoir 65, pp. 413–436.
- Normark, W.R., 1970. Growth patterns of deep-sea fans. *American Association of Petroleum Geologists Bulletin* 54, 2170–2195.
- Normark, W.R., 1978. Fan valley, channels, and depositional lobes on modern submarine fans: characters for recognition of sandy turbidite environments. *Am. Assoc. Pet. Geol. Soc. Lond., Spec. Pucl.*, 94, 63–76.
- Oluboyo, A.P., Gawthorpe, R.L., Bakke, K., Hadler-Jacobsen, F., 2014. Salt tectonic control on deep-water turbidite depositional systems: Miocene, southwestern Lower Congo Basin, offshore Angola. *Basin Research* 26, 597–620.
- Panien, M., Schreurs, G., Pfiffner, A., 2006. Mechanical behavior of granular material used in analogue modelling: insights from grain characterisation, ring-shear test and analogue experiments. *Journal of Structural Geology* 28, 1710–1724.
- Pantin, H.M., Leeder, M.R., 1987. Reverse flow in turbidity currents: the role of internal solitons. *Sedimentology*, 34, 1143–1155.
- Parker, G., Fukushima, Y., Pantin, H.M., 1986. Self-accelerating turbidity currents. *Journal of Fluid Mechanics* 171, 145–181.
- Parson, J.D., 1998. Mixing mechanics in density intrusions. Ph. D. thesis, University of Illinois, Urbana-Champaign.
- Peakall, J., McCaffrey, B., Kneller, B., 2000. A process model for the evolution, morphology, and architecture of sinuous submarine channels. *Journal of Sedimentary Research* 70, 434–448.
- Peel, F.J., Travis, C.J., Hossack, J.R., 1995. Genetic structural provinces and salt tectonics of the Cenozoic offshore US Gulf of Mexico: a preliminary analysis. In: Jackson,

- M.P.A., Roberts, D.G., Snelson, S. (Eds.), Salt Tectonics: A Global Perspective. AAPG Memoir 65, pp. 153–175.
- Peron-Pinvidic, G., Manatschal, G., 2009. The final rifting evolution at deep magma-poor passive margins from Iberia-Newfoundland: a new point of view. *Int. J. Earth Sci.* 98, 1581–1597.
- Philippe, Y., Wittoesch, D., Guerin, G., 2005. Importance of gravity-driven compressional tectonics in northern offshore and deep-offshore Gulf of Mexico: New observations and implications for subsalt interpretation (abs.). AAPG International Conference, AAPG Search and Discovery article 90046, accessed April 19, 2013, http://www.searchanddiscovery.com/documents/abstracts/2005intl_paris/philippe.htm.
- Philippou, M., Corti, G., Sani, F., Bonini, M., Balestrieri, M-L, Molin, P., Willingshofer, E., Sokoutis, D., Cloetingh, S., 2014. Evolution, distribution, and characteristics of rifting in southern Ethiopia. *Tectonics* 33, 485–508.
- Pickering K.T., Hiscott, R.N., 1985. Contained (reflected) turbidity currents from the Middle Ordovician Cloridorme Formation, Quebec, Canada: an alternative to the antidune hypothesis. *Sedimentology* 32, 373–394.
- Pickering, K.T., Hiscott, R.N., Hein, F.J., 1989. Deep marine environments: clastic sedimentation and tectonics. Unwin Hyman, London, 416 pp.
- Pindell, J., Kennan, L., 2001. Kinematic evolution of the Gulf of Mexico and Caribbean. In: Fillon, R.H., Rosen, N.C., Weimer, P., Lowrie, A., Pettingill, H., Phair, R.L., Roberts, H.H., van Hoorn, B. (Eds.), *Petroleum Systems of Deep-Water Basins: Global and Gulf of Mexico Experience*. 21st Annual GCSSEPM Foundation Bob F. Perkins Research Conference, Houston, pp. 193–220.
- Pindell, J., Kennan, L., 2009. Tectonic evolution of the Gulf of Mexico, Caribbean and northern South America in the mantle reference frame: an update. In: James, K., Lorente, M., Pindell, J. (Eds.), *The Origin and Evolution of the Caribbean Plate*, *Geol. Soc. London Spec. Publ.*, vol. 328, pp. 1–55.
- Pirmez, C., Imran, J. 2003. Reconstruction of turbidity currents in Amazon Channel. *Marine and Petroleum Geology* 20, 823–829.
- Podladchikov, Y., Talbot, C., Poliakov, A.N.B., 1993. Numerical models of complex diapirs. *Tectonophysics* 228, 189–198.
- Poliakov, A.N.B., Podladchikov, Y., Talbot, C., 1993. Initiation of salt diapirs with frictional overburdens: numerical experiments. *Tectonophysics* 228, 199–210.
- Porebski, S.J., Meischner, D., Görlich, K., 1991. Quaternary mud turbidites from the South Shetland Trench (West Antarctica): recognition and implication for turbidite facies modelling. *Sedimentology* 38, 691–715.
- Posamentier, H.W., 2001. On the role of flow stripping and the deposition of channel levees and frontal splays in deep-water systems; evidence from 3-D seismic data. AAPG Convention Abstracts with Program, p. A160.
- Prather, B.E., 2000. Calibration and visualization of depositional process models for above-grade slopes: A case study from the Gulf of Mexico. *Marine and Petroleum Geology* 17, 619–638.
- Prather, B.E., 2003. Controls on reservoir distribution, architecture and stratigraphic trapping in slope settings. *Marine and Petroleum Geology* 20, 529–545.

- Prather, B.E., Booth, J.R., Steffens, G.S., and Craig, P.A., 1998. Classification, lithologic calibration, and stratigraphic succession of seismic facies of intraslope basins, deep-water Gulf of Mexico. *American Association of Petroleum Geologists Bulletin* 82, 701–728.
- Prather, B.E., Pirmez, C., Winker, C.D., 2012. Stratigraphy of linked intraslope basins: Brazos-Trinity system western Gulf of Mexico. *SEPM Special Publication* 99, 83–109.
- Pratson, L.F., Haxby, W.F., 1996. What is the slope of U.S. continental slope? *Geology* 24, 3–6.
- Pratson, L.F., Imran, J., Parker, G., Syvitski, J.P.M., Hutton, E., 2000. Debris flows vs. turbidity currents: a modeling comparison of their dynamics and deposits. In: Bouma, A.H., Stone, C.G. (Eds.), *Fine-grained turbidite systems*. AAPG Memoir 72/SEPM Special Publication 68, p. 57–71.
- Prior, D.B., Suhayda, J.N. Lu, N.-Z., Bornhold, B.D., Keller, G.H., Wiseman, W.J., et al., 1989. Storm wave reactivation of a submarine landslide. *Nature* 341, 47–50.
- Prochnow, S.J., Atchley, S.C., Boucher, T.E., Nordt, L.C., Hudec, M.R., 2006. The influence of salt withdrawal subsidence on paleosol maturity and cyclic fluvial deposition in the Upper Triassic Chinle Formation: Castle Valley, Utah. *Sedimentology* 53, 1319–1345.
- Prochnow, S.J., Nordt, L.C., Atchley, S.C., Hudec, M., Boucher, T.E., 2005. Triassic paleosol catenas associated with a salt-withdrawal minibasin in southeastern Utah, U.S.A.. *Rocky Mountain Geology* 40, 25–49.
- Quirk, D.G., Hertle, M., Jeppesen, J.W., Raven, M., Mohriak, W.U., Kann, D.J., Nørgaard, M., Howe, M.J., Hsu, D., Coffey, B., Mendes, M.P., 2013. Rifting, subsidence and continental break-up above a mantle plume in the central South Atlantic. In: Mohriak, W.U., Danforth, A., Post, P.J., Brown, D.E., Tari, G.C., Nemcok, M., Sinha, S.T. (Eds.), *Conjugate Divergent Margins*. *Geol. Soc. London Spec. Publ.*, vol. 369, pp. 185–214.
- Quirk, D.G., Pilcher, R. 2005. 'Flip-flop' salt tectonics. AAPG international conference and Exhibition, Paris, 11-14 September, Abstract Volume, A58.
- Quirk, D.G., Pilcher, R., 2012. Flip-flop salt tectonics. In: . In: Alsop, G.I., Archer, S.G., Hartley, A.J., Grant, N.T., Hodgkinson, R. (Eds.), *Salt Tectonics, Sediments and Prospectivity*. *Geol. Soc. London Spec. Publ.*, vol. 363, pp. 245–264.
- Quirk, D.G., Schødt, N., Lassen, B., Ings, S.J., Hsu, D., Hirsch, K.K., Von Nicolai, C., 2012. Salt tectonics on passive margins: examples from Santos, Campos and Kwanza basins. In: Alsop, G.I., Archer, S.G., Hartley, A.J., Grant N.T., Hodgkinson, R. (Eds.), *Salt Tectonics, Sediments, Prospectivity*. *Geol. Soc. London Spec. Publ.* 363, pp. 207–244.
- Rahimpour-Bonab, H., Shariatnia, Z., Siemann, M.G., 2007. Role of rifting in evaporite deposition in the Great Kavir Basin, central Iran. In: Schreiber, B.C., Lugli, S., Babel, M. (Eds.), *Evaporites Through Space and Time*. *Geol. Soc. London Spec. Publ.*, vol. 285, pp. 69–85.
- Ramberg, H., 1981. *Gravity, deformation and the Earth's crust*. Academic Press, NewYork.
- Reading, H.G., Richards, M., 1994. Turbidite systems in deep-water basin margins classified by grain size and feeder system. *AAPG Bulletin* 78, 792–822.

- Ricci Lucchi, F., Valmori, E., 1980. Basin-wide turbidites in a Miocene, oversupplied deep-sea plain: a geometrical analysis. *Sedimentology* 27, 241–270.
- Roberts, M.J., Metzgar, C.R., Liu, J., Lim, S.J., 2004. Regional assessment of salt weld timing, Campos Basin, Brazil. In: Post, P.J., Olson, D.L., Lyons, K.T., Palmes, S.L., Harrison, P.F., Rosen, N.C. (Eds.), *Salt-sediment interactions and hydrocarbon prospectivity: Concepts, applications, and case studies for the 21st Century*. 24th Annual Research Conference Proceedings, Houston, Texas, Society of Economic Paleontologist and Mineralogists, Gulf Coast Section, pp. 371–389.
- Roca, E., Munoz, J.A., Ferrer, O., Ellouz, N., 2011. The role of the Bay of Biscay Mesozoic extensional structure in the configuration of the Pyrenean orogen: constraints from the MARCONI deep seismic reflection survey. *Tectonics* 30. TC2001. DOI: 10.1029/2010TC002735.
- Rothwell, R.G., Pearce, T.J., Weaver, P.P.E., 1992. Late Quaternary evolution of the Madeira Abyssal Plain, Canary Basin, NE Atlantic. *Basin Research* 4, 103–132.
- Rottman, J.W., Simpson, J.E., 1989. The formation of internal bores in the atmosphere: a laboratory model. *Quart. J. Royal Met. Soc.* 115, 941–963.
- Rottman, J.W., Simpson, J.E., Hunt, J.C.R., 1985. Unsteady gravity current flow over obstacles: some observations and analysis related to the Phase II trials. *J. Hazardous Materials* 11, 325–340.
- Rouby, D., Raillard, S., Guillocheau, F., Bouroullec, R., Nalpas, T., 2002. Kinematics of a growth/raft system on the West African margin using 3-D restoration. *Journal of Structural Geology* 24, 783–796.
- Rouchy, J., Blanc-Valleron, M., 2006. Les évaporites. *Matériaux singuliers, milieu extrêmes*. Collection «Interactions». Vuibert, Paris. 190 p.
- Rowan, M.G., 1995. Structural styles and evolution of allochthonous salt, central Louisiana outer shelf and upper slope. In: Jackson, M.P.A., Roberts, D.G., Snelson, S. (Eds.), *Salt Tectonics: A Global Perspective*. AAPG Memoir 65, pp. 198–228.
- Rowan, M.G., 2014. Passive-margin salt basins: hyperextension, evaporate deposition, and salt tectonics. *Basin Research* 25, 154–182.
- Rowan, M.G., Peel, F.J., Vendeville, B.C., 2004. Gravity driven fold belts on passive margins. In: K.R., McClay (Eds.), *Thrust Tectonics and Hydrocarbon Systems*. AAPG Mem. 82, pp. 157–182.
- Rowan, M.G., Peel, F.J., Vendeville, B.C., Gaullier, V., 2012. Salt tectonics at passive margins: geology versus models—discussion. *Mar. Petrol. Geol.* 37, 184–194.
- Rowan, M.G., Trudgil, B.D., Fiduk, J.C., 2000. Deep-water, salt-cored foldbelts: lessons from the Mississippi Fan and Perdido foldbelts, northern Gulf of Mexico. In: Webster, M., Talwani, M. (Eds.), *Atlantic Rifts and Continental Margins*. Geophys. Monogr. 115, pp. 173–191.
- Rowan, M.G., Vendeville, B.C., 2006. Foldbelts with early salt withdrawal and diapirism: Physical model and examples from the northern Gulf of Mexico and the Flinders Ranges, Australia. *Marine and Petroleum Geology* 23, 871–891.
- Rowan, M.G., Weimer, P., 1998. Salt-sediment interaction, central Louisiana outer shelf and upper slope, northern Gulf of Mexico. *AAPG Bulletin* 82, 1055–1082.
- Salles, T., Lopez, S., Eschard, R., Lerat, O., Mulder, T., Cacas, M., 2008. Turbidity current modelling on geological time scales. *Marine Geology* 248, 127–150.

- Salvador, A., 1987. Late Triassic–Jurassic paleogeography and origin of Gulf of Mexico basin: American Association of Petroleum Geologists Bulletin, vol. 71, pp. 419–451.
- Salvador, A., 1991. Origin and development of the Gulf of Mexico basin. In: Salvador, A. (Ed.), The Gulf of Mexico Basin. Geol. NA, vol. J. Geological Society of America, Boulder, pp. 389–444.
- Sanders, J.E., 1965. Primary sedimentary structures formed by turbidity currents and related resedimentation mechanisms. In: Middleton, G.V. (Ed.), Primary sedimentary structures and their hydrodynamic interpretation. SEPM Spec. Publ. 12, pp. 192–219.
- Satur, N., Hurst, A., Cronin, B.T., Kelling, G., Gürbüz, K. 2000. Sand body geometry in a sand-rich, deep-water clastic system, Miocene Cingöz Formation of southern Turkey. Marine and Petroleum Geology 17, 239–252.
- Sawyer, D.S., Buffler, R.T., Pilger, R.H., Jr., 1991. The crust under the Gulf of Mexico basin, In: Salvador A. (Ed.), The Gulf of Mexico Basin. The Geology of North America, Geological Society of America, Boulder, Colorado, vol. J, pp. 53–72.
- Schellart, W.P., 2002. Analogue modeling of large-scale tectonic processes: an introduction. In: Schellart, W.P., Passchier, C. (Eds.), Analogue modeling of large-scale tectonic processes. Journal of the Virtual Explorer, vol. 7, pp. 1–6.
- Schlee, J. H., 1980. A comparison of two Atlantic-type continental margins. Geological Survey Professional Paper 1167, United State Government Printing Office, Washington.
- Schultz-Ela, D.D., 2001. Excursus on gravity gliding and gravity spreading. Journal of Structural Geology 23, 725–731.
- Seglund, J.A., 1974. Collapse-fault systems of Louisiana Gulf Coast. American Association of Petroleum Geologists Bulletin 58, 2389–2397.
- Shanmugam, G., 2000. 50 years of the turbidite paradigm (1950s–1990s): deep-water processes and facies models. Marine and Petroleum Geology 17, 85–342.
- Shanmugam, G., Moiola, R.J., 1988. Submarine fans: characteristics, models, classification, and reservoir potential. Earth Sci. Rev. 24, 383–428.
- Shanmugam, G., Moiola, R.J., 1991. Types of submarine fan lobes: models and implications. Am. Assoc. Pet. Geol. Bull. 75, 156–179.
- Shanmugam, G., Moiola, R.J., McPherson, J.G., O’Connel, S. 1988. Comparison of modern Mississippi fan with selected ancient fans. Gulf Coast Assoc. Geol. Soc. Trans. 38, 157–165.
- Shimeld, J., 2004, A comparison of salt tectonic subprovinces beneath the Scotian slope and Laurentian fan. In: Post, P.J., Olson, D.L., Lyons, K.T., Palmes, S.L., Harrison, P.F., Rosen, N.C. (Eds.), Salt-sediment interactions and hydrocarbon prospectivity: Concepts, applications, and case studies for the 21st Century. 24th Annual Research Conference Proceedings, Houston, Texas, Society of Economic Paleontologist and Mineralogists, Gulf Coast Section, pp. 502–532.
- Siegenthaler, C., Buhler, J., 1985. The kinematics of turbulent suspension currents (turbidity currents) on inclined boundaries. Marine Geology 64, 19–40.
- Simpson, J.E., 1997. Gravity currents in the Environment and the Laboratory. 2nd ed. Ellis Horwood Series In Environmental Science. Cambridge University Press, UK.
- Simpson, J.E., Britter, R.E., 1979. The dynamics of the head of a gravity current advancing over a horizontal surface. J. Fluid Mech. 94, 477–495.

- Sinclair, H.D., 1994. The influence of lateral basinal slopes on turbidite sedimentation in the Annot Sandstones of SE France. *Journal of Sedimentary Research*, A64, 42–54.
- Sinclair H.D., Tomasso, M., 2002. Depositional evolution of confined turbidite basins. *Journal of Sedimentary Research* 72, 451–456.
- Singh, S.C., 2005. Sumatra earthquake research indicates why trpture propagated northward. *EOS Trans. Am. Geophys. Union* 86 (48), 497–502.
- Skene, K.I., Mulder, T. and Syvitski, J.P.M. (1997) INFL01: a model predicting the behaviour of turbidity currents generated at river mouths. *Comput. Geosci.*, 23, 975–991.
- Sloff, C.J., 1997. *Sedimentation in Reservoirs*. Delft University of Technology, Delft, Ph.D. thesis, 270 p.
- Smith, R., 2004. Silled sub-basins to connected tortuous corridors: sediment distribution systems on topographically complex sub-aqueous slopes. In: Lomas, S.A., Joseph, P. (Eds.), *Confined Turbidite Systems*. *Geol. Soc. London Spec. Publ.* 222, pp. 23–44.
- Sokoutis, D., Willingshofer, E., 2011. Decoupling during continental collision and intra-plate deformation. *Earth and Planetary Science Letters* 305, 435–444.
- Soreghan, M.J., Scholz, C.A., Wells, J.T., 1999. Coarse-grained, deep-water sedimentation along a border fault margin of Lake Malawi, Africa: seismic stratigraphic analysis. *Journal of Sedimentary Research* 69, 832–846.
- Soyinka, O.A., R.M. Slatt, 2004. Thin-bedded turbidite and hyperpyncite(?) mudstones in the Cretaceous Lewis Shale, Carbon County, Wyoming: Preliminary results. In : Scott, E.D., Bouma, A.H. (Eds.), *Depositional processes and characteristics of siltstones, mudstones and shales*. *Spec. Symposium AAPG-SEPM Annual Meeting*, Dallas.
- Spathopoulos, F., 1996. An insight on salt tectonics in the Angola Basin, South Atlantic. In: Blundel, D.J., Alsop, G.I., Davison, J. (Eds.), *Salt Tectonics*. *Geol. Soc. London Spec. Publ.* 100, pp. 153–174.
- Spindler, W.M., 1977. Structure and stratigraphy of a small Plio-Pleistocene depocenter, Louisiana continental shelf. *Gulf Coast Association of Geological Societies Transactions* 27, 180–197.
- Stacey, M.W., Bowen, A.J., 1988. Vertical structure of density of turbidity currents: theory and observations. *J. Geophys. Res.* 93, 3528–3542.
- Steckler, M.S., Watts, A.B., 1978. Subsidence of the Atlantic-type continental margin off New York. *Earth and Planet. Sci, Lett.* 41, 1–13.
- Stern, R.J., Dickinson, W.R., 2010. The Gulf of Mexico is a Jurassic backarc basin. *Geosphere* 6, 739–754.
- Stewart, S.A., Clark, J.A., 1999. Impact of salt on the structure of the central North Sea hydrocarbon fairways. In: Fleet, A.J., Boldy, S.A.R. (Eds.), *Petroleum geology of northwest Europe*. *Proceedings of the 5th Conference*, London, Geological Society of London, pp. 179–200.
- Stow, D.A.V., 1986. Deep clastic seas. In: Reading, H.G. (Ed.), *Sedimentary Environments and Facies*. Blackwell Publishing, Oxford, pp. 399–444.

- Stow, D.A.V., Reading, H.G., Collinson, J.D., 1996. Deep seas. In: Reading, H.G. (Ed.), *Sedimentary Environments: Processes, Facies and Stratigraphy*. Blackwell Science, Oxford, pp. 395–453.
- Stow, D.A.V., Shanmugam, G., 1980. Sequence of structures in fine-grained turbidites: comparison of recent deep-sea and ancient flysch sediments. *Sedimentary Geology* 25, 23–42.
- Sumner, H.S., Robinson, B.A., W.K., Dirks, Holliday, J.C., 1991. Morphology and evolution of salt/mini-basin systems: Lower slope and upper slope, central offshore Louisiana (abs.). *Houston Geological Society Bulletin* 33, 11.
<http://www.searchanddiscovery.com/abstracts/html/1991/gcags/abstracts/1539.htm>
- Syvitski, J.P.M., Hein, F.J., 1991. Sedimentology of an arctic basin: Itirbilung Fjord, Baffin Island, Northwest Territories. *Geo. Survey of Can. Paper*, 91–11.
- Syvitski, J.P.M., Schafer, C.T., 1996. Evidence for an earthquake-triggered basin collapse in Saguenay Fjord, Canada. *Sedim. Geol.* 104, 127–153.
- Talbot, C.J., 1992. Centrifuged models of Gulf of Mexico profiles. *Marine and Petroleum Geology* 9, 412–432.
- Talbot, C.J., Tully, C.P., Woods, P.J.E., 1982. The structural geology of Boulby (Potash) Mine, Cleveland, United Kingdom. *Tectonophysics* 85, 167–204.
- Talling, P.J., 2014. On the triggers, resulting flow types and frequencies of subaqueous sediment density flows in different settings. *Marine Geology* 352, 155–182.
- Talling, P.J., Peakall, J., McCaffrey, W., Amy, L., Sparks, S., 2001. How viscosity and density stratification changes submarine mass flow behavior. *AAPG Convention Abstracts with Program*, p. A197.
- Tankard, A.J., Balkwill, H.R., 1989. Extensional tectonics and stratigraphy of the North Atlantic margins. *AAPG Memoir* 46, 641 pp.
- Tari, G.C., Ashton, P.R., Cotterill, K.L., Molnar, J.S., Sorgenfrei, M.C., Thompson, P.W.A., Valasek, D.W., Fox, J.F., 2001. Examples of deep-water salt tectonics from West Africa: are analogs to the deep-water salt-cored foldbelts of the Gulf of Mexico? In: *GCSSEPM Foundation 21th Annual Bob F. Perkins Research Conference*, pp. 251–270.
- Tari, G.C., Ashton, P.R., Cotterill, K.L., Molnar, J.S., Sorgenfrei, M.C., Thompson, P.W.A., Valasek, D.W., Fox, J.F., 2002. Are West Africa deepwater salt tectonics analogues to the Gulf of Mexico? *Oil Gas J.* 4, 73–81.
- Tari, G.C., Molnar, J., Ashton, P., 2003. Examples of salt tectonics from West Africa: A comparative approach. In: Arthur, T.J., MacGregor, D.S., Cameron, N.R. (Eds.), *Petroleum Geology of Africa: New themes and developing technologies*. *Geol. Soc. London Spec. Publ.* 207, pp. 85–104.
- Thornburg, T.M., Kulm, L.D., Hussong, D.M., 1990. Submarine-fan development in the southern Chile Trench: A dynamic interplay of tectonics and sedimentation. *Geological Society of America Bulletin* 102, 1658–1680.
- Torsvik, T.H., Rousse, S., Labails, C., Smethurst, M., 2009. A new scheme for the opening of the South Atlantic Ocean and the dissection of an Aptian salt basin. *Geophys. J. Int.* 177, 1315–1333.
- Trudgill, B.D., Rowan, M.G., Fiduk, J.C., Weimer, P., Gale, P.E., Korn, B.E., Phair, R.L., Gafford, W.T., Roberts, G.R., Dobbs, S.W., 1999. The Perdido fold belt, northwestern

- deep Gulf of Mexico, Part 1: Structural geometry, evolution and regional implications. *AAPG Bulletin* 83, 88–113.
- Trusheim, F., 1960. Mechanism of salt migration in northern Germany, *AAPG Bull.* 9, 1519–1540.
- Uchupi, E., Austin, J.A., Jr., 1979. The stratigraphy and structure of the Laurentian Cone region. *Canadian Journal of Earth Sciences* 16, 1726–1752.
- Unternehm, P., Péron-Pinvidic, G., Manatschal, G., Sutra, E., 2010. Hyper-extended crust in the South Atlantic: in search of a model. *Petrol. Geosci.* 16, 207–215.
- Unterseh, S., 1999. Cartographie et caractérisation du fond marin par sondeur multifaisceaux. Unpubl. PhD. Thesis, Univ. Nancy, 234pp.
- Van Andel, T.H., Komar, D., 1969. Ponded sediments of the Mid-Atlantic Ridge between 22° and 23° North Latitude. *Geological Society of America Bulletin* 80, 1163–1190.
- Van der Merwe, W.C., Hodgson, D.M., Brunt, R.L., Flint, S.S., 2014. Depositional architecture of sand-attached and channel-lobe transition zones on an exhumed stepped slope mapped over a 2500 km² area. *Geosphere* 10, 1076–1093.
- Vendeville, B.C., 1987. Champs de failles et tectonique en extension: Modelisation expérimentale: Rennes, Mémoire de Géosciences Thesis. Université de Rennes I, 392 p.
- Vendeville, B.C., 2005. Salt tectonics driven by sediment progradation: Part I–Mechanics and kinematics. *American Association of Petroleum Geologists Bulletin* 89, 1071–1079.
- Vendeville, B.C., Cobbold, P.R., 1987. Syn-sedimentary gravitational sliding and listric normal growth faults: Insights from scaled physical models. *Comptes Rendus de l'Académie des Sciences de Paris*, v. 305, série IIa, pp. 1313–1319.
- Vendeville, B.C., Cobbold, P.R., 1988. How normal faulting and sedimentation interact to produce listric fault profiles and stratigraphic wedges. *Journal of Structural Geology* 10, 649–659.
- Vendeville, B.C., Jackson, M.P.A., 1991. Deposition, extension, and the shape of downbuilding salt diapirs. *Am. Assoc. Petrol Geol. Bull.* 75, 683 pp.
- Vendeville, B.C., Jackson, M.P.A., 1992a. The rise of diapirs during thin-skinned extension. *Marine and Petroleum Geology* 9, 331–353.
- Vendeville, B.C., Jackson, M.P.A., 1992b. The fall of diapirs during thin-skinned extension. *Marine and Petroleum Geology* 9, 354–371.
- Vendeville, B.C., Nilsen, K.T., 1995. Episodic growth of salt diapirs driven by horizontal shortening. In: Travis, C.J., Harrison, H., Hudec, M.R., Vendeville, B.C., Peel, F.J., Perkins, B.F. (Eds.), *Salt, sediment, and hydrocarbons*. SEPM Foundation, Gulf Coast Section, 16th Annual Research Conference Program with Papers, pp. 285–295.
- Venus, J.H., Mountney, N.P., McCaffrey, W.D., 2014. Syn-sedimentary salt diapirism as a control on fluvial-system evolution: an example from the proximal Permian Culter Group, SE Utah, USA. *Basin Research*. DOI: 10.1111/bre.12066.
- Volozh, Y., Talbot, C., and Ismail-Zadeh, A., 2003. Salt structures and hydrocarbons in the Pricaspian basin. *American Association of Petroleum Geologists Bulletin* 87, 313–334.
- Walker, R.G., 1978. Deep-water sandstone facies and ancient submarine fans: models for exploration for stratigraphic traps. *American Association of Petroleum Geologists Bulletin* 62, 932–966.

- Warren, J., 2006. *Evaporites: Their Evolution and Economics*, second ed. Blackwell Science, Oxford. 438 p.
- Watts, A.B., Steckler, M.S., 1981. Subsidence and tectonics of Atlantic type continental margins. *Oceanologica Acta, Colloque C3, Geology of Continental Margins* 4, 143–154.
- Weijermars, R., 1986a. Finite strain of laminar flows can be visualized in SGM36-polymer. *Naturwissenschaften* 73, 33–34.
- Weijermars, R., 1986b. Flow behaviour and physical chemistry of bouncing putties and related polymers in view of tectonic laboratory applications. *Tectonophysics* 124, 325–358.
- Weijermars, R., Jackson, M.P.A., Vendeville, B., 1993. Rheological and tectonic modeling of salt provinces. *Tectonophysics* 217, 143–174.
- Weimer, P., Varnai, P., Budhijanto, F.M. et al. 1998. Sequence stratigraphy of Pliocene and Pleistocene turbidite systems, northern Green Canyon and Ewing Bank (offshore Louisiana), northern Gulf of Mexico. *AAPG Bulletin* 82, 918–960.
- Weimer, P., Slatt, R.M., 2007. Introduction to the petroleum geology of deepwater settings. *AAPG Studies in Geology*, No. 57; *AAPG/Datapages Discovery Series*, No. 8.
- Weinberger, R., Lyakhovsky, V., Baer, G., Begin, Z.B., 2006. Mechanical modeling and InSAR measurements of Mount Sedom uplift, Dead Sea basin: Implications of effective viscosity of rock salt. *Geochemistry, Geophysics, Geosystems* 7, 1–20.
- Willingshofer, E., Sokoutis, D., Burg, J.-P., 2005. Lithospheric-scale analogue modelling of collision zones with a pre-existing weak zone. In: Gapais, D., Brun, J.P., Cobbold, P.R. (Eds.), *Deformation Mechanisms, Rheology and Tectonics: from Minerals to the Lithosphere*. The Geological Society of London, Special Publications, 243, 277–294.
- Willingshofer, E., Sokoutis, D., Luth, S.W., Beekman, F., Cloetingh, S., 2013. Subduction and deformation of the continental lithosphere in response to plate and crust-mantle coupling. *Geology* 41, 1239–1242.
- Winker, C.D., 1996. High-resolution seismic stratigraphy of a Late Pleistocene submarine fan ponded by salt-withdrawal mini-basins on the Gulf of Mexico continental slope. 1996 Offshore Technology Conference, Proceedings, OTC 8024, pp. 619–628.
- Winker, C.D., Booth, J.R., 2000. Sedimentary dynamics of the salt-dominated continental slope, Gulf of Mexico: Integration of observations from the seafloor, near-surface, and deep subsurface. In: Weimer, P., Slatt, R.M., Coleman, J., Rossen, N.C., Nelson, H., Bouma, A.H., Styzen, M.J., Lawrence, D.T. (Eds.), *Deepwater reservoirs of the world*. 20th Annual Research Conference Proceedings: Houston, Texas, Society of Economic Paleontologists and Mineralogists, Gulf Coast Section, pp. 1059–1086.
- Withjack, M.O., Schlische, R.W., Olsen, P.E., 2002. Rift-basin structure and its influence on sedimentary systems. In: Renaut, R.W., Ashley, G.M. (Eds.), *Sedimentation in Continental Rifts*. SEPM Special Publication 73, pp. 57–81.
- Worrall, D. M., Snelson, S., 1989. Evolution of the northern Gulf of Mexico, with emphasis on Cenozoic growth faulting and the role of salt. In: Bally, A.W., Palmer, A.R. (Eds.), *The Geology of North American – An overview*, v. A. Geological Society of America, Boulder, pp. 97–138.

References

- Wu, S., 1993. Salt and slope tectonics offshore Louisiana. Ph.D. Dissertation, Rice University, Houston, 251 p.
- Wu, S., Bally, A., Cramez, C., 1990. Allochthonous salt, structure and stratigraphy of the north-eastern Gulf of Mexico. Part II: Structure. *Marine and Petroleum Geology* 7, 334–370.
- Xu, J.P., Noble, M.A., Rosenfeld, L.K., 2004. In-situ measurements of velocity structure within turbidity currents. *Geophysical Research Letters*, 31.
- Zalan, P.V., Severino, M.D.C.G., Rigoti, C.A., Magnavita, L.P., De Oliveira, J.A.B., Vianna, A.R., 2011. An entirely new 3D-view of the crustal and mantle structure of a South Atlantic passive margin – Santos, Campos and Espírito Santo basins, Brazil. *Search Discov.* (#30177)
- Zeng, J., Lowe, D.R., 1997. Numerical simulations of turbidity current flow and sedimentation: I. Theory. *Sedimentology* 44, 67–84.
- Zeng, J., Lowe, D.R., Prior, D.B., Wiseman, W.J., Bornhold, B.D., 1991. Flow properties of turbidity currents in Bute Inlet, British Columbia. *Sedimentology* 38, 975–996.
- Ziegler, P.A., Cloetingh, S., 2004. Dynamic processes controlling evolution of rifted basins. *Earth-Science Reviews* 64, 1–50.

Website

<http://www.cambridge.org/resources/emods/Chapter%2019/19%20Salt%20tectonics.html>

Summary

Passive continental margins display a great diversity of seafloor bathymetries induced by gravity driven extensional faulting and compressional folding, as well as diapiric movements of salt or mud. In many diapirically controlled settings, slope bathymetries are complicated and characterized by numerous ridges, trenches and minibasins such as in the Gulf of Mexico and offshore West Africa. These bathymetries play a significant role in controlling turbidity current behavior, the resulting sediment distribution and the internal architecture. Numerous researchers have investigated the influence of pre-existing or developing minibasins on the behaviour of turbidity currents and the resulting depositional systems using seismic data, analogue field outcrops, and laboratory and numerical experiments. The classic fill-spill model was proposed to describe the depositional process in linked intraslope minibasins in the Gulf of Mexico. However, due to the inherent limitations of present-day geophysical techniques and the limited exposure of field outcrops, the small-scale internal architecture and stacking pattern of such confined or semi-confined turbidite systems are still not well understood. The objective of this thesis is to better understand the interaction between flow, sediment and topography, and attempt to develop conceptual models for the changes in sediment dispersal and stacking patterns in diapirically controlled minibasins on passive margins.

In order to achieve this, we combine laboratory analogue modelling of intraslope minibasins with numerical flow simulations of multi-event turbidity currents. Previous studies on salt tectonics show that minibasins can be bounded by fold-and-fault systems or are sitting above allochthonous or autochthonous salt bodies. Gravity gliding explains well the typical structural zones (extensional, transitional and compressional) of passive margins, and therefore, in our studies, we conducted analogue tectonic sandbox experiments in which the deformations are driven gravity gliding. Sand and silicone putty are used to represent the prekinematic sediment and salt respectively. The experimental results from different setups show that three types of minibasins are formed and distinguished according to their boundary contact relationships: MB1 (no contact with the silicone layer), MB2 (the silicone layer as the basin base) and MB3 (the silicone diapir as the basin flank). The resulting topographies are scanned with a laser beam from which a digital elevation model is

obtained. One topography that is considered most realistic is selected and upscaled to dimensions that typically occur in nature. Furthermore, a channel is added on the shelf and the shelf break to serve as point source for the flows.

Subsequently, a numerical flow simulation software ("FanBuilder", Groenenberg et al., 2009) is employed to model multi-event low-density turbidity currents that flow from the incised channel down into the minibasins on the continental margin. A series of sets of parameters within ranges expected to occur in nature were compiled from literature study and used for the flow simulation experiments. Multiple flow events (non-equilibrium and equilibrium flows) from the same point source were run whereby the deposits were stacked on top of its predecessor. The resulting stratigraphy is then analyzed in 3-D, typically in a series of strike and dip sections. The experimental results of a series of numerical simulations are compared and discussed in terms of flow evolution, flow-deposit interaction, and internal architecture and stacking patterns.

In our models, the turbidity currents show a behaviour that can be divided into three phases: the ponding, the fill-and-spill, and the trapping stages. A significant grain-size partitioning happens at the early fill-and-spill stage, with the coarser grains getting trapped in the up-dip minibasin and finer grains transported by the spillover flows further downslope. Significant deposition in the minibasin takes place on the counterslope after the first minibasin depression. The flow pathway and evolution depend much on the flow volume reaching the up-dip minibasin, the remaining accommodation space, and the topography geometry and gradient. The deposits can smooth the gradient of the counterslope, allow more spillover, but they can also make the bounding ridge grow and move upstream and thereby restrict the flows to the minibasin. Overall, the turbidite system undergoes a sequence of progradation followed by aggradation and retrogradation. A sequence of coarsening- and thickening-upward trends is dominant in the down-dip minibasins, while the upper minibasin shows different sequences at different locations. The group depocenters in three minibasins all migrate towards upstream longitudinally and to the minibasin center laterally, which results in a back-filling stacking pattern. Some supportive evidence from published literature has been found to validate our main results. Recommendations for future research include seismic or outcrop studies, syn-tectonic sedimentation experiments, and numerical simulations of high-density gravity flows.

Samenvatting

De zeebodem in passieve continentale hellingen vertoont een grote variatie in bathymetrie als gevolg van plooiing en verschuiving langs breuken door tektonische compressie en zwaartekracht-gedreven extensie, alsook door de vorming van zout- en kleidiapieren. De topografie van de door diapieren beïnvloede continentale hellingen is complex en wordt getypeerd door ruggen, troggen en minibekkens zoals tegenwoordig kan worden waargenomen in de Golf van Mexico en voor de kust van West Afrika. Deze topografie heeft een grote invloed op het gedrag van troebelingsstromen, de resulterende sedimentverdeling en de bijbehorende interne opbouw. De invloed van reeds bestaande of ontwikkelende minibekkens op het gedrag van troebelingsstromen en hun resulterende afzettingssystemen is reeds door vele onderzoekers bestudeerd door middel van seismische gegevens, ontsluitingen en numerieke- en laboratoriumexperimenten. Op basis hiervan werd het inmiddels klassieke opvullings-en-overstromingsmodel voorgesteld dat het afzettingsproces in onderling verbonden minibekkens op de continentale helling in de Golf van Mexico beschrijft. Echter, door de intrinsieke beperkingen van hedendaagse geofysische technieken en de beperkte ontsluiting van analoge gesteenten worden de interne opbouw en stapelingspatronen nog steeds slecht begrepen. Dit proefschrift heeft tot doel om een beter begrip te vormen van de interactie tussen stroming, sediment en topografie om zo conceptuele modellen te ontwikkelen voor de veranderingen in sedimentverspreiding en stapelingspatronen in door diapieren beïnvloede minibekkens op passieve continentale hellingen.

Om dit doel te bereiken combineren we minibekkens op een continentale helling die in het laboratorium gemaakt zijn met behulp van kleinschalige zandbakexperiment met numerieke simulaties van meervoudige troebelingsstromen. Uit voorgaand onderzoek naar zouttektoniek blijkt dat minibekkens begrensd kunnen zijn door breuk- en plooisystemen. Daarnaast kunnen ze gevormd zijn bovenop autochtone of allochtone zoutlichamen. De karakteristieke structurele zones van passieve continentale hellingen (extensie, transitioneel en compressie) worden verklaard door zwaartekracht-gedreven afschuivingen. Van dit proces wordt in het laboratorium gebruik gemaakt voor de vorming en deformatie van de tektonische zandbakexperiment analogen. Om het sediment en het zout goed te

vertegenwoordigen worden tijdens het zandbakexperiment respectievelijk zand en silicone gel gebruikt. De resultaten van verschillende opstellingen laten zien dat er drie typen minibekken gevormd worden. Deze kunnen herkend worden aan de hand van de grensvlakrelaties: MB1 (geen contact met de silicone laag), MB2 (de silicone laag als de basis van het bekken) en MB3 (de silicone diapier als bekkenrand). De resulterende topografie wordt gescand met een laserstraal, waardoor een digitaal hoogtemodel verkregen wordt. De meest natuurgetrouwe topografie wordt geselecteerd en opgeschaald naar ware grootte. Vervolgens wordt een geul toegevoegd op het deel dat het continentale plat representeert om te dienen als beginpunt voor de troebelingsstromen.

Een numerieke stromingssimulator ('FanBuilder', Groenenberg et al., 2009) wordt gebruikt om een serie van troebelingsstromen met een lage dichtheid te modelleren, die vanuit de ingesneden geul op het continentaal plat naar de minibekken op de continentale helling stromen. Een verscheidenheid aan realistische invoerparameters zoals gedocumenteerd in de literatuur zijn vervolgens gebruikt als randvoorwaarden van de troebelingsstroomsimulaties. Meerdere stromingsgebeurtenissen (zowel evenwichts- als niet-evenwichtsstromingen) worden geïnitieerd vanuit hetzelfde punt op het numeriek stromingsrooster waardoor nieuwe afzettingen telkens bovenop hun voorgangers neergelegd worden. De resulterende opbouw wordt vervolgens geanalyseerd in drie dimensies in een serie van stekkings- en hellingsdoorsneden. De experimentele resultaten van meerdere numerieke simulaties worden vergeleken en bediscussieerd voor wat betreft stromingsontwikkeling, interactie tussen afzettingen en interne architectuur en stapelingspatronen.

Het in onze modellen vertoonde gedrag van troebelingsstromen kan worden onderverdeeld in drie fasen: het verzamelen, opvullen-en-overstromen en het afvangen. Een belangrijke ontwikkeling in de korrelgrootteverdeling van de troebelingsstroomafzetting vindt plaats in de vroege opvul-en-overstromingsfase, waarbij de grotere korrels gevangen worden in het bovenste minibekken en de fijnere korrels door overstroming verder hellingafwaarts worden meegevoerd. Afzettingen vormen met name op de tegenhelling van het eerste minibekken dat de troebelingsstroom bereikt. Het stroming pad en de ontwikkeling in de tijd daarvan zijn afhankelijk van het volume van de troebelingsstroom dat het bovenste minibekken bereikt, de resterende accommodatieruimte en de topografische gradiënt en geometrie. De troebelingsstroomafzettingen kunnen de gradiënt van de tegenhelling van het eerste minibekken verlagen waardoor meer overstroming ontstaat, maar ze kunnen de bekkenrand ook stroomopwaarts opbouwen waardoor stroming naar lager gelegen minibekken juist vermindert. Over het algemeen kunnen de troebelingsstroomafzettingen gekarakteriseerd worden door een opeenvolging van progradatie, gevolgd door aggradatie en retrogradatie. In de stratigrafie is een trend herkenbaar van fijn naar grof sediment in steeds dikker wordende eenheden in de laagste minibekken. Het bovenste minibekken laat een veel heterogenere opbouw zien. De gebieden met de hoogste afzettingssnelheid in de drie minibekken migreren allemaal stroomopwaarts en naar het centrum van de minibekken toe, hetgeen resulteert in een stroomopwaarts opvullingspatroon. De belangrijkste resultaten van

onze modelstudie worden gestaafd door enkele veldstudies die beschreven zijn in de vakliteratuur. Aanbevelingen voor toekomstig onderzoek omvatten het gebruik van seismische studies en het bestuderen van analoge gesteenteontsluitingen, afzettingsexperimenten tijdens tektonische activiteit en numerieke simulaties van door zwaartekracht gedreven stromen met een hogere dichtheid.

Acknowledgements

I would like to express the deepest gratitude to my promoter and supervisor Prof. dr. Stefan M. Luthi. Stefan, thank you so much for providing me such a precious opportunity to perform this project. It is your encouragement and support that stimulated my progress through the four-year PhD research and life. Thanks for organizing the exciting and unforgettable field trip to the Karoo Basin in South Africa, which introduced me into the turbidite world. Thanks also for introducing me to the TecLab at the VU University in Amsterdam to conduct the sandbox experiments. Thanks for supporting me to communicate with the stratigraphic group in University of Liverpool and University of Leeds. And thanks for giving me the opportunity to present my research results at international conferences. In short, I would like to express my heartfelt gratitude for your effort and time.

This projects started with bathymetric analogue modelling at TecLab at the VU University in Amsterdam. I would like to extend many thanks to Dr. Dimitrios Sokoutis and Dr. Ernst Willingshofer. Thanks for your help, effort and patience in guiding me so I could complete the four time-consuming experiments. I would also like to thank my previous colleague Dr. Remco Groenenberg. Remco, thank your for providing your numerical simulation software FanBuilder and all your advices. Another thank goes to Dr. Ricardo S. Jacinto for his useful suggestions about improving parameter setting-up of turbidity-current numerical modelling.

A special thank is addressed to Dr. David Hodgson. David, thank you for inviting me to visit and collaborate with your fantastic research groups at the Universities of Liverpool and Leeds. I always enjoyed the great benefit of your guidance. Thanks for your effort and patience in improving my research methods and my scientific writing.

A harmonious atmosphere in our Applied Geology family is like a piece of wonderful music in my PhD life. I therefore would like to thank my lovely colleagues Adriaan, Andrea, Cees, Duddy, Geertje, Helena, Ilja, Koen, Kevin, Liang, Jianguang, Menno, Nico, Pantelis, Rémi, Rick, Runhai and Wieske. I really enjoyed every lunch time, coffee breaks and other activities we did together.

Acknowledgements

Friendship is one of the most wonderful gifts through peoples' lives, and I would like to appreciate all the cheerful moments with my good friends in Delft. Cong Li, I never forget the wonderful time we spent in Luxemburg and Brussels. Pengpeng Wu, the encouragement from you helped me go through a difficult time. Liang Li and Peipei Dong, you are a warm-hearted couple who always provided me with useful information. Hua Guo, thanks for your patience in talking and listening to me. Ting Zhou, Li Mo, Jianbin Fang, Shuhong Tan, Chang Wang, thanks for your delicious dinners. Thanks to all of my friends in China. Thanks to Prof. dr. Zhiliang He at Petroleum Exploration & Production Research Institute of SINOPEC. Thanks to my previous PhD supervisor, Prof. dr. Zhenkui Jin in China University of Petroleum (Beijing). And thanks to my Master supervisors, Prof. dr. Taiju Yin and Prof. dr. Changmin Zhang at Yangtze University.

The greatest thank appertains to my deeply beloved family, my mother, my aunts and uncles, and my grandpa. It is your love that supports and encourages me to bravely lead my own life. A special thank goes to my husband; Junfeng, you are the brilliant sunshine in my life. Without your support I could not have been able to succeed in my PhD.

Last but not least, I would like to dedicate this thesis to my dearest family.

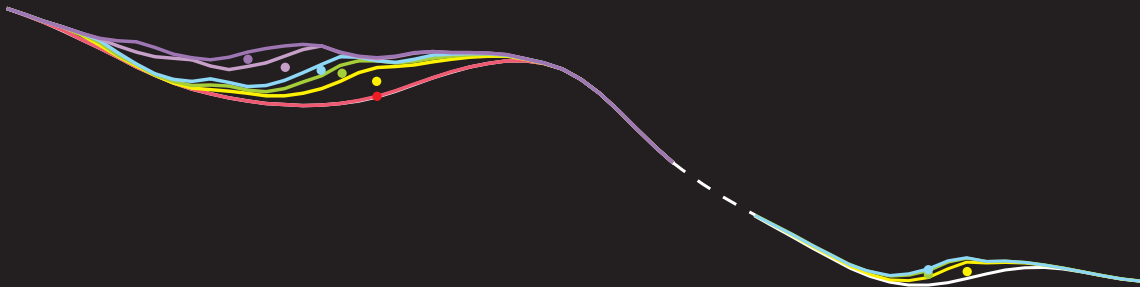
Curriculum Vitae

Xiaoxi Wang was born on 12 December, 1982 in Puyang, an oil city in Henan province, China. In 2002, she started a B.Sc. in Computer Science at Yangtze University. From 2006 to 2009, Xiaoxi studied Geology as a M.Sc. candidate at the same university. For her M.Sc. thesis she studied the stratigraphy sequence, and the microfacies dispersal and stacking patterns of braided-river delta systems in a complex faulted oilfield block, Qaidam Basin, China. After one-year Ph.D. study in Geology at China University of Petroleum (Beijing), Xiaoxi transferred to Delft University of Technology in August, 2010. She started a new Ph.D. research at TU Delft on modelling turbidity currents on complex passive margin topographies, supervised by Prof. dr. Stefan M. Luthi. In this project, Xiaoxi performed analogue experiments of passive margins bearing salt in the ISES tectonic laboratory supervised by Prof. dr. Dimitrios Sokoutis, at the Vrije Universiteit Amsterdam. This project also has a close collaboration with Dr. David Hodgson's stratigraphy group (University of Liverpool and University of Leeds). Xiaoxi has presented her work at numerous conferences. In 2012, she received the Best Poster Award in the research meeting of the Department of Geotechnology and the Department of Earth and Atmospheric Sciences.

List of proceedings and publications:

- Wang, X., Luthi, S.M., Hodgson, D.M., submitted. Evidence for lateral and longitudinal compensation in diapirically controlled minibasins on passive continental margins based on fluid flow modeling. *Sedimentology*.
- Wang, X., Luthi, S.M., Hodgson, D.M., Sokoutis D., Willingshofer, E., 2012. Numerical models of turbidite distribution in submarine diapirically controlled settings. AAPG Annual Convention and Exhibition conference, Long Beach, California, USA.
- Luthi, S.M., Wang, X., 2012. Evidence for lateral and longitudinal compensational stacking in sub-basins based on numerical models of turbidity currents on complex margin topographies. EGU General Assembly, Vienna, Austria.

- Wang, X., Luthi, S.M., Sokoutis, D., Willingshofer, E., Hodgson, D.M., 2012. Modeling of subaqueous gravity flows on complex rift margin topographies. Nederlands Aardwetenschappelijk Congres (NAC) 11, Veldhoven, The Netherlands.
- Wang, X., Luthi, S.M., Sokoutis, D., Willingshofer, E., Hodgson, D.M., 2012. Modeling of subaqueous gravity flows on complex rift margin topographies. Research Meeting, The Department of Geotechnology and the Department of Earth and Atmospheric Sciences.



ISBN 978-94-6295-067-2



9 789462 950672